Correcting Galileo's Energetic Particle Detector Data; Methodology, Implications and Applications

Thesis Submitted for the degree of

Doctor of Philosophy

at Aberystwyth University

Zoë H. Lee-Payne

Supervised by:

Prof Manuel Grande

Institute of Mathematics, Physics and Computer Science

Aberystwyth University

August 2018

‘I therefore concluded, and decided unhesitatingly, that there are three stars in the heavens moving about Jupiter, as Venus and Mercury about the Sun; which at length was established as clear as daylight by numerous other observations.’

Referring to his pioneering telescope observations.

— Galileo Galilei

The Starry Messenger (Mar 1610). Quoted in Edmund Blair Bolles, Galileo's Commandment (1999), 104.

Acknowledgements

This thesis is conducted under a Science and Technology Facilities Council (STFC) studentship to the Solar System Physics group at Aberystwyth University.

I would like to thank my supervisor, Prof Manuel Grande, for his help and for his ability to always manage to introduce me to someone new at conferences. Also, thanks to my second supervisor, Prof Neil Glasser, for offering a different perspective on geology outside of Earth.

I would also like to thank Dr Norbert Krupp, for insight into the EPD; and Dr Peter Kollmann, for access to the EPD data and in-depth explanations to data issues. Special thanks go to, Dr Tom Knight, for python assistance; and, Dr Tony Cook, for access to his research on elevation models; and finally to Jackie Hedley and the office team, for always knowing which form I need to fill out, and the continual re-filling of the coffee room biscuit tin!

Personal thanks go to Jace and Emra for putting up with me during this process, I wouldn't have managed this without you both; and to Miki and Sarah, for our yearly meet ups and our many skype calls. To my Mother, Sue and her boss, Ian for diligently reading through the first draft, you are both grammatical wizards. And last but certainly not least, to the many who have come and gone from the second office on the third floor, you have kept me sane for nearly 4 years and I am very thankful for it!

Abstract

Over the course of its 8-year mission the Energetic Particle Detector, launched in 1989 on the Galileo satellite, took data on the Jovian Particle environment. This thesis focuses on the data from the EPD; specifically, from the CMS telescope on the top of the instrument. Comparing data from the beginning of the mission to the final data retrieved and quantifying the clear discrepancy in the loci defining the elements.

These element loci reveal that the detector is decaying in sensitivity. The amount of energy drop corresponding to each element such that it is clear a dead layer had built up on the front of the detector. The larger element particles lose more energy passing through this dead layer than lighter elements, causing a systematic energy drop as it thickens throughout the mission. This thickening of the dead layer is caused by the radiation impacting onto the detector denaturing the sensitive volume; affecting both the High Rate data and the Real-Time count rate data.

The High rate data is only available in short sections of the mission, mainly during the flybys and periods of interest. Chapter 2 aims to correct this data is based on the nature of the detector, and the build-up of the dead layer. Through the chapter the dead layer thickness is estimated throughout the mission using calibration masses with a simulated depth of dead layer; giving an evolution of the dead layer as the mission progresses.

Knowing the thickness of the dead layer allows a correction to be made using a selection of masses and the known energy lost for the dead layer present. The final correction is made by working backwards; starting with all the possible test masses, and calculating the energy loss of the particle passing through the established dead layer. This loss is the applied to the possible starting energies and a final comparison to real readings is made. This highlights the closest value of the original particle.

Chapter 3 focuses on the Correction of the real time count rate channels, this requires a different approach; the dead layer thickness can only be used in assessing the progress of the correction. Instead, this correction method uses comparative count rates from relative locations in the Jovian system at different times. These are then used to calculate a value of the decay in terms of number of counts hitting the detector. By

systematically applying this value to the counts registered by the detector brings the values closer to the true values. This intensive iterative process encompasses the changing values of counts over the mission and the effects of efficiency dropping over the mission. Each individual count rate channel is processed in this manner.

Chapter 4 is focused on using the results from the correction of the EPD data and using it to evaluate the sputtering on the Surface of the Jovian moons. Looking in detail at flyby data and the sputtering yields available from literature, the erosion effect on the surface can be calculated. By using the sputtering rate, the real effects of the correction can be felt, the misallocation of elements in the original data means the higher numbers of heavier ions greatly impacted the overall erosion.

The final research Chapter, pulls together the previous three to focus on the surface of the Icy moons, specifically Europa. The first half focuses on imaging the surface and the ability to draw more information from the available images. Using digital elevation techniques to develop a height profile and evaluate key features from a different perspective.

With the addition of a digital elevation model the impact of surface erosion is visible. By using geological techniques and combining it with feature formation theory an estimation can be made of the age of the surface features, in a small scale proof-of-concept study.

From this work, much can be done towards research for future Jupiter and high radiation environment instruments; from a perspective of having a greater understanding of the environment as a whole and improving radiation shielding, to also being able to better post collection process new data. The proof-of-concept investigations in Chapter 5 will allow large scale studies of the Europan surface with the arrival of Europa Clipper, and it can easily be adapted to the other moons for use with imaging from the JUICE mission.

Overall the aim is to improve upon current data and then better evaluate the Jovian system and its interaction of the radiation environment with the surfaces of the icy moons.

Contents

Acknowledgements ii
Abstract iii
Contents v
List of Figures viii
List of Tables xv
1 Introduction and Overview 1
1.1 Introduction 1
1.2 Jupiter 2
1.2.1 Aurora 4
1.2.2 Jupiter's radiation environment 6
1.2.3 The Neutral Cloud 8
1.3 Moons 9
1.3.1 Moon Io 9
1.3.2 Moons Ganymede and Callisto 10
1.3.3 Moon Europa 12
1.4 Europa 14
1.4.1 Sputtering 14
1.4.2 Frost 15
1.4.3 Surface Geology: 16
1.5 Europa's ice Layer: Thick or Thin? 22
1.5.1 Relations with Earth Geology: 22
1.5.2 Age of Europa's Surface: 23
1.6 Galileo Orbiter 27
1.6.1 Mission overview: 27
1.6.2 Data Problems 29
1.7 On Board Instruments and Science Objectives: 30
1.7.1 The Solid State Imager, SSI: 31
1.7.2 The Energetic Particle Detector, EPD: 31
2 Pulse Height Analysis Plot Correction, and Estimation of Dead Layer. 33
2.1 The Energetic Particle Detector, EPD 33
2.2 Technical details: 36

2.2.1 A Particle in the EPD 36
2.2.2 Silicon Semi-conductor detector 40
2.3 Data from the Mission: 42
2.3.1 Uses for the data: 46
2.3.2 Problems with the data: 46
2.4 Evaluating the EPD's Dead layer thickness 51
2.4.1 Using SRIM 51
2.4.2 Dead Layer Estimation from PHA graphs 55
2.4.3 Dead Layer Estimation from Calibration 59
2.4.4 Instrument Calibration 66
2.4.5 Results of Dead Layer Thickness Estimations. 69
2.5 Correcting with respect to the Dead Layer 72
2.5.1 Method of correction 73
2.5.2 Implementing the correction 74
2.5.3 Evaluating the New Particle positions 75
2.5.4 Improved Implementation of Correction 78
2.6 Final Corrected Results 82
2.7 Conclusions 87
3 Count Rate Channel Correction and Comparison to Voyager Data 88
3.1 Correcting the EPD data 90
3.1.1 Why the correction is Important 90
3.2 Method for Correction 93
3.2.1 Steps of Correction 94
3.2.2 Problems Encountered During Development of Correction Method 99
3.2.3 Method and Mathematical Derivation 102
3.2.4 First Outputs and Secondary Program Results 103
3.2.5 Initial Correction Analysis and Issues 110
3.3 Power Spectra 114
3.3.1 Comparing Count Rates 114
3.3.2 Energy Spectra: Advantages and Disadvantages 117
3.3.3 Re-checking the Dead Layer Estimations 118
3.3.4 Code upgrades 124
3.4 Final Corrected Count Rates 127
3.4.1 TH1: Iron and 'Heavy' Particles 127

3.4.2 TS1, TS2, TS3: Sulphur 127
3.4.3 TO1, TO2, TO3, TO4: Oxygen 130
3.4.4 TA1, TA2: Helium 133
3.4.5 TP1, TP2, TP3: Hydrogen 134
3.5 Comparison to Voyager Data 137
3.5.1 Major comparisons in the literature: 137
3.5.2 Preparing the data 138
3.5.3 Initial Comparisons 143
3.5.4 Problems with the ratio calculations 148
3.6 Conclusions 154
4 Sputtering on Europa: An Initial Estimation of Surface Age. 155
4.1 Analysis of New EPD data during the Europa flybys. 155
4.1.1 Flyby Data 155
4.1.2 Flux Rate vs. Count Rate 158
4.1.3 Count Distribution 160
4.2 Sputtering 165
4.2.1 Sputtering on Icy Surfaces 165
4.2.2 Sputtering Rate 168
4.2.3 Results and Comparisons 173
4.2.4 Comparison with Current Estimations 176
4.3 Conclusions 179
5 Surface Age 180
5.1 Surface Feature Formation and Cross Cutting 180
5.1.1 Imaging the Surface 183
5.2 Heights of the Features on the Surface 188
5.2.1 Extracting Height Profiles 194
5.2.2 Evaluating Height Change into Surface Age 198
5.3 Conclusions 205
6 Conclusions 206
6.1 General Conclusions 206
6.2 Further Work 209
7 References 211

List of Figures

Figure 1.2-1: Basic overview of the magnetic field of the Earth, the Sun and Jupiter, Pictured scaled as though within a solar wind like drag force [Khurana, 2001]. 3

Figure 1.2-2: The surface spectra of Io. 7

Figure 1.2-3: This data was taken by the Charge Energy Mass Spectrometer (CHEMS) on Cassini during its flyby of Earth and Jupiter (Bagenal, 2007). 7

Figure 1.3-1: A spectrum of the darker areas of Europa's surface, these are the non-icy areas. The best matches for the spectrograph were obtained for hydrated salts; including sulphates and carbonates such as: natron ($Na_2CO_3(10H_2O)$), epsomite ($MgSO_4(7H_2O)$), hexahydrite ($MgSO_4(6H_2O)$). (McCord et al., 1998) 12

Figure 1.4-1: Figure 3 of (Figueredo and Greeley, 2004) showing examples of different formations identified in the paper (a) crater material, (b) chaos, (c) elevated chaos, (d) subdued chaos, (e) double ridge, (f) single ridge, (g) ridge complex, (h) medial-trough ridge, (i) smooth band, (j) ridged band, (k) lineated band, (l) ridged plains, (m) subdued plains, (n) subdued-pitted plains. Where necessary, arrows indicate the feature under consideration. 20

Figure 1.5-1: Figure 4 of (Kattenhorn and Prockter, 2014). The Image shows the similar Earth like plate tectonics that happen on Europa; also highlighting the differences in the warmer convecting layer absorbing the upper layer before it reaches the liquid ocean. 23

Figure 1.6-1: A Public information flyer for Galileo mission produced by NASA. It details the stages of the mission and the milestones reached by the team. 27

Figure 1.6-2: The full orbit path of Galileo with marked orbit numbers and distance isobars [Jun et al., 2005] 29

Figure 2.1-1: line drawing of the EPD system, indicating the LEMMS system and the CMS section (Williams et al., 1992). 33

Figure 2.1-2: The Energetic Particle Detector flight model with flight covers (Williams et al., 1992). 34

Figure 2.2-1: Technical detail of the interior of the CMS flight model (Williams et al., 1992). 36

Figure 2.2-2:TOF versus energy observed in detector KT. Discriminator levels defining the indicated TOF rate channels (solid lines), predicted TOF vs. E curves (dashed lines), and data from accelerator calibrations (points) are shown.[Williams et al., 1992] 39

Figure 2.2-3:Simplified diagram of a generic silicon semi-conductor detector. 40

Figure 2.3-1:Overview of recorded data plotted along the orbit path. Colour scale for the average intensity of the channels with Jupiter marked as the small dashed line in the centre of the orbit loop structure. 43

Figure 2.3-2: Real mission data. PHA analysed data plotted as Time of Flight against Energy. Data taken on 29th September 1996. 44

Figure 2.3-3: left: PHA analysed data plotted as Time of Flight against Energy; data taken on 29th September 1996. Right: PHA analysed data plotted as Time of Flight against Energy; data taken on 27th October 2002, after 7 additional years of mission recording from the PHA plot on the left. 45

Figure 2.3-4: shows the unfurling problems of the main antenna on Galileo[Isbell, 1995]. 47

Figure 2.4-1: visual representation of the effect of the dead layer on the channel boundary lines. Direct comparison between the original line definitions and the lines when 0.04µm dead layer is applied. 53

Figure 2.4-2: visual representation of the effect of the dead layer on the channel boundary lines. Direct comparison between the original line definitions and the lines when 0.10µm dead layer is applied. 54

Figure 2.4-3: visual representation of the effect of the dead layer on the channel boundary lines. Direct comparison between the original line definitions and the lines when 0.16µm dead layer is applied. 55

Figure 2.4-4: PHA Data graph from 1996 data set with overlaid loci best fit line. 56

Figure 2.4-5: PHA plot from 2001 with overlaid trend lines from 1996 with 0.1µm dead layer applied. 57

Figure 2.4-6:PHA plot from late 2002 with overlaid trend lines from 1996 with 0.5µm dead layer applied. 58

Figure 2.4-7:PHA plot from 2002 with overlaid trend lines from 1996 with 0.3µm dead layer applied. 58

Figure 2.4-8: comparison between a 0.1µm dead layer (red line) against a 30% gain drop in energy from the detector (yellow line) 59

Figure 2.4-9: PHA Data graph from 1996 data set with overlaid loci of the generated calibration lines. 61

Figure 2.4-10: Increase in dead layer over mission years determined by best fit data. 65

Figure 2.4-11: Updated Increase in dead layer over mission years determined by best fit data, accounting for instrument calibration. Background markers show the time of each Europa Flyby for context. 68

Figure 2.4-12: Fitting of the increase in dead layer over time. 70

Figure 2.5-1: Warping of the channel boundaries due to varying thicknesses of the dead layer. 73

Figure 2.5-2: Each incoming particle (represented by the Orange star) is tested against the series of bins for the applicable TOF. The binning routine then allocates the most similar shift in energy to the incoming particle. 74

Figure 2.5-3: Data from pre-1999 mission. a) Original data re-plotted for comparison. b) Corrected Data, re-plotted with the original channel boundaries overlaid. 76

Figure 2.5-4: Data from post 1999 mission. a) Original data re-plotted for comparison. b) Corrected Data, re-plotted with the original channel boundaries overlaid. 76

Figure 2.5-5: Diagram based on Table 2.4-2, including the indices used for the correction method where: P represents known masses and associated energies from TOF, K represents known dead layer thicknesses from the table, and J notes the testable masses and their associated energies. 78

Figure 2.5-6: Close Diagram of the main points defining the position of the incoming particle by values in Table 2.4-2. 79

Figure 2.6-1: (a) correction input data against correction output data (b): from 2002 day 295 to 305. 83

Figure 2.6-2: Before (a) and after (b) correction: data from 1996 day 272 to 287. 84
Figure 2.6-3: Before (a) and after (b) correction: data from 1997 day 51 to 57. 84
Figure 2.6-4: Before (a) and after (b) correction: data from 1999 day 180 to 223. 85
Figure 2.6-5: Before (a) and after (b) correction: data from 2000 day 1 to 5. 85
Figure 2.6-6: Before (a) and after (b) correction: data from 2002 day 295 to 305. 86
Figure 3-1: An example of the count rate data set for the TS1 Sulphur channel. Top: full channel read out over the mission, Bottom: full data plotted as average along the radial distance from Jupiter, by year. 88
Figure 3.2-1: Method of evaluating overlaying orbits at different time periods to estimate changes in the data under similar conditions. t_i represents the time stamp associated with readings along the orbit path. 98
Figure 3.2-2: CV for grouped channels. 100
Figure 3.2-3: Trends of the channel count rates. These trends are inversely proportional to the expected values of CV. 101
Figure 3.2-4: Channel TH1 first correction attempt (Pre-correction inset in top right for reference). 104
Figure 3.2-5: Channel TS1 first correction attempt (Pre-correction inset in top right for reference) . 104
Figure 3.2-6: Channel TS2 first correction attempt (Pre-correction inset in top right for reference) . 105
Figure 3.2-7: Channel TS3 first correction attempt(Pre-correction inset in top right for reference) .. 105
Figure 3.2-8: Channel TO1 first correction attempt (Pre-correction inset in top right for reference). 106
Figure 3.2-9: Channel TO2 first correction attempt (Pre-correction inset in top right for reference) 106
Figure 3.2-10: Channel TO4 first correction attempt (Pre-correction inset in top right for reference) 107
Figure 3.2-11: Channel TO3 first correction attempt (Pre-correction inset in top right for reference) 107
Figure 3.2-12: Channel TA1 first correction attempt (Pre-correction inset in top right for reference) 108
Figure 3.2-13: Channel TA2 first correction attempt (Pre-correction inset in top right for reference) 108
Figure 3.2-14: Channel TP1 first correction attempt (Pre-correction inset in top right for reference) 109
Figure 3.2-15: Channel TP2 first correction attempt (Pre-correction inset in top right for reference) 109
Figure 3.2-16: Channel TP3 first correction attempt (Pre-correction inset in top right for reference) 110
Figure 3.2-17: Overview of the Solar flux from the GOES mission data logs. The red vertical line at 12noon on the 18th of the month defines the launch time of the STS-34, NASA Space Shuttle Atlantis; carrying the payload Galileo. 112
Figure 3.3-1: Original data set of channel TS1. The data is very variant depending on distance from Jupiter, each peak visible matches with a close in flyby of Jupiter or its moons. 115
Figure 3.3-2: Energy Spectrum of the three sulphur channels using original uncorrected data set. .. 116

Figure 3.3-3: Energy Spectrum of the three sulphur channels using data processed by the method described above in section 3.2. 116

Figure 3.3-4: 1996 original data with a simulated efficiency drop added. After 1996 the values denoting each line are the percentage value of 1996 counts present, where 1996 is 100% of the counts. 122

Figure 3.3-5: Efficiency drop over mission years by element 123

Figure 3.3-6: Corrected data plotted in the same manner as above; assuming the counts of a channel are evenly distributed across the whole of the energy bounds of the channel. 125

Figure 3.4-1: Final correction of TS1 channel. 128

Figure 3.4-2: Final correction of TS2 channel. 129

Figure 3.4-3: Final correction of TS3 channel 129

Figure 3.4-4: Final correction of TO1 channel 130

Figure 3.4-5: Final correction of TO2 channel 131

Figure 3.4-6: Final correction of TO4 channel 132

Figure 3.4-7: Final correction of TO3 channel 132

Figure 3.4-8: Final correction of TA1 channel 133

Figure 3.4-9: Final correction of TA2 channel 134

Figure 3.4-10: Final correction of TP1 channel 134

Figure 3.4-11: Final correction of TP2 channel 135

Figure 3.4-12: Final correction of TP3 channel 135

Figure 3.5-1: Documented Trajectory of Voyager 2 during its flyby of Jupiter in 1979. Figure 2 of the publication (McNutt et al., 1981) with caption. 141

Figure 3.5-2: Voyager trajectory (red dash line) overview used in *Radioti et al.* overlaid with a grid at every $10R_J$, blue boxed areas show the corrected Galileo data to be used in the correction. 142

Figure 3.5-3: First look at original against corrected data, comparison. The corrected data in red is overlaid on the same plot produced in (Radioti et al., 2005). 143

Figure 3.5-4: Ratio of the integrated power laws of Sulphur against Oxygen at 39KeV/nuc, for the corrected data set, original data set, and Voyager 2 measurements from (Radioti et al., 2005). 144

Figure 3.5-5: Ratio of the integrated power laws of Sulphur against Helium at 89KeV/nuc, for the corrected data set, original data set, and Voyager 2 measurements from (Radioti et al., 2005). 145

Figure 3.5-6: Ratio of the integrated power laws of Sulphur against Helium at 800KeV/nuc, for the corrected data set, original data set, and Voyager 2 measurements from (Radioti et al., 2005). 146

Figure 3.5-7: Ratio of the integrated power laws of Oxygen against Helium at 89KeV/nuc, for the corrected data set, original data set, and Voyager 2 measurements from (Radioti et al., 2005). 147

Figure 3.5-8:Ratio of the integrated power laws of Oxygen against Helium at 800KeV/nuc, for the corrected data set, original data set, and Voyager 2 measurements from Radioti et al., 2005. 147

Figure 3.5-9: Ratio of the integrated power laws of Protons against Helium at: a) 185KeV/nuc and b) 800KeV/nuc, for the corrected data set, original data set, and Voyager 2 measurements from Radioti et al., 2005. 148

Figure 3.5-10: Ratio of the integrated power laws of Sulphur against Helium at 89KeV/nuc, for the pre-1999 corrected data set, original data set, and Voyager 2 measurements from (Radioti et al., 2005). 149

Figure 3.5-11: Ratio of the integrated power laws of Oxygen against Helium at 800KeV/nuc, for the pre-1999 corrected data set, original data set, and Voyager 2 measurements from (Radioti et al., 2005). 150

Figure 3.5-12: Ratio of the integrated power laws of Sulphur against Helium at 800KeV/nuc, for the pre-1999 corrected data set, original data set, and Voyager 2 measurements from (Radioti et al., 2005). 150

Figure 3.5-13: Ratio of the integrated power laws of Oxygen against Helium at 89KeV/nuc, for the pre-1999 corrected data set, original data set, and Voyager 2 measurements from (Radioti et al., 2005). 151

Figure 3.5-14: Ratio of the start TOF MCP counts against the integrated power law of Helium at 185KeV/nuc, for the pre-1999 corrected data set, original data set, and Voyager 2 measurements from (Radioti et al., 2005). 152

Figure 3.5-15: Ratio of the start TOF MCP counts against the integrated power law of Helium at 800KeV/nuc, for the pre-1999 corrected data set, original data set, and Voyager 2 measurements from (Radioti et al., 2005). 153

Figure 4.1-1: Sulphur values of the E12 flyby. Showing the before correction value, the post correction value and the post correction all data average for the distance from Jupiter over the whole mission. 157

Figure 4.1-2: Oxygen values of the E12 flyby. Showing the before correction value, the post correction value and the post correction all data average for the distance from Jupiter over the whole mission. 158

Figure 4.1-3: PHA plot over the E4 flyby overlaid with channel boundaries. Closest approach in 1996 day 354, at 06:52:58. 161

Figure 4.1-4: PHA plot over the E26 flyby overlaid with channel boundaries. Closest approach in 2000 day 3, at 17:59:56. 162

Figure 4.1-5: PHA plot over the E12 flyby overlaid with channel boundaries. Closest approach in 1997 day 350, at 12:03:02. 162

Figure 4.1-6: Histogram of sulphur energy distribution during E12. 163

Figure 4.1-7: Fitting of Sulphur distribution 164

Figure 4.2-1: Billiard Ball dynamical motion showing the four main cases of sputtering. Each initiated by a single particle impacting a surface. 166

Figure 4.2-2: sputtering yields from Cassidy et al., (2013), showing two modelling results, red and blue curves, overlaid with experimental results from Fama et al.,(2008). 168

Figure 4.2-3: Red points: Fit of the Oxygen sputtering yield to be integrated over, channel boundaries are marked in the blue vertical lines. (Blue points show experimental results) 170

Figure 4.2-4: Red points: Fit of the Helium sputtering yield to be integrated over, channel boundaries are marked in the blue vertical lines. (Blue points show experimental results) 171

Figure 4.2-5: Red points: Fit of the Hydrogen sputtering yield to be integrated over, channel boundaries are marked in the blue vertical lines. (Blue points show experimental results) 171

Figure 4.2-6: Fit of the Sulphur sputtering yield to be integrated over, channel boundaries are marked in the blue vertical lines. (Blue points show experimental results) 172

Figure 5.1-1: Ridge formation diagrams from (Greenberg et al., 1998). 182

Figure 5.1-2: Overlapping coverage of the Galileo flybys of Europa and the camera views available from chapter 15 of (Bagenal et al., 2004)..... 184

Figure 5.1-3: Outline map of High resolution areas of coverage from SSI, generated using USGS's (US Geology Survey) PILOT mapping software (https://pilot.wr.usgs.gov/) 184

Figure 5.1-4:Overlapping of singular images from SSI mapped to form a stereo set with which a 3D image and height map can be produced. Image from (Chuang et al., 1998) conference proceedings later published, with caption, in (Kadel et al., 2000). 185

Figure 5.1-5: Composite image of the first set of Images shown in red in Figure 5.1-4. Images taken at: 1998-05-31 21:10:34..... 186

Figure 5.1-6: Composite image of the second image set. Taken at: 1998-05-31 21:17:38. Shown in blue in Figure 5.1-4..... 186

Figure 5.1-7: Position of selected images of Europa's surface at equivalent longitude and Latitude on Earth. 187

Figure 5.2-1: Digital elevation model of overlapping images of Europa. 188

Figure 5.2-2: from Cook and Robinson, 2000; diagram of the stereo image set us required for optimal digital elevation models. 189

Figure 5.2-3: a) DEM overlaid with the outline of the image sets, for clarity in image orientation. b) DEM overlaid with both image sets to show the features between the missing areas. 190

Figure 5.2-4: Notable features highlighted in both original image and DEM for clarity and to illustrate areas of missing heights in the DEM. 191

Figure 5.2-5: Example of the height profile extraction routine output. 193

Figure 5.2-6: Overlay of all height selections investigated. Each profile line cut is marked on the DEM (Bottom) and original image (Top) in cyan. 194

Figure 5.2-7: Lower height profile over the large wide-band linea. 195

Figure 5.2-8: Upper height profile over the large wide-band linea. 195

Figure 5.2-9: Overlaid comparison of the two wide-band profiles, aligned using the highest peak in each profile as a marker. 196

Figure 5.2-10: Upper height profile alongside the large wide-band linea. 197

Figure 5.2-11: Lower height profile alongside the large wide-band linea. 197

Figure 5.2-12: Direct comparison of the lengths of the profiles of interest. Top left: Lower height profile from alongside the large wide-band linea, Top right: both profiles from the wide-band linea, Bottom: Upper heigh profile from alongside the wide-band linea. 198

Figure 5.2-13: Profiles across the Wide-band Linea against the average height from the surface alongside the band. 200

Figure 5.2-14: Height and Position aligned profiles of the Wide-band Linea, with the average of the profiles included. The length of the profiles cropped to the width of the wide-band..... 201

Figure 5.2-15: Height profile above the surrounding surface average with contour profiles at every 10m depth from the surface. 202

Figure 5.2-16: Ice erosion time by depth over the width of the Wide-band linea. 203

List of Tables

Table 1.4-1:Europa's geographical feature list including a feature description and nomenclature 16

Table 1.6-1: Galileo Orbit designation and closest approach/ primary orbit objective 28

Table 1.7-1: List of the Flown Instruments on board the Galileo spacecraft and their principle investigators 30

Table 2.4-1: The Sulphur Ion stopping range in Silicon 52

Table 2.4-2: Energy lost passing through Dead Layer depth of Silicon 53

Table 2.4-3: Time of flights for Real and calibration data to be compared, grouped into elements over the full energy range of the instrument. Missing section designate where the read data was missing or undistinguishable. 60

Table 2.4-4: Initial results from Chi Squared test of dead layer comparison. Bordered cells correspond to the closest matching dead layer for each year. 63

Table 2.4-5: Percentage of fit for 35, 28 and 21 degrees of freedom. 63

Table 2.4-6: Results from Chi Squared test of dead layer comparison with added intermediate dead layers. Bordered boxes correspond to the closest matching dead layer for each year. 64

Table 2.4-7: Results from Chi Squared test of dead layer comparison accounting for the instrument calibration pre-mission launch. Bordered boxes correspond to the closest matching dead layer for each year. 67

Table 3.3-1: shows the chi-squared values from the comparison. The best matches for each year identify a far higher dead layer than expected from the results of the same comparison of the PHA plots 119

Table 3.3-2: Table of chi-squared fits for 1996 data with simulated efficiency drop compared with the yearly data sets. The bordered boxes denote the best fit of efficiency drop for the year in question. The shaded boxes are the best fit year for each efficiency drop. 121

Table 3.3-3: Chi-squared results from the final correction of the count data. The bordered boxes mark the best fit of the data for each year. This is a little distant in the yearly mission years however this can be attributed to the use of 1996 (untouched data) as the calibration set. 126

Table 3.5-1: Relative abundance ratios at specific energy per nucleon used for comparison. 138

Table 3.5-2: Specific Energy per Nucleon converted to Kev for each element. 139

Table 4.1-1: Parameters for converting count rate to intensity. 160

Table 4.1-2: fit parameters a, b, and c, for each element distribution. 164

Table 4.2-1: Channel boundary limits for sputtering yield integration. 169

Table 4.2-2: Estimations of the number of particles lifted from the surface per second over the surface of Europa, due to sputtering, using corrected data. 173

Table 4.2-3: Sputtering rate breakdown during the E4 flyby calculated from original data and corrected data. 174

Table 4.2-4: Sputtering rate average from during the E4 flyby calculated from original data and corrected data 175

Table 4.2-5: Sputtering rate average over all flybys calculated from original data and corrected data. 176

Table 4.2-6: Collection of current literature estimates of sputtering/erosion rates on Europa 177

"The Galileo instrument told us almost nothing about the plasma in the neighbourhood of the Galilean moons. So if there is one most important thing I could ask for, it would be good plasma measurements in the Jovian system"

— Prof. Christopher Russell

Royal Academy of Science honor lecture: The Jupiter's Domain,

February 13th 2013

1 Introduction and Overview

1.1 Introduction

The fifth planet from the Sun in the solar system, Jupiter boasts the largest and most complex system of moons, radiation zones and magnetosphere; bar only to the Sun's own. Visible to the naked eye, Jupiter has been a feature in the night sky for any who cared to look for it; with its motions defining it as a planet in our solar system even before early astronomers had developed heliospheric models for the solar system as we recognise them today.

This thesis focuses on the investigations made by the 1989 NASA Galileo orbiter mission to Jupiter. As the first dedicated mission to Jupiter, Galileo took detailed data from the magnetosphere and the particle environment, whilst also taking the first close range images of Jupiter and the surfaces of its surrounding moons. Its on-board probe descended into the atmosphere of the planet early in the mission providing the first in-situ data of a gas giants atmosphere close-up.

The orbiter itself flew for a total of 14 years. A journey of 6 years led it through two Earth flybys and one Venus flyby before its final approach to Jupiter where it planned to operate for two years to fulfil its prime mission objectives. Eight years and two mission extensions after its arrival at Jupiter, Galileo finished its final orbit and descended into the interior itself following the path of its on-board probe. Over the eight mission years, the instruments proceeded to take and send back a vast array of data including the data key to this study from the Energetic Particle Detector (EPD).

The EPD data reveals extensive information on the Jovian plasma within the magnetosphere; though its data is flawed and not complete due, in part, to the nature of the detector and the environment in which it is recording. These flaws and the correction thereof form the basis of the first two research chapters of this thesis. From there, data analysis can accurately retest composition ratios of trapped Ions, evaluate surface weathering on the icy moons and even assist in the hunt for Europan plumes.

1.2 Jupiter

Jupiter is the closest and largest of the gas giants. It possesses the largest of the planetary magnetospheres in the solar system; closely followed by Saturn's. Earth and Jupiter's magnetospheres share some similarities; though they also vary in some key aspects. The Earth's solar wind driven magnetosphere functions symmetrically down the meridian line, where the larger magnetospheres of the outer planets, more closely resembles the Suns fully rotationally driven system.

Jupiter's magnetosphere dwarfs the Earth's, both in size and strength (Bagenal et al., 2004, Bagenal, 2007, Mauk et al., 2004), reaching 3,500,000km from the bow shock to the planet with the Earth's reaching only 63,000Km. The basic system is much the same; a magnetic dipole with an extended drawn out tail from the pressure of the solar wind. From there the differences become even more evident as the Jovian tail extends almost to the orbit of Saturn at an approximate length of 489,000,000 km, around 7000Rj, with Earth's barely competing at $200R_E$ or 1,270,000km

Internally the Jovian magnetosphere is more similar to that of the Sun in how it is internally driven; both carve out a huge cavity for itself and its satellites within the respective surrounding environment. The Sun's magnetosphere protects the planets from the interstellar wind, for Jupiter it is the solar wind. The magnetosphere captures the hot low-density plasma from Jupiter itself and its four main moons, whilst shielding it from the strong, fast moving solar wind plasma.

The cavity of Jupiter within the solar wind, keeps the majority of the solar wind particles out. Only a small amount, around 1%, enters through the reconnection of the magnetic field at the poles, adding to the plasma composition. Unlike the Earth's magnetosphere the magnetosphere of Jupiter is instead driven from inside. The plasma in the Jovian system comes primarily from the volcanic eruption of its closest large moon Io. The rest, come from the surfaces of the other three large Icy moons Europa, Callisto, and Ganymede. The energy driving the magnetosphere comes from Jupiter itself and its high rotational speed. Its rotating magnetic field generates a bulk of co-rotating plasma within which sit the Galilean moons continually re-fuelling the plasma.

This co-rotation generates a bulge in the magnetic field around the equatorial line (Chané et al., 2013). Most visible on the dayside, it is also responsible for the distance between Jupiter and its bow shock against the solar wind. The more mass there is in the plasma disk the further this distance will be. This culminates in a balancing act between the solar wind pressure and the magnetic field pressure; this produces X-ray aurora around Jupiter's poles (Bhattacharya et al., 2005).

The currents within the system propagate the co-rotation; these currents are in turn generated by the magnetic field. The ions within the magnetosphere are ejecta, mainly from the volcanic activity at Io. As they erupt from Io's surface the fast-moving plasma already frozen into the magnetic field, impacts and ionises these new particles; they are then picked up as the magnetic field flows over them. The pick-up ions begin gyrating around the magnetic field and thus become frozen in as well. These are Io Pick-Up ions (Huddleston et al., 2000). The current combined with the magnetic field carrying the plasma, causes a force of rotation in the form of a JxB force.

The co-rotation is a very powerful force that dictates the shape of Jupiter's magnetosphere, and overwhelming the symmetrical Dungey cycle that affect the Earth's magnetic field (Smith and Aylward, 2009, Walker and Ogino, 2003). At Earth the lack of an internal driving rotation force means the magnetic field of the Sun drags the Earth's magnetic field symmetrically over the poles creating the rotational hemispherical flows of the Dungey cycle. Figure 1.2-1 illustrates how the magnetic fields of the Earth, Sun and Jupiter scale, when under the drag force imposed by solar wind like conditions.

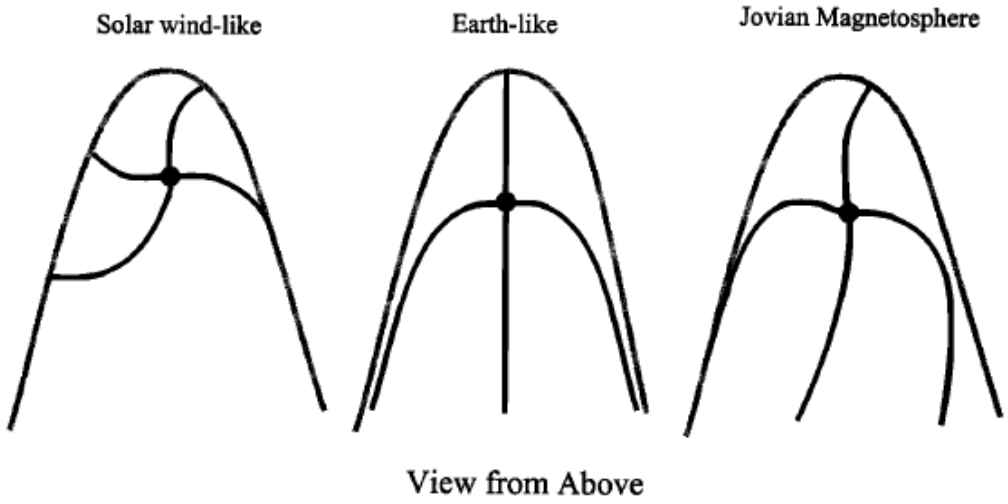

Figure 1.2-1: Basic overview of the magnetic field of the Earth, the Sun and Jupiter, Pictured scaled as though within a solar wind like drag force [Khurana, 2001].

The Sun is a powerful magnetic dipole, positioned within the interstellar wind, similar to a planet in the solar wind, then there is no effect on its co-rotation of its outflowing material. The Earth, on the other hand, shows no rotation effects; its magnetic field flows back with the pull of the wind into the symmetrical cycling that forms the Dungey cycle. Jupiter is a combination of both. There is an asymmetry in the co-rotation of the plasma disk and a point where it breaks down (Cowley and Bunce, 2003). This co-rotation break-down is one of three mechanisms for the Aurora seen at Jupiter.

1.2.1 Aurora

The aurora at Jupiter comes from three sources. The main source is the breakdown of the co-rotating plasma disk. The other sources are the footprints of the four large moons Io, Europa, Ganymede and Callisto, and finally the incoming particles of the solar wind entering through the poles. In Bagenal, (2007) the three types of aurora are described, as well as the influence of the co-rotation on the main aurora.

Aurora at Earth all comes from the solar wind particles entering the magnetosphere through magnetic reconnection over the polar cap (Kivelson and Russell, 1995). This process happens at Jupiter as well but to far less effect. This is the polar cap aurora, the chaotic emissions seen within the auroral oval and common across the polar cap. The chaotic appearance of this comes from the rapidly corotating plasma that converges around the poles, mixing up and disturbing the atmosphere. However, the corotating plasma also emits its own aurora.

The co-rotation speed is dependent on the amount of material being carried frozen into the magnetic field. As more particles from Io become ionised and picked-up by the magnetic field more mass is added to the system and the rotational speed slows down. This is a process called mass loading as the material is loaded in to the co-rotational system. If too much mass enters the system, the energy driving the co-rotation will not be sufficient. At this point, the mass furthest from Jupiter will drop from the magnetic field, no longer frozen in the plasma forms a collection of slower non-corotating plasma. The distance from Jupiter to this break-down point, determines the rotational speed. In the case of true co-

rotation such as with the Sun, the material needs to be rotating at the speed that Jupiter rotates as can be seen in the Parker Spiral (Khurana, 2001).

When the plasma is not fully co-rotating, any plasma outside the co-rotation boundary will no longer be in the magnetospheric current system. This means that the plasma is free to move up and down the magnetic field lines. The bounce motion of the plasma is the most critical here as it is this motion that allows the ions of the plasma to escape the magnetic field at the poles and into the ionosphere/ atmosphere of Jupiter, causing the Aurora.

This plasma, from the moon Io's volcanic activity, forms the very strongly visible auroral oval. This aurora emits in the X-ray, fuelled by very energetic ions. When comparing to the strongest auroral emissions that happen on Earth; at around 4eV for a green 5577A emission, and even less at 1.96eV for red 6633A emission, this X-ray emission is in the region of 12 keV all the way up to 120keV (Kivelson and Russell, 1995).

This strength of the solar wind compares directly to visibility of the aurora. On Earth the aurora is very closely dependent on the magnetic polarity of the solar wind. However, at Jupiter it has very little effect on the auroral emissions (Bagenal, 2007, Walker and Ogino, 2003). When there is a high solar wind pressure onto the dayside of Jupiter's magnetosphere, the Jupiter's bow shock moves inwards towards Jupiter. The co-rotation in this scenario is far more efficient; the rotational mass is confined closer to the planet making the angular force needed to keep it moving, less. Therefore, there is less mass dropping from the magnetic field and making its way towards the poles.

The final form of visible aurora at Jupiter is from the four Galilean moons: Io, Europa, Ganymede and Callisto (Bagenal, 2007). The intrinsic magnetic field of Ganymede and the induced magnetic fields of the other moons causes turbulence in Jupiters magnetic field as it passes over the moons in their orbits around Jupiter. This turbulence is enough to upset the co-rotating particles, causing them to drop from the magnetic field and travel to the poles. Because of how the magnetic field is structured, the footprint of the moons on the surface of Jupiter maps to where that magnetic field line passes into the surface of the planet.

The least is known about the moon's auroral footprints and the mechanisms of the disturbances the moons cause. The most common theory is that the disturbances trigger Alfven perturbations.

1.2.2 Jupiter's radiation environment

The co-rotation of highly energetic particles generates a large volume of local space in Jupiter's magnetosphere that is highly hostile. This plasma disk is the name given to the bulk of the corotating particles and is the focus of the research; its ion composition and the effect it has on the moons of Jupiter will also be investigated.

The majority of the material that fills the plasma disk comes from the moon Io; as previously mentioned. The remaining ion composition comes from three sources: Jupiter itself, the other large icy moons, and from the solar wind. Each source has a distinct composition making it simple to tell where the plasma is coming from. The most complex of these compositions, come from the surfaces of the icy moons. Positioned within the plasma disk, the surfaces of the moons have very little protection, the passing particles erode material from the surface, some of which contributed to the mass loading into the plasma.

The composition of the plasma has been analysed from many of the flybys of Jupiter and most recently by the Energetic Particle Detector (EPD) on the Galileo Orbiter. Figure 1.2-3 shows the data from CHEMS on Cassini as it made flybys of both Earth and Jupiter (Bagenal, 2007). The contributions from the solar wind is easily visible as the H^+ He^{++} and He^+ the rest of the composition visible is mainly from Io. The trace elements from the other moons, that give clues to the internal composition of the ice, are very hard to categorise in this plot.

The energy of the ions in Figure 1.2-3 is around 100KeV, where the multiply ionised charged states can be clearly seen. This has been measured by the eight spacecraft that have visited the Jovian system, including Ulysses and the two Voyager missions. The most significant of the visitors was the Galileo Orbiter taking measurements between 1995 and 2003 (Jun et al., 2005).

There is a very broad range of particle energies found along the plasma disk although the largest population of high energies is found closest to the centre. The energies range

from a few KeV all the way up to and above 11MeV (Jun et al., 2005). There is a higher density of particles near to the centre of the disk. This is due to the co-rotation. The further out from Jupiter the plasma is, the currents weaken dropping the particles to become part of the inflowing particles causing the Aurora.

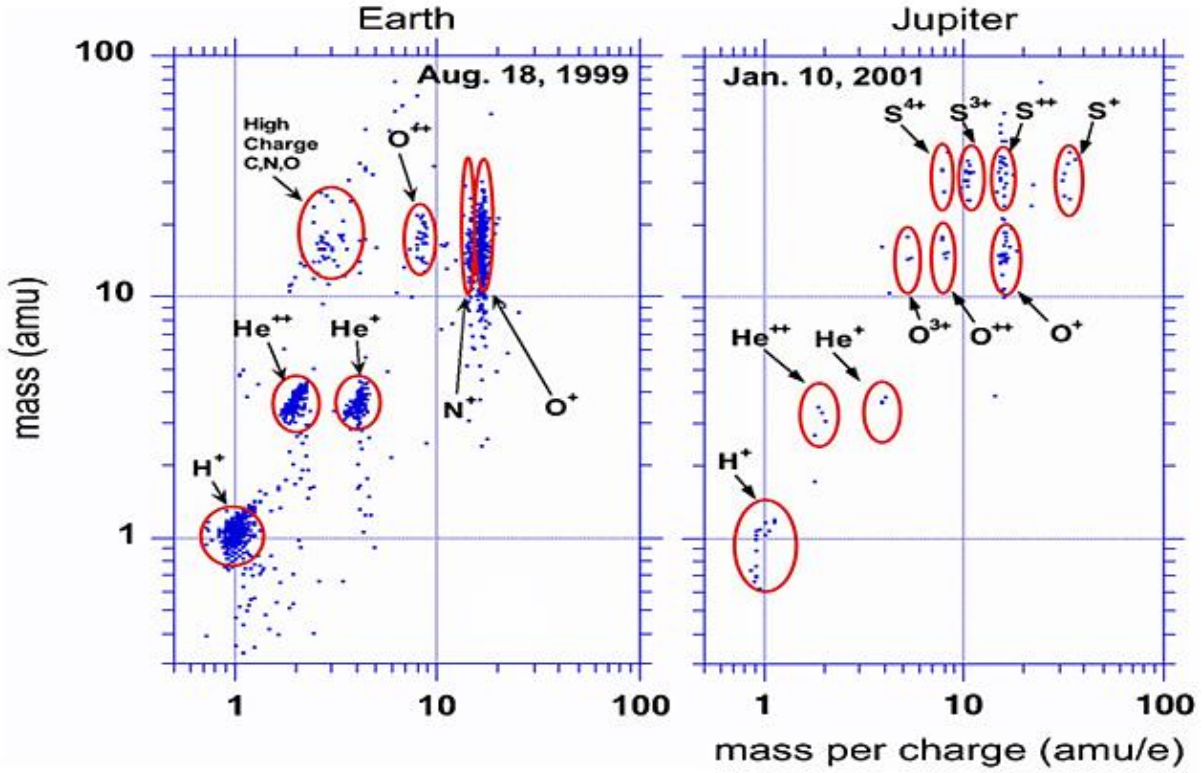

Figure 1.2-3: This data was taken by the Charge Energy Mass Spectrometer (CHEMS) on Cassini during its flyby of Earth and Jupiter (Bagenal, 2007).

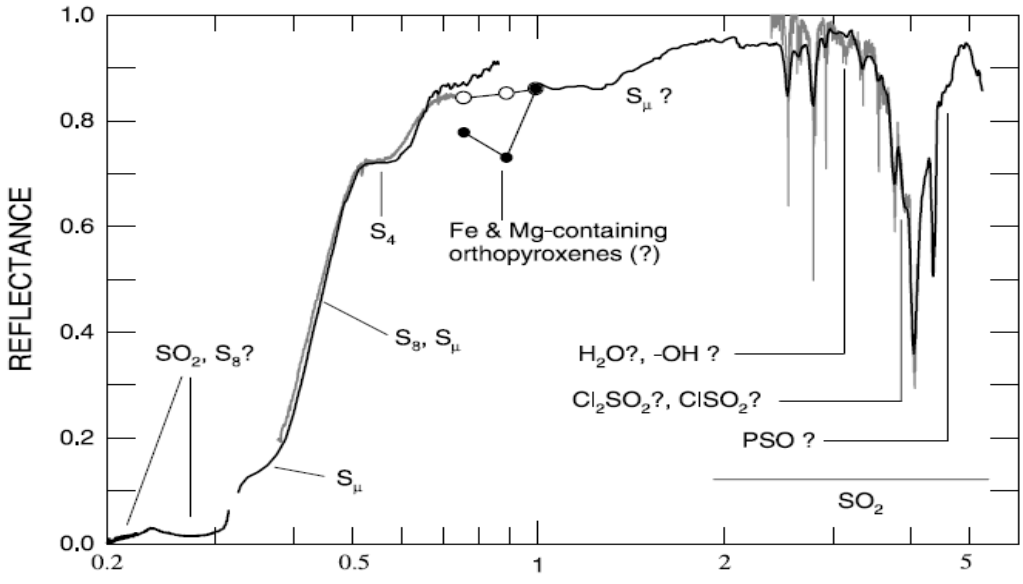

Figure 1.2-2: The surface spectra of Io.

Composite spectra done by: (Dalton et al., 2010) the bottom axis shows wavelength in µm.

1.2.3 The Neutral Cloud

The neutral cloud signifies a small oasis in the adverse conditions of the Jovian plasma disk. Whilst not fully confirmed the non-ionised particles that form this torus are expected to sit around the orbit of Europa; in a doughnut shape surrounding Jupiter.

The existence of a neutral cloud surrounding Io in the same manner was confirmed using ground based observation methods (Skinner and Durrance, 1986); the high volume of material exuded into the plasma disk is slowly ionised and energised as the plasma disk passes over the material. This process however, as described earlier, is slow. The rate at which the material is picked up, does not surpass the amount of material produced. Thus leaving neutral particles in the wake of Io's orbit. These particles form the torus of neutrals.

The same process is expected to produce the neutral torus surrounding Europa; where radiation surface weathering ejecting particles is the source (Bagenal et al., 2015, Burger and Johnson, 2004). On Io, the particles are ejected from the high volcanic activity on the surface of the moon. On Europa, the energetic particles from the plasma disk are impacting onto the surface and removing the top surface layer. This process is sputtering. This ejects particles from the icy surfaces, including particulates from the deeper ocean that have travelled to the surface layers through geological processes discussed later. The composition of the neutral cloud will have far higher abundances of these trace elements, such as sodium and magnesium in varying molecule combinations, than the plasma disk itself, as the mass of co-rotating material will not have diluted the concentrations.

1.3 Moons

Jupiter has 63 known moons, the most of all of the planets. The four most familiar are the Galilean Moons: Io, Europa, Ganymede and Callisto. Discovered by Galileo in 1610 they were the only known moons of Jupiter for quite some time. The other moons are considerably smaller with higher irregularities in their shapes. Most of these small moons, many thought to be asteroids, were captured by Jupiter's strong gravity. The nomenclature of Jupiter's moons bases around the Roman mythology of Jupiter the Sky God and the surrounding stories and family trees.

Io is the closest of the Galilean moons to Jupiter. With its highly active surface, it differs from the other moons considerably. Its distinctive surface composition is far less icy and composed mainly of sulphur. Its many volcanoes expelling sulphur, oxygen and potassium into the plasma disk, Io is considered the most unusual of the large Jovian moons, due to its lack of ice. Of the others, Ganymede is the largest moon in the Solar System, with a diameter of 5,286km; followed in size by Europa and then Callisto.

Europa, Callisto and, Ganymede have liquid water ocean underneath a thick ice/ rock surface (Nimmo et al., 2005). This ice layer is most analogous to the tectonic plate system found on Earth. On Europa the thickness of the ice is estimated to be between 1km and 30km deep (Billings and Kattenhorn, 2005); covered in an extensive network of linea, chaos terrain and craters. These features mark it as having a very geologically active surface (Figueredo and Greeley, 2004). Ganymede whilst larger than Europa has the same formation of Icy crust over a liquid ocean. Callisto however, has a heavily cratered older, icy, rocky surface with a water ocean beneath (Morrison and Burns, 1976).

1.3.1 Moon Io

Io is the closest to Jupiter of the four Galilean moons. Its composition is mostly of sulphur dioxide and a mixture of sulphur S_8 (Baklouti et al., 2008). Measurements have also confirmed the presence of Potassium, Chlorine and Sodium. These are all based on its reflectance spectra taken by flybys and also by using ground or space based telescopes (Dalton et al., 2010). The sodium, potassium and chlorine all come from the volcanism on the surface. The magma erupting will carry the composition signature of the inner rocks.

The sulphur identified around Io is not only from the volcanism but also from sputtering on the surface as happens on the other moons.

The composition is determined by matching known spectra to the spectra recorded of the surface. The method for identifying remotely sensed spectra involves knowing approximate elements to start at when matching the measured spectra, against known spectra, then analysing the comparison. The same is done for all the Jovian moons, although some elements are harder to identify than others are; for example, certain peaks are easily identifiable but others may be compounds with no outstanding identifier. The spectra are worked from to find the most suitable match for the finer composition of the surface salts (Hendrix et al., 1998).

Figure 1.2-2 is a composition of many spectra of Io and the advances in their species identification, from various papers compiled by Dalton et al., (2010). The spectrum is composed mostly of SO_2 frost; this is the main species found on the surface. The identification of it as frost comes from the crystalline structure, which affects the signature on the spectra. Water and other frost forming species exhibit the same effect, such that even the crystalline structure of the water ice on the other moons is identifiable.

Around the equator of Io, suspected higher deposits from the volcanic venting of gaseous SO_2 appeared observable, however; Baklouti et al., (2008), has shown this to be unrealistic. The volcano rich equator is more highly affected by the tidal power of Jupiter thus more prone to volcanic activity through the active crust. Images of Io showing red Polar Regions suggest that S_4 is highly likely to be coming from this area. Galileo resolved spectra of the dark lava areas found Fe, Mg and rich Orthopyroxenes. Na_2, S, as well as Na, K and Cl escape as salts NaCl and KCl in the magma (Lellouch, 2005).

1.3.2 Moons Ganymede and Callisto

Ganymede and Callisto are the less known of the four Galilean moons. They are both similar to each other whilst having their own unique features. They share much of the same surface composition (Dalton et al., 2010) with SO_2, CO_2, H_2S and C – H bonds having been found on Ganymede using the same spectroscopy methods as described for Io. The CO_2 is primarily found in the dark regions of terrain of Ganymede (Hendrix and Johnson, 2008);

with the other regions being mainly icy materials. The same compounds exist on the rocky areas of Callisto's surface, whilst larger sections of the surface display higher content of icy materials; like that which makeup Europa's and Ganymede's surface.

The ice structure varies over the four moons. Io being the closest has undergone the most heating and stress leading to it having barely any water ice. The three remaining moons all contain water ice of differing forms. Europa is majoritively amorphous ice; this is ice structured like a liquid but frozen in place from super-cooling as it reaches the surface. Callisto's surface crust is mainly made up of crystalline ice, this is the same as ice that can be found in any freezer; it has particular crystal structures that it can use and that define it as crystalline ice on a spectrograph. Ganymede has a combination of both amorphous and crystalline ice. Amorphous ice can become crystalline under heating, and vice versa when particle radiation disrupts the amorphous ice; as Ganymede is the middle moon this combination is expected.

The key differences to differentiate one moon from the others are; Ganymede has a significant magnetic field and Callisto has a marked atmosphere. These are both unusual for moons making them very important for study.

Ganymede's magnetic field, as well as being a very interesting feature of the moon means that we know less about the interior than we do of Europa. The intrinsic magnetic field masks the disturbances in Jupiter's magnetic field that can be seen at Europa (Kivelson et al., 1997). These disturbances can be attributed to the salinity of the Europan sub surface ocean, and the same can be done at Callisto (Khurana et al., 1998). However, the existence of a magnetic field does mean that assumptions can be made on the structure of its interior.

The same method of looking for disturbances in Jupiter's magnetic field have been applied to Callisto to show that its interior is non-differentiated (Kuskov and Kronrod, 2005). In its formation, it did not spin up enough to separate out the traditional layers seen in a planet. This means the surface and the inner composition are mostly the same. This is also partially determined from the mass/ volume relation and the assumed densities.

The existence of Callisto's atmosphere is very unusual and unique in the Jovian system (Hendrix and Johnson, 2008, Moore et al., 2004). From the known harsh conditions of the radiation environment, any atmospheres should have quickly been lost to the pick-up

ions. Calculations have shown that an atmosphere of Callisto's size would be stripped away in around 4 days by the incoming energetic particles. However, despite this Callisto has a distinct CO_2 atmosphere, which would require consistent fuelling to sustain itself. The source of this is suspected to be sublimation from the icy surface, however this is only speculation from the few Galileo flybys.

1.3.3 Moon Europa

Europa is one of the most well-known of the 4 Galilean moons. Its surface, environment, and interior have all been intensely investigated over many years (Carlson et al., 2009). This is because Europa is the most likely candidate body for harbouring life outside of the Earth. It has a very thick icy crust, which is a very effective shield against the rigours of the Jovian system. In addition, its liquid ocean beneath this crust stays warm enough to be within the extremes that microbes on Earth can survive (Martin and McMinn, 2018).

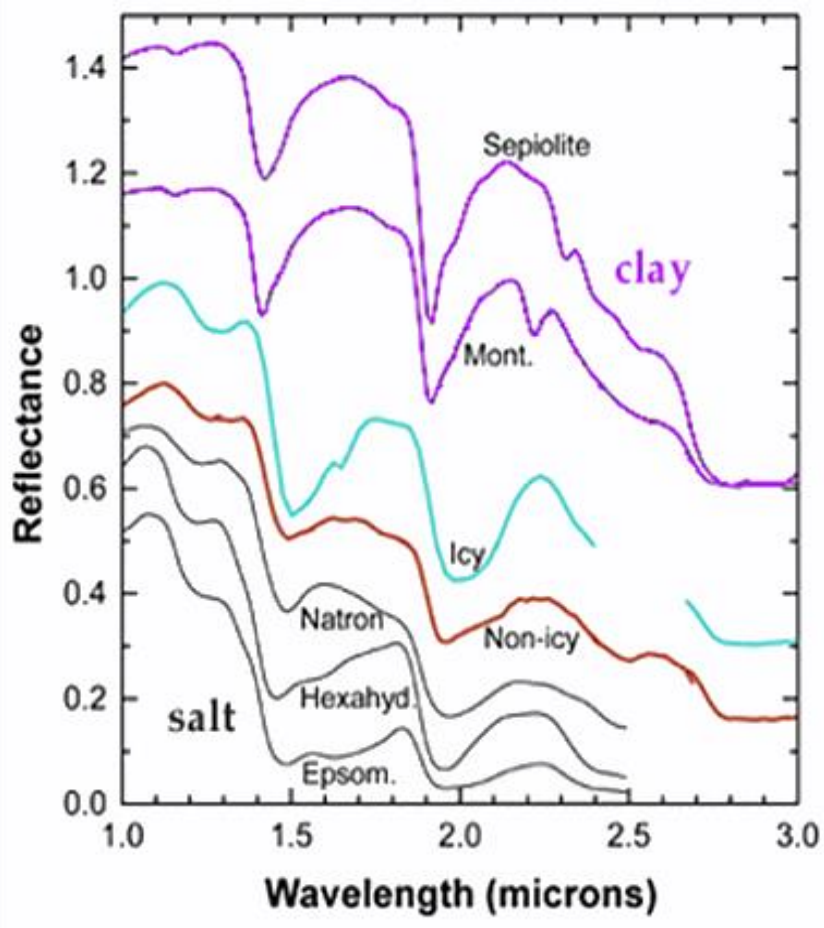

Figure 1.3-1: A spectrum of the darker areas of Europa's surface, these are the non-icy areas. The best matches for the spectrograph were obtained for hydrated salts; including sulphates and carbonates such as: natron ($Na_2CO_3(10H_2O)$), epsomite ($MgSO_4(7H_2O)$), hexahydrite ($MgSO_4(6H_2O)$). (McCord et al., 1998)

The disturbances in the magnetic field of Jupiter confirm the existence of Europa's liquid ocean, as described previously (Kivelson et al., 2000, Prieto-Ballesteros et al., 2005). The salinity of the liquid layer was vital to the discovery of this. The salt in the water allows it to conduct to some extent causing currents to run along and under the surface. These currents can in turn affect the magnetic field as it passes across. NaCl and H_2SO_4 are the most likely salts and sulphate brines present in the water that are causing this salinity (Prieto-Ballesteros et al., 2005); these have both been identified in the plasma disk, indicating that there is a mechanism on Europa for transporting these molecules from the deep ocean to the icy surface, such that they can be sputtered off.

A slushy semi-liquid ice water layer under the ice crust of Europa, whilst under some debate; allows for the tectonic movements of the icy surface (Billings and Kattenhorn, 2005). The surface of Europa, has a similar system of movement to the tectonic plates of Earth. However, where the Earth's plates distinctively form seven major tectonic regions, Europa's surface is not so simple. Split into many small sections, the surface movement follows the tidal forces present under the surface. Many of the plates overlap forming intricate patterns that when traced back show the scars of older movement in the marks on the surface (Kattenhorn and Prockter, 2014). These overlapping patterns indicate how the boundaries of the plates have moved and changed since the formation of Europa.

The overall composition of Europa is much the same as the three other moons. A surface shell made up of icy material, Europa also displays darker areas across its surface. These indicate material that is either recently deposited from impacting energetic particles or surface recently exposed by tectonic motions. The darker areas have spectra as shown in Figure 1.3-1. Whilst the definitions of the peaks shown are not certain, the indicated compositions are the current best matches from lab research.

There is also shown to be Na and S and small amounts of Mg present, these are likely to be from Io and the particles impacting the surface rather than from the ocean underneath the ice. However, they may be a combination of both with the incoming particle staying on the surface and a surface particle ejected off with transference of energy. As mentioned earlier these materials impacting on the surface are then transported further into the interior layers.

1.4 Europa

Europa's orbit sits it directly in the plasma disk of Jupiter. From the EPD data, the environment is a very harsh and unforgiving place to be. However, the total exposure that the moons are a victim to is not as much as it could be. Research undertaken by Paranicas et al., (2007) has shown that the moons themselves are deflectors for the radiation. This means that some of the higher energy particles do not reach the surface, instead missing the moon altogether, having been diverted by the magnetic field. This is a spatial effect with some areas of the surface being more protected than others are; the areas affected are also dependent on the energy of the incoming particle.

When the particles do reach the surface, the impact with the surface particles has some interesting effects. This effect is sputtering.

1.4.1 Sputtering

The sputtering yield is the ratio of how many particles are leaving the surface against how many are hitting the surface. A yield of one would be that every incoming particle is knocking another particle away. For a yield over one then there is erosion of the material the particles are hitting, for less than one then there is deposition.

Knowing the composition of the plasma hitting the surface allows for accurate predictions of sputtering patterns. From here the erosion or deposition of particles on the surface of Europa can be calculated.

The sputtering is modelled using a program called SRIM: Stopping and Range of Ions in Matter (Ziegler et al., 2010). This program uses Monte-Carlo method modelling to trace individual particle trajectories and calculate their surface impact interactions. The program uses the surface binding energies and the impact speed to calculate which of the above outcomes is applicable to each of the particles. There are modes to the accuracy of the calculations as it is used in many applications of particle motion modelling; for sputtering calculations ‘Monolayer Collision Steps/ Surface Sputtering’ must be used.

Sputtering is the main form of erosion that affect the surface of Europa and the rest of the Jovian moons. The high-energy particles detected by Galileo’s EPD instrument are impacting the moon’s surface. The orbital motion of the moons is slower than the rotational

speed of the plasma disk meaning that it is mainly the backside of the moons that are being hit; however, there is still impacting on the front side as the moons orbital paths push them through the plasma. At current estimates the sputtering effect is likely to be eroding the surface of Europa at 14 mm of surface removed every 1 million years (Tiscareno and Geissler, 2003). These estimates make no allowances for deposition of material back onto the surface or for the probability of impacting particles being obstructed (Paranicas et al., 2007).

1.4.2 Frost

The mechanism of sputtering on the surface of Europa lifts a large amount of the surface material. This material is free to move in the thin exosphere and is either picked up by the plasma disk or redeposited back on the surface (Tiscareno and Geissler, 2003). This redistribution onto the surface comes in the form of frost.

Frost is a process of deposition on the surfaces of the moons, Europa included. The sputtering effect that the impacting particles have on the surface, causes loose non-ionised material close to the surface, without the energy to escape the pull of the moon. The suspension of particles in this way is only possible if there is sufficient pressure. The pressure is dependent on the overall pressure of the gas in the area, the temperature of the gas and the amount of additional material already present.

These conditions are calculated in the same way on Earth and they govern the formation of dew and frost on the ground. On Europa the condensation becomes immediately frost missing the liquid phase, unlike on Earth where there is the possibility of dew when the temperature is cooler.

As an addition to the deposition of frost onto the surfaces of the moons, sublimation directly from the surface also occurs. Sublimation is the opposite effect of frost, the icy material on exposed areas is eroded directly into loose gas particles. This erosion has been highly studied on Callisto (Howard and Moore, 2008), but may also be present on the surface of the other moons.

1.4.3 Surface Geology:

The geology of Europa is very active compared with that of Earth. With a conservative estimated surface age of 60Ma (Ip et al., 2000) compared to Earth's long established estimation of 200Ma; Europa's surface is constantly changing and complicated to date. The icy shell is part of the reason for this along with Europa's proximity to Jupiter adding gravitational stresses that planets like Earth do not face.

Linea: Most Europan lineae are named after characters and places in the legends of Cadmus and Europa; others are named after important megalithicstone rows built by the Neolithic peoples of Britain and France.

Linea	Named after:
Adonis Linea	Adonis
Agave Linea	Agave
Agenor Linea	Agenor
Alphesiboea Linea	Alphesiboea
Androgeos Linea	Androgeus
Argiope Linea	Argiope
Asterius Linea	Asterius
Astypalaea Linea	Astypalaea
Autonoë Linea	Autonoë
Belus Linea	Belus the Egyptian
Butterdon Linea	Butterdon Hill, England
Cadmus Linea	Cadmus
Chthonius Linea	Chthonius
Corick Linea	Corick, Northern Ireland
Drizzlecomb Linea	Drizzlecombe, England
Drumskinny Linea	Drumskinny, Northern Ireland
Echion Linea	Echion
Euphemus Linea	Euphemus
Glaukos Linea	Glaucus
Harmonia Linea	Harmonia
Hyperenor Linea	Hyperenor
Ino Linea	Ino
Katreus Linea	Katreus
Kennet Linea	West Kennet Long Barrow, England
Libya Linea	Libya
Mehen Linea	Mehen, Brittany
Merrivale Linea	Merrivale, Devon, England
Minos Linea	Minos
Onga Linea	Onga
Pelagon Linea	Pelagon
Pelorus Linea	Pelorus
Phineus Linea	Phineus
Phoenix Linea	Phoenix, brother of Agenor
Rhadamanthys Linea	Rhadamanthys
Sarpedon Linea	Sarpedon, son of Europa
Sharpitor Linea	Sharpitor, England
Sparti Linea	Spartes
Staldon Linea	Stalldown Barrow, England
Tectamus Linea	Tectamus
Telephassa Linea	Telephassa
Thasus Linea	Thasus
Thynia Linea	Thynia
Tormsdale Linea	Tormsdale, Scotland
Udaeus Linea	Udaeus
Yelland Linea	Yelland, England

Craters: Most of the craters that are large enough to have names are named after prominent figures in Celtic myths and folklore.

Crater	Named after:
Áine	Áine
Amergin	Amergin
Angus	Angus
Avagddu	Avagddu
Balor	Balor
Brigid	Brigid
Camulus	Camulus
Cilix	Cilix
Cliodhna	Cliodhna
Cormac	Cormac mac Airt
Deirdre	Deirdre
Diarmud	Diarmuid Ua Duibhne
Dylan	Dylan Eil Ton
Elathan	Elathan
Govannan	Govannan
Gráinne	Gráinne
Gwydion	Gwydion
Llyr	Llyr
Mael Duin	Mael Dúin
Maeve	Maeve
Manannán	Manannán mac Lir
Math	Math ap Mathonwy
Morvran	Morvran
Niamh	Niamh
Oisín	Oísin
Pryderi	Pryderi
Pwyll	Pwyll
Rhiannon	Rhiannon
Taliesin	Taliesin
Tegid	Tegid Veol
Uaithne	Uaithne

Regiones: Europan regiones (regions) are named after locations in Celtic mythology.

Regiones:	Named after:
Annwn Regio	Annwn, Welsh otherworld
Argadnel Regio	Argadnel, Celtic paradise
Balagtan Regio	Balagtan Pass
Dyfed Regio	Kingdom of Dyfed
Moytura Regio	Magh Tuiredh, Irish battlesite
Powys Regio	Kingdom of Powys
Tara Regio	Hill of Tara, Ireland
Falga Regio	Inis Fer Falga, Irish legendary island

Chaos: On Europa, regions of chaotic terrain are named after places in Celtic mythology.

Chaos	Named after:
Arran Chaos	Isle of Arran, Scotland
Conamara Chaos	Connemara, Ireland
Murias Chaos	Murias
Narbeth Chaos	Narbeth, Wales
Rathmore Chaos	Rathmore, Ireland

Flexus: A flexus is a low, curved ridge with a scalloped pattern. Europan flexūs are named after the places visited by Europa during her journey with Zeus the bull.

Flexus:	Named after:
Cilicia Flexus	Cilicia
Delphi Flexus	Delphi
Gortyna Flexus	Gortyna
Phocis Flexus	Phocis
Sidon Flexus	Sidon

Large Ring Features: These impact structures are named after important locations in ancient history.

Ring feature:	Named after:
Callanish	Callanish, Scotland
Tyre (FormerlyListed as a Maculae)	Tyre, Lebanon

Maculae: Europan maculae (dark spots) are named after locations in Greek mythology, especially in the legend of Cadmus and his search for his sister, Europa.

Maculae:	Named after:
Boeotia Macula	Boeotia
Castalia Macula	Castalia
Cyclades Macula	Cyclades
Thera Macula	Thera
Thrace Macula	Thrace

Table 1.4-1:Europa's geographical feature list including a feature description and nomenclature

There are many features marring the surface of Europa; each of them denoting differing mechanisms attributed to their formation. Each type of feature has its own nomenclature stemming from Greek Mythology.

Table 1.4-1 shows the current identified features list and the associated feature type. There are seven types of identified features. They are in some cases gathered in specific areas of the moon, with others spread evenly over the surface. Only the largest of them have specific names as many are very common across the surface. As more spacecraft visit Europa, the clearer the available pictures will become allowing more and more named identifiable features.

1.4.3.1 Lineaments or Linea:

Linea are linear features in the landscape, which indicate the underlying geological structure: typically, a fault aligned valley, a series of faults, fold aligned hills or a straight coastline (or any combination of such).

On Europa there are four distinct stages of lineament, Kattenhorn., (2002) suggested that each stage can be linked to an age range. However, there are cases where supposed older linea overlay younger looking features implying that this scale isn't fully complete, or the mechanisms moving the feature from one stage to another is not fully understood. In suspected age the features are as follows (examples in Figure 1.4-1):

- Fractures (Youngest of the lineaments): These are very narrow and tend to only show-up as a one-pixel wide line on images even at very high resolution.
- Ridges (next youngest): These have a raised relief (100 – 200m altitude) they can have double or multiple ridges symmetrically on both sides. These can also form as a Flexus formation (Table 1.4-1) also known as a cycloidal ridge.
- Triple bands: (Older): These have multiple ridge sets flanked by smooth dark margins. Overall they tend to be far wider than the younger lineaments over 5Km.
- Ancient bands (Oldest): These are very similar to the triple bands but they are no longer active. As they age, they relax, brightening past the albedo of the surrounding surface.

Ridges are the most abundant type of Linea, covering most of the visible surface in a net like mesh. These ridges are the most useful for determining the age of an area of the surface. Their formation cuts across older formations and newer formations in turn cut across them. This crosscutting is a geological dating time-lining technique. The basis of this technique will be used later to investigate the ages of features and the suspected erosion between a cross-cut.

1.4.3.2 Chaos Terrain:

Chaos terrain is broken up land area. It consists of blocks of surface, with older fractions of formations visible upon it. Surrounding these blocks are undetermined crushed and raised material in between. The formation mechanism of chaos terrain is widely unknown. There are many theories on how it may have formed (Collins et al., 2000). However, these all depend on the thickness of the icy shell or other unknown or immeasurable factors.

The size of chaos area is varied over the surface; it is most likely that larger areas are merged smaller patches (Figueredo and Greeley, 2004). Chaos can be categorised by its appearance into three main groups, these are, chaos, raised chaos and subdued chaos.

The most common formation of chaos lies reasonably flat to the surface with distinct blocks of older features amongst jumbles of smaller pieces, surrounded by unidentifiable frozen slush like material.

In raised chaos the larger blocks are lifted from the surface. These larger blocks dominate the chaos area, and are easily identified by the shadows cast on the surrounding frozen slush. Raised chaos is often confined in smaller areas, also lifted appearing elevated from the surrounding surface.

Subdued chaos is the hardest to spot and identify, it appears to be highly eroded chaos. It is very flat and mostly featureless but without the defining features of other areas of surface. These chaos terrain types can be seen in b), c) and d) in Figure 1.4-1.

1.4.3.3 Other Formations:

Apart from linea and chaos terrain, there are many other geological formations easily visible on the surface of Europa (Table 1.4-1). These formations are far less common,

only occurring in specific areas. This character of the features gives clues as to the underpinning mechanisms.

Macula: Maculae are dark areas of surface that appear sunken compared to the surrounding area. They are uneven and thought to be the most active areas of the surface. Their colouring is most likely to come from under-surface water and minerals breaking through the surface and staining the ice with salts.

Most theories are in agreement that maculae are active regions of chaos formation over shallow subsurface water (Schmidt et al., 2011). The thickness of the icy shell of Europa is still under debate on the topic of the Maculae and the formation mechanisms. By studying the structure of maculae, it is hoped conditions for their formation would offer some limits to the ice thickness expected in these areas.

Craters: Visible all over the surface of each of the four moons, Europa included, the age of the surface can be calculated in relation to the number and visibility of the craters. Crater counting and surface dating has been perfected on the Moon and is applied to surfaces all over the solar system. There are a few drawbacks for crater ageing a surface; the quicker the surface is recycling material, either volcanically on Io or from radiation weathering on Europa, the younger the surface appears geologically. Crater counting can only estimate age relative to the resurfacing rate. In the case of Europa, the surface is visibly very young; there are very few craters. This is due to the high radiation weathering on Europa erasing any craters quickly in a geological time scale. The composition of the surface can also hide the features of craters; the icy surface heats up with the impact and the ice melts. This melting fills in the craters making them indistinguishable from the surrounding surface.

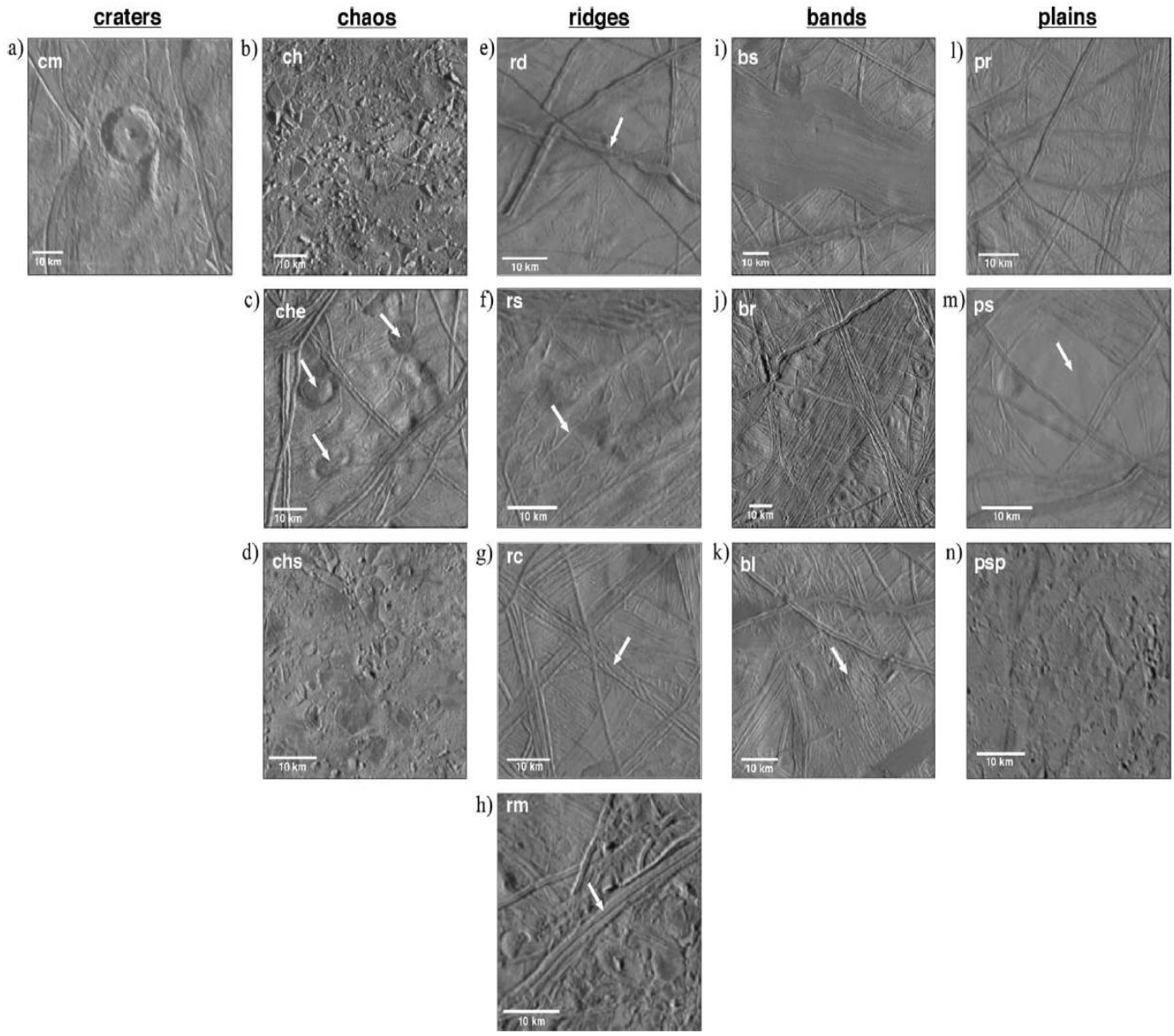

Figure 1.4-1: Figure 3 of (Figueredo and Greeley, 2004) showing examples of different formations identified in the paper (a) crater material, (b) chaos, (c) elevated chaos, (d) subdued chaos, (e) double ridge, (f) single ridge, (g) ridge complex, (h) medial-trough ridge, (i) smooth band, (j) ridged band, (k) lineated band, (l) ridged plains, (m) subdued plains, (n) subdued-pitted plains. Where necessary, arrows indicate the feature under consideration.

Ring features: Much like craters, these are impact formations. They are rings of darker material that are visible on the surface. They appear to be craters but they have none of the key features such a deep basin, raised rims or central peaks. It is most likely that rings are formed from impacts much the same as craters, the difference in appearance has been theorised to be due to the impacted surface structure (Moore et al., 1998). There is also some debate on the connection between ring features and chaos; it may be possible that these form from impact that fully penetrate the ice. This, if confirmed, would be very significant as a possible formation mechanism for chaos.

Regiones: Europa's surface has formed into regions much like Earth's tectonic plate system; these are distinct enough that they are individually classified. Whilst these are not precisely features, they are identified areas of interest that can be used for global navigation when referring to features within them.

Flexus: Flexus are unique formations that are very similar to ridges and linea. However, during their formation the diurnal pattern of Europa's movement caused them to form in a cycloidal pattern. The name, Flexus, is related to the distinctive scalloped shape they carve out across the Europan surface, primarily caused by the flexing of the icy crust. They are often also labelled as cycloidal cracks.

Europa's spin and orbit drive their formation by diurnal variations. It is suspected that the position of the flexus can be attributed to a point in time, or within an orbital pattern, that the flexus was formed (Hurford et al., 2007).

1.5 Europa's ice Layer: Thick or Thin?

The thickness of Europa's ice layer has caused debate for many years. As mentioned above, many of the surface features formation theories assume a thickness of the ice. This makes it a pivotal point in formation theories and our understanding of the surface structure.

The thickness of the ice is commonly estimated to be between 1km and 30km thick (Billings and Kattenhorn, 2005); these estimates can be inclusive or exclusive of the 'slush ice' ductile layer that divides the solid surface crust from the inner ocean. There are also many methods for determining the thickness of the ice: Table 1 from the paper Billings and Kattenhorn., (2005) compiles the various methods used by many researchers and their underlying model assumptions.

For the purposes of this research, the thickness and the underlying formation mechanisms of the surface features are less of a concern. The identification and classification of the formations is the focus. This does not mean that the thickness of the ice is not important; only that the research is focusing on the appearance of the features and the time scales over which they change.

1.5.1 Relations with Earth Geology:

No matter which thickness of ice theory you support, the layers in the ice will be the same. The outer surface is a solid crust layer that is brittle but also elastic, this layer is under the most tension from the gravitational pulls of Jupiter and the other moons in the surrounding area. It also bears the scars of this in the cracks and marks where the surface is broken, moved and created.

This layer is analogous to the outer crust tectonic layer of Earth. It undergoes the same processes that the Earth's crust does in forming tectonic boundaries. The types of boundaries that form are as described in section 5 of Fossen., (2010). These boundaries make up the majority of the mechanism for the features that are on the surface, further pointing to the similarities of the two systems.

The next layer down under the brittle ice crust is the 'slush' or partially melted ice. This ductile layer compares with the lithosphere in an Earth analogy. Much like the Earth's lithosphere it allows the outer plates to move and interact. The gravitational stresses that the outer layer undergo are absorbed by this layer, even affecting the processes at plate boundaries in the depth that they can affect the ice as shown in Figure 1.5-1 taken form Kattenhorn and Prockter., (2014).

The final layer is then the water layer. This is the inner most layer and is not included in the thickness values; the depth of the seas is normally considered to be around 100km. Combined with the middle layer the salinity and movement of the liquid portions was the key to identifying the liquid ocean in the first place (Kivelson et al., 2000, Prieto-Ballesteros et al., 2005)

1.5.2 Age of Europa's Surface:

There is much estimation on the age of features of the moon Europa; all concluded using a variety of methods and ageing techniques. A fault found in many of these estimations is a lack of overarching timescale; either dating a feature in relation to another

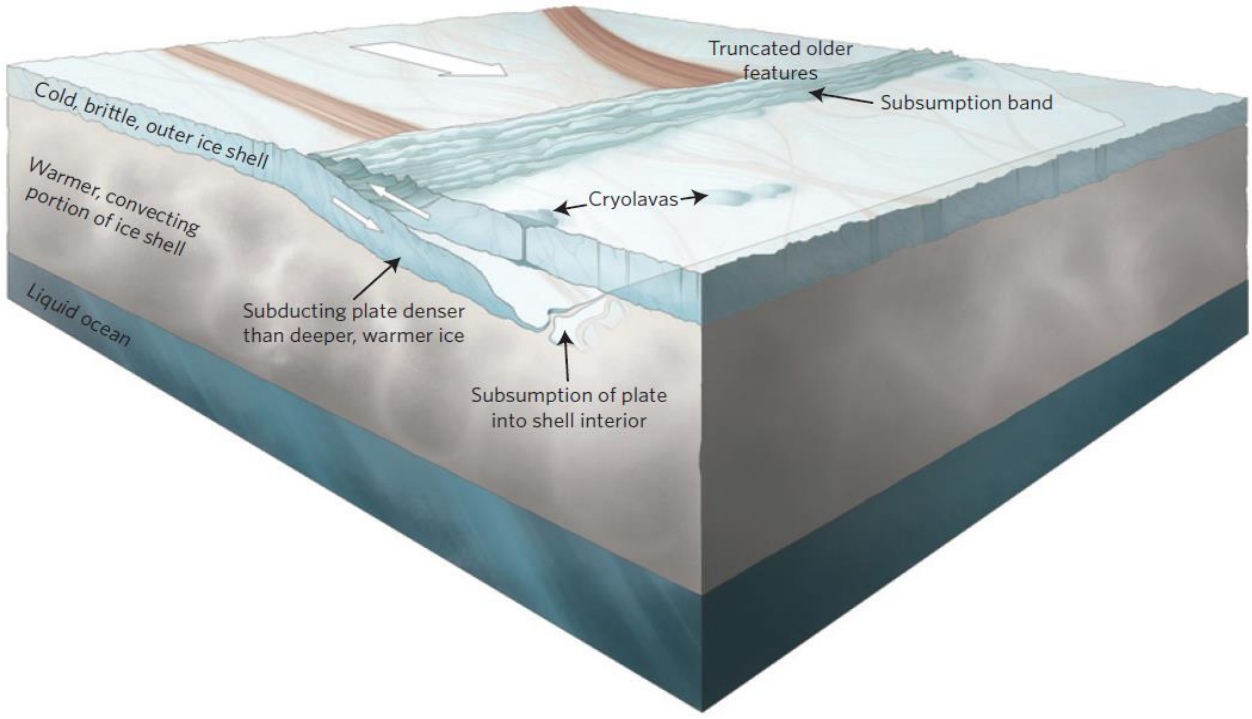

Figure 1.5-1: Figure 4 of (Kattenhorn and Prockter, 2014). The Image shows the similar Earth like plate tectonics that happen on Europa; also highlighting the differences in the warmer convecting layer absorbing the upper layer before it reaches the liquid ocean.

or in relation to the most recent resurfacing of the area. The overall time scales of the surface and the time taken for feature mechanisms are still unknown.

The cause of this inaccuracy in dating is the unknown quantity of the surface weathering. Knowing an accurate value for material excavated from the surface over a period, would allow a scale to be set between feature ages. Once such a scale has been set, a cross correlation of ages can be undertaken, with the aim of building an age map over the surface.

1.5.2.1 Crater counting:

As mentioned above, crater counting is the best method for dating the age of a planetary surface; its common use is for dating rocky solar bodies such as the Moon, Mercury and Mars. Based on the meteorite numbers expected in the local space, the time taken to cover the surface to the point of craters overlaying old craters is measurable (Bierhaus et al., 2005, Zahnle et al., 1998).

Crater counting on Europa and the other icy moons is considerably harder. Within the confines of Jupiter's magnetosphere and substantial gravity, the abundance of meteorites and small impacting bodies is highly variable (Zahnle et al., 2008). Another setback of the Jovian system is the nature of the moons; they are icy bodies rather than rock or regolith. Many of the models developed for cratering estimations on the Moon are not suitable in conjunction with the softer ice on the surface.

Zahnle et al., (2008), used models for secondary cratering from the initial impacts to explain the mismatch in the number of meteorites predicted and the number of counted craters and their sizes. The model showed that as well as increasing the number of counted craters expected there was also the dust and ice regolith from the impact that could be obscuring other craters. They also suspect there may be transference between the moons from this uplifting of material. The date arrived at from the model testing is 60Myr to 100Myr.

1.5.2.2 Large body Impacts and Freezing Times:

Based on estimations of the ice thickness, size, and commonness of impactors in the Jovian system it is possible that Europa has been hit by large impactors at some point in its

lifetime. These craters would have been large enough to penetrate the ice layer to the ocean beneath (Cox and Bauer, 2015).

There is some debate on whether this kind of breach would lead to ring formations or to chaos terrain. However, if such an impact occurred there would be some time before the breach in the ice would refreeze. This, knowing the approximate statistical regularity of such impactors gives a baseline for the age of the current surface. There is currently no exposed breach of the Europan surface therefore its age can be limited to the approximate regularity of the large impactors; Cox and Bauer., (2015), estimates 90Myrs.

1.5.2.3 Linea Crosscutting:

The linea have tightly wrapped the surface of the moon since its formation. Cutting across the surface, they show the movement and stress marks of the surface. Most importantly they also offer an estimation of the surface age. Where one linea overcuts another the newest line is the most recent. Using this very simple conclusion, the areas and ages of the surface are determinable.

There are some problems with this method however. The linea that litter the surface are very numerous. Tracing these linea is complex, in some cases the probable most recent linea do not always appear as uncut lines. There is also possible contamination from other formations found across the surface.

Section 1.4.3 outlines the approximate ages of each stage of linea (Kattenhorn, 2002). The basis of this is the width of the linea. When the linea are first formed, it is a single very thin ridge. Over time the same area is stressed again and again, the same mechanism adding material each time, spreading out into secondary ridges. This can continue until larger many ridged plains are formed. When considering cross-cutting of the linea there are also any cases where suspected older linea paths overlay thinner ‘newer’ paths (Aydin, 2006). This may be due to the movement of the initial stress on the surface, once the stress is gone there is no mechanism to add more ridges and widen the feature.

The age of the surface of Europa remains in contention with ages ranging from 30Myr up to 100Myrs. This large gap range is something that this research aims to focus on. Using the weathering times of the surface, the amount of time taken to erode a feature

completely may give a more definite value for the oldest age that a feature on the surface can be.

1.6 Galileo Orbiter

Galileo orbiter was a NASA project to explore the reaches of Jupiter. It would be the first spacecraft to enter the orbit around Jupiter and the first in-depth study of a gas giant of the solar system (Figure 1.6-1). Over 800 people worked as part of the mission crew, in total costing approximately $1.4 billion. Getting to Jupiter was no easy task for the Galileo team, the journey from launch to arrival at Jupiter involved multiple flybys; two of Earth, one of Venus and two flybys of asteroids along the way traveling 4 billion km on its six-year journey (Johnson, 2000).

During its time in the Jovian system, Galileo took many measurements of the magnetosphere, its interior and the environment around the moons. The instrument of interest that took this in-situ environmental data was the Energetic Particle Detector, EPD.

1.6.1 Mission overview:

Launched on the 18th October 1989 on board space Shuttle Atlantis, Galileo spent seven years in deep space travelling to its ultimate destination; Jupiter. Arriving on 7th December 1995, the many instruments on board took data up to the final impact with Jupiter on 21st September 2003.

Figure 1.6-1: A Public information flyer for Galileo mission produced by NASA. It details the stages of the mission and the milestones reached by the team.

Orbit	Closest approach in Kilometres (Miles)	Date in Pacific time	Date in day of year (YYYY-DOY)	Mission Objective
G1	835 (519)	27 June 1996	1996-179	
G2	260 (161)	6 September 1996	1996-250	
C3	1,136 (705)	4 November 1996	1996-309	
E4	692 (429)	19 December 1996	1996-354	
J5	no close flyby			
E6	586 (363)	20 February 1997	1997-51	Primary Mission
G7	3,102 (1,926)	5 April 1997	1997-95	
G8	1,603 (995)	7 May 1997	1997-127	
C9	418 (260)	25 June 1997	1997-176	
C10	539 (335)	17 September 1997	1997-260	
E11	2,042 (1,266)	6 November 1997	1997-310	
E12	196 (122)	16 December 1997	1997-350	
J13	3,562 (2,212)	10 February 1998	1998-41	
E14	1,645 (1,022)	28 March 1998	1998-88	
E15	2,515 (1,562)	31 May 1998	1998-151	
E16	1,830 (1,136)	21 July 1998	1998-202	
E17	3,582 (2,224)	26 September 1998	1998-269	
E18	2,273 (1,412)	22 November 1998	1998-326	Galileo Europa Mission
E19	1,439 (894)	1 February 1999	1999-32	
C20	1,315 (817)	5 May 1999	1999-125	
C21	1,047 (650)	30 June 1999	1999-181	
C22	2,296 (1,426)	14 August 1999	1999-226	
C23	1,057 (656)	16 September 1999	1999-259	
I24	611 (379)	11 October 1999	1999-284	
I25	300 (186)	25 November 1999	1999-330	
E26	351 (218)	3 January 2000	2000-3	
I27	198 (123)	22 February 2000	2000-53	
G28	1,000 (600)	20 May 2000	2000-141	
-	-	15 June 2000 to 15 November 2000		
G29	2,321 (1,441)	28 December 2000	2000-363	Galileo Millennium Mission
C30	138 (86)	25 May 2001	2001-145	
I31	200 (120)	5 August 2001	2001-218	
I32	181 (112)	16 October 2001	2001-289	
I33	102 (63)	17 January 2002	2002-17	
Amalthea 34	160 (99)	4 November 2002	2002-309	
Jupiter 35	(impact)	21 September 2003	2003-264	

Table 1.6-1: Galileo Orbit designation and closest approach/ primary orbit objective

It orbited Jupiter thirty-five times over three mission objectives taking endless measurements over 10 major instruments, split between the spinning and non-spinning sections of the satellite. Each orbit had a primary goal Table 1.6-1 shows the closest approach of each of the orbits, the designation of the orbit itself, and the current primary mission objective. Along with this is Figure 1.6-1 showing the full orbit path around Jupiter with the orbit designation marked.

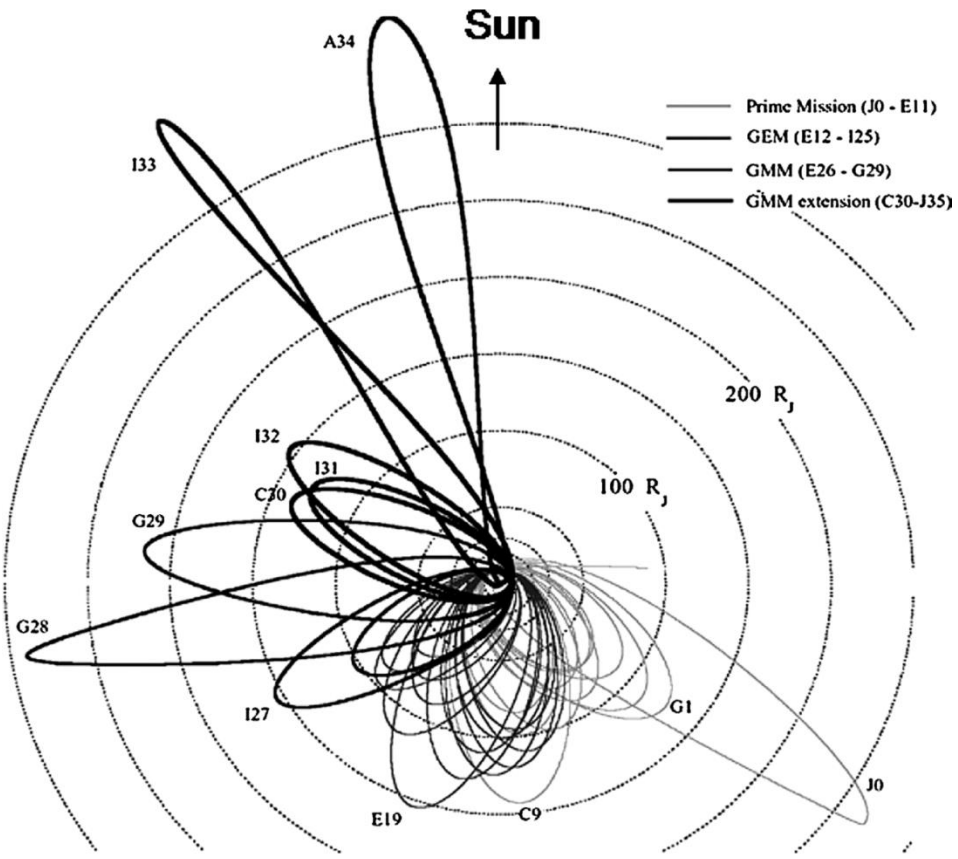

Figure 1.6-2: The full orbit path of Galileo with marked orbit numbers and distance isobars [Jun et al., 2005]

1.6.2 Data Problems

A problem faced by many, if not all, missions is how to select and retrieve the best set of data available. For the Galileo team this task became even harder with the failures of the main antenna and the subsequent use of only the smaller low gain antenna, more on this later.

As Galileo awoke from its main deep space travel section of its journey to Jupiter, its primary antenna failed to unfurl. This antenna was the main communication antenna and should have handled all the data downlink of the mission. With this failure, the team were

limited in the data they received and carefully selected over the entire of the recorded mission, which was most vital. This led to gaps in all the available data.

Whilst it is usual for there to be a trade-off in data, stemming from the limits of the craft to the number of instruments that have power at one time, there is also a priority in the instrument teams for how much data retrieval occurs for each instrument. These calculations are arranged before launch in a standard mission, however with antenna problems and far more restrictions on data bandwidth these had to be quickly re-calculated.

1.7 On Board Instruments and Science Objectives:

There were twelve on board instruments flown on the Galileo spacecraft (Table 1.7-1), each with their own science objectives and aims, measuring different aspects of the Jovian environment. Over the scope on the orbit insertion to the end of the nominal mission each instrument was allocated data and measuring time to complete its objectives. Some instruments performed better than others, and all suffered with the reduction of communication as described in the previous section.

Experiment Name	Spun/De-spun section	Principal Investigator(s)
Near Infrared Mapping Spectrometer (NIMS)	De-spun section	Carlson, Robert
Ultraviolet Spectrometer and Extreme Ultraviolet Spectrometer (UVS/EUVS)	De-spun section	Hord, Charles
Magnetometer (MAG)	Spinning section	Kivelson, Margaret
Plasma Detector (PLS)	Spinning section	Frank, Louis
Energetic Particles Detector (EPD)	Spinning section	Williams, Donald
Plasma Wave Spectrometer (PWS)	Spinning section	Gurnett, Donald
Photopolarimeter-Radiometer (PPR)	De-spun section	Hansen, James
Dust Detection System (DDS)	Spinning section	Grun, Eberhard
Solid-State Imaging (SSI)	De-spun section	Belton, Michael
Radio Science: Celestial Mechanics (RS)	Spinning section	Anderson, John
Radio Science: Propagation (RS)	Spinning section	Eshleman, Von, Howard, H.
Heavy Ion Counter (HIC)	Spinning section	Stone, Edward

Table 1.7-1: List of the Flown Instruments on board the Galileo spacecraft and their principle investigators

There are two main instruments that this study will focus on and use collected data from. The main data instrument is the Energetic Particle Detector, EPD. The main visuals instrument is the Solid State Imager, SSI.

1.7.1 The Solid State Imager, SSI:

The SSI was designed to capture Jupiter and its satellites, using a multi-spectral, high-resolution, charge-coupled device (CCD) camera. The instrument was designed under Dr Michael Belton of the National Optical Astronomy Observatories, Tucson, AZ, U.S.A (Belton, 2000, Belton et al., 1992). The images used in chapter five were captured by the SSI; the images are used to gain insight into the heights of the surface and the overall age, including individual feature age.

The data used in this study aligns with two of the main primary science objectives of the instrument which were to; determine the geologic processes which formed the surfaces of the Galilean satellites. They hoped to achieve this by mapping them at a spatial resolution of less than 1 km and over a range of viewing and lighting angles. The instrument also aimed to identify and map the distribution of ices and minerals on the various satellite surfaces.

The optical system used was a modified flight spare of that flown on Voyager. The camera telescope was a 1500 nm focal length (f/8.5), all-spherical, catadioptric telescope, 90 cm in length and 25 cm in diameter. The field of view of the telescope was 0.46 degrees with an angular resolution of 10.16 microradians/pixel. The camera was operated in eight filtered band passes from 350-1100 nm. The eight-position filter wheel, contained three broad-band filters: violet (404 nm), green (559 nm), and red (671 nm). Four of the filters are in the near-infrared: two for methane (727 nm and 889 nm), one for continuum measurements (756 nm), and one for near-infrared mapping (986 nm). The final filter was a clear filter (611 nm) with a very broad (440 nm) passband.

The images from the three broad-band filters and the clear filter, are the most used in the study. The clarity of the images is the most important, with high resolution for identifying features. Only a very small collection of images available are useful for the investigation; the aim being to generate height profiles. This limits the image areas to places imaged at high resolution with multiple angles; from there the heights can be obtained.

1.7.2 The Energetic Particle Detector, EPD:

The EPD was designed to measure the characteristics of particle population in the Jovian magnetosphere. These are important in determining the size, shape, and dynamics of

the system. The instrument was developed under Dr Donald Williams at the Johns Hopkins Applied Physics Laboratory (Belton et al., 1992, Williams et al., 1992). The data used in chapters two, three and four are from the EPD; the aim of the research is the study and investigation of the measurements taken over the course of the mission. Then for the following chapters, the aim is to use the data to investigate the sputtering on the surface of the moons of Jupiter.

The EPD, mounted on the spinning end of the spacecraft, boasts a full 4π view of the environment, achieved by combining main spacecraft rotation with the stepper motor the EPD was mounted on. It took only 6 watts to power the electronics of the instrument and only an additional 4 watts for the survival heaters. The size was small too at 19.5cm by 21cm by 36.1 cm, weighing in at 10.5 kg.

Despite the problems with Galileo's high gain antenna deployment, there is a large amount of data available from the EPD. It had a high data collection rate and a time resolution of 2.67 sec down to 0.33 seconds dependent on channel. Although the detector could take data at this rate, the actual downloaded data from the EPD tended to be 11min averaged data.

The EPD had the ability to take measurements of many aspects of the Jovian plasma. The instrument itself contains two parts: The Composition Measurements System, CMS and Low-Energy Magnetospheric Measurements System, LEMMS. When considering the energetic particle environment, the CMS is the most valuable of the data obtained by the EPD. The composition of the particles measured using the time of flight of the particles and the energy. Using the energy and the velocity the mass of the particle is calculable.

2 Pulse Height Analysis Plot Correction, and Estimation of Dead Layer.

2.1 The Energetic Particle Detector, EPD

As mentioned in section 1.7.2 the Energetic Particle Detector consists of two main instruments: The Composition Measurements System, CMS and Low-Energy Magnetospheric Measurements System, LEMMS.

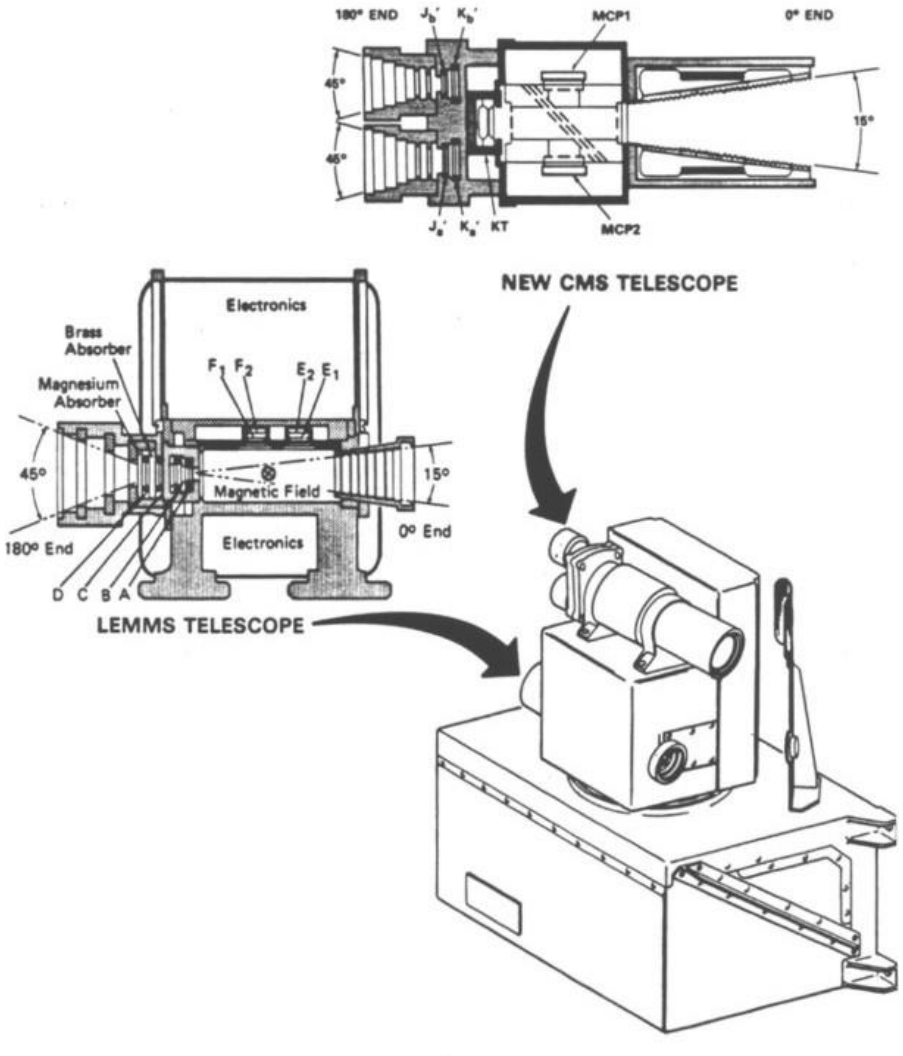

Figure 2.1-1: line drawing of the EPD system, indicating the LEMMS system and the CMS section (Williams et al., 1992).

The composition measurement system or CMS makes up one-half of the instrumentation on the Energetic particle detector on the Galileo Spacecraft Figure 2.1-1.

Composed of multiple detectors and a time of flight measurement system it allowed the sampling of the radiation zones of Jupiter. The aim of the instrument was to measure the composition of the areas that it sampled by taking the energy and the time of flight of the particles and comparing these results.

The CMS itself contains two separate measurement systems, mounted at opposing ends of the instrument. These ends are the 0° and the 180° end. The 180° end mounts two telescopes that collected ions such as to measure the Ion energy loss. These two telescopes had very different apertures; the bottom mounted had a 54° aperture allowing a high number of particles into the measuring chamber. The top mounted aperture was only 23° wide meaning the entering particles were highly collimated allowing for more precise measurements from a smaller sample size (Williams et al., 1992, Jun et al., 2005).

Inside each aperture, there are a set of two detectors. The outermost J_a and J_b (top and bottom mounted respectively) were designed to measure the energy as the ions pass through them before impacting the second detectors K_a and K_b (also top and bottom

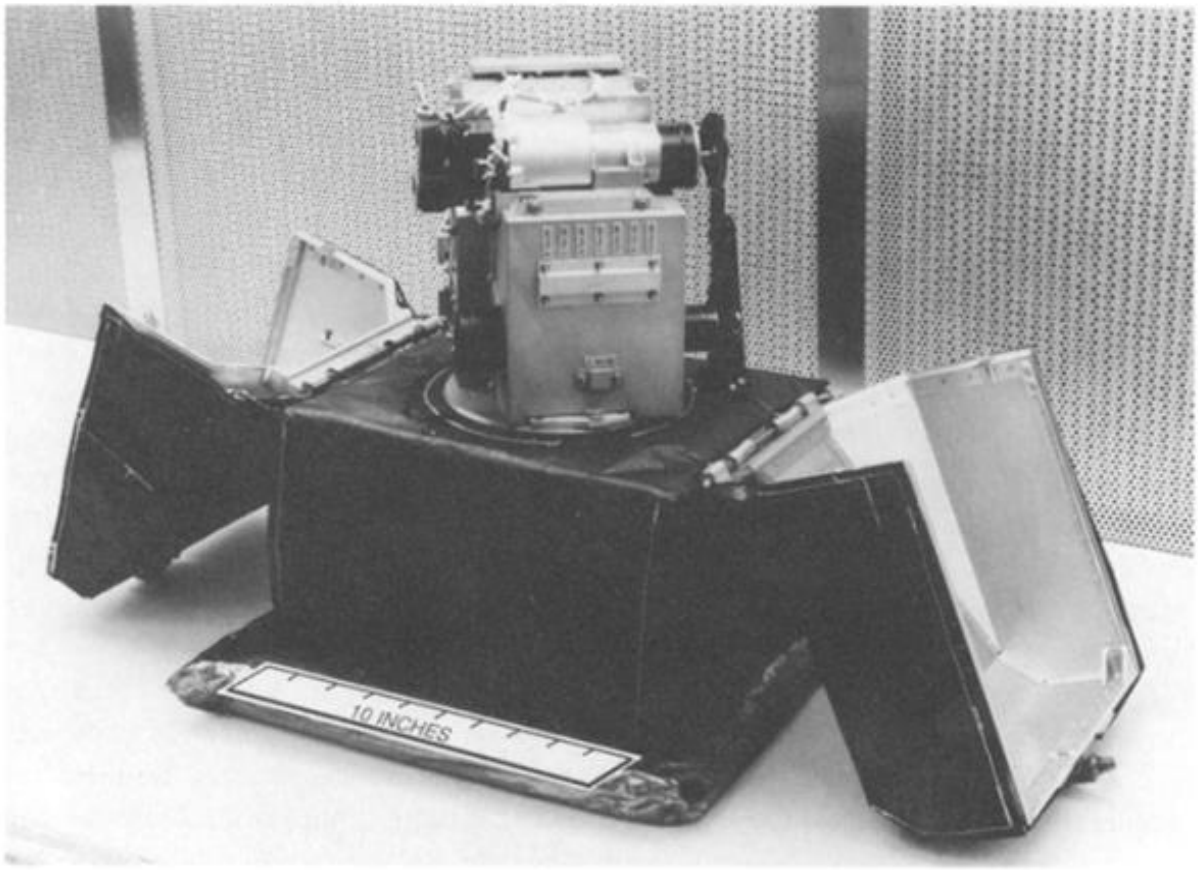

Figure 2.1-2: The Energetic Particle Detector flight model with flight covers (Williams et al., 1992).

mounted respectively). The K detectors measure the residual energy of the particles as they impact. From this measurement and the energy of the particle as it passes through the J set of detectors, the total energy can be determined for the very high-energy range, specifically for electrons.

2.2 Technical details:

The instrument of focus is the Time of Flight detector. It consists of a parylene foil and the main detector separated by a 0.0377-metre distance, that acts as a start and stop signal from the electrons emitted as the particle passes through them. The start/ stop signal combined with the distance between the foils gives the velocity of the moving particles. Once the particles have passed through the foils and been timed they impact into a silicon semiconductor detector, KT. The energy measured from KT combined with the velocity of the particle allows the calculation of the mass of the impacting particle, using the equation:

$$E = \frac{1}{2}mv^2 \tag{1}$$

Rearranged such that mass, m is the unknown variable, v is the velocity and E is the energy measured by the final detector.

2.2.1 A Particle in the EPD

From Figure 2.2-1 the path of a particle inside the instrument may not be a clear one to follow. The inner workings of the EPD are technical and precise aiming to produce the most accurate data.

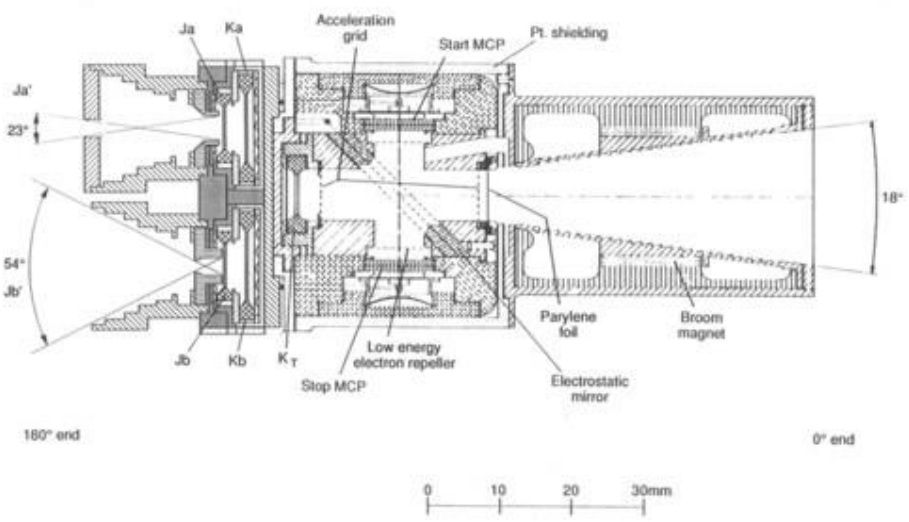

Figure 2.2-1: Technical detail of the interior of the CMS flight model (Williams et al., 1992).

For a particle entering into the CMS 0° end (Figure 2.2-1), the path to being a known particle requires many steps which are as follows (Williams et al., 1992);

- First, the particle must enter the aperture: mounted on the rotating arm of Galileos main body. Additionally, the EPD sits on a stepper motor rotating the whole of the instrument round and back again. With the normal running program of the EPD, this allows the CMS to have a four Pi view of the Jovian environment.
- The CMS 180° telescopes have some limited sections of the rotation sequence as Galileos arm and main body can block it. The 0° end can capture very similar data from the environment as the 180° end, the intention being that simultaneous data was not required.
- The aperture itself is 18° wide and leads directly into a collimator, combined with a sweeping magnetic field. This shields the detector from the lowest energy particles that are undetectable by the detector. Those prevented from entering the system are electrons lower than 265keV.
- After passing through the collimator, the particles then pass through the first of obstructions on the way to the final detector; A 36µgcm^{-2} praylene foil, mounted on a 90% transparent, doubly aluminised, stainless steel grid to prevent background and scattered light from entering the system. Directly after this foil there is a secondary foil. This holds the sole purpose of releasing a secondary electron moving in the direction of the particle. This electron is traveling far faster than the particle, travels into the time of flight chamber, and reflects off an electrostatic mirror directing it upwards.
- From here, it impacts the first Microchannel plate (MCP1) this is the 'start' signal for the timing system. The microchannel plates are 1.4cm Diameter with a pore size of 12µ for an 80/1 ratio. The 200MΩ plates operated in a chevron configuration at a gain of 5x106. The plates are also very sensitive to contamination; to combat this, the whole telescope was purged with nitrogen (N_2) up until the launch.
- The 'end' signal comes as the energetic particle hits the final detector, this gives off a secondary electron. The electron moves back into the timing chamber; this prevents contamination of the final detector. The same process happens again; this time the electron hitting the opposite side of the electrostatic mirror and deflects downwards to the location of the second microchannel plate (MCP2).

- With the speed of the electrons and the distance they travel as well as the distance travelled by the particle, the speed of the particle can be determined from the carefully calibrated timing chamber.
- The final solid-state detector KT then measures the energy of the particle. This detector area is 50mm^2 with a thickness of 12.6µm and measures the ion energy of the particle. With this energy and the speed of the particle now, a known quantity the mass of the particle can now be determined. In this step there are corrections applied to the base reading to calibrate for pulse height and for dead layer on the detector. This is a set amount and does not change during the mission; this inability to change the values is why there is such variance from the results at the beginning and end of the mission.

When plotting the results from the system a TOF graph is used (time of flight against energy), this is also referred to as a PHA graph (pulse height analysis). Within these, there are grouping loci that determine the mass of the particle that made the readings. During the calibration and instrument testing, the measured results show the loci they expected to see. The plots include the estimates from Voyager flybys as to the composition of the radiation zones (Figure 2.2-2).

Figure 2.2-2 shows the main calibration results used for the system; it details both the recording system and the expected results from data samples and predicted results. The recording system for the TOF and the solid-state detector divides into 13 sections or channels. The vertical and slanted dividers on the calibration show these. The vertical lines are the energy discriminators and the slanted lines mark the mass discriminators. The dashed lines are the expected loci for the various elements anticipated to be in the Jovian radiation system. These lines form from the masses and the ranges of energy values within what the detector can measure; using equation (1), the predicted time of flights can be determined from the energies used.

The sample data points, taken from calibration runs at Goddard Space Flight Centre and University of Rutgers accelerators, show where the telescope was calibrated with beams of H, He, C, O, Ne, Na, S, Ar, Fe, and Kr, from energies below 100 keV to over 10 MeV.

Thirteen composition channels, as defined by the energy and mass discriminators collect the data ranges.

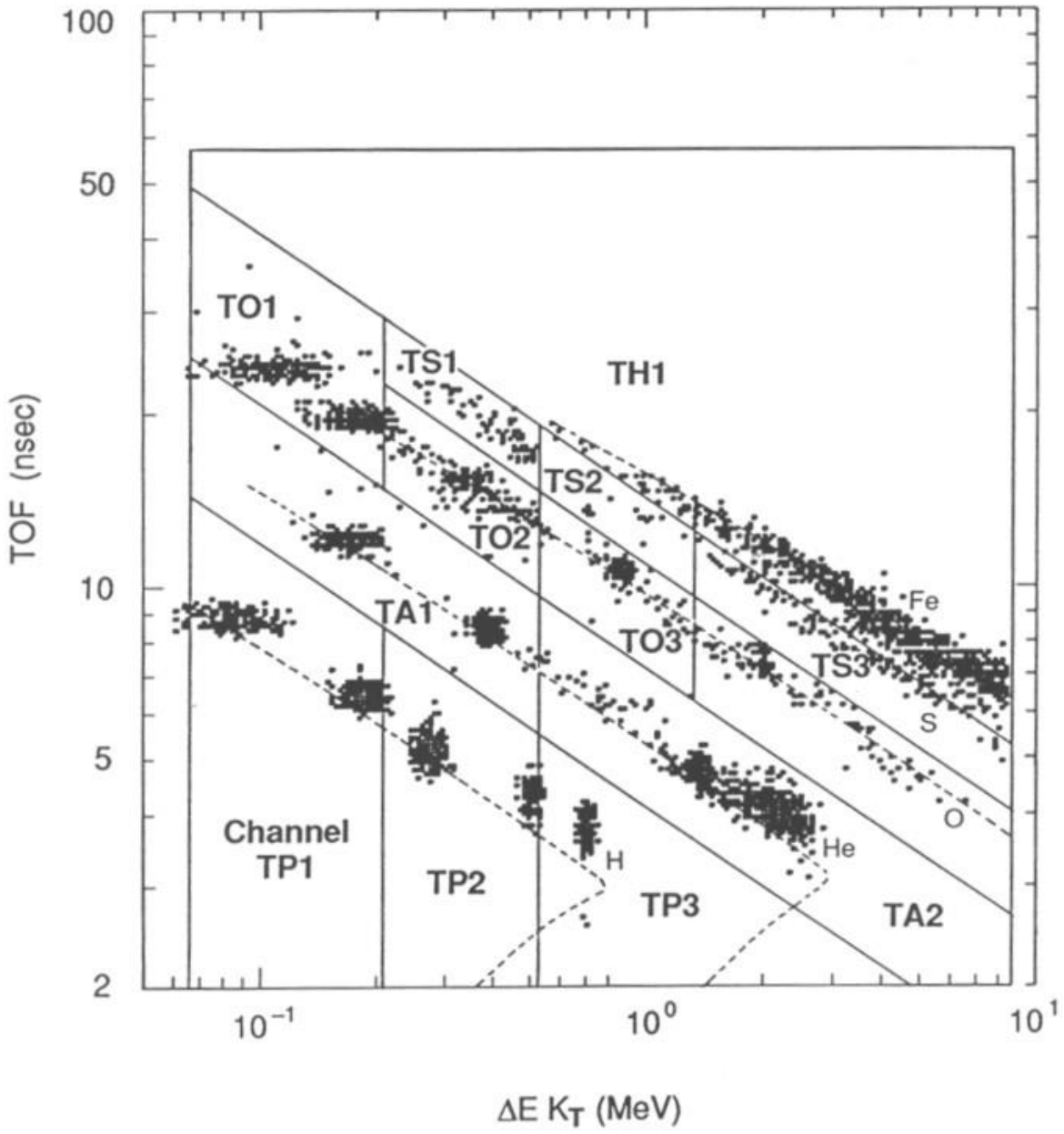

Figure 2.2-2:TOF versus energy observed in detector KT. Discriminator levels defining the indicated TOF rate channels (solid lines), predicted TOF vs. E curves (dashed lines), and data from accelerator calibrations (points) are shown.[Williams et al., 1992]

Each channel is an accumulation based composition rate channel; they provide flux rates and angular information from the most abundant species in the defined ranges. For a more cohesive spectral and elemental resolution, a 256 – channel pulse height analysis (PHA) of the energy and TOF signals for individual events produce graphs as seen in Figure 2.3-2. An average of four PHA analysed events per second are used to make up this graph,

these operate under a four level priority system used to obtain a balanced coverage over all species and energy.

As well as the priority system, a valid TOF event requires a triple coincidence; the start MCP event, followed within 60 ns by a stop MCP event, and finally a coincident KT energy pulse. The data collection is also protected by the sweeping collimator magnet preventing electrons < 185 keV from reaching the front foil, and electrons < 265 keV from directly reaching the rear detector; and finally the whole system is protected by a minimum of 3.8 g cm^2 of platinum.

2.2.2 Silicon Semi-conductor detector

Semi-conductors have been used for radiation and particle detection for many years, the close band gap properties attributed with semiconductors makes them perfect for detecting energy impacting on the surface. Silicon and Germanium are ideal for use in particle detectors as they possess the typical semi-conductor traits whilst also being simple to work with and easy to obtain.

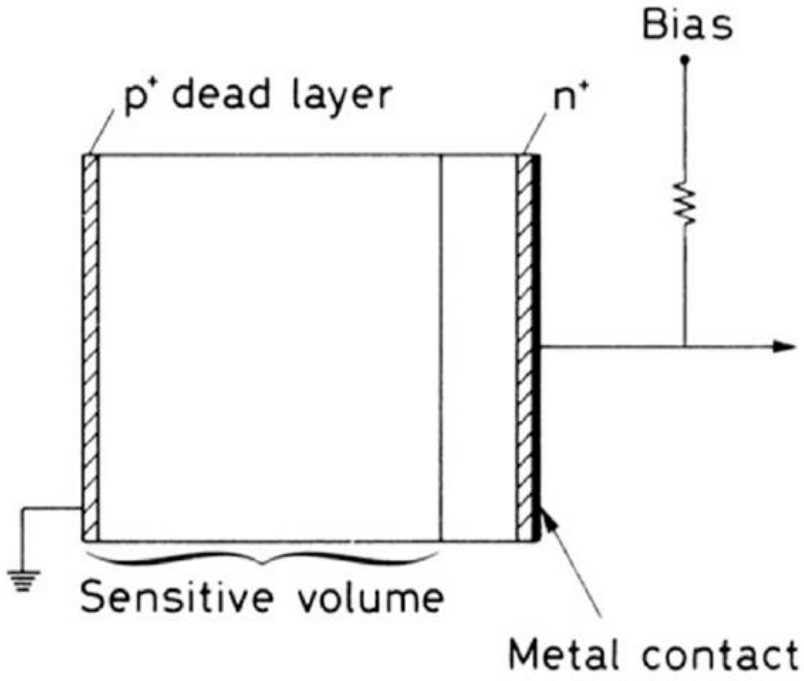

Figure 2.2-3:Simplified diagram of a generic silicon semi-conductor detector.

The detector works by applying a strong negative bias to the thin sheet of semiconductor. This increases the natural band gap of the material. In semi-conductors, this is usually quite small, but it is present unlike in true conductors. For silicon, the resting band

gap is 1.22eV whereas germanium sits at 0.66eV. For the detectors in the EPD silicon is the primary material used.

In all elements the valance and conduction band determine whether it is a conductor or not. The Valance band carries the electrons tightly bound to the shells such that a current is not flowing, in a conductor band there are some free electrons that have spaces around them. This allows a current to pass through it. In silicon where these are very close, the tightly held electrons in the valance band can easily be excited into the conduction band; this causes a current. This is a diode in the simplest form.

The silicon used in detectors is not pure; most often it is doped into N and P sections. N doping adds a loose electron in the valance band; this is most often done using Antimony, Arsenic or Phosphorous. P doping adds an almost full shell of electrons to the conduction band, this in effect adding a 'hole' for electrons to be excited into; Boron, Aluminium or Gallium are commonly used in P doping.

When a P and N doped semiconductor are next to each other, the free electrons and open electron holes intermingle and a conductor like interaction happens such that a current can pass through. That is until a negative bias is applied i.e. a negative voltage applied to the N doped side of the semiconductor. This bias reduces the size of the PN junction holding the electrons in the P doped material and the keeping the Holes to the N doped material. This forms a sensitive volume in between.

Now when an incoming particle hits the reversed bias doped detector (P doped side) the particle exchanges energy giving the silicon the energy it has. This excited an electron in the sensitive volume of the PN junction causing it to excite in to the N doped material. Such a small movement triggers small currents to temporarily flow, this counteracting the negative bias. This counteraction is measureable as a drop in the bias voltage and with proper electronics, measured as the energy present in the impacting particle as it hits the detector.

2.3 Data from the Mission:

The energetic particle detector took data for over 8 years from 1996 on its arrival at Jupiter until 2003 when Galileo made its descent into Jupiter's atmosphere as the finale of the mission. The EPD completed its mission as it took data for the whole mission, with much of it sent back to the ground based teams.

The orbit was not a constant orbit. The satellite moved from as far as 150 Jovian radii (one Jovian Radius, JR = 71,492Km) to as close as three Jovian radii; and finally the decent into Jupiter measured the close interior, far further in than any mission had ever taken data for Jupiter before. This far-reaching path included 35 full orbits divided into the various mission sections, each mission extension added as the current mission ended until the satellite was beyond feasible science (Figure 1.6-2 and Table 1.6-1). The closest approach values in Table 1.6-1 refer to the closest approach to the body of interest. The body of interest is determined by the Orbit descriptor before the number: J for Jupiter, G for Ganymede, C for Callisto, E for Europa and finally I for Io (Williams, 1996).

The recording of the data was also not continuous for the whole mission. Energy requirements; as is the case on any mission, determine how many of the instruments on board can be run simultaneously. This means there are sections of mission with no data. Visible in Figure 2.3-1 the orbit and recording patterns show large open ended orbits where no data is available. For all of the time the detector was recording data there is a point marked on the orbit path; nicely demonstrating how much of the mission there is data. In reality there is a lot of down time for this instrument, considering that there were 35 orbits in all and only 15 or so can be made out in Figure 2.3-1, but this is also to do with data being sent back to earth and the constraints from that; more on these shortcomings later.

Most important is the data now made accessible. This data is now widely available; the constraints of the USAs NASA funding are that all of the data collected has to be accessible to the public eventually. As the mission end is now over 10 years ago, the data is downloadable in a variety of forms from the NASA archives (http://ppi.pds.nasa.gov/data/GO-J-EPD-2-REDR-RTS-SCAN-AVG-V1.0/BROWSE/ (21/07/2016)).

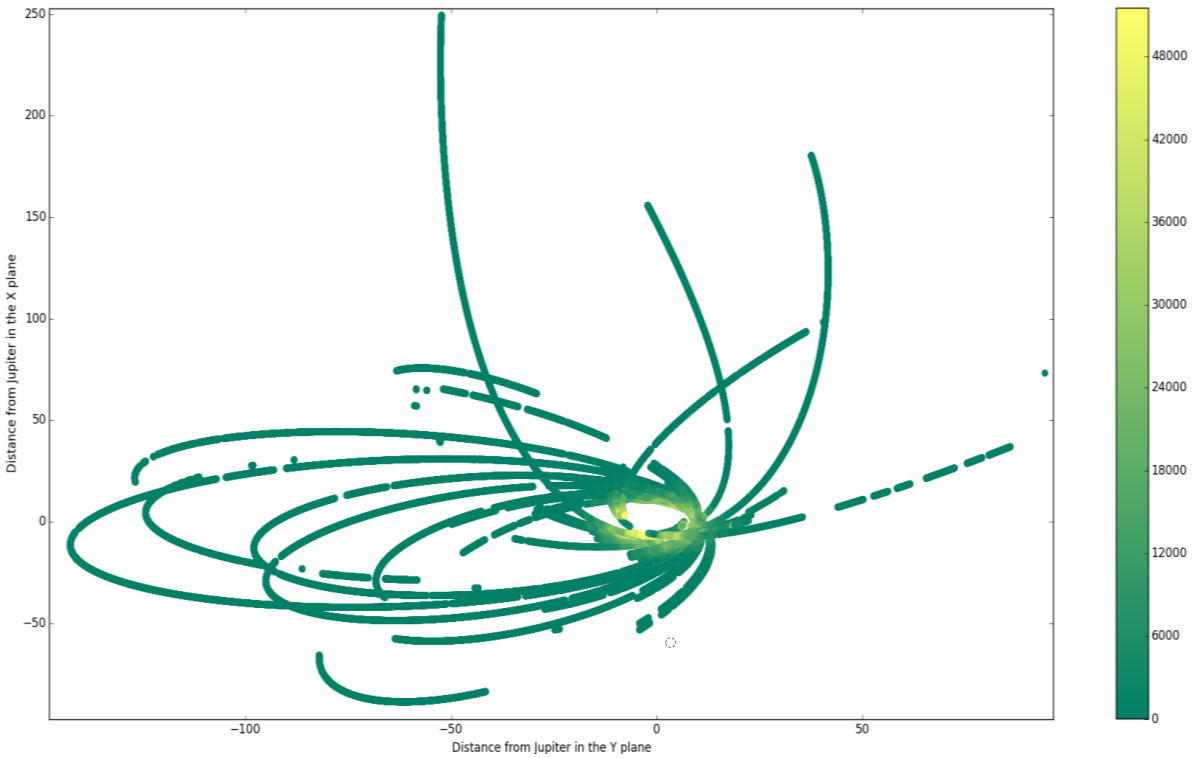

Figure 2.3-1:Overview of recorded data plotted along the orbit path. Colour scale for the average intensity of the channels with Jupiter marked as the small dashed line in the centre of the orbit loop structure.

The data used for this research is ready processed and cleaned up by the mission analysis teams. The data has come from two sources: Dr Norbert Krupp from the Max Planck Institute for Solar System Research, Göttingen, Germany, and from Dr Peter Kollmann from both The Johns Hopkins University Applied Physics Laboratory, Maryland, USA and Max Planck Institute for Solar System Research.

Whilst both provide the same data in essence, the data from Max Planck Institute was ready formatted to be used with the IDL (Interactive Data Language) software that was pre - written for the data processing, e.g. the PHA analysis graphs are made using this software. The other set of data was a full listing of all of the accumulative data values with corresponding time intervals. This full listing is the data that will be used primarily, however the Max Planck Institute data is the most commonly used to show and display the results of the mission (Figure 2.3-2).

Of the taken, the height of the spacecraft in relation to Jupiter's equator is also important. The co-rotation of the magnetosphere means the radiation zone lies close to the equator ward area around Jupiter. As far as the data is concerned there is no point where the instrument was not in the radiation disk; it can be concluded from this that there is no

need to exclude some data over others or make use of particular data, it can all be treated the same.

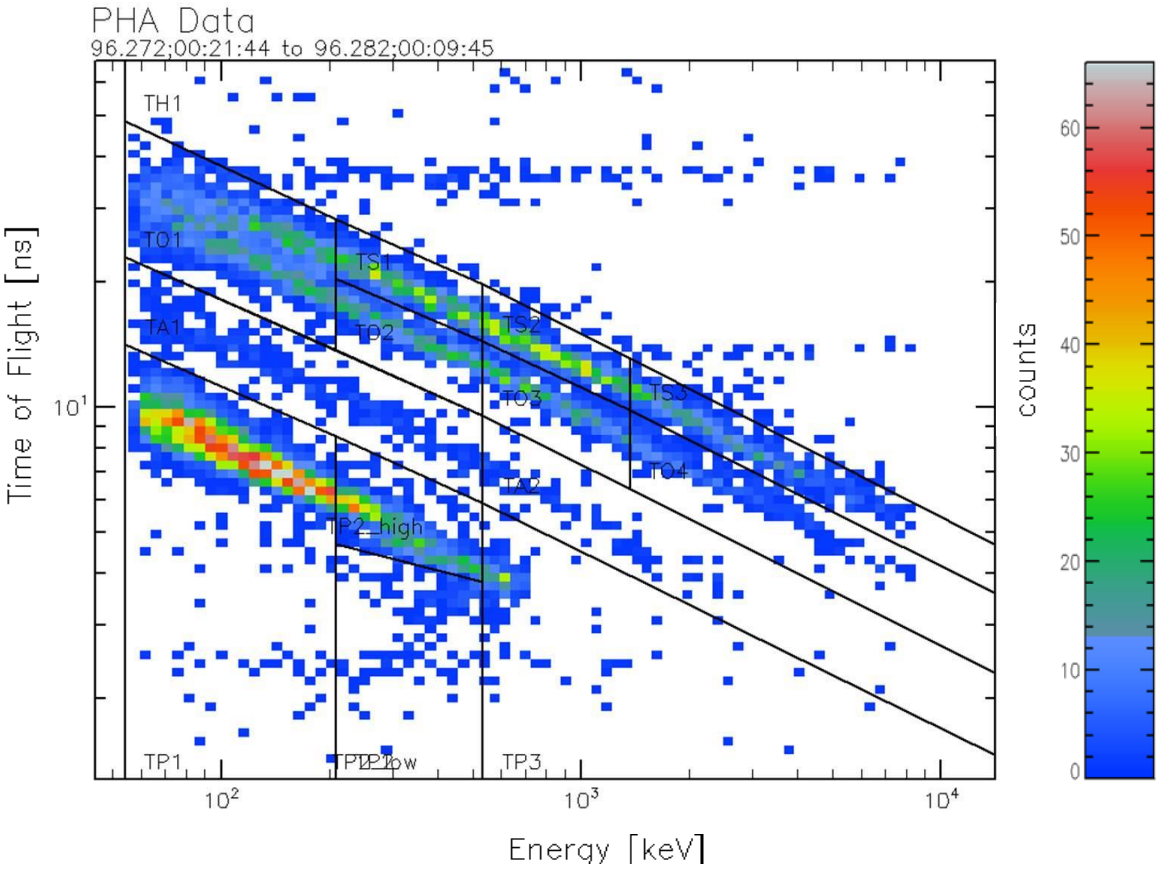

Figure 2.3-2: Real mission data. PHA analysed data plotted as Time of Flight against Energy. Data taken on 29th September 1996

The final recording of the impact with Jupiter is anomalous data, it has been removed from the main bulk of data for this study and treated as a separate event that has not yet been used. This is a very small section of the flight path during which Galileo was directed into the interior of the Planet and as many instruments were turned on as possible including the EPD. This data is somewhat anomalous when looking at the averages year by year. However, it is very valuable information that it is vital to keep. Removing it for general data analysis cuts down on its distortion of the averages for the 2003 data.

Figure 2.3-2 is a PHA: Time of Flight against Energy plot. It is from the first year of the mission from 29th Sep 1996 until 9th October 1996. Here the data has come out as expected. This example of data and many like it allows studies of the particles in the Jovian system. Note how well the mass loci fall within the channel boundaries in the mass discriminator lines as described earlier.

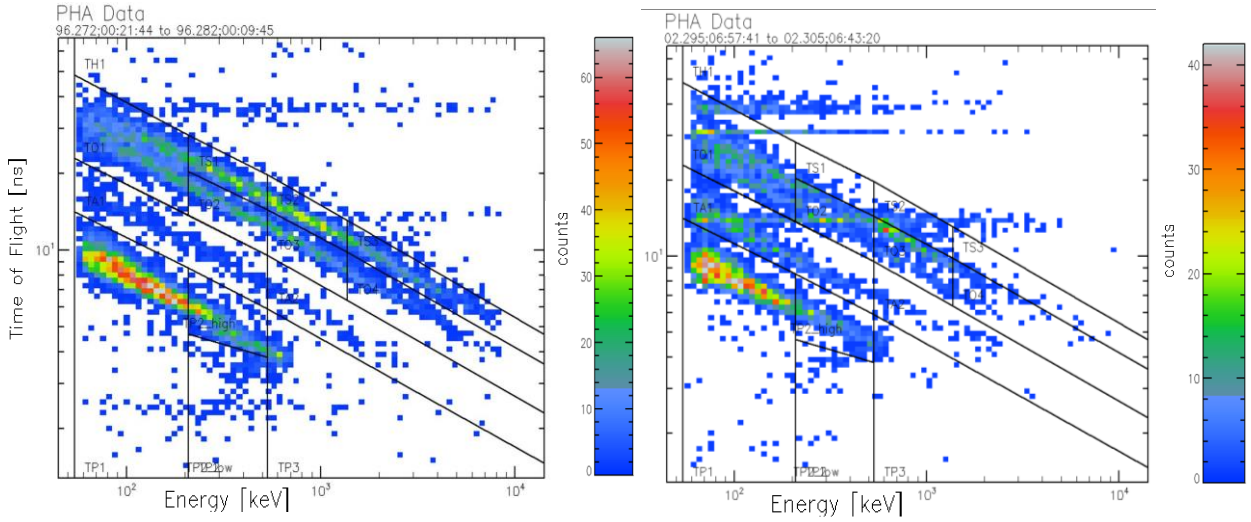

Figure 2.3-3: left: PHA analysed data plotted as Time of Flight against Energy; data taken on 29th September 1996. Right: PHA analysed data plotted as Time of Flight against Energy; data taken on 27th October 2002, after 7 additional years of mission recording from the PHA plot on the left.

The locations of the Loci and the intensity of the readings are the most notable changes during the scope of the recordings taken. Figure 2.3-3 shows a comparison between the early readings in 1996, to the later readings in 2002. The left image is the same as that in Figure 2.3-2. The right image follows the left image by seven years and perfectly illustrates the changes in the quality of the recorded data.

Notable differences:

1. The most obvious is the location of the mass loci. The sulphur line in particular had dropped completely out of the TS channels and is not being recorded in the oxygen channels

   The same is also happening with the oxygen lines and to a lesser extent the Hydrogen and the helium. The heavier mass element lines are being affected more so.
2. The other main difference affecting the data is the drop in overall sensitivity, there is a significant drop for events displayed in the right hand image of Figure 2.3-3. The overall point count and the extent of the mass loci have lessened.
3. The final change comes in the form of anomalous data. At approximately 15 and 20ns Time of Flight across the whole of the energies there is a solid line of data that is different from the others surrounding them. This is most likely a fault in the TOF detector.

2.3.1 Uses for the data:

The data from the Galileo Mission has formed the basis of most of the knowledge we have of the Jovian system. As the only craft to have taken major and extensive in-situ measurements of Jupiter, itself and the surrounding magnetosphere and radiation zones the wealth of knowledge that Galileo provided is so far unparalleled.

Even focusing on the EPD alone, the kind of research undertaken following the Galileo mission is far reaching. Many research groups focus on areas such as the ion and electron spectra (Sorensen et al., 2005) of both near and far from Jupiter; this can also reveal information on the auroral precipitation at Jupiter (Bhattacharya et al., 2005). Whilst much of the data used focus on the electron, flux and energy there have been many studies into and using the ion fluxes provided by the EPD (Radioti et al., 2005). The focus of these is in modelling the complex Jovian system; investigating the complex changing ratios of components, the ion pickup charging and the sources for the ions and the energy imparted to them.

Future mission planning uses many of these models for further investigations. Both the JUICE and JUNO missions will have used the most accurate radiation models when considering adequate protection for the sensitive on-board instruments. Accounting for the correct amount of radiation is vital in making sure that the instrument isn't damaged during the mission as well as having a stable value for the expected background readings allowing the new data taken to be a further step up.

A recurring theme in the papers using the data and those that have used any of the other EPD equipment is a statement on the viability of the collected data. There are several recurring problems with Galileo data, many of which researchers encountered during its use.

2.3.2 Problems with the data:

Over the course of the journey and the mission itself, the Galileo craft exhibited a number of faults in relation to the data taking, management and recovery. The most demanding and pressing of these problems began with the failure to unfurl the main antenna before the arrival at Jupiter.

2.3.2.1 The Antenna

From the launch of the mission in October 1989 to the first flyby of Earth in Dec 1990 the main antenna was stowed for launch and deep space flight, meaning the 18 tines that formed the umbrella shape of the antenna were held together to protect them. During the flyby, the instruments were tested and the data sent back to Earth for further trials of the data management systems. As the antenna began to unfurl, three of the 18 tines became stuck. This meant the main antenna had the appearance of a slightly crumpled lopsided umbrella (Figure 2.3-4).

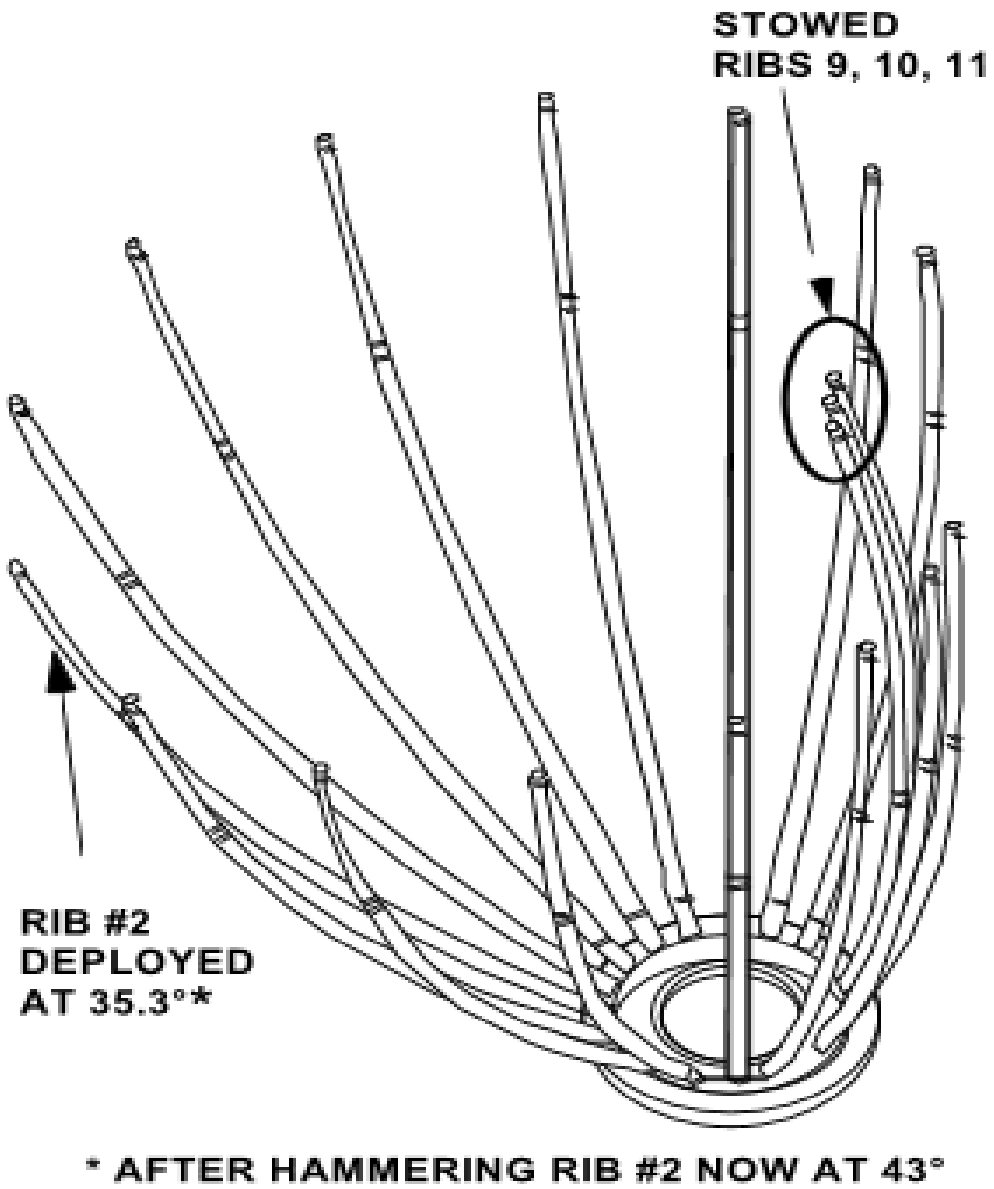

Figure 2.3-4: shows the unfurling problems of the main antenna on Galileo[Isbell, 1995].

It was determined, from a full size replica built at NASA's Jet Propulsion Laboratory that the fault came from the time Galileo spent in storage and during transit before the launch. The delays in launch from a May launch to an October launch were cause by the Challenger disaster; resulting in NASA reviewing the safety of Liquid fuelled rockets. This review and subsequent change to a solid fuelled rocket for Galileo meant that the Journey was also extended leaving the craft in deep space sleep for longer than planned; another factor in the non-functioning antenna.

2.3.2.2 Loss of Data Volume

The smaller low gain antenna salvaged the loss of the main antenna; however, this change meant that much of the data recovery was limited. The most notable consequence of this is that there are large chunks of data missing in the EPD data. This is a deliberate decision of the mission operatives who, with limited data transfer, had to choose selectively during data retrieval.

This is an already existing problem, further exacerbated by the restricted data relay. In a perfect system, all the instruments on a craft would run simultaneously; and all of the data taken, returned to Earth. This is far from the truth for all missions. In hindsight, the amount of data salvaged, through the smaller antenna, was substantial against the problems they faced.

2.3.2.3 Detector Decay

The third major problem with the EPD data is from the instrument itself. The main part of the Time of Flight system, is the energy detector at the back of the timing section; this detector is a silicon semi-conductor detector as described in section 2.2.2.

The nature of the semi-conductor detector is the cause of the changes seen in the data as illustrated by Figure 2.3-3. The thickening of the dead layer is caused by the large number of high-energy particles impacting the silicon. As each particle passes through the P doped material the energy imparted is denatured a small amount. This most likely reduces the number of bound electrons in the outermost surface of the detector. The dead layer increases as the most exposed outer layer of the silicon decayed first. As the particles measured pass through this portion of the detector, damage is then affecting the next layers down. The deeper into the surface of the silicon the lesser the effect the particles have as

some will penetrate more than others will. This effect does not affect the sensitive volume in its ability to measure energy. The PN junction determines the sensitive volume by equilibrium; the sensitive volume still functions in the same manner.

The addition of a dead layer to the front of the detector produces consistent changes in the data that are seen with the 'decay' progressing fast to begin with and then slowing as the detector becomes less sensitive and the particles do not penetrate as far into the sensitive layer.

The changes in the data, or decay, form as particles pass through the dead layer. The dead layer adds an additional thickness that particle passes through before it meets the sensitive layer. In passing through the dead layer, the particle has already lost some of its energy. The sensitive layer then measures a lower energy it should for the incoming particle. In the case of the EPD recording system, as the dead layer thickens the particle impacts are often attributed to the wrong channel as the energies become lower and lower.

Knowing that the measurement of the energy is lower than it should be is quite enlightening when analysing the differences between the left and right images in Figure 2.3-3. Initially looking at the two images it appears that the ion element loci are moving down, i.e. the Time of flight measurement is losing time. However, knowing the energy is systematically lower it is more likely that instead the loci are moving to the left. This gives the same appearance but for very different reasons, and as such can be corrected for.

As mentioned in many papers (Mauk et al., 2004, Clark et al., 2016) that have used the EPD data in some way, there were inbuilt precautions and safeguards to deal with a build-up of a dead layer. Whilst they had good foresight to expect the necessity of this, the actual severity of the decay exceeded the expected amount such that many groups and papers using the data have selected to use only the first two years out of eight for any data analysis. In part, this is due to how easily correctable this early data is.

Using the earlier, more accurate data as shown in Figure 2.3-3 PHA graphs, simple methods are applicable for making appropriate adjustments for the data. These processes are described in the appendices of Mauk et al., (2004). However, as the mission progresses and the amount of data sent back to Earth built-up, the ratio of data against data gap from the EPD widened. Thus, leaving larger and larger gaps in the data, these gaps are a

hindrance in adjusting the data correctly, as there is more uncertainty in what may have happened in between.

2.4 Evaluating the EPD's Dead layer thickness

The most important step in re-analysing the data from here is to assure the existence of a dead layer; making sure that it is the dead layer at fault rather than another unknown cause of the misread data.

By considering the movement of the data lines this is achievable. From an understanding of how the dead layer would affect the data, the next step is to identify if this is the movement that is present in the data. There are many ways of doing this: the simplest being a direct comparison of the most visible paths of the loci in the PHA graphs. There are two methods that offer direct numerical comparisons. These are, first, using the PHA values against the calibration values. The second is using the numerical data count rates to generate a Power spectrum for each element, covered later in Chapter 3.

All the methods require the calculation of the energy drop induced by the dead layer. The software SRIM: Stopping Ranges in Matter fulfils this purpose.

2.4.1 Using SRIM

Stopping Ranges in Matter or SRIM is a collection of software packages created by James Ziegler, which calculate many features of the transport of ions in matter. Amongst others, the main programs can calculate, the Ion Stopping and Range in Targets, Ion Implantation, Sputtering, Ion Transmission and Ion Beam Therapy. The applications of this software are hugely wide reaching from medical aspects of radiation oncology to sputtering calculations of surface interactions in deep space.

The stopping range functionality allows the evaluation of the decay in the EPD data. These ranges come in a table for each element that is required. The Table 2.4-1 consists of the following columns. The first is the energy of the Ion. These range from 100keV up to 4 MeV or 4000 keV, this range is the approximate range displayed on the PHA graphs for the Time of Flight plots. The next two columns contain the electronic and nuclear stopping values. These are values used in calculating the overall stopping range, with the combination of contributions from each changing as the energy changes. For very low

SULPHUR

Ion energy		dE/dx Elec	dE/dx Nuclear	Projected range		Longitudinal straggling		Lateral straggling	
100	keV	1.488	1.554	1222	Å	423	Å	315	Å
110	keV	1.541	1.504	1340	Å	454	Å	341	Å
120	keV	1.588	1.458	1459	Å	485	Å	366	Å
130	keV	1.631	1.415	1578	Å	514	Å	390	Å
140	keV	1.672	1.375	1698	Å	544	Å	415	Å
150	keV	1.711	1.338	1819	Å	572	Å	439	Å
160	keV	1.749	1.302	1940	Å	600	Å	463	Å
170	keV	1.786	1.269	2061	Å	628	Å	487	Å
180	keV	1.822	1.238	2183	Å	655	Å	510	Å
200	keV	1.893	1.181	2427	Å	707	Å	557	Å
225	keV	1.98	1.117	2733	Å	770	Å	615	Å
250	keV	2.066	1.062	3037	Å	829	Å	671	Å
275	keV	2.153	1.012	3341	Å	886	Å	726	Å
300	keV	2.24	0.9674	3642	Å	939	Å	780	Å
325	keV	2.329	0.9273	3940	Å	990	Å	832	Å
350	keV	2.419	0.8909	4235	Å	1038	Å	884	Å
375	keV	2.51	0.8577	4526	Å	1083	Å	933	Å
400	keV	2.601	0.8273	4813	Å	1126	Å	981	Å
450	keV	2.787	0.7734	5375	Å	1206	Å	1074	Å
500	keV	2.974	0.7271	5918	Å	1279	Å	1160	Å
550	keV	3.162	0.6868	6444	Å	1344	Å	1241	Å
600	keV	3.35	0.6513	6952	Å	1402	Å	1317	Å
650	keV	3.537	0.6198	7443	Å	1455	Å	1388	Å
700	keV	3.722	0.5917	7918	Å	1504	Å	1454	Å
800	keV	4.085	0.5433	8823	Å	1590	Å	1575	Å
900	keV	4.436	0.5032	9674	Å	1663	Å	1682	Å
1	MeV	4.775	0.4693	1.05	µm	1726	Å	1777	Å
1.1	MeV	5.099	0.4402	1.12	µm	1780	Å	1862	Å
1.2	MeV	5.41	0.4149	1.2	µm	1828	Å	1939	Å
1.3	MeV	5.707	0.3927	1.27	µm	1870	Å	2009	Å
1.4	MeV	5.991	0.373	1.33	µm	1907	Å	2073	Å
1.5	MeV	6.263	0.3554	1.4	µm	1941	Å	2132	Å
1.6	MeV	6.522	0.3396	1.46	µm	1971	Å	2186	Å
1.7	MeV	6.771	0.3254	1.52	µm	1999	Å	2237	Å
1.8	MeV	7.008	0.3123	1.58	µm	2024	Å	2284	Å
2	MeV	7.454	0.2895	1.69	µm	2072	Å	2369	Å
2.25	MeV	7.963	0.2658	1.82	µm	2125	Å	2461	Å
2.5	MeV	8.426	0.246	1.94	µm	2169	Å	2543	Å
2.75	MeV	8.849	0.2292	2.06	µm	2208	Å	2614	Å
3	MeV	9.237	0.2148	2.18	µm	2243	Å	2679	Å
3.25	MeV	9.596	0.2022	2.29	µm	2273	Å	2737	Å
3.5	MeV	9.929	0.1912	2.39	µm	2301	Å	2791	Å
3.75	MeV	10.24	0.1815	2.5	µm	2326	Å	2840	Å
4	MeV	10.53	0.1727	2.6	µm	2349	Å	2885	Å

Table 2.4-1: The Sulphur Ion stopping range in Silicon

energy particles, the nuclear component is dominant, as the particle gains energy the electric component takes over in dominance.

The fourth column is the most important in this study, this column being the projected range. The distance the particle will travel once it has reached the surface it is impacting into.

This can also be looked at another way; in that if a particle travels through a distance of material then it will lose the associated amount of energy. Knowing that the dead layer consists of the same silicon as the sensitive layer the amount of energy lost passing through a variety of dead layers is simple to read off Table 2.4-2.

Element	0.0 µm	0.05 µm	0.1 µm	0.15 µm	0.2 µm	0.25 µm	0.3 µm	0.35 µm	0.4 µm	0.5 µm
Iron	0	64	123	182	241	300	359	418	477	595
Sulphur	0	38	80	122	164	205	247	289	331	414
Oxygen	0	17	40	63	86	109	132	155	178	224
Helium	0	4	9	15	21	27	33	39	45	57
Hydrogen	0	2	7	12	17	21	26	31	36	46

Table 2.4-2: Energy lost passing through Dead Layer depth of Silicon

For the most part any attempt at correcting the data counts for the later mission years has been done by re allocating the channel values individually. An interesting aside is

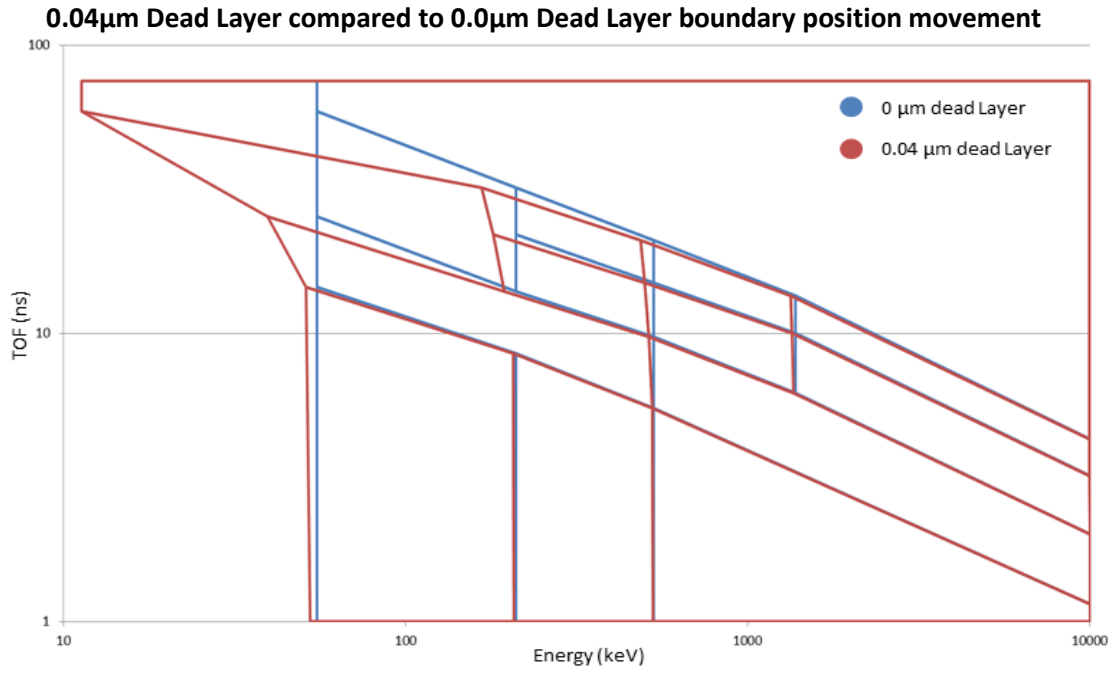

Figure 2.4-1: visual representation of the effect of the dead layer on the channel boundary lines. Direct comparison between the original line definitions and the lines when 0.04µm dead layer is applied.

to instead reposition the channels themselves to show how much damage a dead layer would have caused to the channel allocations.

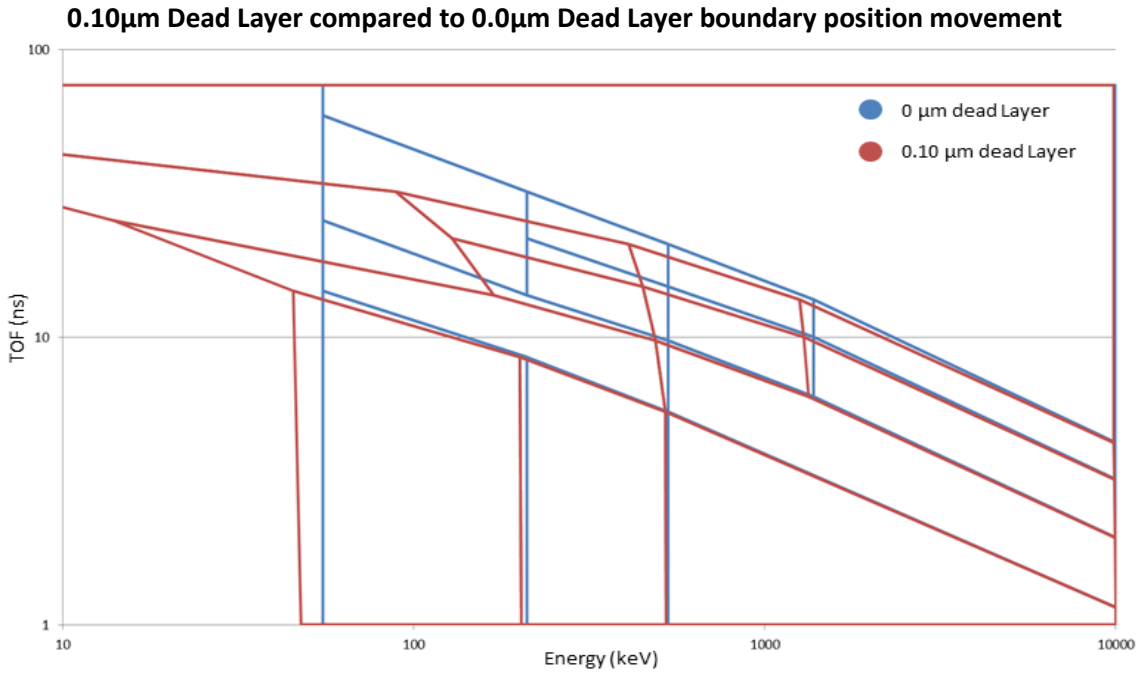

Figure 2.4-2: visual representation of the effect of the dead layer on the channel boundary lines. Direct comparison between the original line definitions and the lines when 0.10µm dead layer is applied.

To do this the position of each channel boundary needs to be found; working backwards from the PHA plots and then comparing to the channel boundary descriptions the points can all be found. From there each point needs to be allocated into an element. This means evaluating which of the dead layer corrections in Table 2.4-2 will be added to the values of the boundaries between each channel. Once this is done a picture can be built up of what is actually happening with the data and how badly the mismeasurement can affect the science being pulled from the mission.

Figure 2.4-1, Figure 2.4-2 and Figure 2.4-3, show the movement of the boundary line with a dead layer applied to them. Whilst not greatly useful in the correcting of the data, this is helpful in giving perspective. The effect that the correction will have on the data and where the data is affected is rather abstract when envisioning the moving of the boundaries determined by energy values. As you can see from the movement of the lines, the higher energy data points are not as badly affected.

0.16µm Dead Layer compared to 0.0µm Dead Layer boundary position movement

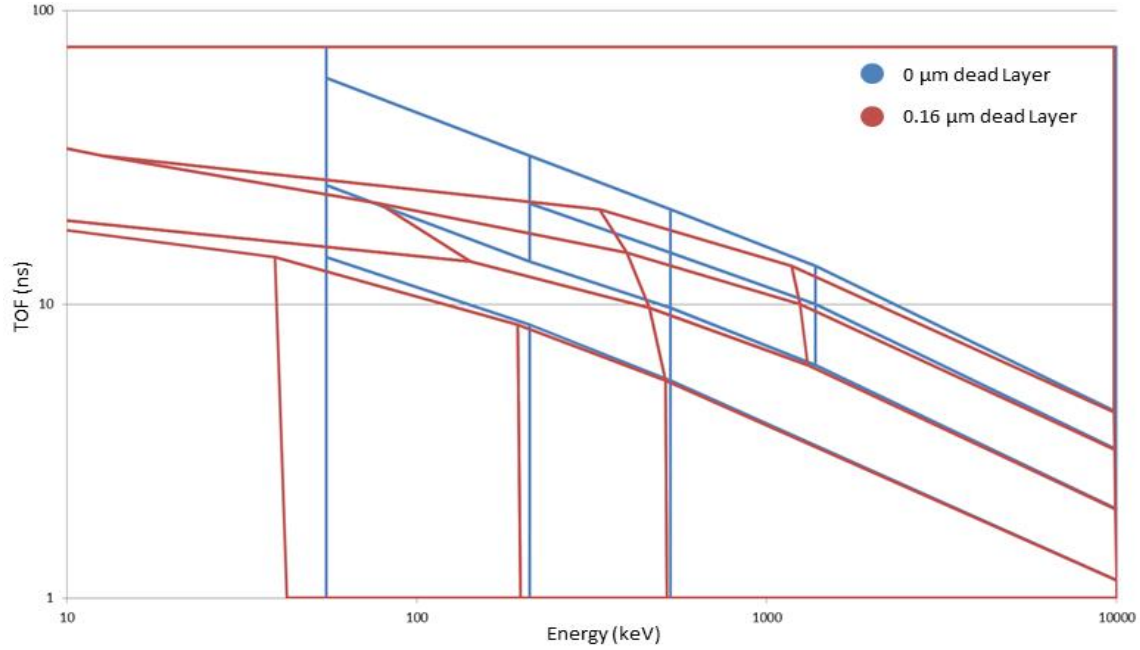

Figure 2.4-3: visual representation of the effect of the dead layer on the channel boundary lines. Direct comparison between the original line definitions and the lines when 0.16µm dead layer is applied.

2.4.2 Dead Layer Estimation from PHA graphs

This first attempt at categorizing the Dead layer thickness begins with the values of energy changes given in the table above (Table 2.4-2). By assuming that there is a dead layer present the loci visible in the PHA graphs from the later years should match up with a line formed from an earlier data set with a dead layer applied to it. Taking the earliest good PHA graph (Figure 2.3-2) taken over a 11 day period beginning on 29th Sep 1996, the loci can be mapped out and converted into a set of TOF and Energy data points.

The first problem in comparing this data in this manner is how to define the lines of the loci in the PHA graphs. The data points calculated during the plotting of the raw data is not conducive for extracting groups or loci from. The huge number of overlaying data points makes plotting individual trend lines for each of the element problematic.

PHA graphs are an accumulation of a set of data points, they are plotted on dual log scales and each channel has a normalization factor to keep the boundaries between the channels smooth. These factors make plotting a trend line for each locus additionally complicated. With this in mind, the plotting the trend line by hand allows the greatest amount of accuracy as possibly; shown in the following Figure 2.4-4

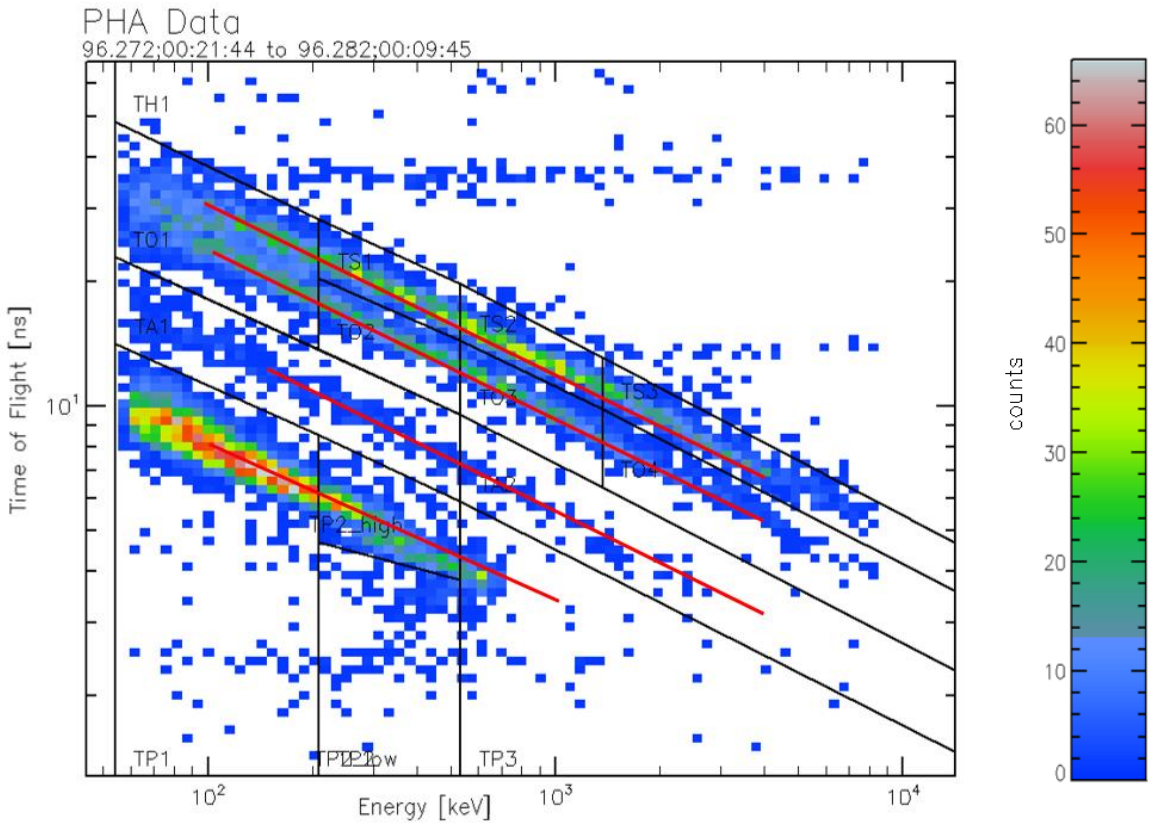

Figure 2.4-4: PHA Data graph from 1996 data set with overlaid loci best fit line

The trend line position comes from the energy at the centre point of each channel box, and then the TOF values picked as to best position that lies to match the locus of each element. Applying the dead layer to the energies is then as simple as adding a value of energy to each point based on the loci it is fitting.

The next step in this comparison is applying the newly calculated dead layer lines to the ageing real data. The following PHA graphs show how the applied dead layers fit as the years of the mission progress. The Figure 2.4-5, Figure 2.4-7 and Figure 2.4-6 are the snapshots of the comparisons showing the best of the matches for each set of PHA graphs and dead layers.

Whilst it may be that these fits are comparable, there are many places where there are more improvement options. Best seen in Figure 2.4-6, the Proton fit differs from the real data, the values appearing considerably rotated and lower than predicted. This illustrates the need for more definitive effects of the dead layer. The dead layer affects the Protons far less than it does the heavier elements. Also seen in Figure 2.4-7 and Figure 2.4-5 the dead

layer Loci seem to have rotated in relation to the mission data. This could be a positioning problem but it could also be illuminating further problems with this kind of comparison.

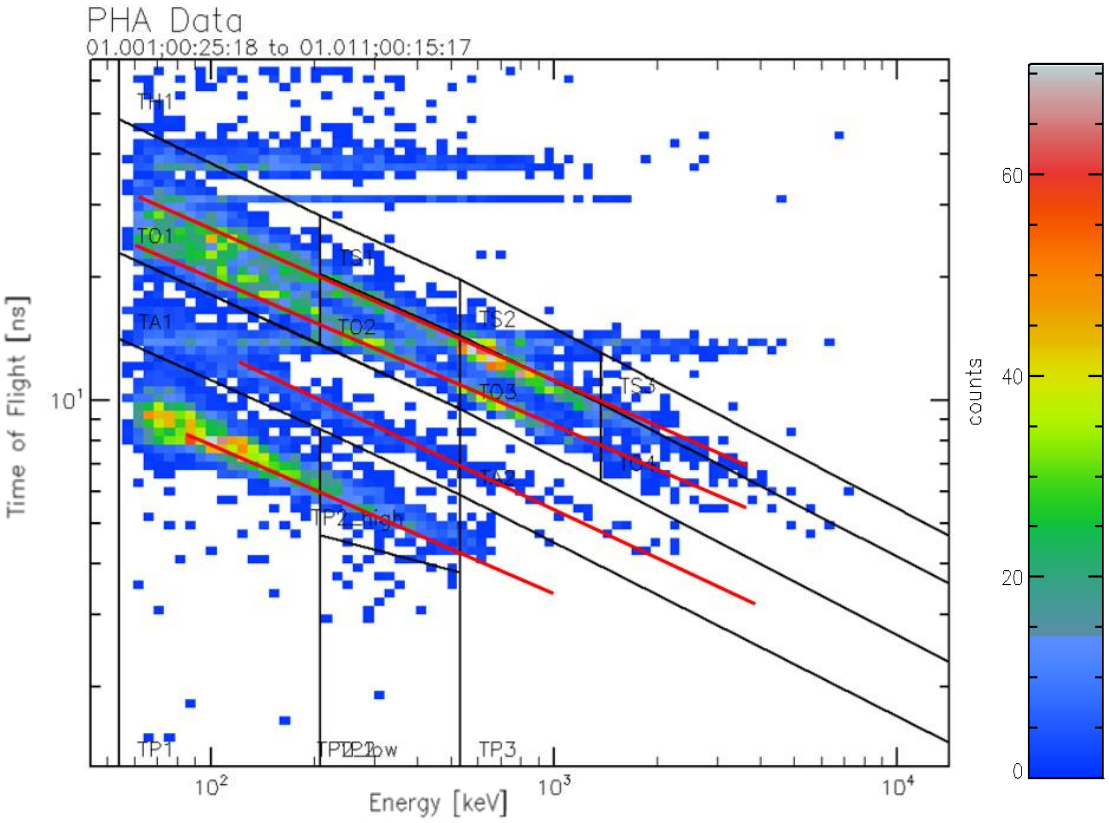

Figure 2.4-5: PHA plot from 2001 with overlaid trend lines from 1996 with 0.1µm dead layer applied.

The rotational aspect of the trend lines is a feature of using log against log scales for the PHA graphs, it also stems from the attributes of particles passing through a material and depositing energy. The slower the particle and the larger the size of the particle the more energy will be lost as it passes through. However, with the computation to produce the PHA graphs there may be a normalization that affects where the data lies. This would come from the very lowest energy particles not passing through the detector at all; this would shift the normalization towards the centre of the channel boxes.

This disparity in the later years between the dead layer loci and the PHA graphs requires further testing. Figure 2.4-8 shows a comparison between the 0.1µm dead layers against an applied gain drop in the detector measurement system. A gain drop is systematic and unaffected by the elements or the amount being recorded. Most likely deterioration in the electronics recording the impact energies would cause this.

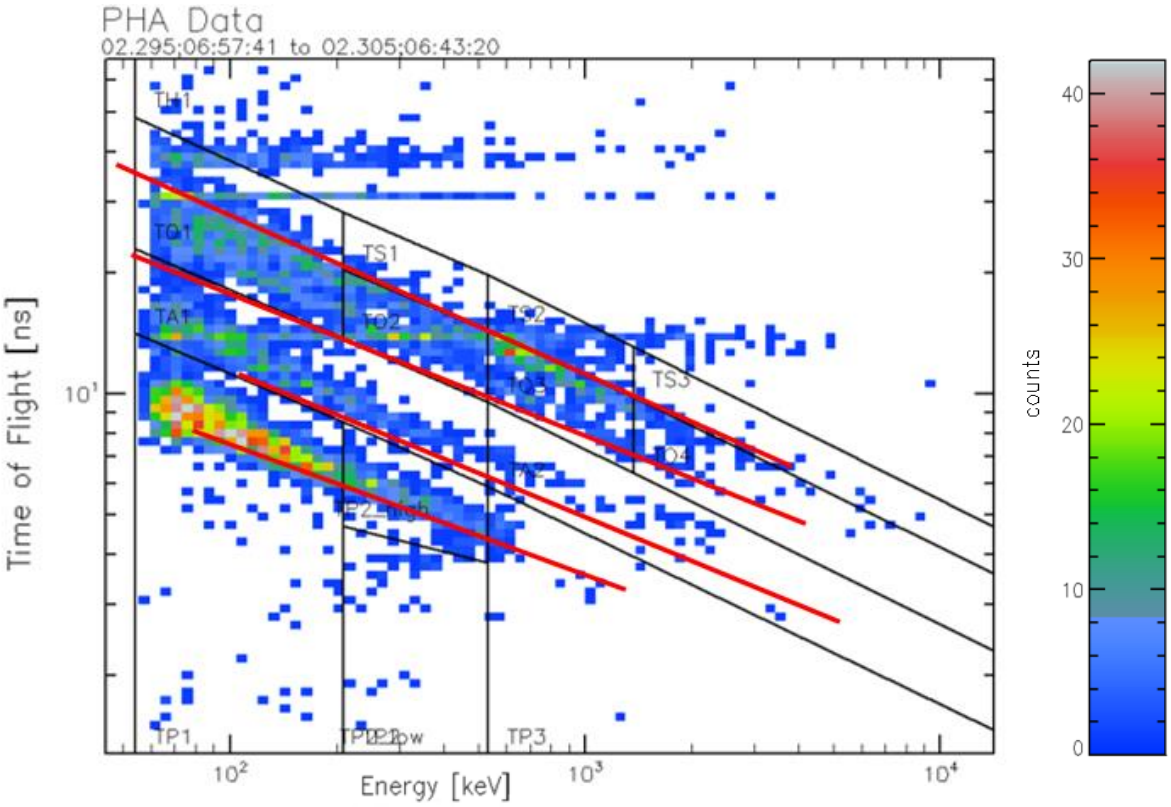

Figure 2.4-7:PHA plot from 2002 with overlaid trend lines from 1996 with 0.3µm dead layer applied.

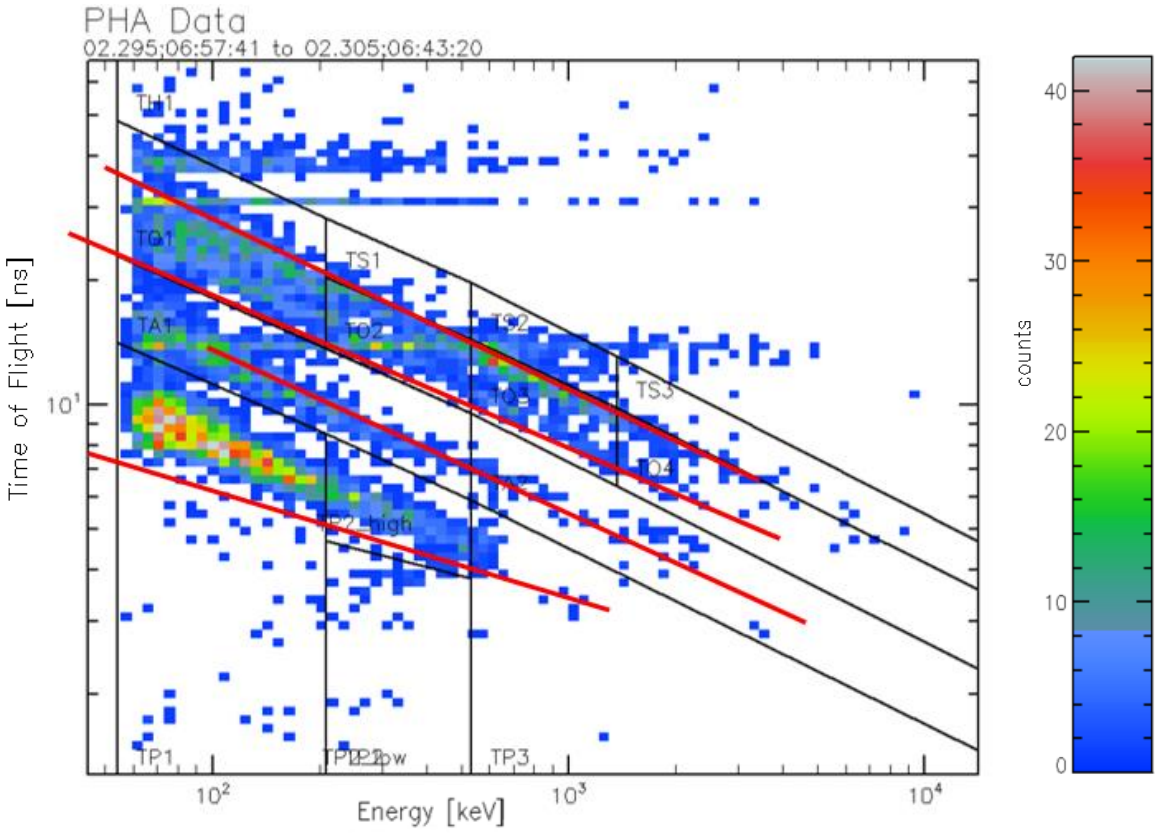

Figure 2.4-6:PHA plot from late 2002 with overlaid trend lines from 1996 with 0.5µm dead layer applied.

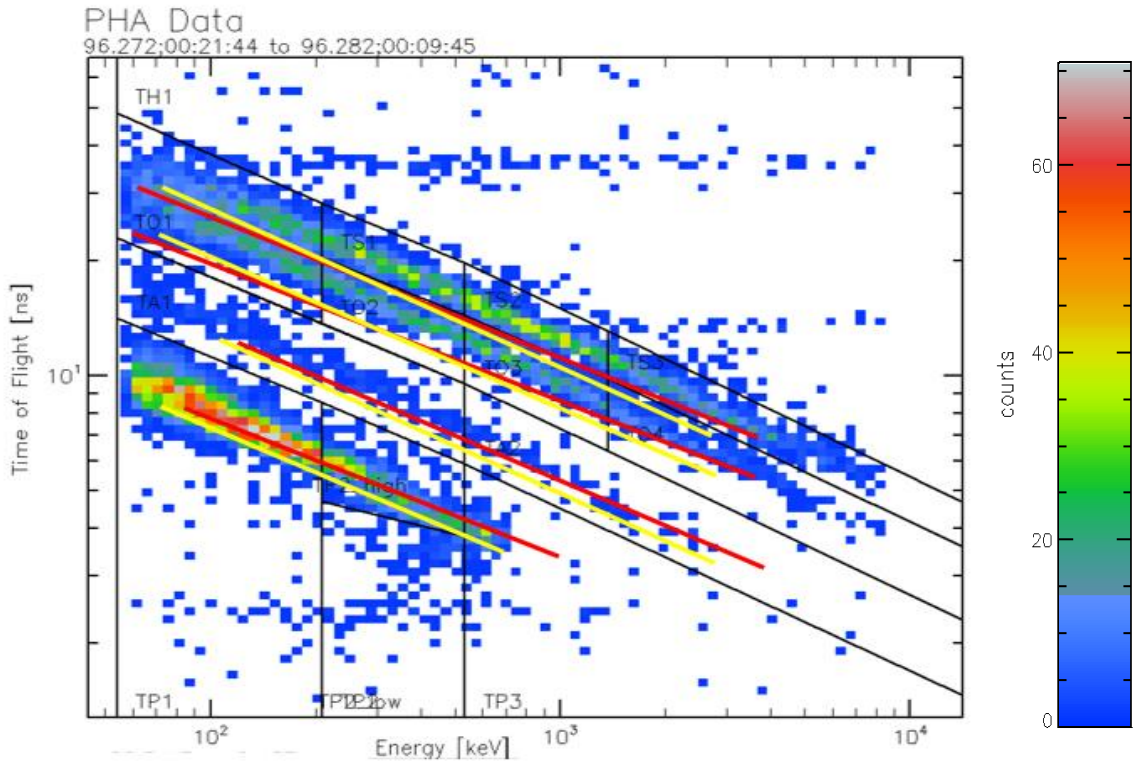

Figure 2.4-8: comparison between a 0.1µm dead layer (red line) against a 30% gain drop in energy from the detector (yellow line) .

At this point, it becomes clear from the comparison that it is impossible to determine which the better fit to the real data is. The gain drop investigations are important and in the following chapter, these will come into consideration again. To continue in this line of investigation the comparison needs a quantitative calculation.

2.4.3 Dead Layer Estimation from Calibration

Using the same Energy loss Table 2.4-2, the Dead Layer change of the PHA graphs is comparable. Using the kinetic energy equation (1) and knowing the elements expected in the magnetosphere, calculating a calibration line for each of the loci is possible. These represent each locus for each element. Calculating these calibration lines requires a set of energies; these energies are spaced over the range that the detector can detect. Once the energies have been determined, applying them to equation (1) with the appropriate element mass results in a time of flight value for each energy. This gives a known calibration data set with which to compare the real and dead layer data sets.

Element	Energy (keV)	Actual data: 1996.272 TOF (ns)	Actual Data: 1997.051 TOF (ns)	Actual Data: 1999.18 TOF (ns)	Actual Data: 2000.001 TOF (ns)	Actual Data: 2002.295 TOF (ns)	Calibration data TOF (ns)
Iron	100	55.1	49.3	-	-	-	65.6
	200	39.2	35.2				46.4
	500	25.0	22.5				29.3
	1000	17.8	16.1				20.7
	2000	12.7	11.5				14.6
	5000	8.1	7.3				9.2
	7000	6.8	6.2				7.8
Oxygen	100	37.3	33.6	31.9	29.8	28.2	48.6
	200	27.0	24.6	23.3	22.0	20.8	34.3
	500	17.7	16.3	15.3	14.7	13.9	21.7
	1000	12.8	12.0	11.2	10.8	10.2	15.3
	2000	9.3	8.8	8.2	8.0	7.5	10.8
	5000	6.1	5.8	5.4	5.3	5.0	6.8
	7000	5.2	5.0	4.6	4.6	4.3	5.8
Sulphur	100	25.7	25.7	23.6	23.5	22.7	34.4
	200	18.8	18.6	17.1	17.1	16.5	24.3
	500	12.4	12.2	11.2	11.1	10.9	15.4
	1000	9.1	8.8	8.1	8.1	7.9	10.9
	2000	6.7	6.4	5.9	5.8	5.8	7.7
	5000	4.4	4.2	3.9	3.8	3.8	4.8
	7000	3.8	3.6	3.3	3.3	3.3	4.1
Helium	100	15.8	15.9	13.8		13.0	17.1
	200	11.3	11.4	10.1		9.6	12.0
	500	7.3	7.3	6.7		6.5	7.6
	1000	5.2	5.3	4.9	-	4.8	5.4
	2000	3.8	3.8	3.6		3.5	3.8
	5000	2.4	2.4	2.4		2.4	2.4
	7000	2.1	2.1	2.1		2.1	2.0
Hydrogen	100	7.9	7.5	7.8	7.9	7.8	8.6
	200	5.7	5.5	5.8	5.9	5.9	6.1
	500	3.7	3.6	3.8	4.0	4.0	3.8
	1000	2.7	2.7	2.8	3.0	3.0	2.7
	2000	2.0	2.0	2.1	2.2	2.3	1.9
	5000	1.3	1.3	1.4	1.5	1.6	1.2
	7000	1.1	1.1	1.2	1.3	1.4	1.0

Table 2.4-3: Time of flights for Real and calibration data to be compared, grouped into elements over the full energy range of the instrument. Missing section designate where the read data was missing or undistinguishable.

Using a calibration data set is favourable as it also allows any inconsistencies in the earliest of the real data sets to become apparent. In the previous method, the comparison was against the “best” known data. However, this may not have been the best data. During

the journey phase of the mission there may have been additional factors causing the data to reduce in quality. The calibration data will eliminate any chance of this being the case.

The overall method for comparison is the same. The energy depletion from Table 2.4-2 can be added to each calibration line for each Dead Layer; this would then give a calibrated dead layer data set. Again, this is preferable over using the 1996 data set as it could be at fault itself. Figure 2.4 9 shows how different the real and the calculated calibration lines are; this discrepancy is likely to have been removed in the instrument itself as they account for the nature of the silicon-semiconductor detector. By using the comparison method, it will be possible to determine the amount the instrument was calibrated by using the best match of the early data sets.

The real dated data in Table 2.4-3 match the overlaid loci from section 2.4.3. In that section they were overlaid to match the lengths of the visible loci cutting them short of the length of the full limits of the detector. If left this way the comparison suffers with inconsistencies, the solution to this is re-plotting the real data sets to match the full range of the detector to match the calibration lines. Overall, this ensured that the comparison was for only the time of flight component

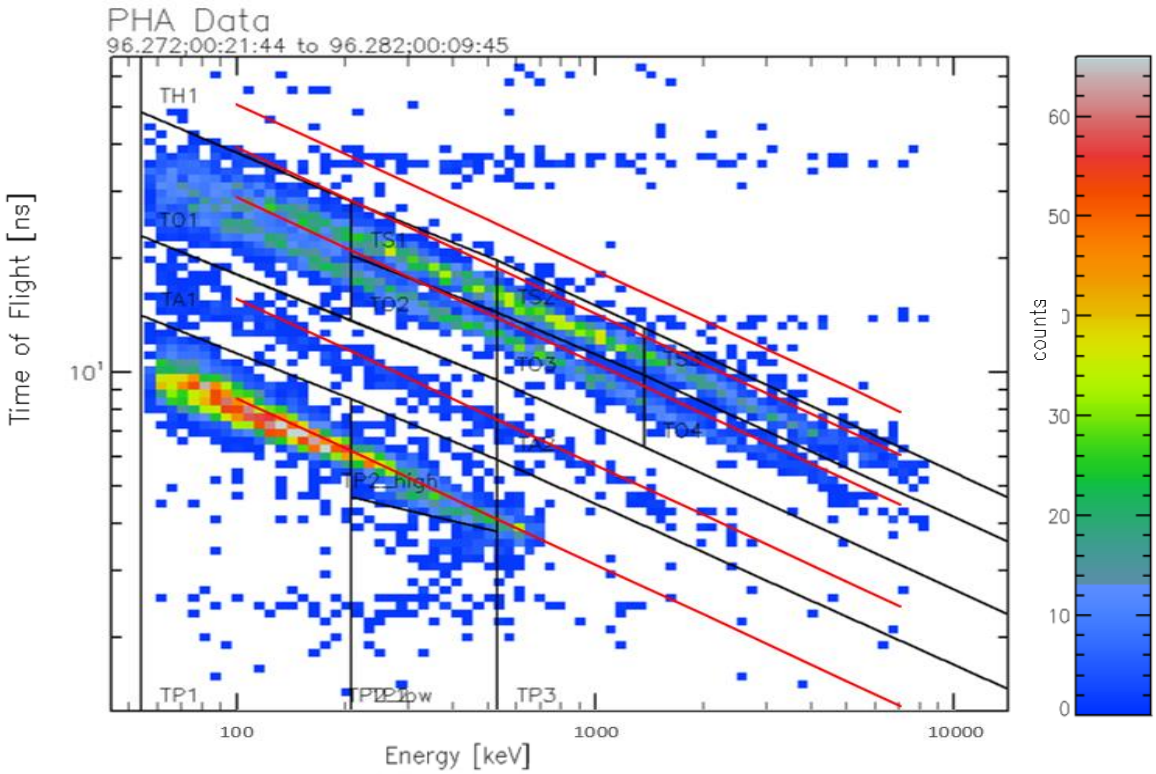

Figure 2.4-9: PHA Data graph from 1996 data set with overlaid loci of the generated calibration lines.

The comparison encompasses five of the PHA plots, over the 8 years of data, to be compared with the set of calibration data and the dead layer shifted calibration data. With the high number of dead layer shifted calibration data sets, this totalled the comparisons at 65. For each calibration of the 65, there were seven energies for each of the five elemental loci giving 35 data points for comparison in each set.

The comparison is being analysed using the Chi Squared Test.

2.4.3.1 The Chi Squared test:

The Pearson's Chi squared test, is a test of goodness of fit. It primarily establishes whether the observed frequency of a value differs from the expected frequency. The chi square test computes a percentage difference by incrementally evaluating the pairs of values compared, the final percentage being the sum of these. Based on the number of pairs of values being evaluated the significance of the result changes. This is the Degrees of Freedom of the test and calculated thusly:

$$\mathrm{DF} = (\mathrm{r} - 1) * (\mathrm{c} - 1) \tag{2}$$

The degrees of Freedom value, DF, uses equation (2); it evaluates the number of rows (r) and columns (c) in the calculation. The comparison of the real data to calibration/ dead layer data consists of 2 columns and 35 rows. The columns contain the two sets of data being compared, the rows are the number of values contained within the 5 loci lines as individual data points. As stated earlier this value is 35 for each data set. The DF is then 34 for all of the comparisons, which use the full sets of data. This is not always the case as in some of the later mission PHA graphs suffer from the contamination of the data making the loci of some elements hard to make out. In these cases, the comparison is only for the viable data; i.e. if the set is missing the Iron line, then for a fair comparison the calibration iron line will not be required.

The calculation of the comparison by Chi Squared uses a simple formula:

$$\chi^2 = \sum_{i=1}^{n} \frac{(O_i - E_i)^2}{E_i} \tag{3}$$

This is interpreted by using i as the row in the data being looked at; the O is then the Observed value the value that is being compared with the calibration data. Following on the

value E is the Expected value i.e. the calibration value. Each of these are put into the formula for each row of the 35, then the results are summed together to give the overall value of the Chi Squared.

2.4.3.2 Results of Chi Squared test

The results from a chi-squared test can seem rather abstract before comparing to the percentage values in the degrees of freedom listings. Below (Table 2.4-4) are the raw values of the initial testing over a small range of dead layers to check that the presence of a dead layer was indeed visible.

Chi2	1996.272 (35)	1997.051 (35)	1999.18 (28)	2000.001 (21)	2002.925 (28)
Calibration data	15.06094646	26.46541957	23.10817004	25.48189894	32.19466966
Dead layer 0.1 µm	2.71435066	3.212442716	4.762503789	5.582523523	8.78770264
Dead layer 0.2 µm	25.39834029	13.47081028	4.364358152	3.484343672	4.408567708
Dead layer 0.3 µm	23.27916045	11.38686941	2.493790649	2.180111736	2.975910741
Dead layer 0.4 µm	36.02203293	20.36029964	8.06665624	8.179938233	8.360001914
Dead layer 0.5 µm	34.07596028	18.59538823	6.820883099	3.942261729	3.881966518

Table 2.4-4: Initial results from Chi Squared test of dead layer comparison. Bordered cells correspond to the closest matching dead layer for each year.

DoF	0.999	0.995	0.99	0.975	0.9	0.5	0.2	0.1	0.05	0.025	0.02	0.01	0.005
35	14.05	16.50	17.78	19.80	24.8	34.3	40.67	44.90	48.60	51.96	52.99	56.06	58.96
28	10.4	12.5	13.6	15.3	18.9	27.3	34	37.9	41.3	44.5	45.4	48.3	51
21	6.454	8.04	8.9	10.3	13.2	20.3	26.2	29.6	32.7	35.5	36.3	38.9	41.4

Table 2.4-5: Percentage of fit for 35, 28 and 21 degrees of freedom.

Chi2	1996.272 (35)	1997.051 (35)	1999.18 (28)	2000.001 (21)	2002.925 (28)
Calibration data	15.06094646	26.46541957	23.10817004	25.48189894	32.19466966
Dead layer 0.025 µm	9.880733925	19.59068993	18.19752532	20.43190863	26.40984965
Dead layer 0.05 µm	5.52990995	13.1216425	13.21068122	15.0829368	20.17443363
Dead layer 0.075 µm	2.503094727	6.869446588	8.664885501	10.13069007	14.34709531
Dead layer 0.1 µm	2.71435066	3.212442716	4.762503789	5.582523523	8.78770264
Dead layer 0.125 µm	9.089186333	4.677730399	4.078996603	3.901534102	6.282267381
Dead layer 0.15 µm	17.76964628	9.20531227	4.434557977	3.842587828	5.52704447
Dead layer 0.175 µm	17.71351979	9.412014792	4.856917052	3.350570505	6.037854252
Dead layer 0.2 µm	25.39834029	13.47081028	4.364358152	3.484343672	4.408567708
Dead layer 0.225 µm	26.65089435	13.00356411	2.972211545	2.292471966	3.059615475
Dead layer 0.25 µm	33.00265141	18.30475997	4.786692353	3.819569875	4.320916144
Dead layer 0.275 µm	27.63820129	14.05663275	2.821892558	2.514753585	2.988457283
Dead layer 0.3 µm	23.27916045	11.38686941	2.493790649	2.180111736	2.975910741
Dead layer 0.325 µm	18.00894663	8.104824472	1.667557038	1.827861645	2.948199054
Dead layer 0.35 µm	28.23937683	13.76562822	2.059415466	1.68064769	2.287364617
Dead layer 0.375 µm	21.47273043	10.36418133	2.280336107	2.001383827	2.971849346
Dead layer 0.4 µm	36.02203293	20.36029964	8.06665624	8.179938233	8.360001914
Dead layer 0.5 µm	34.07596028	18.59538823	6.820883099	3.942261729	3.881966518

Table 2.4-6: Results from Chi Squared test of dead layer comparison with added intermediate dead layers. Bordered boxes correspond to the closest matching dead layer for each year.

The aim of the small range and large increment step test was to check that the method was a valid way of testing the comparison. From the range of values computed and the general trends, this method is a huge leap in quantifying the dead layer from the previous method.

The values in Table 2.4-5 show the corresponding percentage of fit for the values produced by the chi squared comparison. When looking at the initial values (Table 2.4-4) the values highlighted are the smallest values for each of the dead layers tested.

Using the comparison in this manner, comparing dead layer to year instead of vice versa, gives more of an insight into where each of the dead layers match. This comparison really highlights how close the data sets really are. Even as the dead layer increases the chi squared still produced around 90% match for 2002 data, seen by comparing the values in Table 2.4-6 with the percentile values in Table 2.4-5.

When analysing by year and matching a dead layer values to each year (as designated by the bordered boxes in Table 2.4-4) there is a more linear progression. This

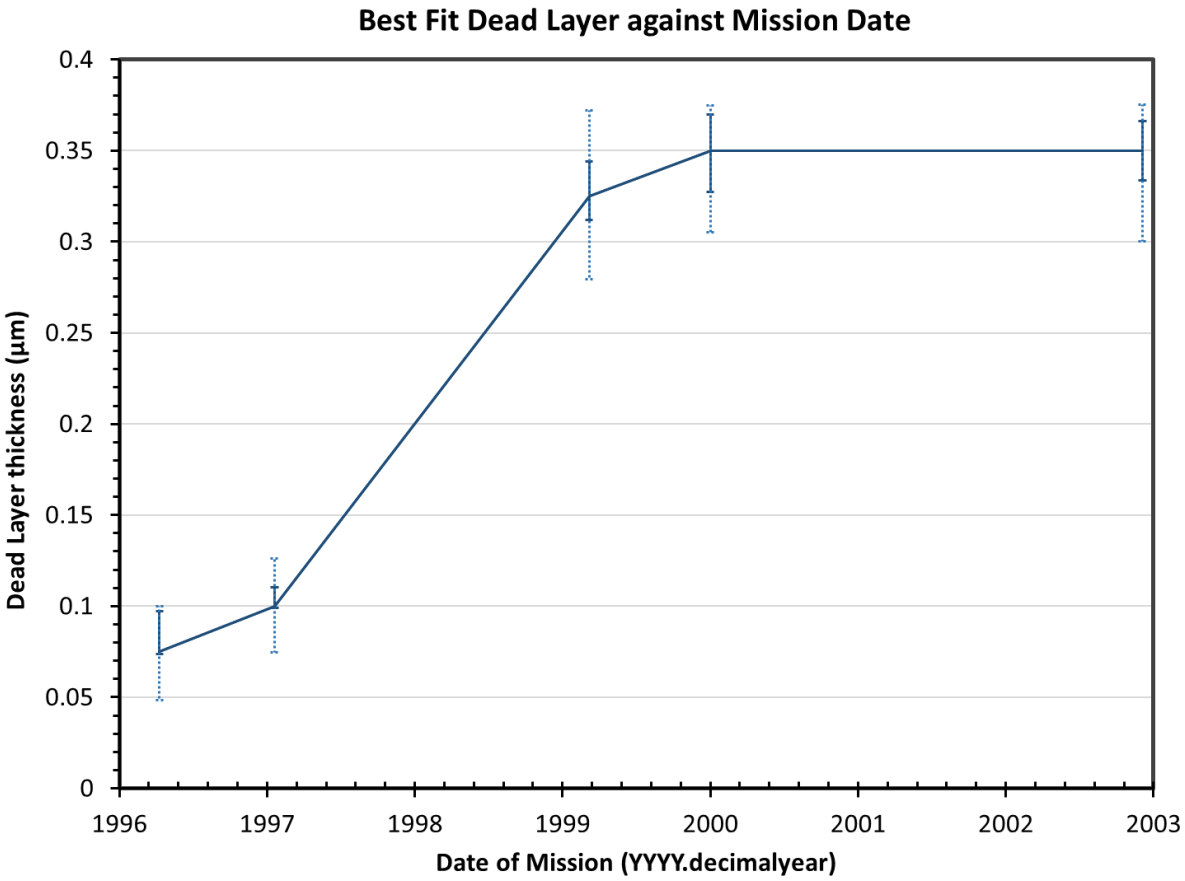

Figure 2.4-10: Increase in dead layer over mission years determined by best fit data.

identifies a true value of the dead layer being around the 0.1 to 0.2µm thickness. To distinguish this further, more values of intermediate dead layers are calculated.

In this table of results (above Table 2.4-6) the same highlighting (closest match of year for each dead layer) and bordering (closest match of dead layer for each year) has been done to show the lowest values of each of the comparison sets. This time there are more dead layer layers between the calibration data and the 0.3µm, this is to narrow down the focus for identifying the overall best match.

The best way to visualise this data is to view it in graph form. The data gaps in the yearly sections are clearly visible and the non-steady accumulation of growth of the dead layer is visible (Figure 2.4-10). In Figure 2.4-10 the darkest central blue line shows the best fit of the dead layers compared. The smaller of the error bars show the percentage difference in the next closest fit of dead layer. These error bars are the closest dead layer compared either side of the best fit, the second set of error bars shows the next closest. This gives some insight into how close each fit is to each other; giving a value for how much the fit would need to change before considered being in the next.

2.4.4 Instrument Calibration

This method of using calculated calibration line to compare to real data, assumes that the instrument is recording perfectly and, the particles hitting the detector are being read accurately before the mission. Unfortunately, no instrument is perfect, hence why all instruments are tested before launch by recording known values and adjusting the readings so that they match the known inputs. This instrument calibration accounts for the doping of the silicon-semiconductor used for the detector, this is an unavoidable ‘dead layer’ caused by the doping process and inconsistencies in the silicon, rather than by particles impacting.

This instrument calibration can be seen in Figure 2.4-10; as the, theoretically perfect, calibration lines do not match with the data from the start of the mission. Whilst there is the possibility of there being decay to the detector during the journey, it wouldn’t be as high as can be seen here. Instead this is where the instrument has been calibrated to. The dead layer present in the detector in the first case is approximately 0.075µm.

This needs to be accounted for in the comparisons and will thus improve the estimation of the dead layer. Instead of simulating an energy drop in the calculated calibration values, the energy values at 0.075µm are used instead. This means the energy loss as the dead layer builds up from particle impaction, begins smaller than it would have

Chi2	1996.272 (35)	1997.051 (35)	1999.182 (28)	2000.001 (21)	2002.925 (28)
Calibration data	2.184613763	6.209382838	8.38407312	9.970182142	14.2112936
Dead layer 0.025 µm	2.943337384	3.174568906	5.432752975	6.455153481	9.959296642
Dead layer 0.05 µm	7.790371506	3.87312295	3.820879092	4.4478216	7.369929328
Dead layer 0.075 µm	9.529234361	4.350978034	3.134910108	3.664617314	6.19277638
Dead layer 0.1 µm	15.18563415	6.81525799	2.537153169	2.664093118	4.602456748
Dead layer 0.125 µm	22.4740634	11.06328357	2.730191613	2.325580213	3.758417014
Dead layer 0.15 µm	29.27087397	15.34272634	3.215476819	2.430750672	3.572376109
Dead layer 0.175 µm	30.61227778	16.19322735	3.169608843	2.369485373	3.364074083
Dead layer 0.2 µm	27.69775444	14.18191252	2.721102375	2.147470553	3.074623255
Dead layer 0.225 µm	23.43183638	11.29479737	1.956786922	1.801033102	2.802245943
Dead layer 0.25 µm	18.42732753	8.180933279	1.613923361	1.809955521	2.965312206
Dead layer 0.275 µm	32.32344423	17.06557713	2.886404247	2.158595896	2.714901829
Dead layer 0.3 µm	21.66597088	10.08005672	1.548378204	1.591877046	2.537667851
Dead layer 0.325 µm	34.70773029	18.57634706	2.795922029	2.020521775	2.478881527
Dead layer 0.35 µm	27.6586854	13.34488223	3.334025111	2.188250991	2.016655118
Dead layer 0.375 µm	31.72850979	16.55232475	2.567900289	2.064976698	2.593085847
Dead layer 0.4 µm	27.52244997	14.6446626	4.684167385	3.232421362	3.348329963
Dead layer 0.5 µm	29.00452573	17.07786233	6.922756628	4.48787159	4.414800522

Table 2.4-7: Results from Chi Squared test of dead layer comparison accounting for the instrument calibration pre-mission launch. Bordered boxes correspond to the closest matching dead layer for each year.

done if the initial 0.075µm was simply

ignored. e.g. the energy loss of an oxygen particle through 0.025µm is around 6keV whereas for 0.025µm in addition to the 0.075µm it is 40keV. At thicker depths this difference doesn't make much difference, however it allows a higher depth of dead layer to be investigated and helps to smooth the dead layer build up in the early years of the mission.

Having adjusted the calibration data for this instrument calibration, the comparison can be re-computed using the chi squared method.

Table 2.4-7 shows how the early increases in the dead layer have been smoothed by accounting for the pre-mission calibration. The start of mission is now showing as a 0µm of dead layer, which how the instrument should have been calibrated. There is still a possibility there was some build-up of a dead layer during the flight phase, however the most accurate method to test for this is to compare real data with data taken during the instrument testing, which is not available from the NASA archives.

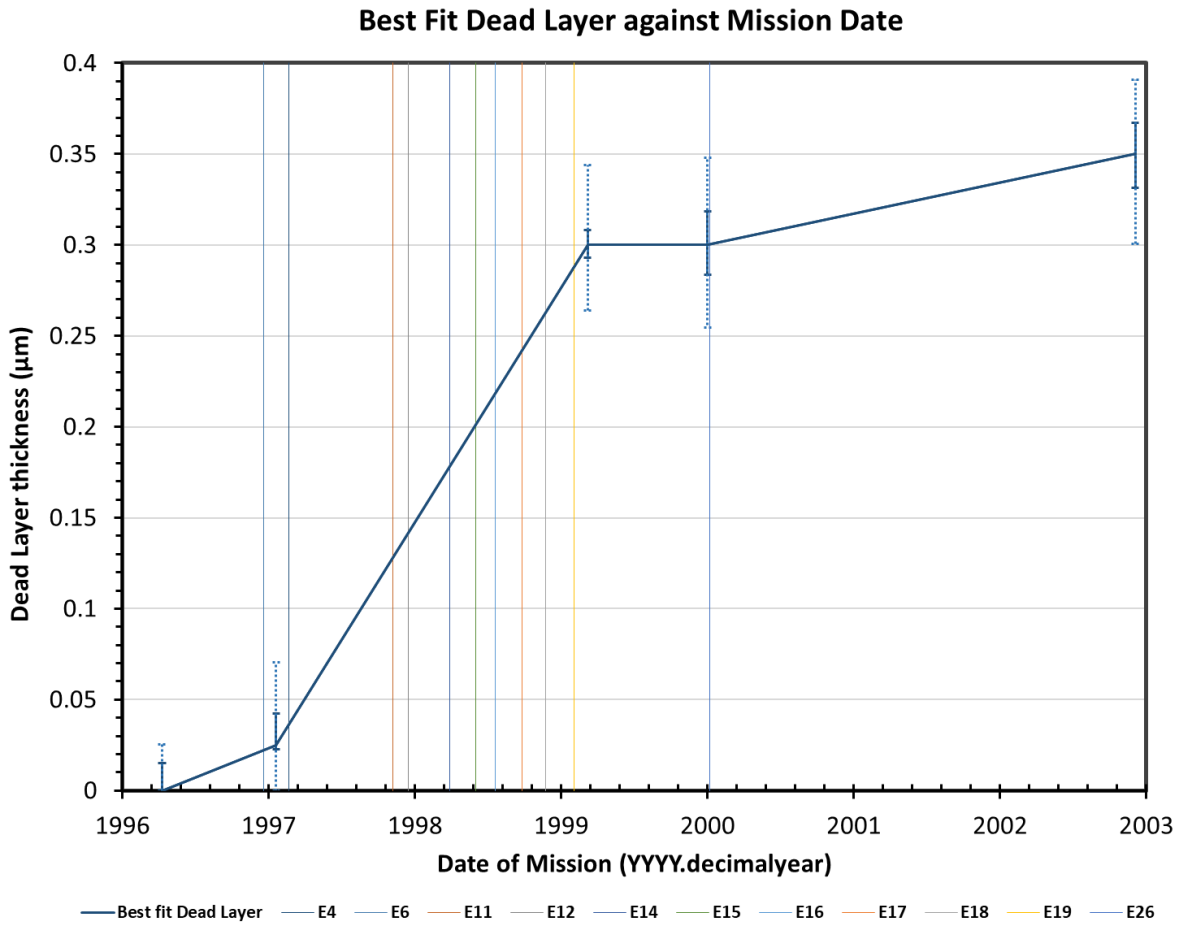

Figure 2.4-11: Updated Increase in dead layer over mission years determined by best fit data, accounting for instrument calibration. Background markers show the time of each Europa Flyby for context.

Plotting these results in the same form as Figure 2.4-10, shows how the overall thickness of the dead layer is much the same, only the rate of the increase has changed. The updated plot is Figure 2.4-11. The increase in the dead layer over the mission is well explainable by the phases of the mission and how the expected results would be causing the dead layer.

2.4.5 Results of Dead Layer Thickness Estimations.

The initial phase of the mission, ran from insertion in 1995, to orbit 11 around Europa late 1997. During this phase the spacecraft only ventured towards the inner moons 3 times, choosing to stay in the less energetic areas around Callisto and Ganymede. After this phase the mission was extended to encompass Europa, where until 2000, it completed 10 orbits including Europa and Io flybys (Figure 2.4-11); this section of the mission can be clearly seen in the rapid increase in the dead layer build up. Being closer to Io and Europa the particles are at far higher density and more likely to be of a higher mass species, all of which will contribute to a faster build-up of the dead layer.

The next phase of the mission is the Galileo Millennium Mission, beginning in 2000 until impact with Jupiter in 2003. This phase included flybys of all 4 moons and the smaller moon Amalthea. At this point of the mission the dead layer is now quite thick. Incoming particles are all losing energy to a significant amount, thus the energy being deposited in the sensitive volume is less than at than during previous phases. The growth of the dead layer slows. The upward trend in this phase most likely comes from the three flybys of Io at the very end of the mission. The higher density of ions around Io, from its volcanic activity, would have been a significant problem for the detector.

From this research, the estimation of a dead layer build-up has been determined. Whilst the initial attempt at comparison by eye did not produce sufficient clarity, making a numerical chi-squared test produced the expected increase in dead layer towards the end of the mission. The final analysis of the chi-squared results identifies a 0.35µm thickness of dead layer with error between 0.3315µm and 0.367µm.

The error of these dead layers compares the fit of the next nearest dead layers then evaluates the point in thickness that the next dead layer would have been a better match. This is an unusual way of determining the boundaries of a fit. However, in using this method

the accuracy of the fit is well illustrated. The closer the error bars are, the more accurate the fit.

There is also the possibility that there is more error than is accounted for in the error bars shown. As mentioned to begin with, the values used for the real data are approximated by eye; there would also be systematic error present in the SRIM data used in calculating the dead layer energy drops. In addition, the missing/ patchy data causing missing element loci in some of the real data sets, can throw off the calculations, as they are not all compared completely fairly.

Plotting a best-fit line of the dead layer build up is also a complicated matter. Generally, the growth of the dead layer should be an inverse exponential, fast increasing to begin with and tending to a maximum thickness. This thickness is when the dead layer is thick enough to stop all particles from penetrating the detector, thus no more of the sensitive volume will be denatured. The build-up is well described above, however, unlike in the traditional shape of a Ln(x) graph, the dead layer can never be less than zero; this is unphysical. To account for this when fitting, a stepped function of this with an exponential is used in Figure 2.4-12.

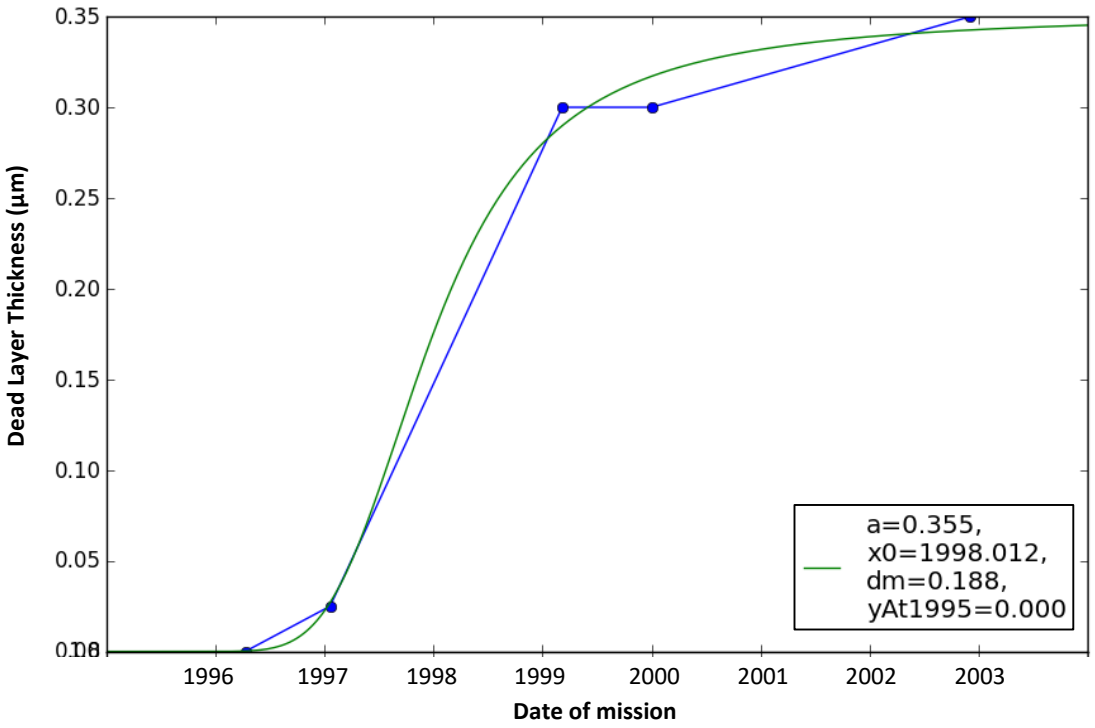

Figure 2.4-12: Fitting of the increase in dead layer over time.

2.4.5.1 Other Estimation Methods

Another indication of the dead layer not used in this investigation, is the turning of the Hydrogen and helium tracks. Figure 2.2-2 is the calibration of the data, the dashed lines show the predicated tracks of each element and where they should appear when measured. The predicted hydrogen and helium lines are interesting in that at the higher energies, they turn and show lower energies at shorter time of flights.

The turning of the loci is because of the thickness of the detector's sensitive volume. When a particle stops within the volume, all the energy it started with has been deposited in the volume. This is the case with the majority of the particles hitting the detector. However, if the particle passes all the way through, then it still has energy when it exits meaning it hasn't deposited all its energy. The very high energies of Helium and Hydrogen have the possibility of doing this and causing the turning back of the loci.

Knowing the thickness of the detector, the specific turning point of each element can be calculated. Thus, the movement of this turning point can be used to measure the thickness of the dead layer at any point in the mission. There are a few problems with this however, there is quite a wide spread of particles in the real data where the turning points are. In each case the specific distance would only be an estimate. As the change in the turning point would be so small, any error in measuring this would result in huge deviations in the thickness of the dead layer.

Because of the expected error in using this method it was not used for accurately determining the dead layer. However, the presence of the turning point movement from the early mission data to the late mission data is highly encouraging and shows there is a significant change in the dead layer present over the course of the mission.

2.5 Correcting with respect to the Dead Layer

The previous section determined an estimation of the dead layer build up. The numerical chi-squared test produced the expected trend in dead layer towards the end of the mission. With the knowledge of the thickness of the dead layer and the increase over time a correction of the PHA plots can be made. The process for this is relatively straightforward.

The PHA plots themselves contain a high resolution of data points over a very short time scale. The data is extracted from the original plotting software written for the mission in IDL. To extract the full data set; Peter Kollmann from Johns Hopkins University Applied Physics Laboratory (APL) provided the necessary input criteria to produce the data set as an output file whilst running the software over the full duration of the mission. The input criteria are usually limited to the period over which the PHA graphs are plotted for, with each plot a collection of points over dates of interest. But, in this case, over the whole mission the PHA graph offers very little useful information as is it all the available data overlaid. Only the output file is of use as each data point has its own associated time and thus knowing how much the dead layer increases over the mission, its own thickness of dead layer can be attributed to it.

The high-resolution data available from the PHA graphs is very limited, only around periods of interest such as the flybys and insertions were recorded. This was to gain insight into the key areas whilst limiting the amount of data required to be sent back, as a knock on from the antenna problems.

The sparseness of the data set helps, in some ways, to explain the best fit of the dead layer from the previous section (2.4.5). The dead layer calibrations can only be fit with the data that is available, thus the intermediary years would help to fill out the evolution of the dead layer (Figure 2.4-10). This is something that cannot be corrected for and so must be considered when looking at both the estimations of the dead layer and the corrections made in the following section based off the values.

2.5.1 Method of correction

The process of correcting is made complicated by the fact the shift in the energy is determined by the mass of the particle. However, the drop in energy measured means the mass of the particle cannot be determined from the measurements taken by the instrument.

The process of correction is then thus; working out how much decay a set thickness of dead layer would produce, applying this to a general form of the data. Then mapping real data onto this so that the energy shift is already known for a point, which can then be added back onto the data point. This is based on some known relations: the mass change over the limits of the detector, and the energy shift dependent on specific mass. Using these, the limits of the detector can then be shifted based on the thickness of the dead layer. Along with the limits of the detector channels can also be shifted with the dead layer.

With the limits re-calibrated to thicknesses of dead layers, as shown in Figure 2.5-1, the data can be applied within the new limits. This figure is a far more accurate version of that shown in Figure 2.4-1, Figure 2.4-2and Figure 2.4-3.Depending on the positions the data points fall on, the amount of energy the limits have been shifted by will be the amount of energy the data point needs to be corrected by; the actual correction of the shift in the data.

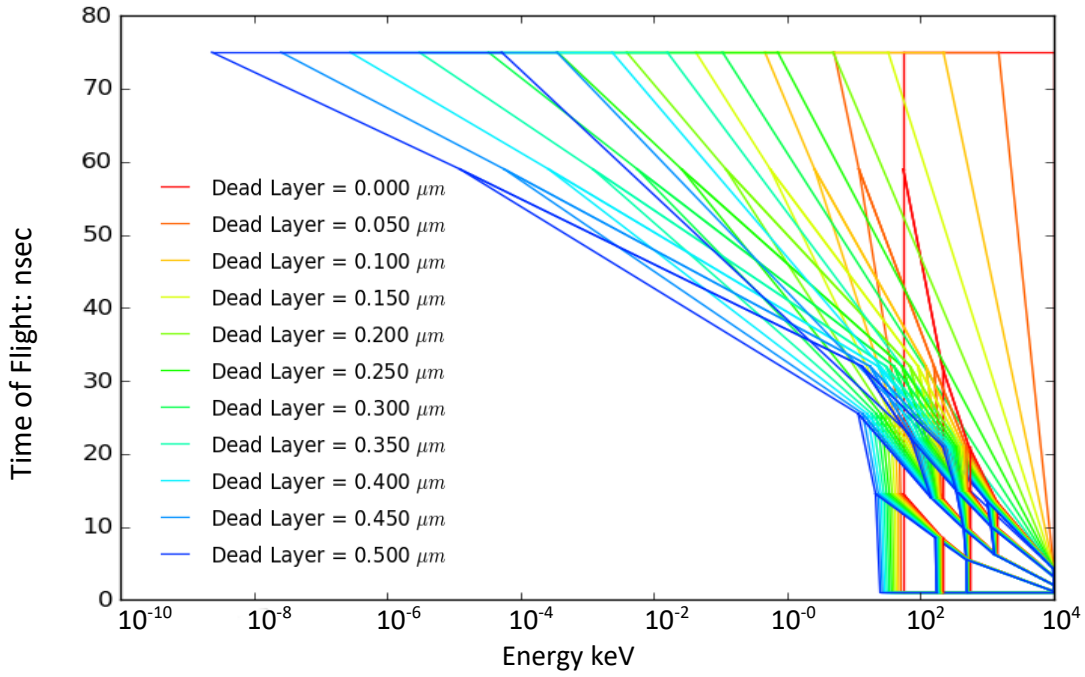

Figure 2.5-1: Warping of the channel boundaries due to varying thicknesses of the dead layer.

2.5.2 Implementing the correction

The method described above is all based on the relation of mass, to energy loss with dead layer thickness. The mass of the particles will not stay constant over the correction, as the energy is changed the mass that can be calculated by the recorded data, will increase as the recorded energy is increased. The Time of Flight however, is constant and will not change; this is an advantage as the TOF values are always a known quantity.

Using the kinetic energy equation (1) a simple function can be built to calculate the mass for all variances of TOF (i.e. velocity) and, energy. Over the full range of values that the detector can measure and allocate a particle to; some are simply unphysical. These are gathered around the extremes: the very low energy and low TOF, the very high energy and long TOF, and most of the boundaries. Whilst these areas do have very odd and high shifts in energy, there are very few particles that will naturally fall in these areas.

Using equation (1), produces a scale of masses over the limits of the detector. This adds complexity when working out the energy shift of these masses when passing through the material of the dead layer. For known masses, i.e. those of common elements, the depth to which they will penetrate a material is already known, these are the values used for generating the simulated dead layers on the calibration line in section 2.4.1. This energy is calculated using SRIM. However, SRIM only provides the values for impacting particles; these all have very specific masses as shown in Table 2.4-2.

Figure 2.5-1, shows the shifting of the limits of the detector. In this case the channel boundaries were shifted to the various dead layers. Instead of using the channel boundaries, the method for correction used a basic grid over the limits; 50x50 bins evenly split over the logged values of both Energy and TOF. For each particle measured the TOF is stable and is used for selecting the bin row to be used. From there each particle has 50 bins of energy that it could belong in.

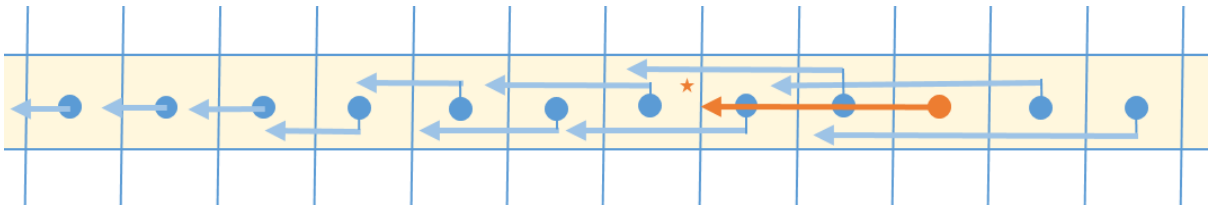

Figure 2.5-2: Each incoming particle (represented by the Orange star) is tested against the series of bins for the applicable TOF. The binning routine then allocates the most similar shift in energy to the incoming particle.

Each bin has a defined centre of mass. This central point has an associated mass from its TOF and its Energy, and thus also a known value of energy lost for the dead layer at the time of the incoming particle. Each of the 50 central points and the energy shift of each one is checked against the position of the incoming energy of the new particle and the closest match will be selected for the particle.

In Figure 2.5-2 each square defines a bin over the grid of the detector limits, the yellowed area shows the row of bins selected by the value of the TOF. The star shows the incoming particle; any incoming particle will not be an exact match to the TOF values, so the nearest bin will be chosen. Each bin's central point is shown as a dot; each of the shifts associated with the centres and their masses are shown as the connected arrows.

The orange dot and arrow show how the process determines the closest shift value. The end of the arrow would be at the energy reading the point would be shifted to. This energy is the closest to the energy of the incoming particle. Thus, this shift in energy that is best for this particle. Applying this to the whole of the data set gives the corrected data; which can then be directly plotted as TOF against energy.

2.5.3 Evaluating the New Particle positions

Re-plotting the values alongside the original values, truly illustrates how much the data has changed over the duration of the mission. Instead of plotting the values for each flyby, the following figures show the data split at 1999. This is near the midpoint of the mission, with the group sizes being small enough that the general trends can be seen without swamping the data in volume of points.

Figure 2.5-3 shows the data from the start of the mission until 1999, the format of this figure shows the original untouched data along with the correction of the same data. The data has been re-plotted in both cases; so, they can be directly compared. The original boundaries of the channels have been plotted overtop to show the movement between the boundaries. In the corrected 1999 data (Figure 2.5-3b) the loci for Oxygen and Sulphur are more distinct. There is very little movement in the positioning of the loci; however, data before this time of the mission was commonly used as it was far more consistent than later data.

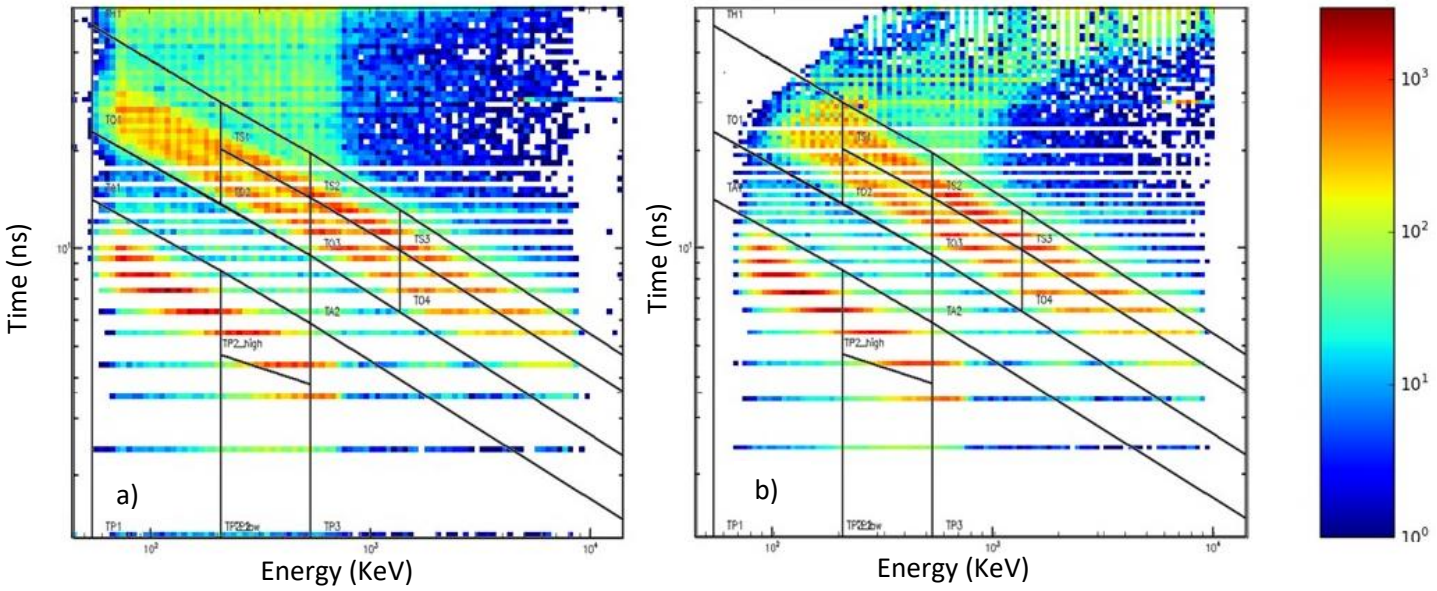

Figure 2.5-3: Data from pre-1999 mission. a) Original data re-plotted for comparison. b) Corrected Data, re-plotted with the original channel boundaries overlaid.

Figure 2.5-4 shows the original and corrected data from 1999 and onwards to the end of the mission. This is the data that was most effected by the increase in the dead layer, and there is some considerable improvement in the amount of data fitting in the correct box. However, this still is not perfect.

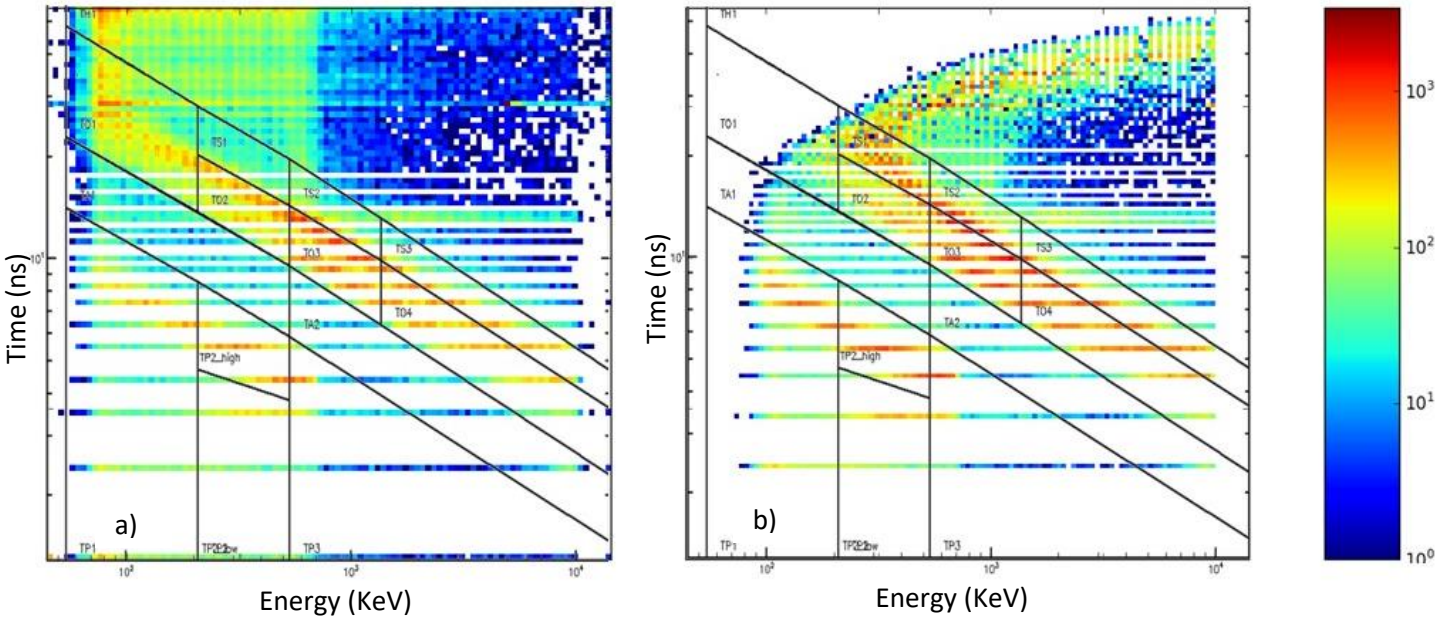

Figure 2.5-4: Data from post 1999 mission. a) Original data re-plotted for comparison. b) Corrected Data, re-plotted with the original channel boundaries overlaid.

Using a grid to determine the position of the particles, results in some pixellation of the output and incurs errors based on the fineness of the grid. As well as being computationally intense, the gridding method can be very imprecise with many of the particles being missed and not being binned accordingly. Further problems with the correction stem from the feasibility of the limits of the detector. At very long TOF and low Energies, the relative masses of the expected particle became far heavier is than realistic; this caused some problems in the movement of the boundary grid.

In some places the amount of energy required for an appropriate mass particle to pass through the thickness of dead layer was larger than the initial energy. As the correction was calculated in log scale to account for the original boundary boxes; these now negative energies proved problematic. Instead the shifting had to be limited to the initial energy, stunting the shifting in the longer TOF values. Fortunately, the particles populating these areas are accidental readings; most commonly coming from errant start or stop signals or electronic noise. Whilst they have been included in the correction they can be mostly ignored.

However, in accounting for this there is the notable effect this has on the data in the form of the distinct sweep of the data, from the top left to top right. The void of data shows where particles would have appeared, if they had had enough energy to make it through the dead layer. This is escalated by the later 2002 data when the detectors truly began to have more faults than simply the initial dead layer. Figure 2.5-4 shows this.

The priority system also affects the data when plotting in larger date ranges, the distinct cut offs around the channels TS2 and TO3 mark a border of the priority recording system. When this border is shifted it creates the sweeping line in Figure 2.5-4b that could be mistaken for an artefact in the plot. These problems with the priority system cannot be altered as they are intrinsic in the original data, though some of the issues in the final plots can be improved upon.

2.5.4 Improved Implementation of Correction

The main issues to be improved upon are all caused by the gridding and binning process of the correction. The inaccuracy of the grid can be improved upon and in the process improving the pixellation of the data in the final output. In the process of improving this, removing the binning of the data will vastly reduce the computation time of the process.

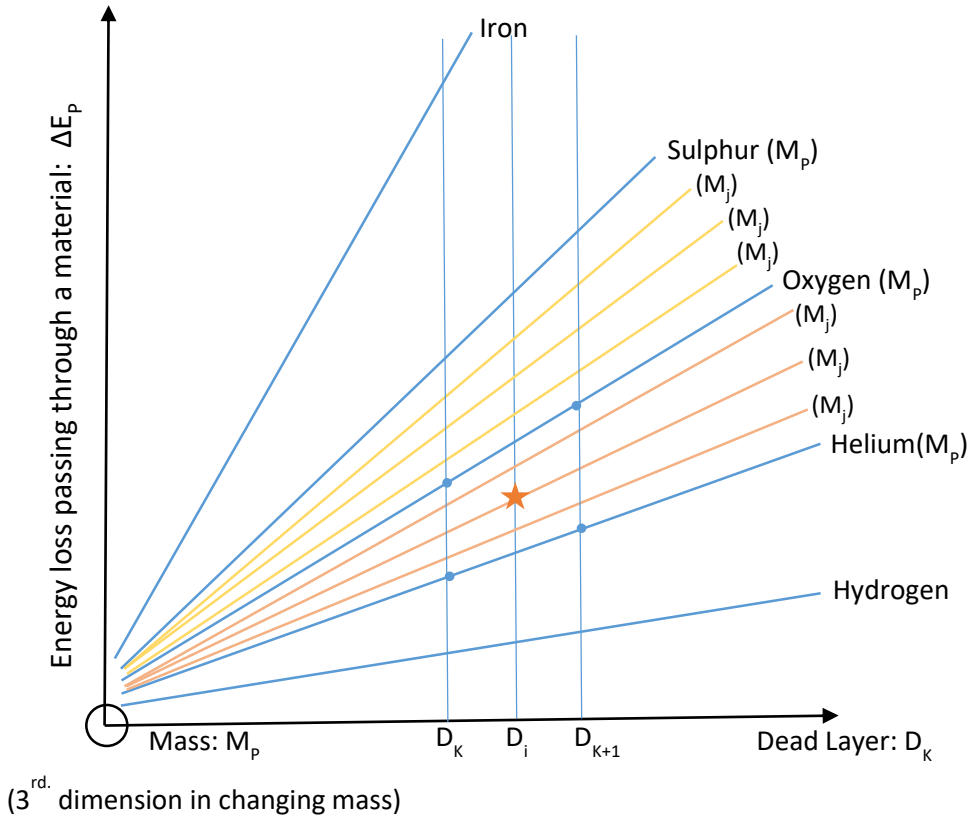

Figure 2.5-5: Diagram based on Table 2.4-2, including the indices used for the correction method where: P represents known masses and associated energies from TOF, K represents known dead layer thicknesses from the table, and J notes the testable masses and their associated energies.

The basis of the improved correction much the same as the previous. Instead of using the central point of a grid box, instead; the known inputs can be used to calculate a range of masses, and thus energy shifts, that are allowed for the particle. These within the range can then be tested for the best match in much the same way as before.

Figure 2.5-5 shows the starting point of the correction method; Table 2.4-2 contains values of energy loss (ΔE_P) for known mass species (M_P), against dead layer thickness (D_K). All the measured values from the EPD will fall somewhere on this plot, all measured values are denoted with the indices i; Measured energy (E_i) and associated mass (M_i) at a point in

time that determines the thickness of the dead layer (D_i). Using these inputs and the known values the energy lost by the particle can be compared to values of possible losses/masses. M_J, are the masses to be tested; these are limited by physical masses i.e. every mass is a factor of a single proton mass. This limits the amount of possible masses the incoming particle could have whilst making sure the correction is physical.

For every measured particle, the first step is to determine the closest of the known values on the diagram above. There are a few limits that can be used to determine this. For mass, the actual mass of the particle must be larger than the mass originally measured (note: whilst mass isn't directly measured it is determined using equation (1). The mass of the particle must also be possible to be measured by the detector, the upper limit is set by the limits that are expected in the detector in this case the mass maximum is Iron. Not every particle may fall into these limits, these are the very high TOF and Energy that are not likely to be real readings but rather false signals.

Between these boundaries there will be many test masses, M_J. For each mass the energy of that mass at the input TOF is calculated using:

$$M_J = \frac{2\,\tau_i^2}{\Delta^2}\,E_J \tag{4}$$

Along with these values of M_J and E_J, the correction also needs the thickness of the dead layer. This is far simpler; each point's position in time will fall between two of the D_K values.

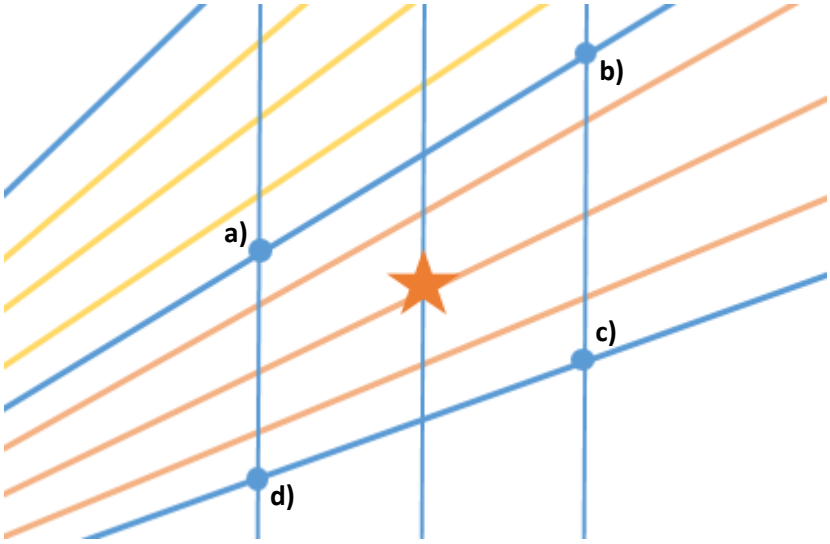

Figure 2.5-6: Close Diagram of the main points defining the position of the incoming particle by values in Table 2.4-2.

Figure 2.5-5 has four main points highlighted around the incoming particle, these have been highlighted in Figure 2.5-6 for ease of description. The next step uses these coordinates to generate the change in energy for the testable masses: ΔE_J. The coordinates are given below:

$$a = \left(M_P, D_{K-1}, \Delta E_{P,K-1}\right) \qquad b = \left(M_P, D_K, \Delta E_{P,K}\right)$$

$$c = \left(M_{P-1}, D_{K-1}, \Delta E_{P-1,K-1}\right) \qquad d = \left(M_{P-1}, D_K, \Delta E_{P-1,K}\right)$$

Connecting these points is done in two steps, the first in vertical pairs ac and bd. Along these lines the values of ΔE_J can be found for the dead layers D_{K-1} and D_K. At D_{K-1} the equation is:

$$\Delta E_{J,K-1} = \frac{\Delta E_{P,K-1} - \Delta E_{P-1,K-1}}{M_P - M_{P-1}} \left(M_J - M_P\right) + \Delta E_{P,K-1} \tag{5}$$

At D_K the equation is then:

$$\Delta E_{J,K} = \frac{\Delta E_{P,K} - \Delta E_{P-1,K}}{M_P - M_{P-1}} \left(M_J - M_P\right) + \Delta E_{P,K} \tag{6}$$

Dependent on the indices of J any point between a) and c) will have the coordinates described by a point e). The other joining line, b) and d), will contain a point with the coordinates described by point f).

$$e = \left(M_J, D_{K-1}, \Delta E_{J,K-1}\right) \qquad f = \left(M_J, D_K, \Delta E_{J,K}\right)$$

The next step is to connect these sets of points together for the value of D_i this is done in the same way as above, using a straight line to connect them. The equation for this is then:

$$\Delta E_{J,i} = \frac{\Delta E_{J,K} - \Delta E_{J,K-1}}{D_K - D_{K-1}} \left(D_i - D_K\right) + \Delta E_{J,K} \tag{7}$$

These are now testable changes in energy to be compared with the original measured energy and the base test energy. The measured energy added to the change in energy for each test energy should be very close to the test energy. Equation (8) shows the formula for this; the closer this value is to zero the more likely the correct test mass is being used. Once this has been determined then the shift in energy can be added onto the measured energy.

$$E_i + \Delta E_{J,i} - E_J = 0 \tag{8}$$

Each particle's energy measurement is now corrected to the position it should have been measured in. This may not be perfect for every particle, but it will be the best possible from the initial conditions measured.

2.6 Final Corrected Results

The initial estimation of the dead layer is based on 5 key dates in the mission; for an accurate comparisons and review of the correction, the original dates are the best to compare the new results against. It is likely that the correction will not be perfect; there is error an in the estimation of the dead layer thickness, and in the energy lost in the particle passing through the dead layer. How much these will have affected the data will become apparent when reviewing the data.

All the original data has been plotted using the original IDL package written for the mission. The corrected data is replotted using Python making an effort to match the plotting style of the original for comparison. Unfortunately, due to how the IDL package calls the data, and the format the data is stored in, it is not simple to update the data files and plot the corrected data using the same software.

The comparison of the new data to original PHA plots, is far from perfect and shows some of the faults with the correction method. Overall the correction is promising; the loci of the expected elements falling far closer to the channel boxes. The correction falls short in two key ways:

Spurious data: the correction can only correct the points it's given. If a data point is an artefact in the original data set, then it will appear in the correction in a similar position. The final year of the mission suffered the worst for unaccountable data such as this, leading to the data seen in Figure 2.6-6. The curious tracks traveling bottom left to top right are entirely artefacts of further breaking of the detector. The timing system of the EPD degraded along with the Semiconductor detector, leaving overly long flight times for high energies, or registering times of flight without the accompanying energy readings. In comparison the lack of these visually obvious tracks in the original data is odd. It is possible the plotting software removed some of the more categorically obvious 'bad' data, before the final product, that has remained in the file data.

Better correction effects at lower energies: this is a fault of the numerical values in Table 2.4-2. These values represent the amount of energy a particle would use to penetrate the given thickness of Silicon. However, this energy would be less if the particle passed directly through the silicon. This is the upper limit of the energy that a particle can lose;

these values are used because there would otherwise be too many unknowns for the correction. The amount of energy lost is a factor of the thickness of the dead layer, the mass of the particle and, the initial energy the particle entered the dead layer with. From the measured data, only the thickness of the dead layer is known. This is not enough information to base the correction on, so an approximation had to be used here.

Despite this shortcoming, the consistency in using this table of values in the estimation of the dead layer, by using it to simulate shifts in calibration lines; means this fault is quite minimal. The estimation of the dead layer is already scaled to using this upper limit of energy loss used in the correction.

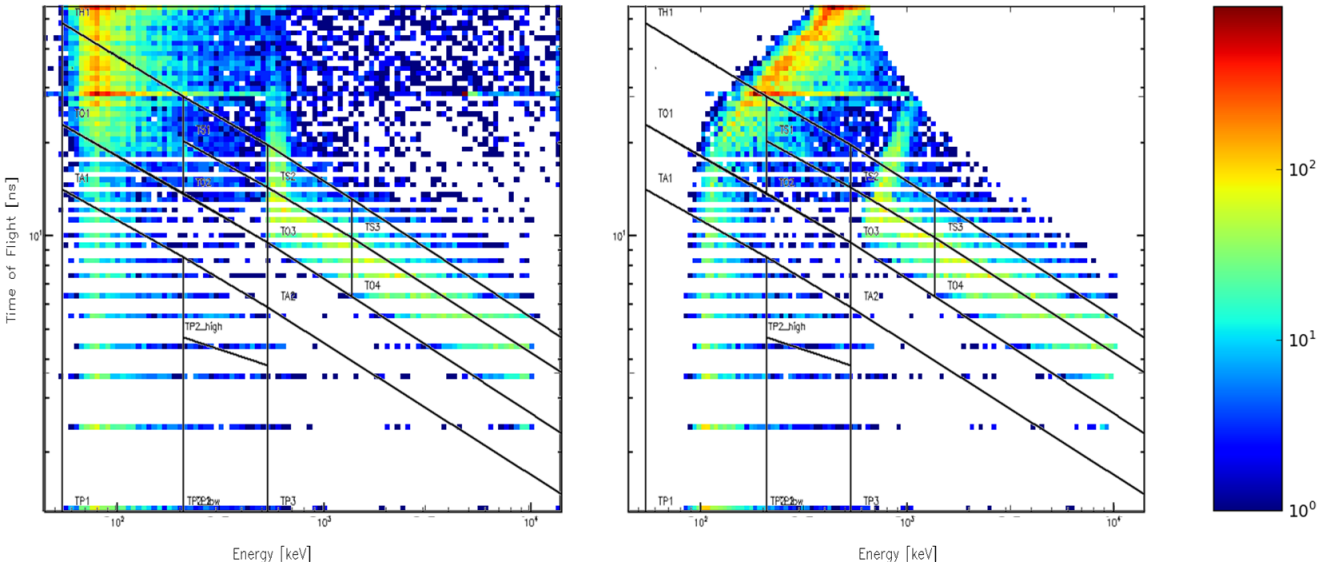

Figure 2.6-1: (a) correction input data against correction output data (b): from 2002 day 295 to 305.

Overall the efficiency of the correction is good; computationally and visually. Only in the very last of the high rate mission data (Figure 2.6-6) does the corrected data appear less than satisfactory. In this figure the elemental loci are almost indistinguishable amongst sulphur and oxygen; the whole of the readings is swamped by the artefacts and errors of the original data. Figure 2.6-1 shows how much of these effects are from the data itself. The figure shows the input and output data of the correction, clearly illuminating how much the original plotting routine dealt with errant data.

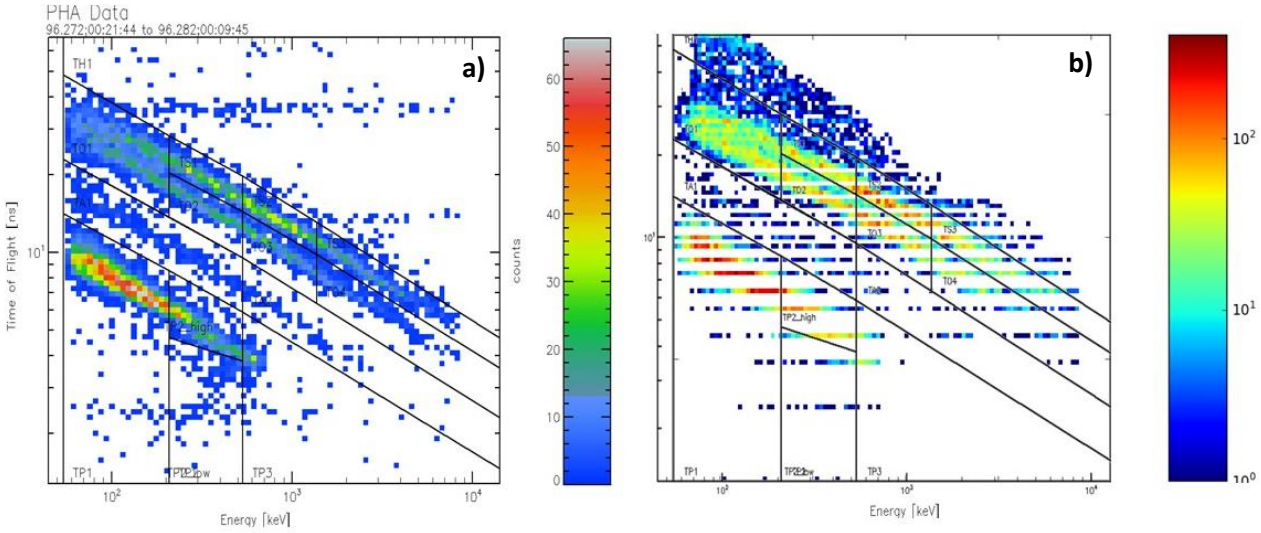

Figure 2.6-2: Before (a) and after (b) correction: data from 1996 day 272 to 287.

Figure 2.6-2, Figure 2.6-3, Figure 2.6-4, and Figure 2.6-5 have fared far better, resulting in only minor anomalies. Figure 2.6-5 has the clearest final results of the correction. The oxygen locus now sits firmly in the TO channel boxes with the sulphur track above; now also with in its own channels. The sulphur locus has not returned to its original position entirely, the faults of the correction affecting the sulphur most at the higher energies. Had the sulphur line extended further in to TO1 channel box, the correction within this area would have been the least affected by these faults.

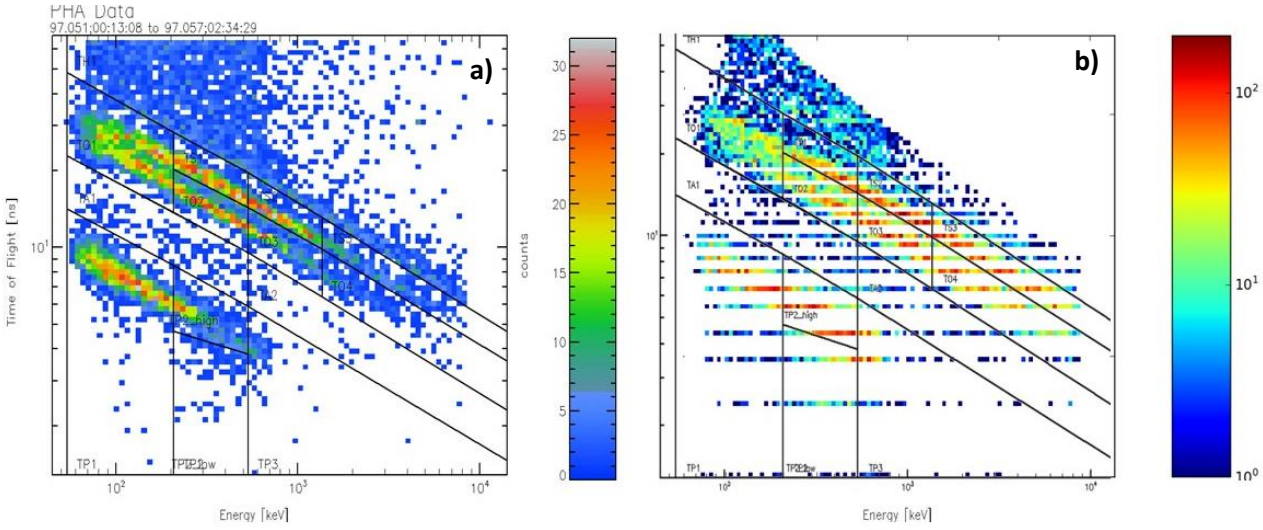

Figure 2.6-3: Before (a) and after (b) correction: data from 1997 day 51 to 57.

Furthering the correction from here could only be achieved by improving the values in Table 2.4-2, overall of the process of the estimation and correction this is the largest source of error in the calculations. Improving this table is no easy feat however. The most

accurate form of the values varies with starting energy, so a simple method would be to average the energy lost over the energy limits of the detector. Again, this would not be perfect. Using this method would produce best results in the mid-range of energy with the high and low energy suffering consequently.

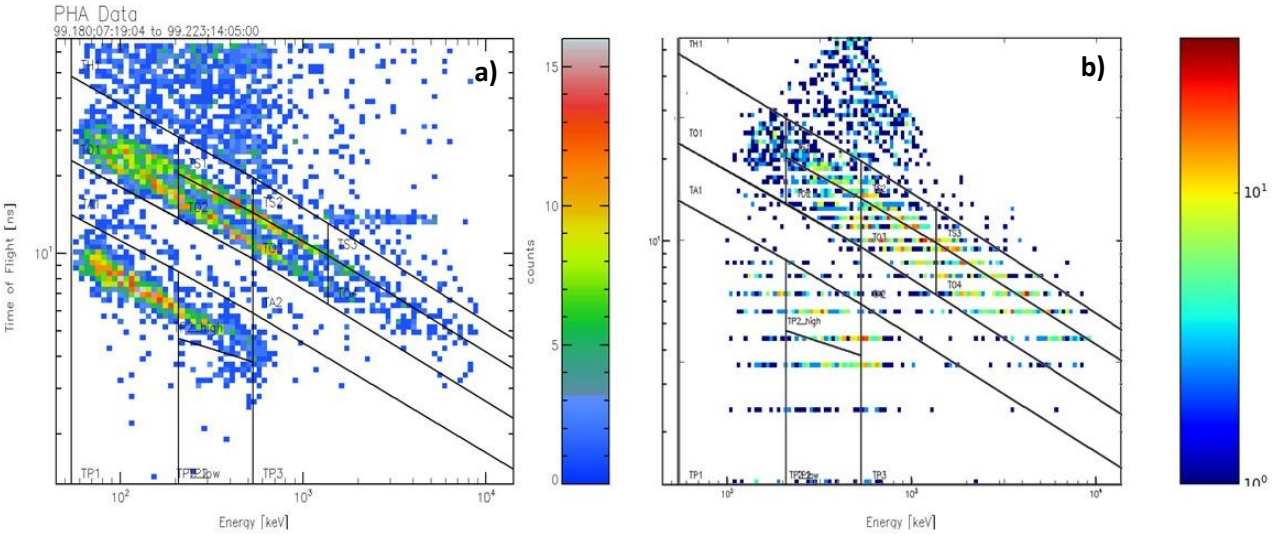

Figure 2.6-4: Before (a) and after (b) correction: data from 1999 day 180 to 223.

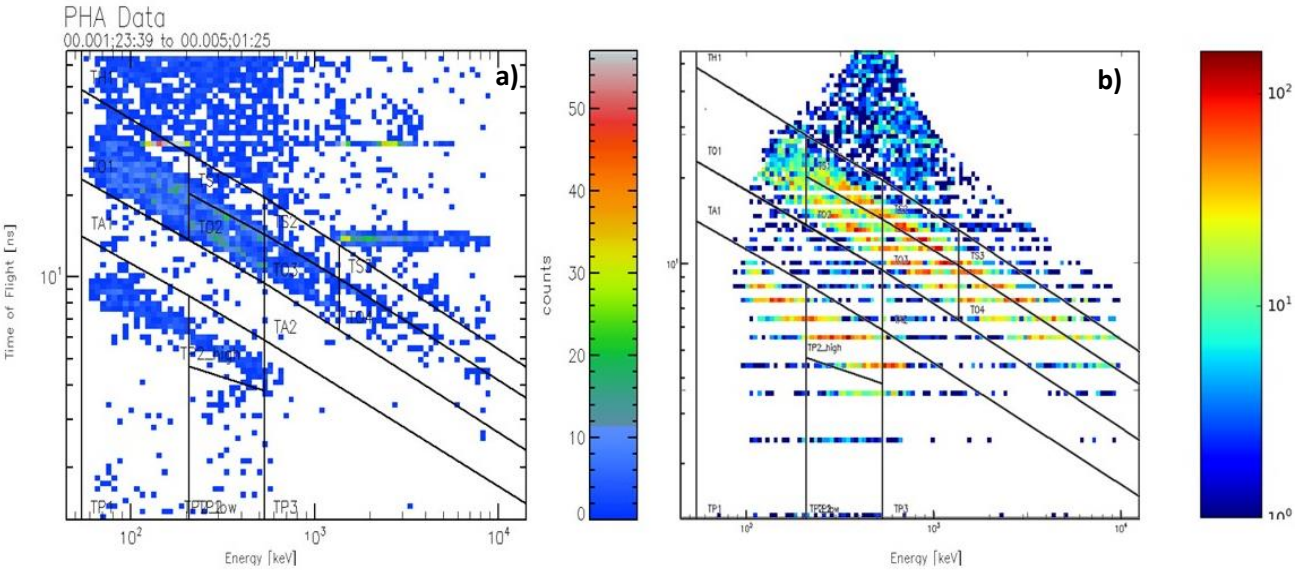

Figure 2.6-5: Before (a) and after (b) correction: data from 2000 day 1 to 5.

Without prior knowledge of the initial energy of the particle there is no explicit way to correctly calculate the energy lost to the dead layer, and whilst this could be calculated for the calibration lines in section 2.4, it could not be extrapolated into the correction process. A misbalance may cause more faults than simply keeping the consistency of averages.

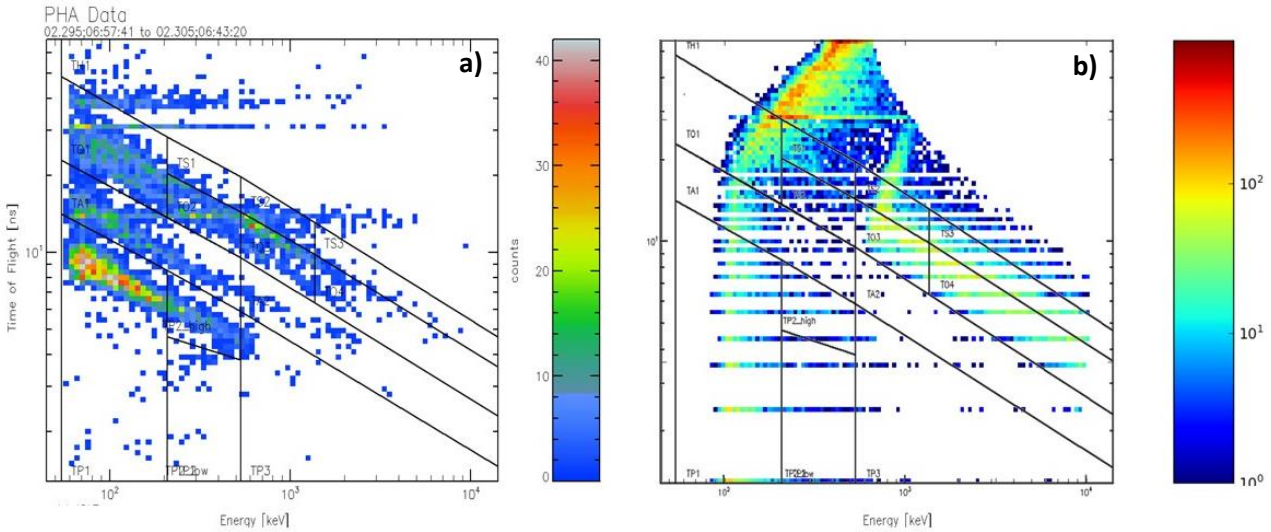

Figure 2.6-6: Before (a) and after (b) correction: data from 2002 day 295 to 305.

2.7 Conclusions

The pulse height analysis (PHA) plots have long offered a comprehensive breakdown of the composition of the plasma in the Jovian plasma disk. The degradation of the energy readings vastly altered the measured compositions during the later mission, impairing the analysis of the environment surrounding each moon.

The correction process utilises the ground calibration and the theory of the principles of the detector. The estimations of the severity of the dead layer increase offer both a basis for the correction and a yard stick to assess the effectiveness of the correction itself.

Overall the methods devised to assess the level of degradation and then complete the correction, were effective. The accuracy of the degradation estimation and the correction are limited by the values in Table 2.4-2. These are only the static values of the energy loss, where in practice these will change dependent on the initial energy of the incoming particle. However, in using the static values consistently throughout the correction the error incurred by this is minimised.

The final results of the correction, shown in 2.6, are the best that can be achieved with the information available. Despite this, the effect of the correction puts the plasma composition within the expected ranges for all the element loci.

3 Count Rate Channel Correction and Comparison to Voyager Data

Having corrected the PHA plots of the EPD, a significant portion of the data is now in a more useable state. However, these now corrected plots are only half the story. Each channel visible in the PHA plot contains an additional data set of full count readings. These are 11-minute averages and span a huge portion of the mission; far more than the high rate PHA plots which covered only the dates of interest. The full data set for a single channel is shown in Figure 3-1, full data plotted as average along the radial distance from Jupiter, by year.

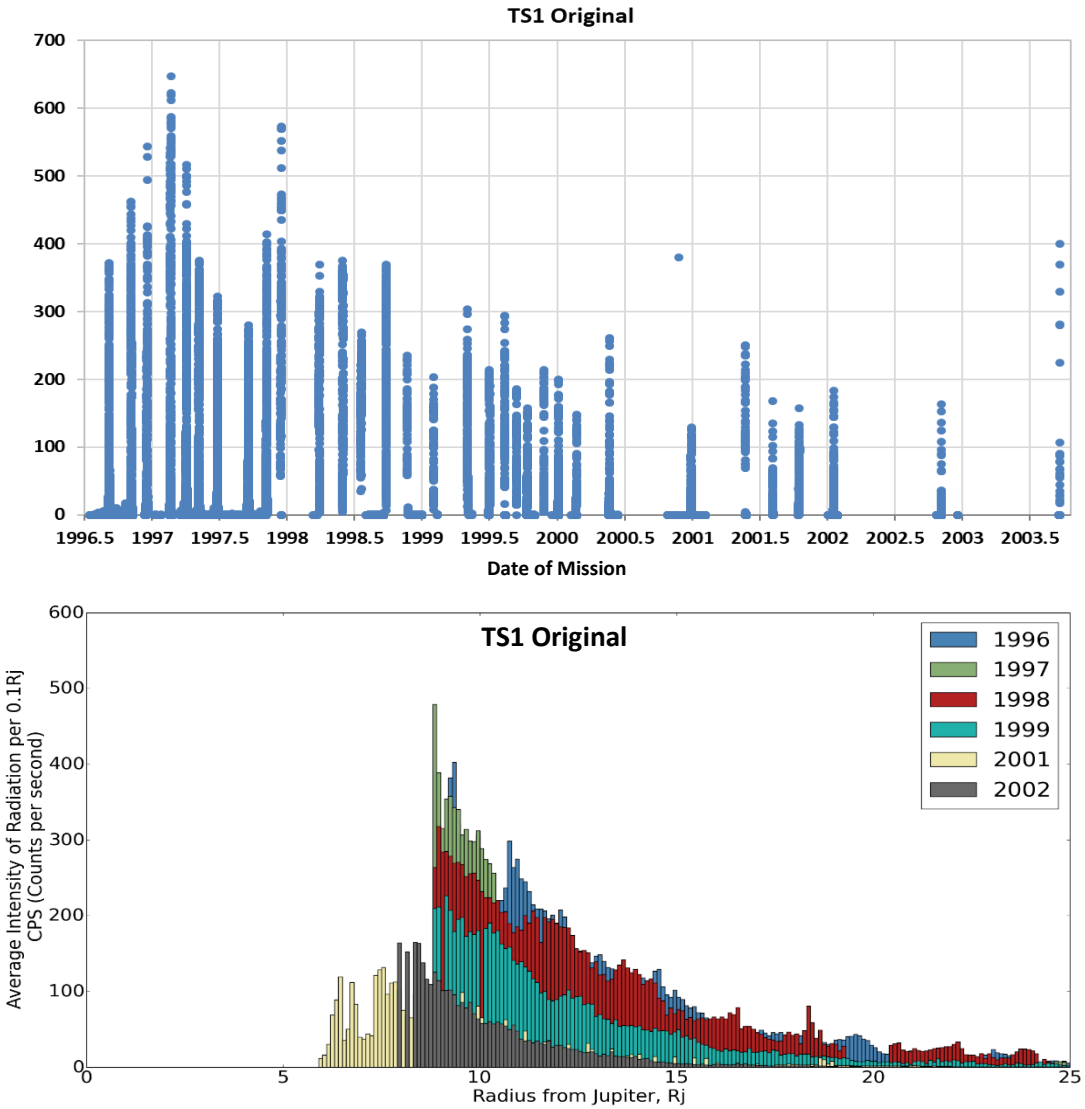

Figure 3-1: An example of the count rate data set for the TS1 Sulphur channel. Top: full channel read out over the mission, Bottom: full data plotted as average along the radial distance from Jupiter, by year.

The bottom plot of Figure 3-1 shows the decay in the count rate data the clearest. By plotting the counts as an average by radial distance from Jupiter, and overlaying this by year, the changes in the data are very obvious. Using averages of the counts by radius means that the profile of the data should be the same year by year. The obvious drops in each progressive year of the mission show the loss of counts.

The PHA plots gives another visual clue of what is happening in the count rate data. The dead layer is likely to have the same effects, with counts in sulphur channels dropping and oxygen counts rising over the mission.

3.1 Correcting the EPD data

For the EPD data there is no single or simple method to correct all 13 channels, in such a way as to account for both drops in counts, increases in counts or combinations of both; instead a custom-built program is built to achieve a consistent correction over all the channels. The aims of correcting the data are to have a data set that does not vary over the span of the mission. Whilst the individual readings will no doubt fluctuate over the orbits of the mission; the average of each year's worth of data, or the average at a given radius, should be consistent.

Making this into a working system poses many challenges, identifying the mechanisms behind changes in the count rates is the first step of this process. Whist the dead layer is key, when considering the PHA plots, how the migrating loci pass across the channel boundaries will be key in fixing the data. Overall, it is highly unlikely that the dead layer effect on the count rates can be simply undone. The data in the PHA plots contains data of time of flight against energy, where the individual channel data is count rates against energy. This means the dead layer does not correspond directly to the count rate number. Instead, a better attempt is to investigate how each channel is changing individually and go about applying a fix for these changes. This bypasses having to calculate one channel based on another.

The dead layer analysis in the previous section is reusable for comparing the original to the adjusted data again once the correction is complete. In this case, the time of flight will instead be the count rates for each of the channels with the energy changing in the same manner related to the dead layer. Using this same method as before, comparing each year to a calibration with added dead layer, confirms the initial estimation of the dead layer. This will also allow a checking of the corrected data to show how efficient the correction is.

3.1.1 Why the correction is Important

As mentioned previously, most publications that have undertaken research using Galileo's EPD data have used only the very early data. This accounts for the deterioration in the latter data whilst also allowing the use of the data. This is perfectly reasonable when considering the Jovian system and undertaking large scale modelling of the system. The

initial years of data survived well enough that sufficient boundaries are available for the models.

However, most of the latter data comprises of the Icy Moon flybys. From 2000 onwards, the mission objectives changed to optimise the Europa and other moon flybys. As the overall mission time ticked upwards, the data deterioration also increased, leaving most of the Galilean moon flybys firmly within the decayed data. This becomes even worse later in the mission as flybys of Io and the closer reaches of the Jovian magnetosphere are undertaken. Not only this, but close to Jupiter regions deal out more damage to the detectors accelerating the decay in the readings.

The aim of this research is to study Europa and the outer icy moons. If most of the data from the flybys sits within the degraded data sets, then any analysis undertaken on the moons is also subject to suspicion. Correcting the data sets is a starting point for any research undertaken on the moons.

An Important question before undertaking the task of correcting the data is; how much does the degradation of the data affect analysis of the moons? In any of the additional aspects of the mission, the degradation does become significant. This covers all the main flybys of Europa and Io, these were only undertaken in the very last parts of the mission. When looking at the dead layer estimates from section 2.4 the amount of change in the data from beginning to end is obvious. Largely the most important change in the data is the comparative ratios of the elements.

As shown above, with the increase in decay the counts are more often miscategorised from Sulphur to Oxygen. The main influence these particles have on the moons is in the form of sputtering; where the element or mass of the impactor has the most repercussions. For example, a sulphur particle will have a higher sputtering yield than an oxygen particle. From looking at the drop in the data, it is safe to predict that there is a large miscalculation in the overall amount of sputtering erosion on the surface. The new estimation of the sputtering values on the surface will transpire in the following chapters, using the corrected data.

A further use for the data comes with the announcement (Northon et al., 2016 and Roth et al., 2014) of the possibility of Europan Plumes. When analysing the data from the

flybys it may be possible to find occurrences when Galileo detected a plume. This is only possible if the data is reliable and if the surrounding background data is reliable. This is the motivation for correcting the whole of the data set rather than only the places of interest. The rest of the data offers insight into the on-going stable environment that an event, like a plume, could be identified from.

3.2 Method for Correction

Understanding the data is the first step in computing the correction. As described in section 2.3 there are many problems associated with the data. The bulk of these are associated with the problems in the recording and the amount of data received from the mission. These are the first things that need fixing so that the correction is using the best of the available data.

The data files used for the correction, again, come from Dr. Peter Kollmann; at The Johns Hopkins University Applied Physics Laboratory in the USA. He kindly provided the data files that are already complied into a usable form. The files are the rate channels subtracted from the background calibrations; each channel is also contained in a single file with a corresponding radius and position of the orbit and the rate date stamp from the instrument.

Having a corresponding date and orbital position for each of the data points means there are a lot of available improvements for the data. First the main problems that need tackling are:

- Missing Sections of Data: As the number of energetic particles hitting the detector determines the decay of the detector, any missing data is vital. This missing particle impacts will have just as much influence on the correction as any of the measured impacts in the data. This involves not only determining where the data is missing but also developing a method for estimating the data that is missing.
- Dead Layer Energy Drops: due to the nature of the channels and the format the data is in, knowing the amount the energy is dropping by is not very useful without more context. Each channel has a specific boundary of energy and such whilst the boundaries are moveable as done in section 2.4.1, the count rates for the channels cannot be so simply re-allocated.
- Nonstandard Energy Drop per Element per Channel: much in the same way that the energy change is unique to each channel, the amount the readings are dropping is non-uniform. This means that each channel will need individual calculations.

Most of these problems with the data need fixing before the true correcting of the data even begins, most importantly the missing data. However, they all pose investigation into the movement of the particle counts between each channel box.

The non-uniform energy drops per channel and the fact that the dead layer results from the previous chapter is not usable with this format of data set, means the correction needs an alternative approach. When looking at the channels as simply boxes, as the particles drift across, the particles in the sulphur box will be lost from the sulphur box and gained in the oxygen box. This is while the oxygen box is also losing particles to the helium box. However, in the case of oxygen, and to some extent helium, rate of particles gained from the higher channels overwhelms the rate of particles being lost to the lower ones. This results in channels that need decreasing rather than increasing over the course of the mission.

The possibility of channels such as oxygen requiring a decreasing correction as opposed to the increasing of the sulphur means each channel will necessitate individual processing. The availability of the data is also limited to the count rate, as an individual value per channel, for each time step of the mission. This all means that the correction of the data is far more complex than simply adjusting the energy values of each recording. However, it does offer the ability to cross check the values once the correction has been completed by using a power law of count rate against the energy of the channel. The energy movement is comparable to the movement in section 2.4 so a dead layer in the data can be simulated and compared to estimate how effective the correction is. It follows the logical step that the corrected data will exhibit less of a dead layer than the non-corrected data.

3.2.1 Steps of Correction

Following section 3.2 there are many complex steps and sequences to correcting this data. Each channel's data file contains in the region of 84, 000 data points from the entirety of the eight years. Considering data was taken around every 11 minutes for a full eight years that would tally to over 420, 000 data points, there are clearly large amounts of missing data; most likely from detector down time.

Along with this missing data, an amount to correct by needs to be calculated. This correction value must be both unique, but also consistent over the 13 channels. Developing

a method for this that considers the increasing and decreasing of the channels is complex. The following sections describe the method for dealing with these problems, ensuring the correcting of the data is assured and as fool proof as it can be.

1. Fill the missing data: Knowing that the dead layer builds up with each impact on the semiconductor means every count is vital in working out how much build up is attributed to a number of incoming particles. Each data point has an attributed timestamp. These are a standard time apart from one another. By comparing difference in time between one-time stamp and another it is possible to determine if there is one or more missing data points.
   Wherever these missing points are, a new time stamp generates with a corresponding placeholder value for the count rate. These placeholders make it simple to keep track of where there was new data added.
2. Fill the placeholders: With the position of the missing data identified, the next step is filling it. There are a few steps involved with doing this:
   a. During the filling phase of adding placeholders to the main channel files, the accompanying orbiter position in the Jovian system receives the same additions. This data set is a three-part set containing the X, Y and Z coordinates of the spacecraft position, in JSO system coordinates (relative to orbit plane). A filling routine from the Python Pandas library allows the interpolation across the gaps in each of the three data sets. As each set must be continuous and smooth this process is individual for each axis of the orbit. Knowing the position of the spacecraft is vital for the next step in the process.
   b. The next step involves gathering the channel values by the accompanying radius values. Calculating the radius values is a simple computation of Pythagoras using the axis positional data of x and y position.
   c. For each group of channel values between a radius bin, an average is taken. These bins form a picture of the change in relative abundances as the distance from Jupiter increases, when split and averaged by year these averages offer a clear image of hoe the count rates are dropping over the mission. More on this later, with the full selection of channels presented in

this way. These averages allow the estimation of the values that will take the place of the placeholder in the channel data files.

d. For each placeholder value in a channel, it can now be replaced by the average at the same radius. As each placeholder also has an accompanying orbit position, its radius at time of measurement can be determined and the value of the average at the radius swapped out for it.

3. Generating and filling the placeholders provides a far more complete view of the mission, and a basis for the correction to begin. The next step is finding the correction value to be used for each channel. This correction value is a description of how the channel is changing over the course of the mission in terms of how many impact detections are being allocated to each channel as the overall count rates drop. The correction value is a calculation involving a few parameters from each channel, under specific conditions. The process from this is below:

   a. Identify mission overlaps: over the course of the mission, there were many points where the orbit paths re-crossed a position in space, these positions give a perspective of the change in measurements over time. As the detector becomes progressively decayed, the readings for the same place in the system will be different as the detector wrongly allocates the counts. This uses the assumption that a place in the Jovian system will be generally stable over two to three years, excluding flybys. Figure 3.2-1 shows how these overlaps may occur and how the times of the overlaps are used.

   b. For each overlap point identified, a group of time stamps of the relevant data is available. These are grouped by overlap. For each individual group of data, the time between each orbit is needed along with the total count dose on the detector between the times of the overlap; this may include one or more full orbits. As well as this, the difference in the first reading and the last reading is taken.

   c. The calculations performed on each group are:

$$Time\ Difference = T_{Start} - T_{End} \tag{9}$$

Where the T_{Start} and T_{End} denote the indices of the start and stop times, this gives the total number of time steps in the interval rather than a value in seconds.

$$Channel\ change\ = C_{T_{End}} - C_{T_{start}} \tag{10}$$

$$Channel\ Sum = \sum_{i=T_{start}}^{T_{end}} C_i \tag{11}$$

$$Change\ per\ increment\ of\ time = \frac{Channel\ change}{Time\ difference} \tag{12}$$

$$Impacts\ per\ increment\ of\ time = \frac{Channel\ Sum}{Time\ difference} \tag{13}$$

   d. The number of impacts per data reading along with the overall change per data reading is the key result required from each group of overlapping orbits. Averaging each of these values gives an overall change per increment and impact per increment.

Initially this average was over the whole of the mission. However, in testing the correction it clearly was to general a value for each channel. Instead, the overlaps are grouped by year of the mission to give a set of eight yearly averaged values per channel.

4. The sets of values for each channel forms the basis of CV (Correction value) applied to each channel.

$$CV = \frac{Average\ (change\ per\ increment)}{Average\ (impact\ per\ increment)} \tag{14}$$

Initially it was assumed this CV would always be positive; however, it was later determined to be incorrect, in the case of Oxygen the CV will be negative to account for the increasing values. This assumption came from generalising the system only from the sulphur channels that trends in the count rates would always be decreasing.

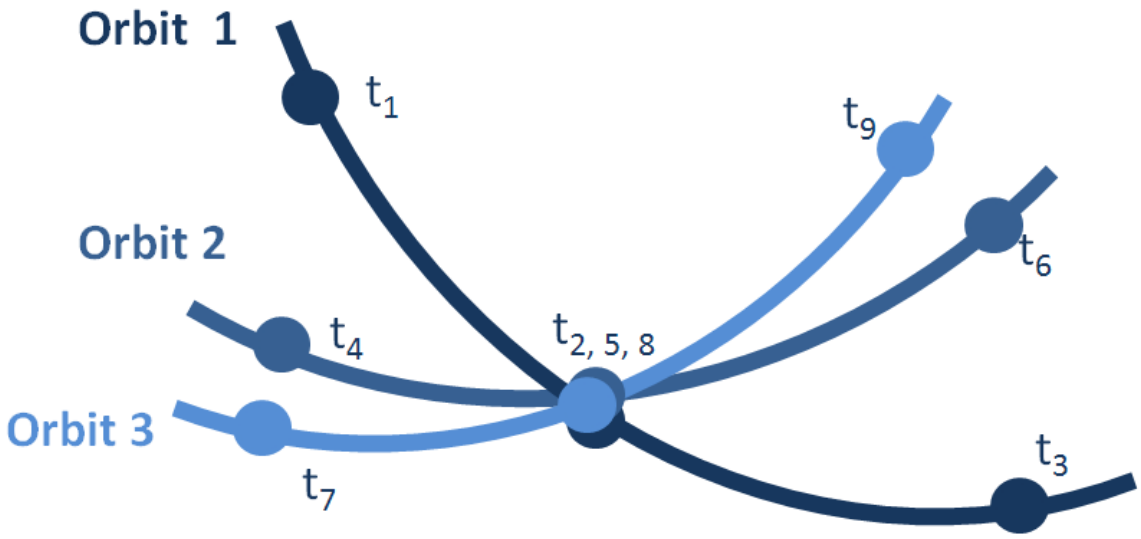

Figure 3.2-1: Method of evaluating overlaying orbits at different time periods to estimate changes in the data under similar conditions. t_i represents the time stamp associated with readings along the orbit path.

5. The correction value quantifies the change in the data as an amount of change against an impact recorded by the channel. The next step is then to apply this to the number of impacts on each channel. This must be an iterative process as each time the CV is applied and the count rates increase, there will be more counts to be accounted for. For each iteration the processing steps are as follows:
    a. The first iteration is unique in the process and serves to set up for the rest of the data set. There are no previous additional counts to account for so some of the steps are not required.
    b. First iteration: The count rate is multiplied by CV for the year and channel applicable. This value is added to the original count rate and the amount added is recorded.
    c. All other iterations: the same multiplication is applied as in the first iteration, following by again adding the new counts to the original value and recording the addition. The additional step sums the amount of total added counts so far and again multiplies by the CV. The summation of the added counts represents all to the counts that have hit the detector but have not yet been accounted for in terms of the change they will have on the detector. However, this backlog of counts becomes very big very quickly and simply adding it to the new value along with the additional counts from the first step

creates exponentially big count rates when the detector may have been recording very little.

d. Instead, this accumulation is applied to the current iteration as a percentage of the original value. This preserves the very sparse regions of space in the far radii of Jupiter. The percentage amount, whilst initially applied as an arbitrary percentile, does in fact respond to another aspect of the detector that had not yet been considered.

6. The final step of the process is housekeeping. The initial processing of the data set includes adding a huge amount of data to the set to account for the large sections of no data being taking during the mission. This dummy data, whilst useful for this application is not real data and cannot be treated as such. Removing this data is straightforward, using the date file containing the placeholder values, the location of the added data is known and can be used to identify the “real” data and save it in a separate file.

3.2.2 Problems Encountered During Development of Correction Method

The devolvement of this correction method was not simple or immediate. Built on a trial and error system to determine the best method for achieving the values, the best fit of the values to the previous years of the mission determined how effective the correction was functioning. This process of testing is described later in this section and is used to show the effectiveness of the final correction and data set.

The first major adjustment to the process, was allowing the CV values to be negative. In the initial testing only, the Sulphur channel TS1 had the correction applied to it, whilst done for simplicity the CV for Sulphur only exhibited positive values. As logically, the data drops over time meaning for every count recorded there will be a reduction in the reading so a correction value needs to be positive to add counts rather than a negative correction that will remove counts.

Once the preliminary method proved effective for the Sulphur channel and the method was tested overall of the set of channels, the flaw was identified. Changing the code

to allow for negative values was simple; however, it did allow the CV values to be far more diverse. This is the next of the significant problems to overcome.

The first rudimentary method for determining the CV from the cross over points had limitations. If the conditions for the crossover points were too constraining, there wasn't enough data to generate the CV for each year. On the other hand, if the constraints were set too widely then the CV tended to be larger than expected and unrealistic. The constraints determined how close the orbits had to be for it to be considered a crossing point. The focus of the crossing points was in the Jovian equatorial plane, the x and y coordinate of the orbits; also included was a secondary condition of the height or inclination of the orbit, the z coordinate. For most cases the smaller these constraints could be, the better; however, to get reasonable values and enough crossover points this was around 3Rj or approximately 200km in the (x, y) plane.

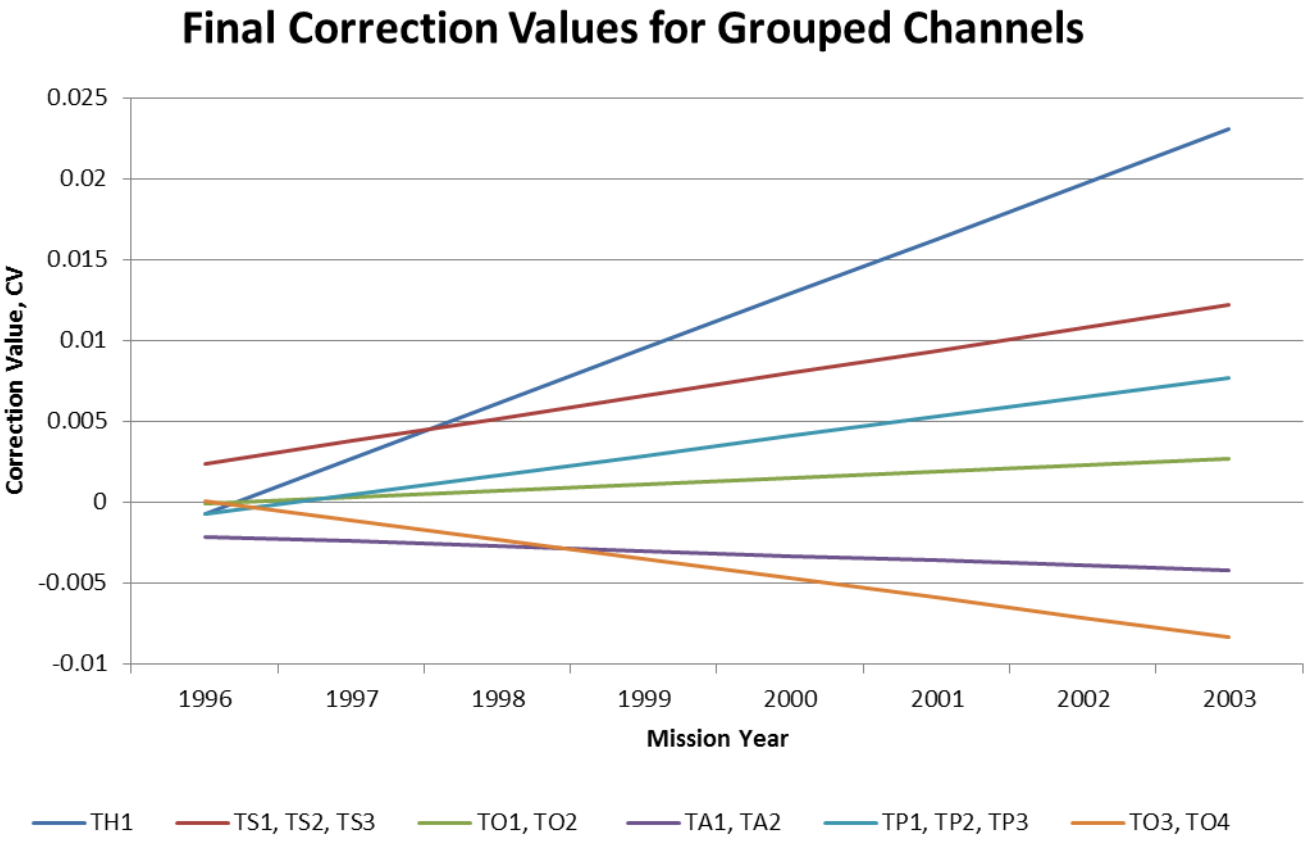

Figure 3.2-2: CV for grouped channels.

The decision to generate a CV value for each year meant that these crossover points were further limited as they could not be orbits from differing years. For 1996 and 2003 there is only a partial year of data, these years immediately suffered in a lack of viable

crossover points to use in generating a CV value. To combat this, the CV for years 1996, 2003, and 2002 (which had far more elliptical orbit paths and thus naturally fewer crossover points) were calculated using an interpolation of the other years.

Even using these adjustments to generate more accurate and reasonable values for each channel it became clear that in the sparser channels the CV value could be very variable. A final measure to combat this was to take advantage of the priority system (described in 2.2.1) implemented in the recording measurement system, and to group the channels to stabilise the values. By simply adding each value in a channel to those in another channel, the CV is still calculated to be an average of change in counts per count measured. It also gives the process larger numbers to work with initially, and reducing the chance of a calculation faulting over a zero-count value.

The priority system keeps the counts recorded in each channel stable so that the less common channel's counts are recorded over an easily filled channel. This stops the proton channel from swamping the values of Sulphur and Oxygen. The priority system divides the low and high energies of Sulphur and Oxygen, despite this the way the correction focuses or

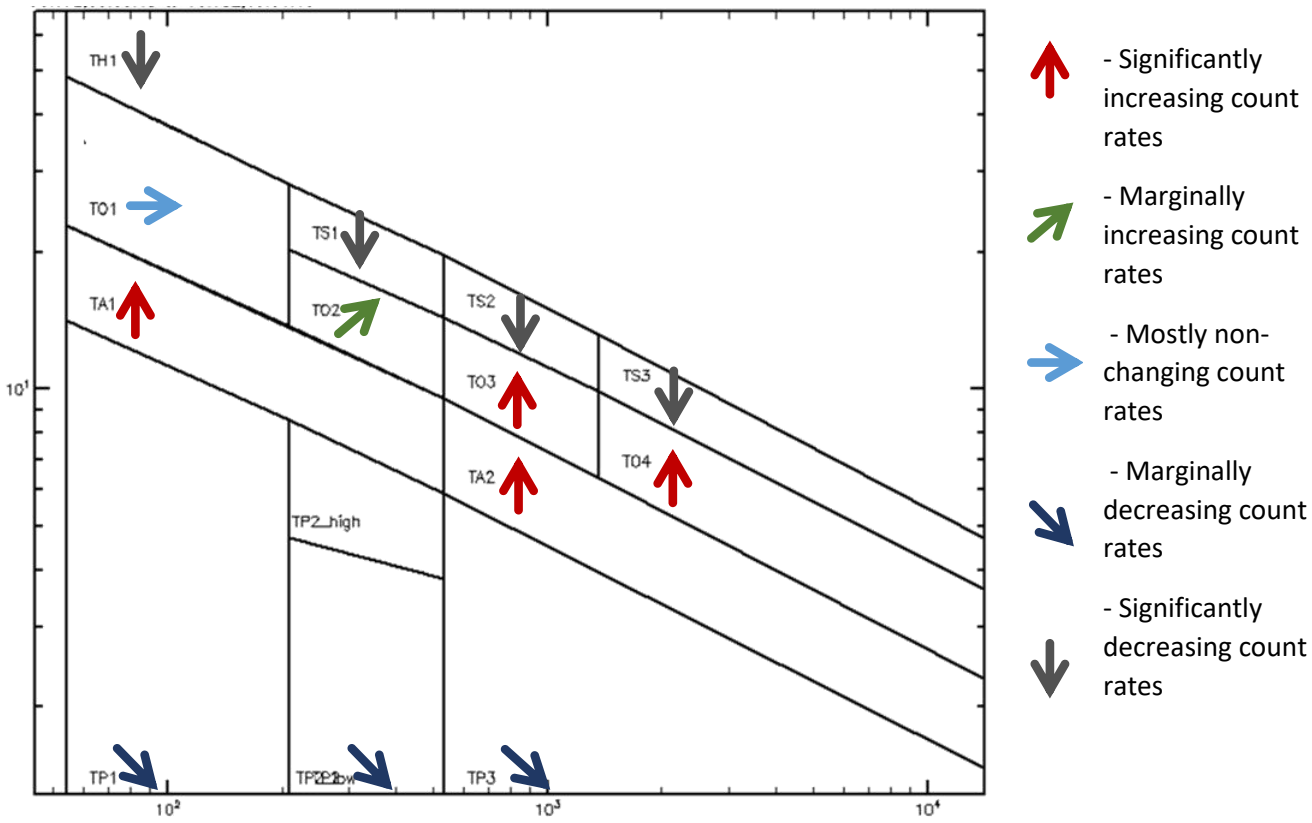

Figure 3.2-3: Trends of the channel count rates. These trends are inversely proportional to the expected values of CV.

each channel individually means that even if the CV comes from a group over the priority it will not change the effectiveness of the correction. The CV value itself will not be adversely affected by a grouping across two priorities; regardless of the overall counts, the CV is evaluating the change in the channels.

The final values for the CV shown in Figure 3.2-2 demonstrate how the channels are affected by the degradation. The larger mass species exhibit higher drops in count rates. Along with this the nature of the counts "slipping" into the wrong channels is visible, namely in the Oxygen channels. The generalised trends of the channels (Figure 3.2-3) are inversely proportional to the CV values.

3.2.3 Method and Mathematical Derivation

The approach of the correction is quite unusual in this case; instead of coding a derived method instead, the method grew and evolved by trial and error with the final mathematical explanation described in full later. As follows, here are the mathematical equations behind the method described above. They are derived from the steps involved in the correction, as steps in discrete iterations that are pulled together to form a cohesive formula for the full process.

The derivation begins with the first three iterations of a channel data set:

$$j_1 = (j_1 CV) + j_1 \tag{15}$$

$$j_2 = (j_2 CV) + \frac{j_2 CV(j_1 CV)}{100} + j_2 \tag{16}$$

$$j_3 = (j_3 CV) + \frac{j_3 CV(j_1 CV + j_2 CV)}{100} + j_3 \tag{17}$$

Where j_1, j_2 and j_3 are the first three data values from a given channel data set, and CV is the correction value calculated above in section 3.2.2. The first iteration is unique; but all following iterations can be generalised to be in terms of j_n. The division by 100, is an added factor to keep the correction from increasing too far, this is later adapted and identified after further investigation.

$$j_n = (j_n CV) + \frac{j_n CV(\sum_{i=1}^{n-1} j_i) CV}{100} + j_n \tag{18}$$

In a simplified form:

$$j_n = j_n(1 + CV) + \frac{j_n CV^2}{100}\left(\sum_{i=1}^{n-1} j_i\right) \quad (19)$$

Using the definition of CV from above the value can be converted into terms of j. In doing this, the new term introduced, J, represents the Average of j.

$$CV = \frac{Average \Delta j \ per \ n}{Average \ j \ per \ n} \quad (20)$$

$$CV = \frac{\Delta J}{J} \quad (21)$$

This average J can also be used to simplify the summation of the j_n in equation (19). An average is defined as the summation of all the values in a set divided by the number of values in the set. Therefore, the summation of j_n is the average multiplied by the number of values summed; in this case n.

$$j_n = j_n\left(1 + \frac{\Delta J}{J}\right) + \frac{j_n \Delta J^2}{100(J^2)} Jn \quad (22)$$

$$j_n = j_n\left(1 + \frac{\Delta J}{J}\right) + \frac{j_n \Delta J^2 n}{100J} \quad (23)$$

$$j_n = j_n\left(1 + \frac{\Delta J}{J} + \frac{\Delta J^2 n}{100J}\right) \quad (24)$$

This is the state of the correction formula at the stage of first results; whilst there are updates to this, they are described in subsequent sections along with the reasoning behind them. The accompanying code detailing this is included as an appendix.

3.2.4 First Outputs and Secondary Program Results

Once many of the initial problems were sufficiently developed and a working method settled on, the 13 CMS channels had the correction applied to them. Whilst the focus for Europa's surface is the Sulphur and Oxygen, correcting the rest of the channels allows for far further reaching work to be conducted in the future.

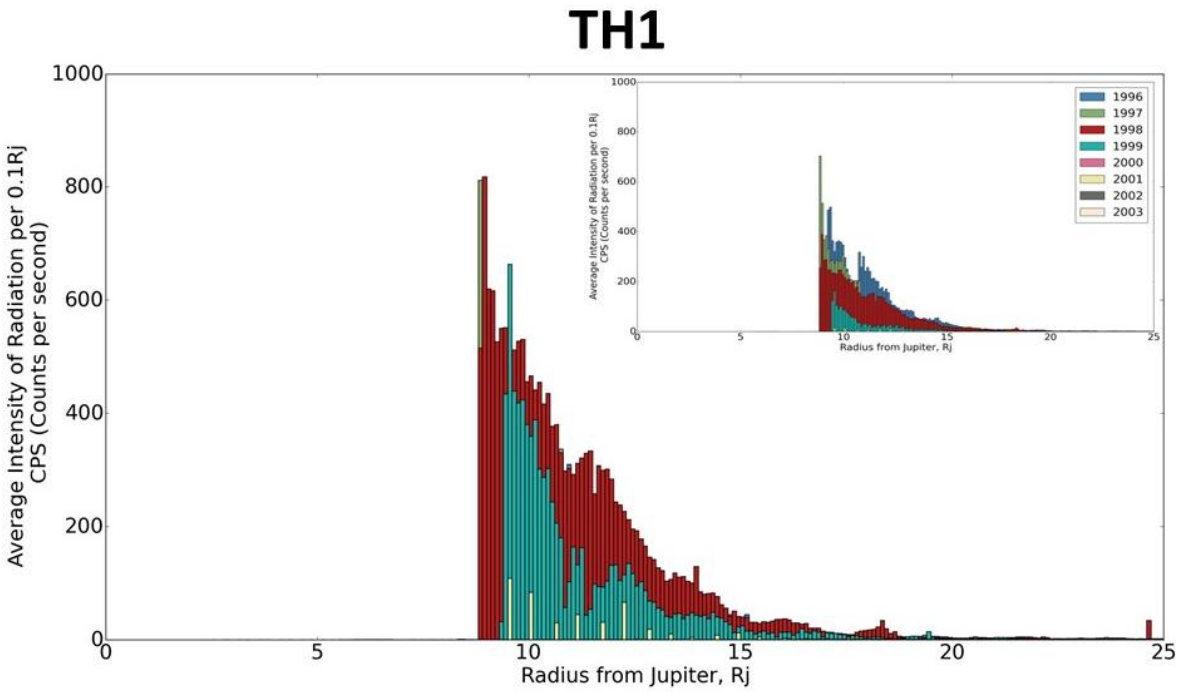

Figure 3.2-4: Channel TH1 first correction attempt (Pre-correction inset in top right for reference)

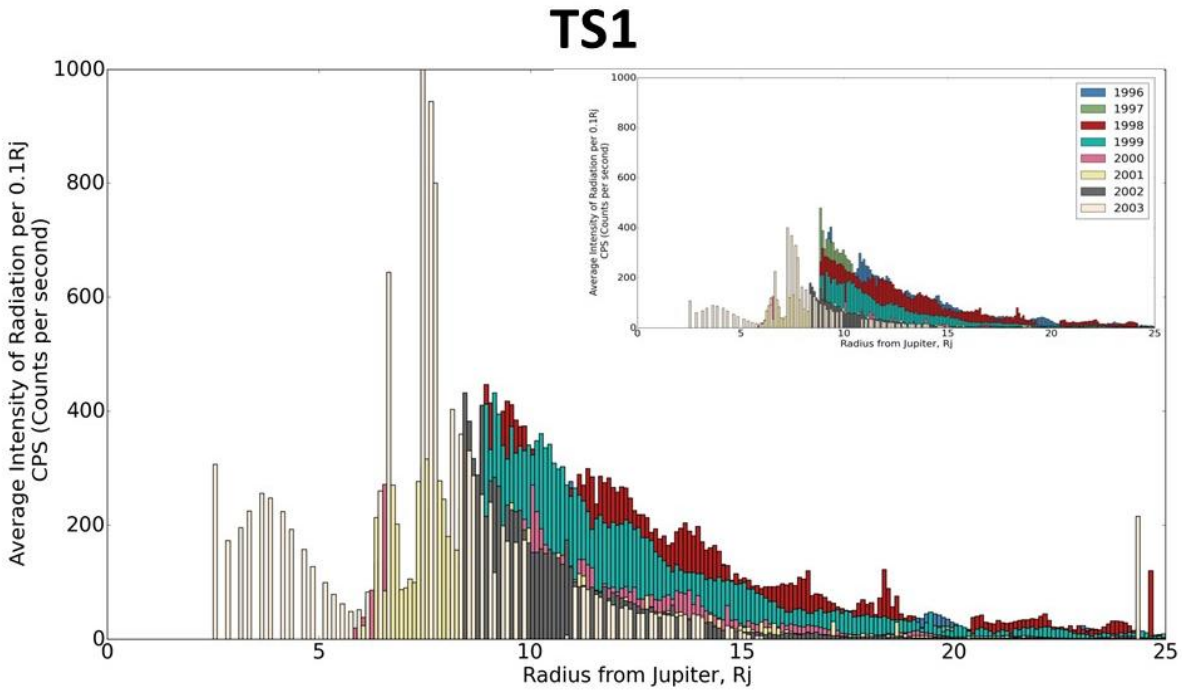

Figure 3.2-5: Channel TS1 first correction attempt (Pre-correction inset in top right for reference)

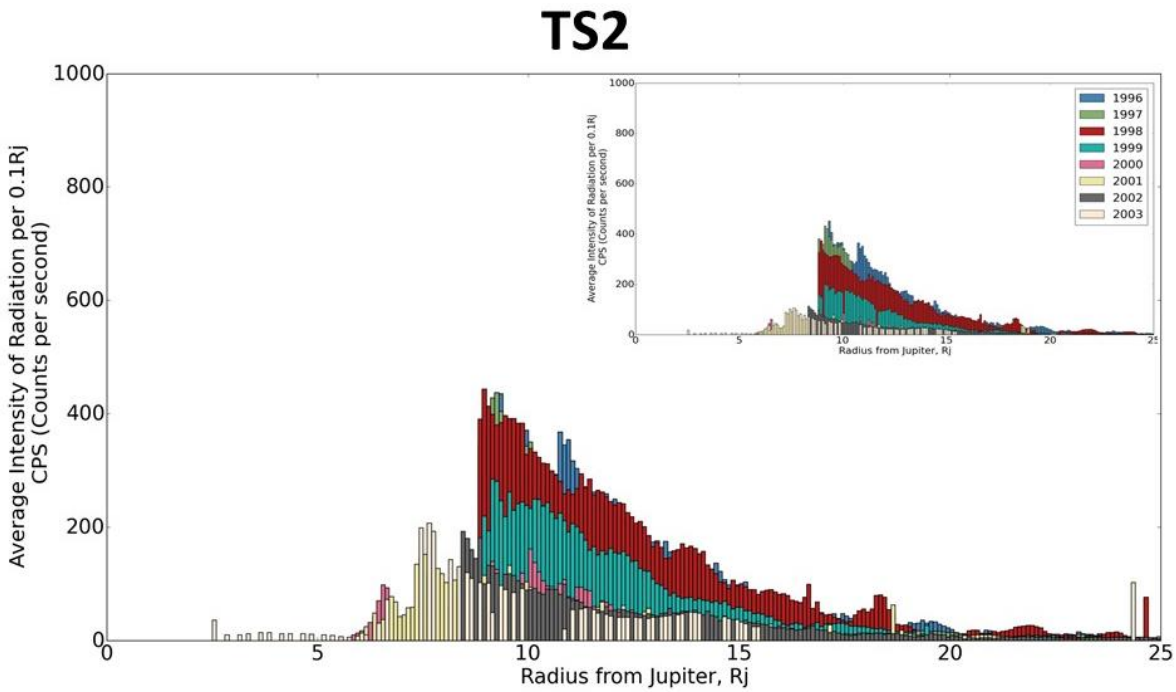

Figure 3.2-6: Channel TS2 first correction attempt (Pre-correction inset in top right for reference)

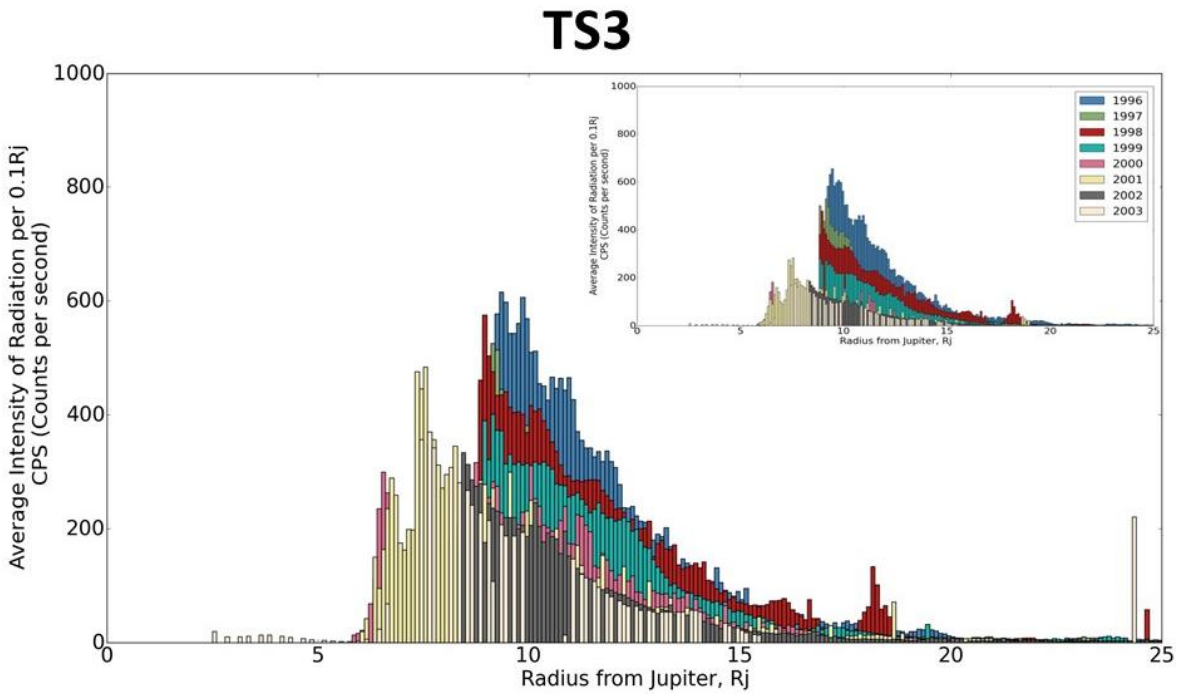

Figure 3.2-7: Channel TS3 first correction attempt(Pre-correction inset in top right for reference)

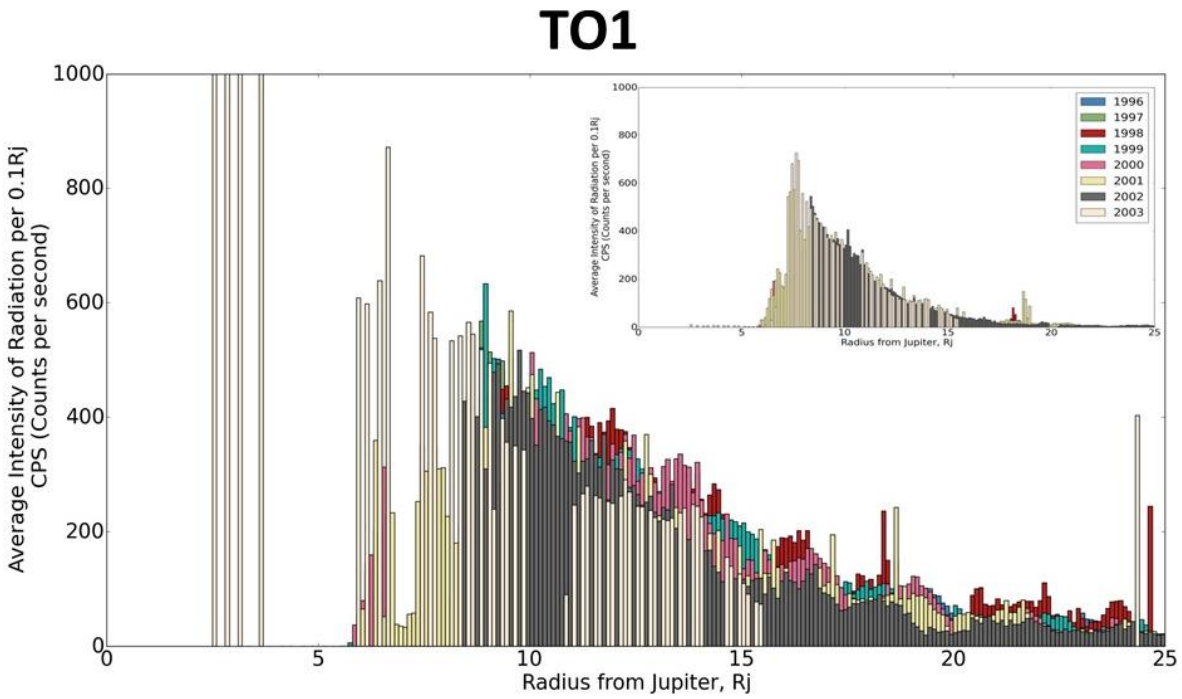

Figure 3.2-8: Channel TO1 first correction attempt (Pre-correction inset in top right for reference)

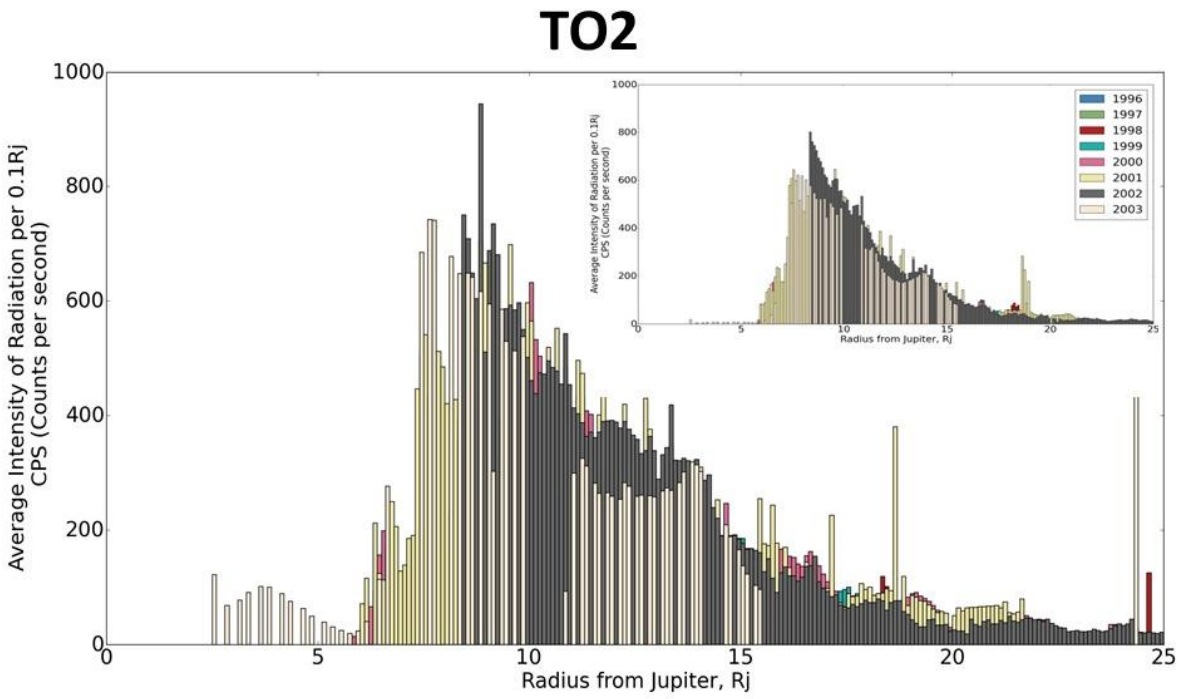

Figure 3.2-9: Channel TO2 first correction attempt (Pre-correction inset in top right for reference)

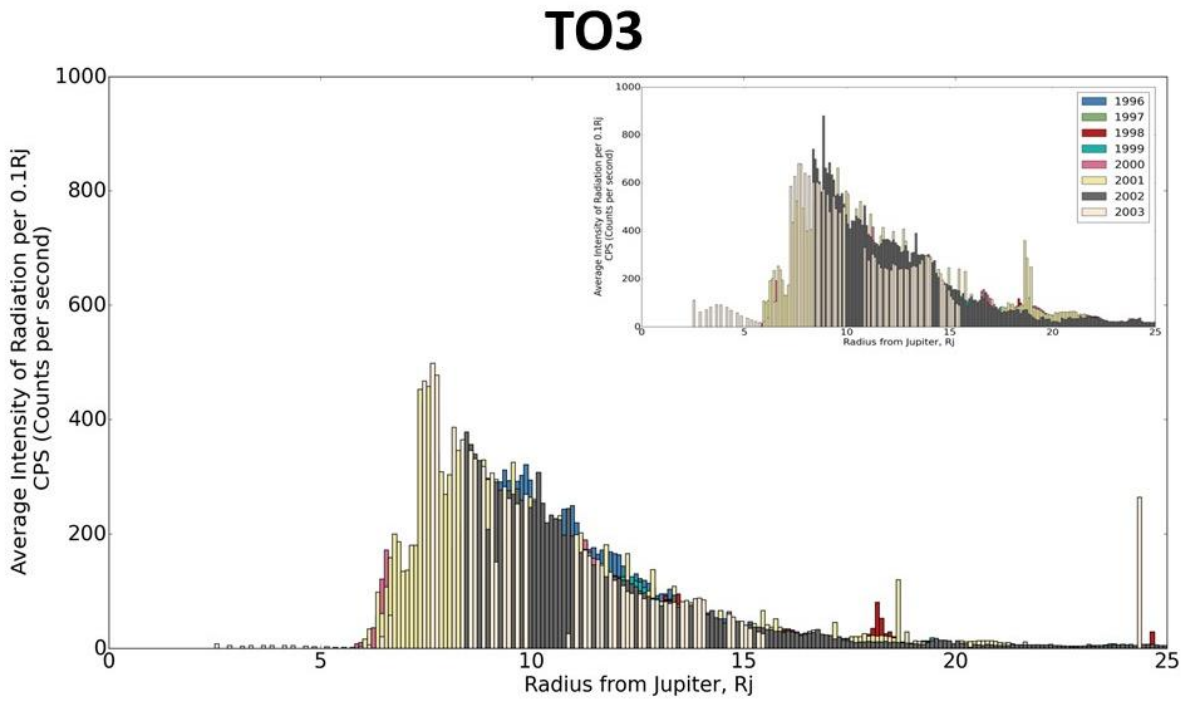

Figure 3.2-11: Channel TO3 first correction attempt (Pre-correction inset in top right for reference)

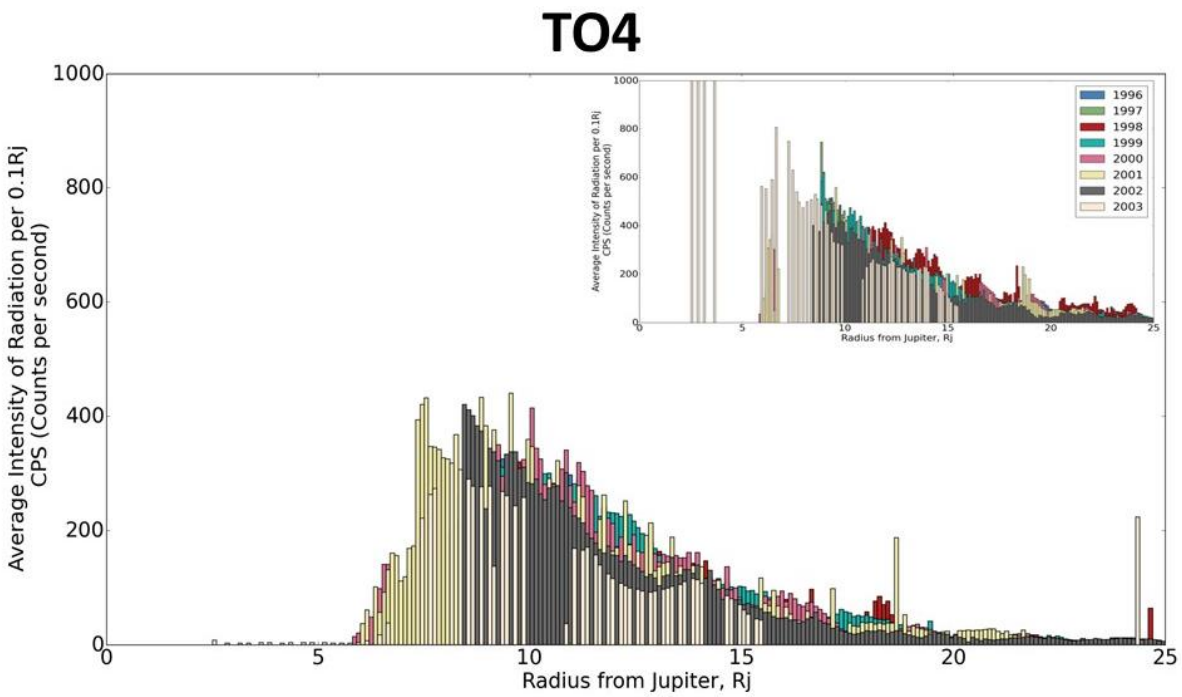

Figure 3.2-10: Channel TO4 first correction attempt (Pre-correction inset in top right for reference)

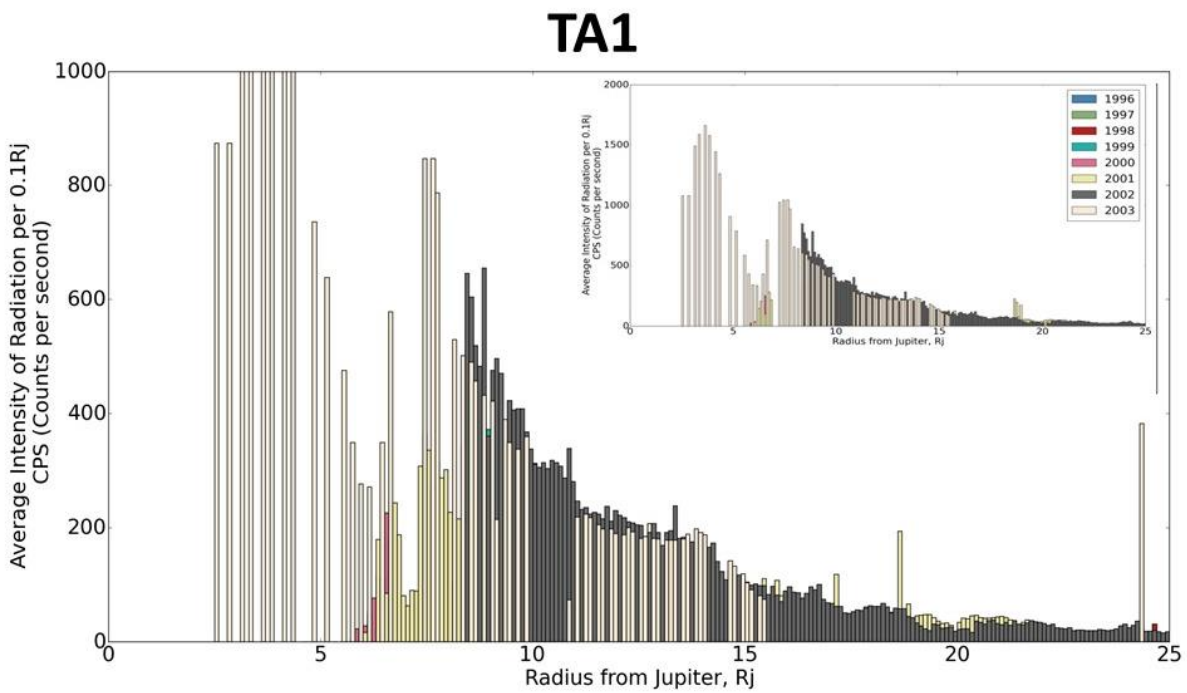

Figure 3.2-12: Channel TA1 first correction attempt (Pre-correction inset in top right for reference)

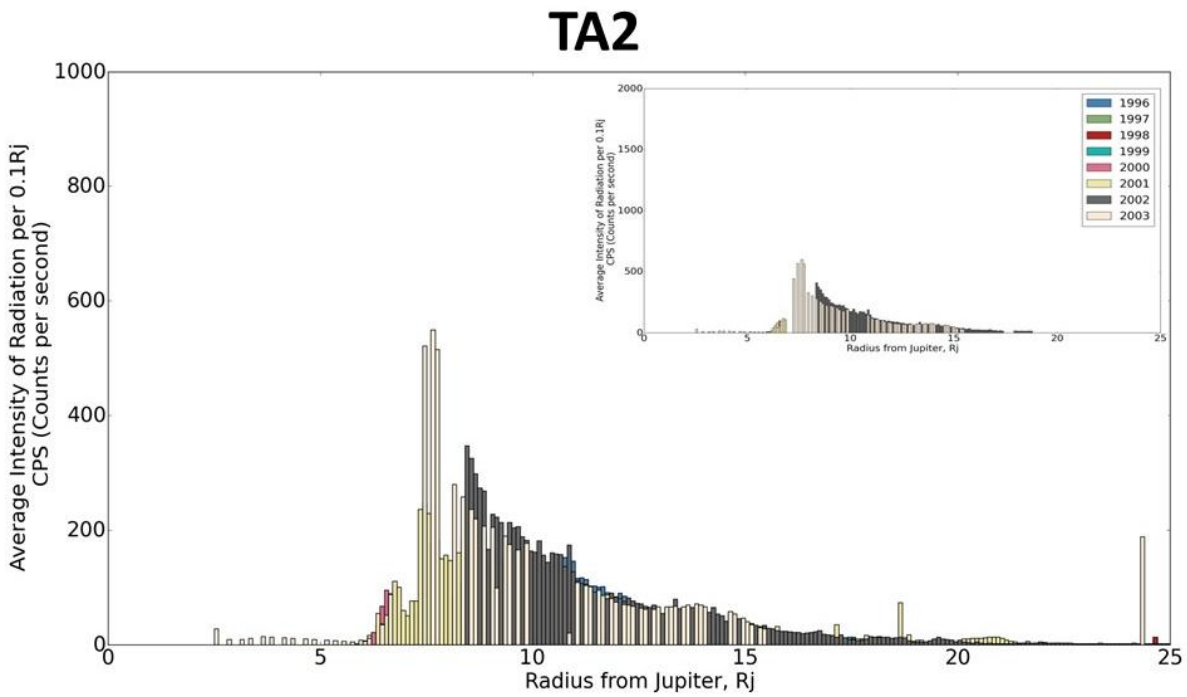

Figure 3.2-13: Channel TA2 first correction attempt (Pre-correction inset in top right for reference)

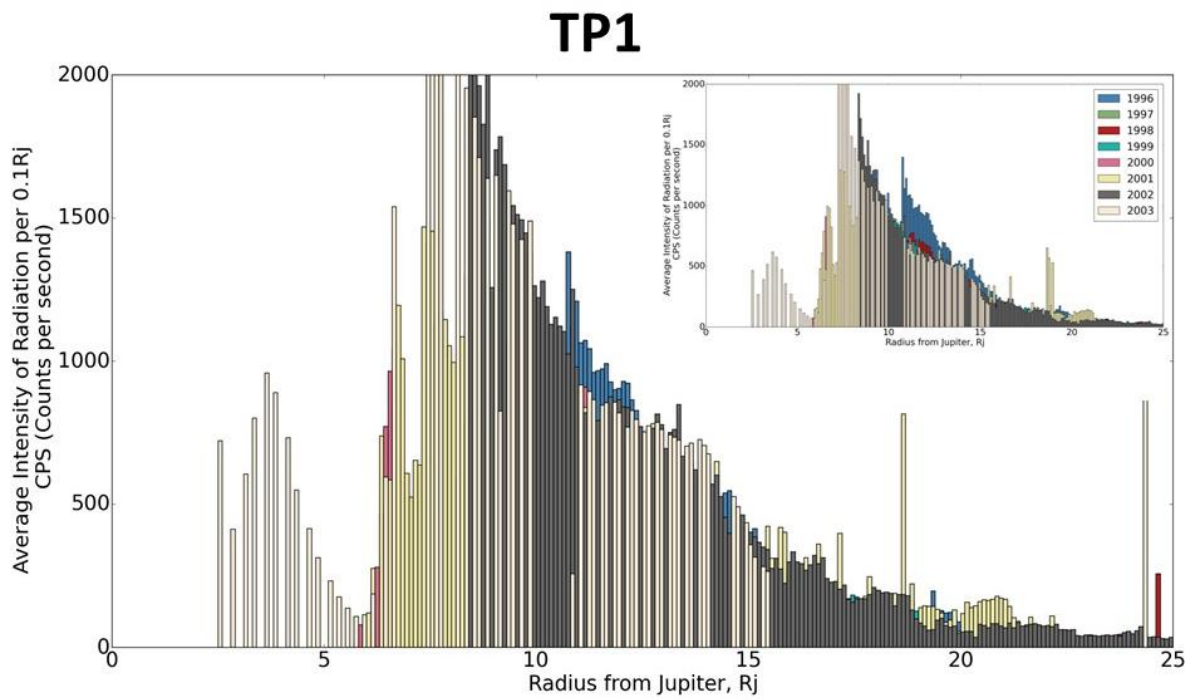

Figure 3.2-14: Channel TP1 first correction attempt (Pre-correction inset in top right for reference)

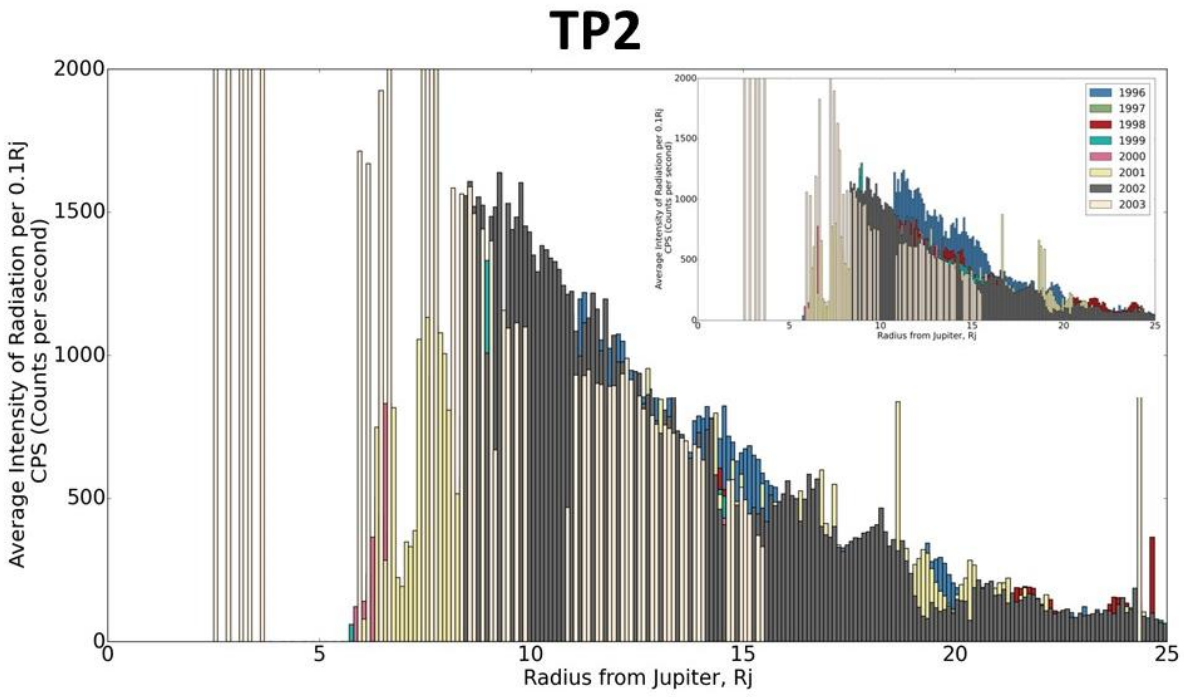

Figure 3.2-15: Channel TP2 first correction attempt (Pre-correction inset in top right for reference)

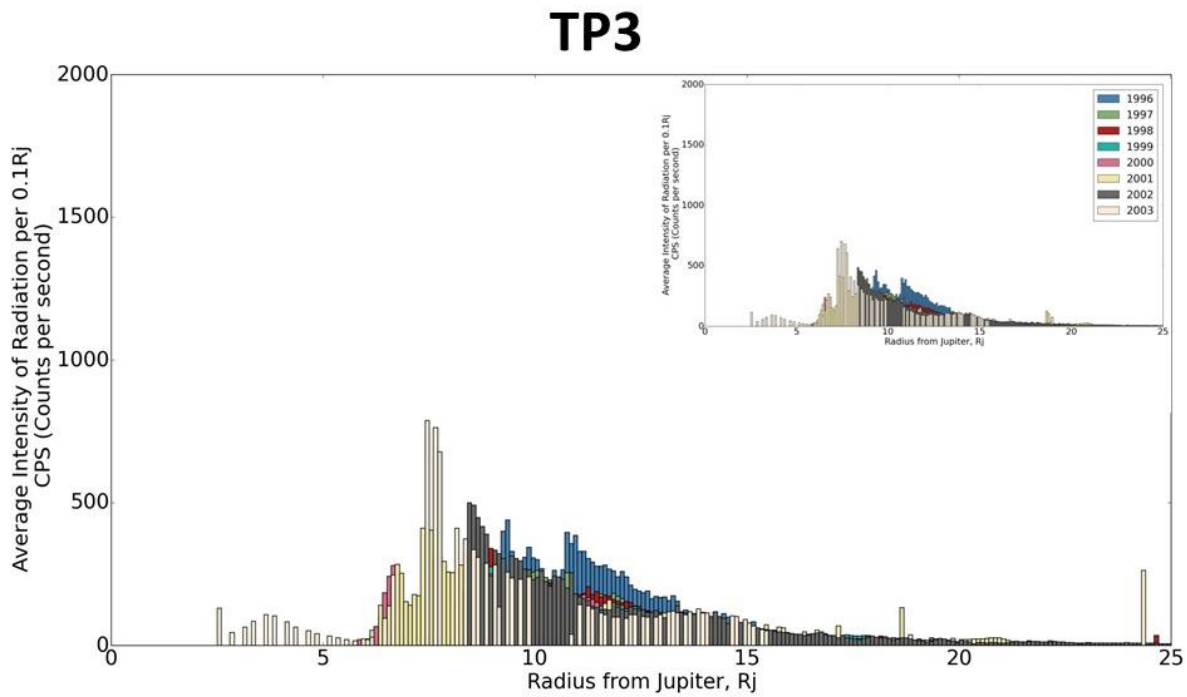

Figure 3.2-16: Channel TP3 first correction attempt (Pre-correction inset in top right for reference)

As a method derived from the principal changes in the data, the first attempt at correction is very optimistic. Some channels work better than others, this itself is an effect of how the channels are interconnected in feeding into one another. However, the amount of information that the channels can provide limits what the correction can achieve without further investigation into how the data is changing.

3.2.5 Initial Correction Analysis and Issues

The correction works best on the channels that measure the smaller particles; i.e. those that are least effected by the dead layer build up on the front of the detector. This is primarily the Hydrogen and Helium channels. The Helium channels suffer a little from the Oxygen particles being miss-allocated into it, although this is only minor. The Sulphur and Oxygen channels are the most complex to correct and this is shown in the 7 channels shown above (Figure 3.2-5, Figure 3.2-6, Figure 3.2-7, Figure 3.2-8, Figure 3.2-9, Figure 3.2-10, Figure 3.2-11), they all however have very different problems depending on which element they measure.

Sulphur requires the most correcting of all the elements measured. As the largest mass particle, it is the most affected by the build-up of a dead layer; looking at the 3 channels Figure 3.2-5, Figure 3.2-6 and Figure 3.2-7 there is still a drop over the years even

in the corrected data that hasn't been completely dealt with. Looking specifically at TS3 (Figure 3.2-7), the correction improves as it goes on; with the 1996 profile along with 1998 and 1999 profile still being clearly visible in the corrected graph. On the other hand, the later years of the mission are far more improved, though not enough to restore it to the original profile. The other two Sulphur channels exhibit similar problems.

An interesting side effect is seen in TS2 channel (Figure 3.2-6) where the overall counts of the plot is higher in the corrected data. This is something that is entirely plausible. Despite many considering the early years of the EPD data set to be useable (Mauk et al., 2004) it is very possible that the data set may have sustained damage before it even reached Jupiter.

The most complex of the channels to correct are the Oxygen channels. As well as the dead layer build up, the influx of the sulphur particles into the wrong channel boundaries, add an additional level of complexity to the matter. This is in some way combated by the negative correction value, however this still is not perfect and in the case of TO1 and TO4 channels (Figure 3.2-8 and Figure 3.2-10) the CV over corrects the increases.

To further the explanation as to why the correction at this stage is not working correctly is the nature of CV generated. Calculating the CV for each mission year gives a full overview of how the decay in the detector is changing; viewing it this way, the more damage the channel takes, the higher the correction needs to be. However, in the later years, only comparing to the previous or current year means the CV does not show the true extent of the decay. Changing the calculation to account for this is far more complicated, it would require setting far more confining limits on the overlaps, or even manually identifying the overlaps. There is also the possibility that this would limit the data so much that there is very little chance of getting any data out at all.

Another fault in the CV values is that it assumes that all the counts available from the filled data sets are the all counts hitting the detector. This is most likely not the case. Some of the reasons this may be are:

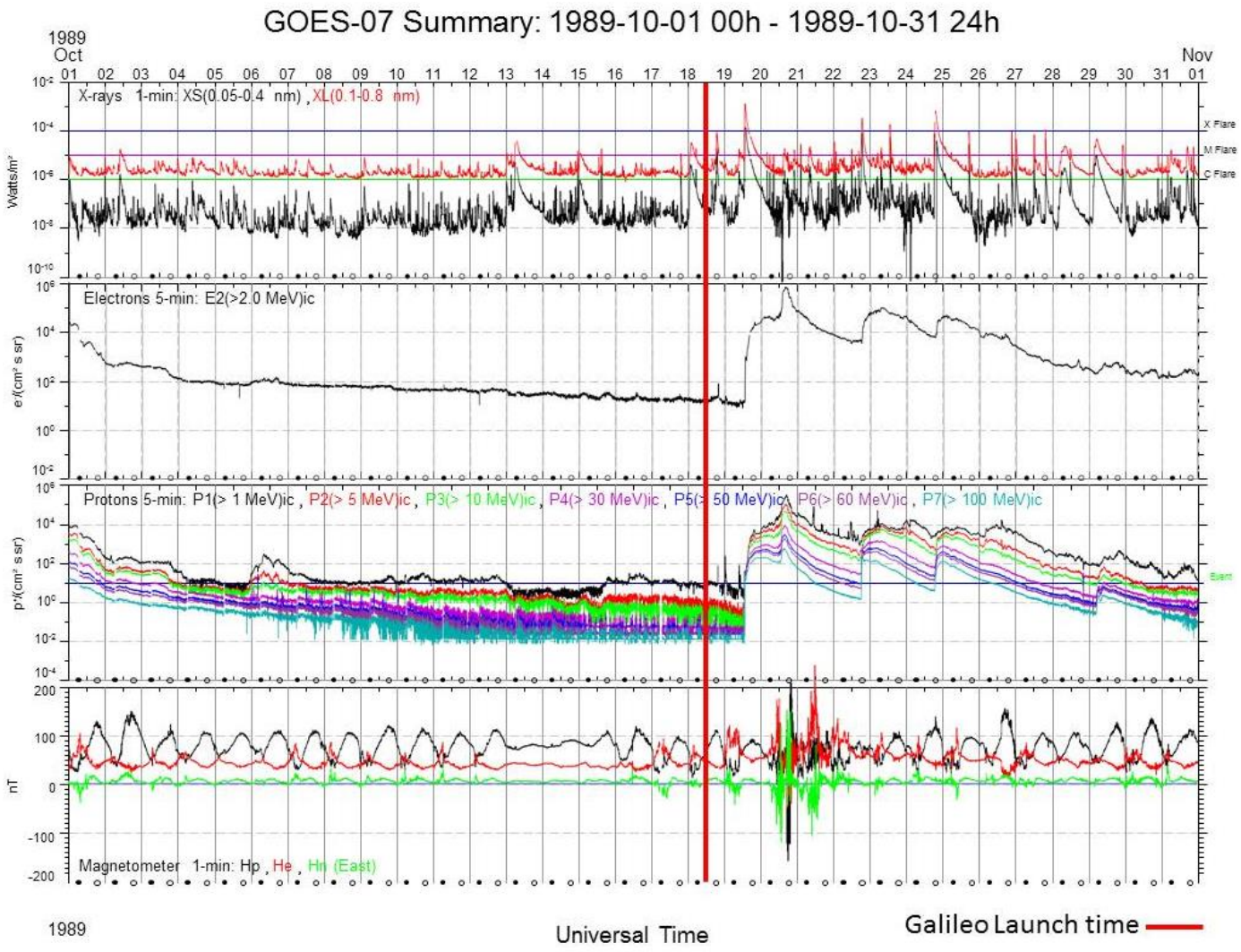

Figure 3.2-17: Overview of the Solar flux from the GOES mission data logs. The red vertical line at 12noon on the 18th of the month defines the launch time of the STS-34, NASA Space Shuttle Atlantis; carrying the payload Galileo.

Previous decay in the detector: During the long journey from Earth to Jupiter, Galileo took many calibration measurements at Earth and Venus during its gravitational assists. These measurements themselves are innocuous enough however; they confirm that the protective covers from launch were removed soon after exposing the instruments to the solar wind. Galileo was launched in October 1989, a famously active year of solar activity, consisting of 6 major identified events classified at the high end of M-class flares into the X-class (Reeves et al., 1992). One such event happened only days after the launch from Kennedy Space Centre, Florida. The GOSE logs for the month of October 1989 clearly show the disturbance reaching Earth just barely 24 hours after the separation of Galileo from the shuttle Atlantis. This event was an X-class solar eruption boasting fluxes of protons as high as $x10^6$ (cm^2 s^{-1} sr^{-1}). These particles could have affected the instruments in the same way the particles in the Jovian system did.

If any particles from the event detected in the GOES data set, adversely affect the detector, then there is an amount of counts wrongly allocated already. Unfortunately, there is not a completely untouched data set from Jupiter to provide a calibration against so this problem is not solvable. It also returns in the next section where a calibration set is ideally required and measures must be adapted to make up for this.

Non-measured particle impacts: Whilst great care has been taken to account for all of the particles missed in the data gaps, where no recordings were taken, there are more particles hitting the detector during operation that are not accounted for. Other defects and damage to the instrument is a possibility for this kind of fault. For a count to be measured there is a three-point confirmation; a positive signal from the start timer of the TOF system, a positive signal from the end timer of the TOF system and a valid energy measurement from the end detector. This means any malfunction in the TOF measurement system will invalidate a count at the main detector; something that has clearly happened when considering the PHA graphs from near the end of the mission and the anomalous readings spread along the top sections in bands (Figure 2.3-3; right).

The amount that a detector measures against how many particles that impact is the gain or efficiency of a detector. Whilst there is a fault in the overall measuring in terms of the channels there is also a drop in the efficiency of measurement of the detector also. Evaluating this and additional corrections for this are covered in the following section.

3.3 Power Spectra

This upcoming section details the further investigations of the correction so far. Using similar methods to the dead layer investigations in section 2.4; the before and after correction data values are evaluated to determine the effectiveness of the correction as well as delving into further adjustments for the correction methods.

3.3.1 Comparing Count Rates

In section 2.4 the evaluation of the PHA graphs determined the extent of the dead layer by comparing the movement of the count rate peaks against calibration lines moving under the addition of a dead layer. This method has the advantage of comparing against computed calibration data, however it used only small snippets of high priority record data to generate the PHA plots with the loci visible rather than the overall bulk count rates.

The PHA plots are valuable in their own right; however, the data range they cover is not as extensive or dense as the individual channel count rates used for the correction. The general method used for comparing is the same. However instead of using Time of Flight against Energy; the comparison uses Count Rates against Energy. Very similar plots to the PHA graphs are producible in this way but first they need some refining as each element in this case has only two or three values to form the loci from.

Using the data generated in Section 2.4.1 of how the channel boundaries would change under dead layers allows both an accurate measurement of the energy bounds of each channel, and the movement of these bounds for comparison to dead layers. The central position of each channel, even under dead layer, provides the energy for each channel to match to the count rates. As each boundary moves the point marking the centre moves accordingly rather than just applying the change in energy, for a value of dead layer, to each locus as done in section 2.5.2.

Using these energies for each channel and the accompanying count rates generates a distribution of the counts per energy, or an energy spectrum. This spectrum is in the form of a power law, i.e. a straight line when plotted in logarithmic scale. This Power spectrum is very variable for each species over the course of the mission, depending highly on the position of the spacecraft and the local environment.

As the overall effectiveness of the correction is being tested, the day-to-day variations are not as vital and a trendline of the full data set can be used (Figure 3.3-1). Figure 3.3-1 shows the how the trendline used is generated. The overall appearance of these figures demonstrates how hard it is to classify the drop in the data. Unless the instrument is within 50 Jovian radii of Jupiter, the values measured are very low with each peak in the figure matching with the orbital flybys of Jupiter itself or its moons. The overall trend is however that the flyby peaks slowly drop away as the mission progresses. Considering that the later flybys focus on the closer in moon Io these values should be even higher than the early Europa flybys. This simplification allows the generation of a spectrum for each year thus a data set for each species and year is now available.

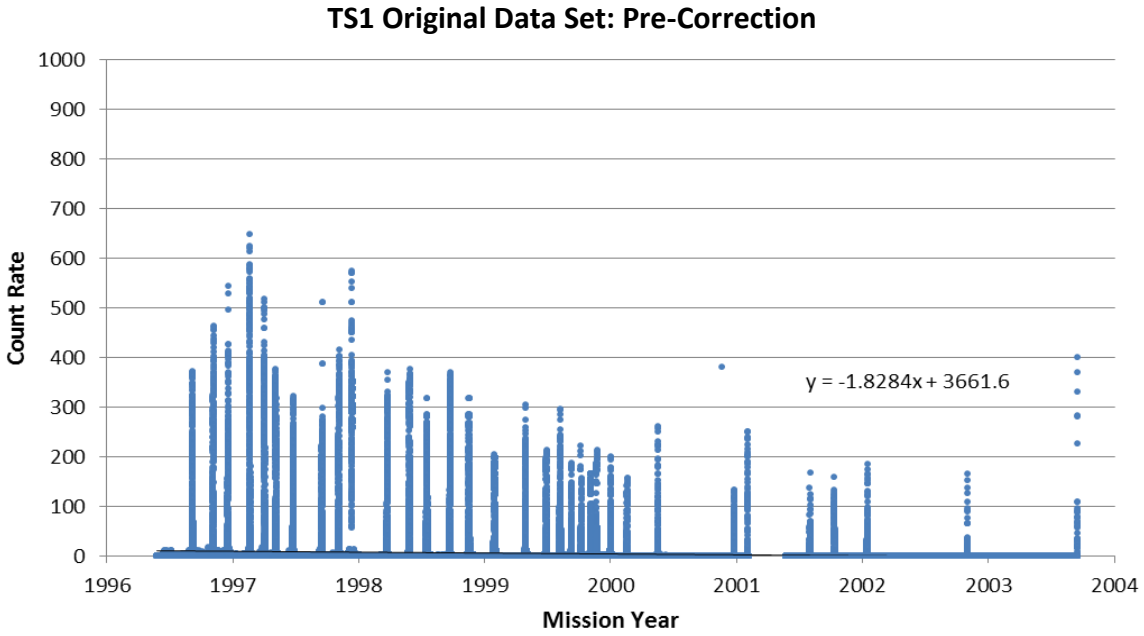

Figure 3.3-1: Original data set of channel TS1. The data is very variant depending on distance from Jupiter, each peak visible matches with a close in flyby of Jupiter or its moons.

To make these spectra as accurate as possible, there are some assumptions to be made about the channels and changes to the evaluation based on this. The counts for each channel are not all at a single energy; the distribution along the channel of the counts is even. To deal with this dividing each value for an individual channel by the energy boundaries of the channel, provides a more realistic amount of counts in a very limited energy range.

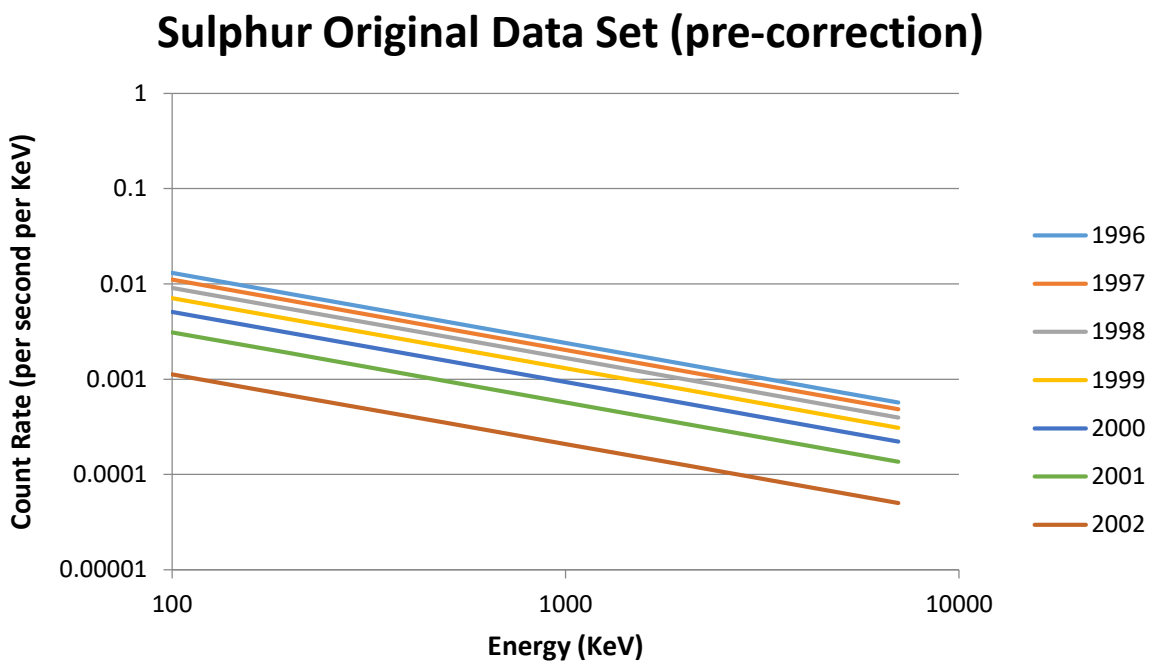

Figure 3.3-2: Energy Spectrum of the three sulphur channels using original uncorrected data set.

Shown in Figure 3.3-2 and Figure 3.3-3 is the spectrum for Sulphur as the original data and with the first correction attempt applied. The improvement in the corrected version is visible but overall not perfect. Whilst some of the discrepancies are from the decision to average the data using linear trends, there is still a significant drop within the

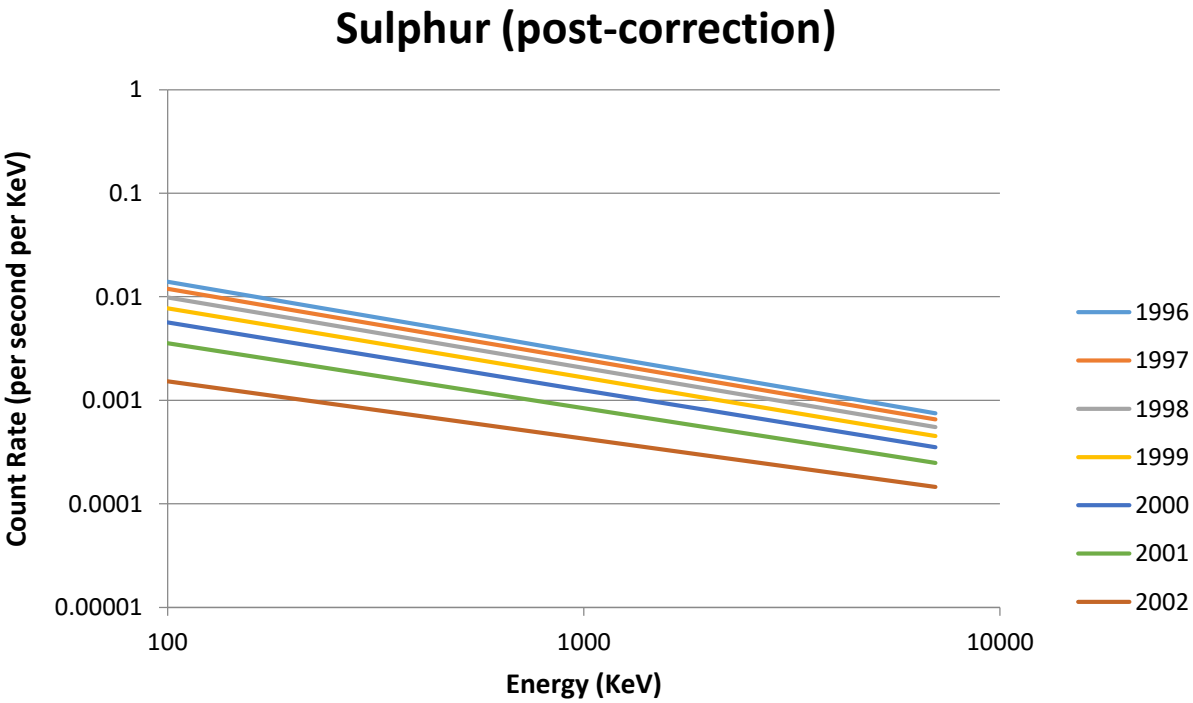

Figure 3.3-3: Energy Spectrum of the three sulphur channels using data processed by the method described above in section 3.2.

data sets. In hindsight, the most accurate method for this kind of comparison requires isolating each peak and averaging each peak individually, this would eliminate the unevenness of the orbit flybys and the very high quantities of low values from the distant tail of the magnetosphere. With less time constraints completing this work would produce somewhat better results for the overall correction however in the interest of using the data for further analysis, this method produces sufficient results for the adjustment of the correction.

3.3.2 Energy Spectra: Advantages and Disadvantages

Using a power law based spectrum for each element has advantages and disadvantages; some of which are already covered. The most important of which are covered below:

3.3.2.1 Advantages:

The main advantage is the ability to compare the values and analyse them against the initial reading to determine the changes. The fact that the same method as in section 2.4 is repeatable gives good continuity whilst also allowing the dead layer energy change calculations for further use.

Whilst it is the same method, the comparison using the PHA plots from section 2.4 only categorise the position of each element, determining how accurately the appropriate channel is measuring each point. However, this does not evaluate the overall count rate. This method focuses on the overall counts, under the assumption that the channels are now allocating the recorded points correctly, with the missing points not recorded at all.

Along with checking the overall efficiency of the detector readings, the dead layer presence can also be determined along with the reduction of dead layer from the first trial of the correction.

3.3.2.2 Disadvantages:

The main disadvantage of this method is not with the method itself but with the data available. In section 2.4 the data for both the dead layer additions and the yearly data set had a calibration data set to compare with. When using a spectrum of counts there is no distinct calculable value that could form the basis of a calibration data set. This means that

the dead layer energy changes are of the earliest, assumed most accurate, data that is the 1996 data set.

A further disadvantage is how some of the channels are not suitable for generating the spectrums. For example, the heavy ions measured by TH1 have only a single channel. This is not enough to form spectra. In the same way, the helium comes from only two channel points as oppose to Sulphur with three to draw from. The Oxygen spectrum suffers from the loss of TO1 channel, its shape overlaps with the lines of the Sulphur channels counting both species rather than exclusively Oxygen.

3.3.3 Re-checking the Dead Layer Estimations

Implementing the same method as in section 2.4 here allows a comparison of the 1996 data with a simulated dead layer, to the later years of the data. This method has proved to be simple yet effective for the initial dead layer investigations. However, whist the method is sound, when applying it to the count rate against energy power spectrums the results are far from conclusive.

Regardless of the dead layer applied to the data, only the very early data is in any way statistically significant. This means the initial estimation of dead layer is either incorrect, or that there is more going on in the new data set than meets the eye.

The changes made by a dead layer are only seen in the energy axis rather than the overall count rates, this would appear as an anticlockwise rotation of the locus or a flattening of the power law. With the count rate data, as the energy is fixed based on channel, the expected result is that the low energy counts would drop further than the high energy ones which would appear as the same rotation as expected from an energy movement.

Instead, the chi-squared shows a grouping of significance in the early data. As the years of the mission increase, the farther the data appears to move from the dead layer estimations. Trying to fit this to a dead layer with additional at 0.5 μm thickness to show the same trends and very little improvement in the Chi-squared values. This dead layer did not fit to any of the count rate data, leading to the belief that this method is not suitable for this

data set. To investigate further, Figure 3.3- shows the plotted values of each of the data sets in the comparison; the reasons for the clumping of significance are clear.

Chi2	1996	1997	1998	1999	2000	2001	2002	2003
Dead Layer 0.02 µm	0.0002	0.0026	0.0148	0.0452	0.1019	0.2331	0.6598	1.6267
Dead Layer 0.04 µm	0.0007	0.0016	0.0118	0.0389	0.0913	0.2139	0.6129	1.5582
Dead Layer 0.06 µm	0.0018	0.0012	0.0094	0.0334	0.0818	0.1959	0.5673	1.5034
Dead Layer 0.08 µm	0.0031	0.0014	0.0080	0.0295	0.0746	0.1821	0.5315	1.4629
Dead Layer 0.1 µm	0.0048	0.0018	0.0066	0.0253	0.0667	0.1665	0.4921	1.4014
Dead Layer 0.12 µm	0.0069	0.0026	0.0058	0.0218	0.0598	0.1526	0.4560	1.3445
Dead Layer 0.14 µm	0.0091	0.0038	0.0056	0.0193	0.0543	0.1410	0.4249	1.2964
Dead Layer 0.16 µm	0.0116	0.0053	0.0056	0.0172	0.0492	0.1300	0.3958	1.2449
Dead Layer 0.18 µm	0.0141	0.0067	0.0055	0.0148	0.0436	0.1181	0.3663	1.1698
Dead Layer 0.2 µm	0.0167	0.0086	0.0065	0.0144	0.0415	0.1125	0.3505	1.1461

Table 3.3-1: shows the chi-squared values from the comparison. The best matches for each year identify a far higher dead layer than expected from the results of the same comparison of the PHA plots.

Over the yearly intervals in Figure 3.3-, the red lines plotted in descending order of year with 1996 the highest values and 2002 as the lowest red line, the count rates are dropping. Figure 3.3-4 better illustrates this by separating the colour of each year. When compared to the simulated dead layer the values are dropping far too much to be comparable to any of the dead layers. Instead, it is more likely that there is a drop in the counts recorded as well as a dead layer being present. By taking the 1996 data as the calibration set again, the efficiency drop is simulated and shown in Figure 3.3-4.

Now instead of using a dead layer against yearly data comparison, the comparison instead is of efficiency drop against yearly data. The same process is used the Chi-squared results can be analysed in the same way.

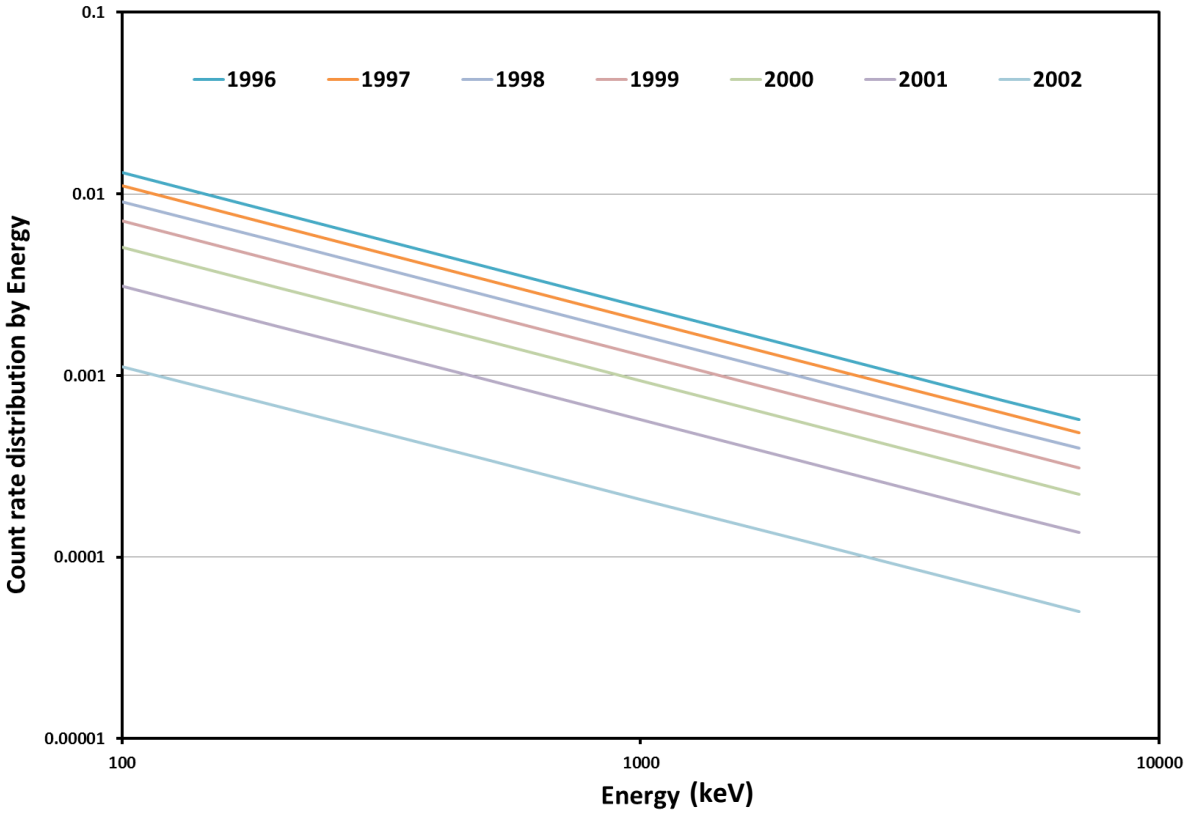

Figure 3.3-4: Plot of the yearly changes in the count rates against energy. The yearly changes are averaged over the whole mission to see the general trends in the data that would otherwise be masked by peaks in the data cause by orbit manoeuvres.

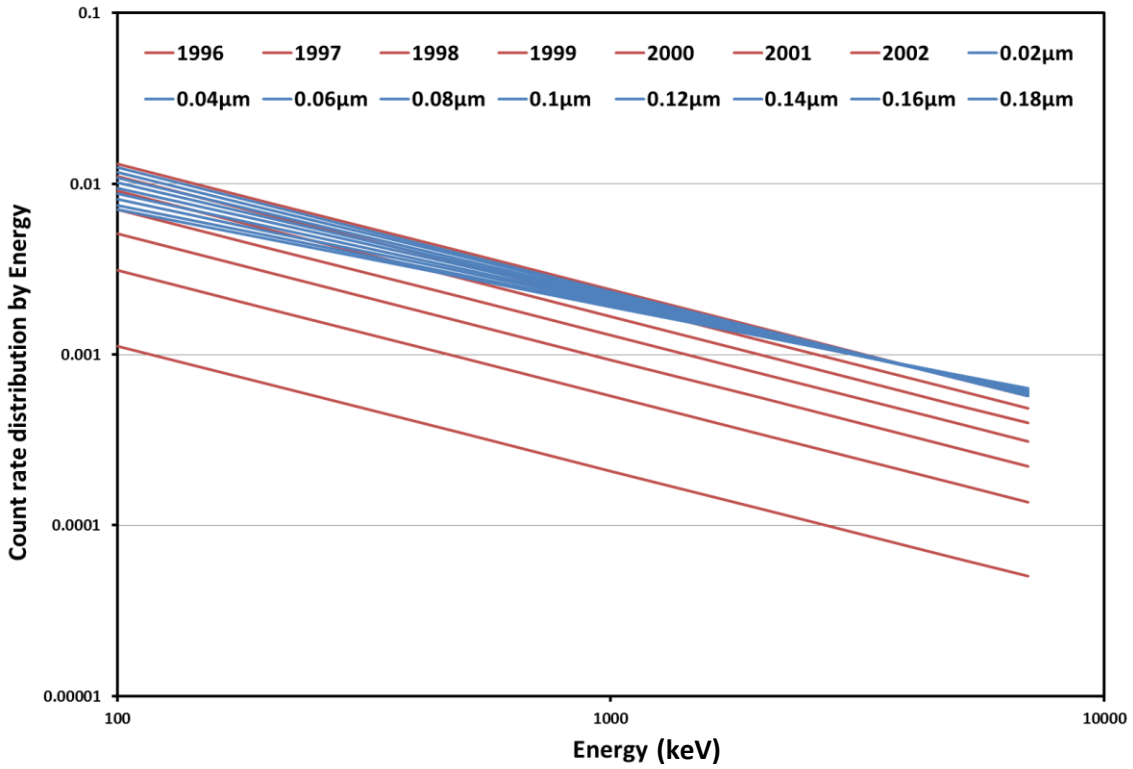

Figure 3.3-5: plot of the Values being compared in the Chi squared test. The Blue lines represent the 1996 data with simulated dead layers applied. The Red lines are the yearly data values for count rates assuming an even distribution in energy over the channel boundaries.

	1996	1997	1998	1999	2000	2001	2002
1996/ Calibration	0	0.000824	0.00403	0.011627	0.028786	0.07336	0.291134
95%	7.45E-05	0.000374	0.002822	0.009236	0.024283	0.064086	0.260269
90%	0.0003	9.82E-05	0.001824	0.007109	0.020142	0.055395	0.230988
85%	0.000675	2.34E-07	0.001043	0.005261	0.016388	0.047338	0.203453
80%	0.001202	8E-05	0.000479	0.00369	0.013021	0.039913	0.177665
75%	0.001879	0.000337	0.000132	0.002397	0.01004	0.033122	0.153624
70%	0.002706	0.000773	1.14E-06	0.001382	0.007447	0.026963	0.13133
65%	0.003679	0.001382	8.63E-05	0.000648	0.00525	0.021464	0.110884
60%	0.004807	0.002171	0.000388	0.000187	0.003428	0.016568	0.092075
55%	0.006086	0.003139	0.000907	3.51E-06	0.001993	0.012305	0.075012
50%	0.007515	0.004284	0.001642	9.83E-05	0.000945	0.008674	0.059697
45%	0.009095	0.005607	0.002594	0.000471	0.000283	0.005677	0.046129
40%	0.010816	0.007099	0.003756	0.001117	8.97E-06	0.003323	0.034363
35%	0.012697	0.008776	0.005141	0.002044	0.000119	0.001589	0.02428
30%	0.014728	0.010631	0.006742	0.003249	0.000616	0.000487	0.015943
25%	0.016909	0.012664	0.00856	0.004731	0.0015	1.83E-05	0.009353
20%	0.019241	0.014874	0.010595	0.006492	0.00277	0.000183	0.00451
15%	0.021724	0.017263	0.012847	0.00853	0.004428	0.00098	0.001414
10%	0.024344	0.019815	0.015302	0.010833	0.00646	0.002401	6.73E-05

Table 3.3-2: Table of chi-squared fits for 1996 data with simulated efficiency drop compared with the yearly data sets. The bordered boxes denote the best fit of efficiency drop for the year in question. The shaded boxes are the best fit year for each efficiency drop.

Table 3.3-2 contains the chi-squared results for the comparison of efficiency against the yearly data sets. There is a strong correlation with the increase in years and the drop in the efficiency. Due to the plotting routines used in Figure 2.3-3 and the differences in the

type of data used to make each plot, this drop in efficiency is only visible when looking only at the count rates.

This table consists of data from Sulphur channels; the same results are true when done for the other three elements. This drop in efficiency is most likely due to the start and stop MCP detectors (Figure 2.2-1); it is consistent over the other elements. Each count in a channel will only register if there are three positive signals. These come from the start MCP as the particle enters the time of flight chamber, the stop MCP as the particle leaves the time of flight chamber and the final signal as an energy measurement from the end detector. If the MCP detectors are also decaying over the mission, then there will be a drop in efficiency.

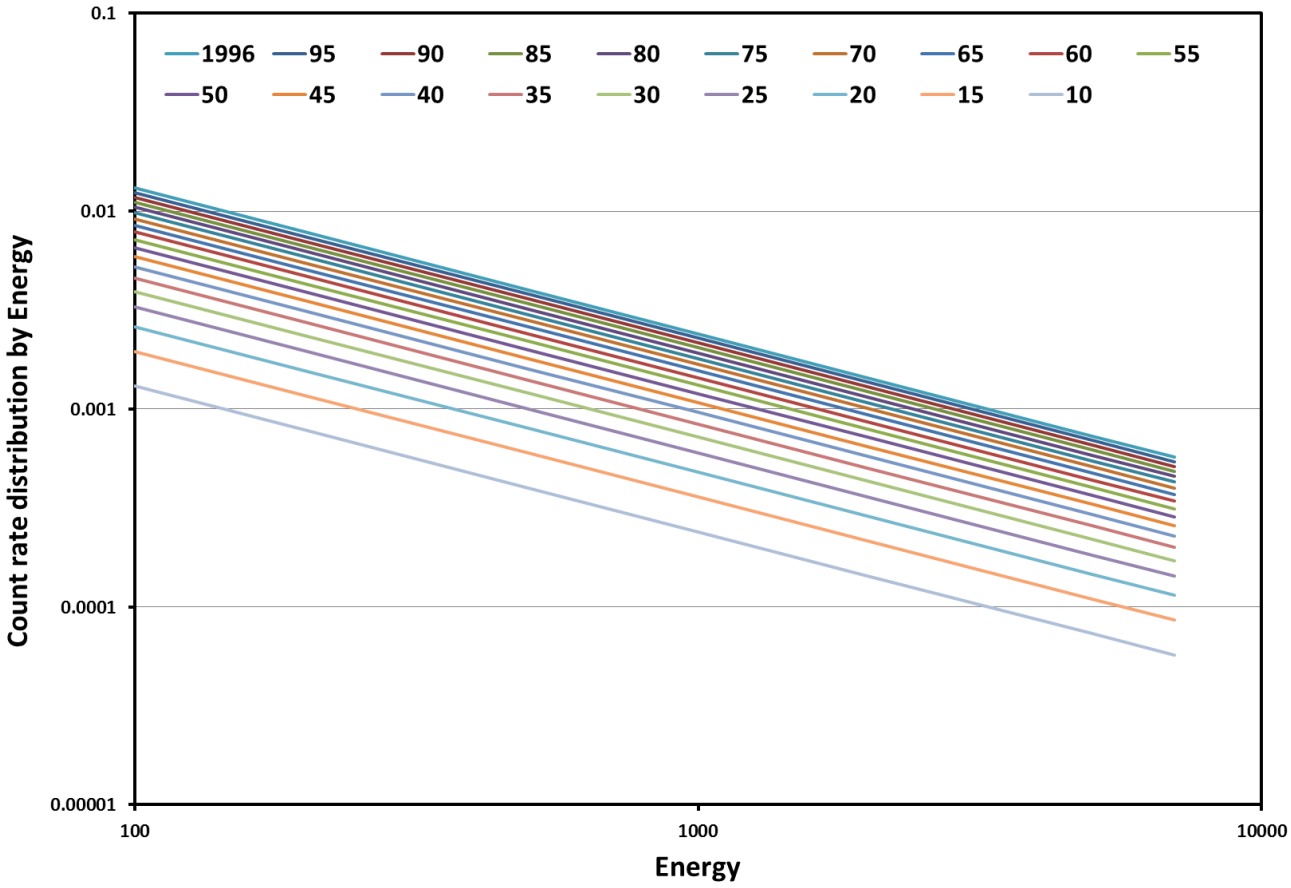

Figure 3.3-4: 1996 original data with a simulated efficiency drop added. After 1996 the values denoting each line are the percentage value of 1996 counts present, where 1996 is 100% of the counts.

Over the mission it is likely that the sensitivity of the MCPs were increased remotely by increasing the gain on the detectors. The gain can only be adjusted so much, as such this is a common problem with using MCPs for longer missions. An issue associated with

increasing the gain in any instrument is that it cannot then be effectively calibrated. In this case even with the gain increase there is still a drop in particles being measured, i.e. the gain hasn't been increased enough. The gain increases can be seen periodically in the data; looking at Figure 3.3-1, each main peak corresponds to a perijove of the orbit, when comparing the peaks there is an increase in the peak height after orbit 7. This is likely an increase in the gains of the detectors to account for dead layers and other degradation.

These gain increases haven't impacted on the correction process, primarily because they were not as effective as hoped and the overall trend is still towards a drop in count rates. Because of this they have not been accounted for, however in future work it would be an interesting exercise to find the precise dates and scales of these system adjustments and compare them to the data.

The drop in data can be seen over all the channel elements (shown in Figure 3.3-5); the consistency across all the channels confirms there is a system wide problem such as that caused by the MCPs not reliably identifying the start and stop signals. This overall efficiency drop needs to be included into the correction. This is the missing piece for the correction to get reliably corrected data.

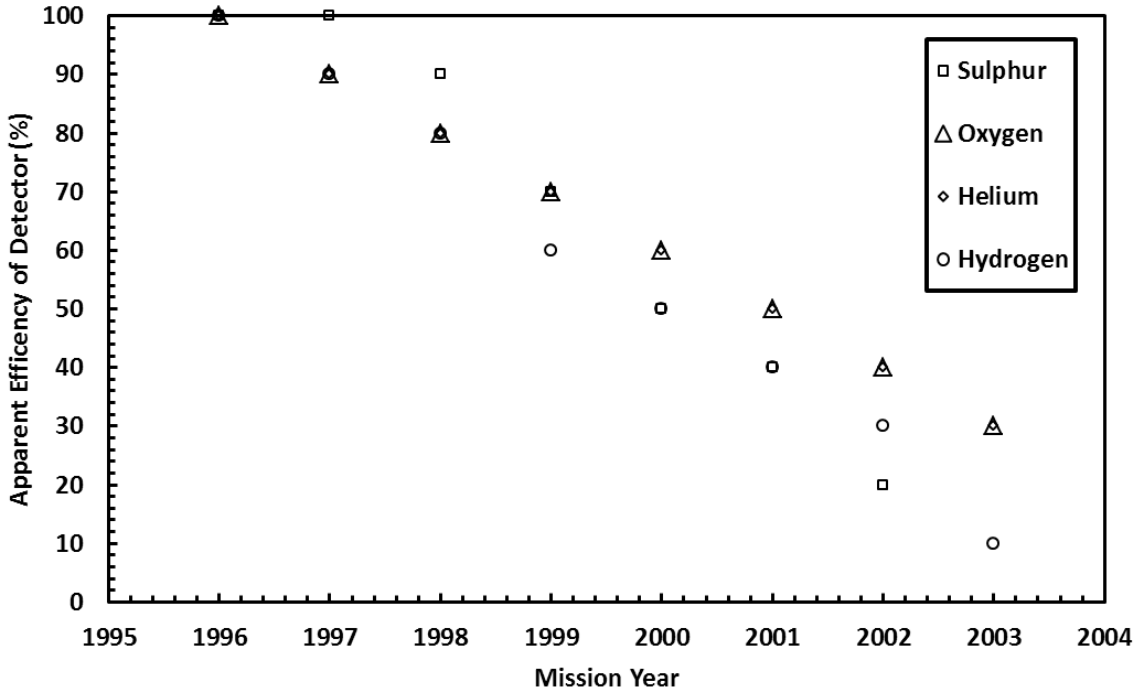

Figure 3.3-5: Efficiency drop over mission years by element

3.3.4 Code upgrades

Adding the efficiency drop to the coded correction method is in fact simpler than expected. Using the methodology from above and the theory behind the decisions, there is an already added factor that constrains the correction to stop it from increasing exponentially. This is the value of 100 talked about earlier.

From section 3.2.3 the formula of the correction method sits as in equation (24), the factor of 100 present in the formula is the constraining value. The values of efficiency vary from 100 to 10. At the beginning of the mission the factor of 100 (from now on referred to as Eff as in equation (25)) limits the correction so only a small amount of the contribution from added counts is added i.e. a lot of the counts are being picked up already. This corresponds to the beginning of mission high efficiency in the system, with very few counts being missed. At the end of the mission, the correction alone is not accounting for all the missed particles, lowering the Eff values increases the contribution of correction from the additional particles. This matches well with the lowering of efficiency in the system.

$$j_n = j_n\left(1 + \frac{\Delta J}{J} + \frac{\Delta J^2 n}{100J}\right) \tag{24}$$

$$j_n = j_n\left(1 + \frac{\Delta J}{J} + \frac{\Delta J^2 n}{(Eff)J}\right) \tag{25}$$

Implementing this is straightforward. The trend of efficiency in all the channels is linear, making the progression through time very simple to tie to the timestamps of the data set. From initial tests on the major channels, this addition appears to fix the major problems with the overall code whist still allowing the fluctuations in the data to stand out and rather than the added correction swamping the data. This addition to the correction does not translate to all the channels perfectly. The TH1 channel for example, the efficiency drop is not testable and whilst it is reasonable to assume that it would comply with the rest of the data; the size and breadth of the channel make it hard to use. In this case, as the use of the channel for the rest of the study is very limited the channel remains as it was from the original correction. The data has been corrected; however, it is very hard to test the effectiveness of this.

Following are the newly generated data sets with the efficiency included, re-tested using the same method as the channel sets in the original data. Figure 3.3-6 shows the corrected count rates displayed in the same way as the previous data set. The grouping of the yearly values is a significant improvement from the original data.

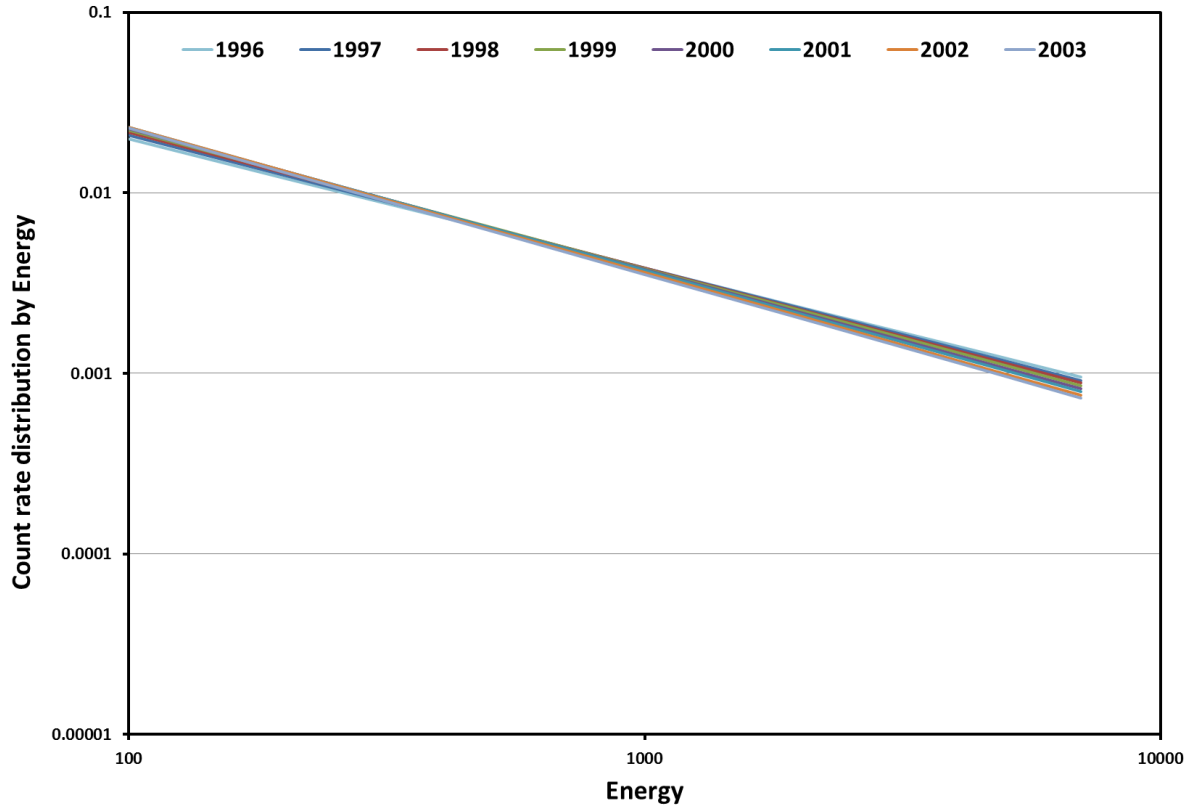

Figure 3.3-6: Corrected data plotted in the same manner as above; assuming the counts of a channel are evenly distributed across the whole of the energy bounds of the channel.

The data also shows a significant improvement when compared to the original data using the Chi-squared method from above, however there is some disparity in how it is compared to the original 1996 calibration data and so does not match as well as expected in the first year. This is a shortcoming of having to use the 1996 data as the calibration data rather than using a true calibration number, and may have affected the accuracy of the correction in the first few years. Considering the 1996 as calibration data, it forces the assumption that the efficiency and the dead layer are at zero in 1996.

Table 3.3-3 shows the results of re-applying the Chi-squared method to the data to show how improved it is against the original untouched data. The far higher grouping towards the zero dead layer, shows significant improvements to the set, and from looking at the Comparison of the sulphur the counts against energy in Figure 3.3-6, it is clearly not an issue with the data being spread away from the calibration.

Chi2	1996	1997	1998	1999	2000	2001	2002	2003
Dead Layer 0.02 µm	0.029	0.020	0.015	0.012	0.011	0.012	0.016	0.022
Dead Layer 0.04 µm	0.026	0.019	0.015	0.013	0.013	0.014	0.018	0.025
Dead Layer 0.06 µm	0.024	0.018	0.015	0.014	0.015	0.017	0.021	0.029
Dead Layer 0.08 µm	0.022	0.018	0.016	0.015	0.017	0.020	0.024	0.032
Dead Layer 0.1 µm	0.021	0.018	0.017	0.017	0.019	0.022	0.028	0.036
Dead Layer 0.12 µm	0.021	0.018	0.018	0.019	0.021	0.025	0.031	0.040
Dead Layer 0.14 µm	0.021	0.019	0.019	0.021	0.024	0.028	0.034	0.043
Dead Layer 0.16 µm	0.021	0.020	0.021	0.023	0.027	0.031	0.038	0.047
Dead Layer 0.18 µm	0.021	0.021	0.023	0.025	0.029	0.034	0.040	0.050
Dead Layer 0.2 µm	0.022	0.022	0.024	0.027	0.031	0.037	0.044	0.054

Table 3.3-3: Chi-squared results from the final correction of the count data. The bordered boxes mark the best fit of the data for each year. This is a little distant in the yearly mission years however this can be attributed to the use of 1996 (untouched data) as the calibration set.

The higher dad layer readings from 1996 to 1998 are from using 1996 data as the calibration. The corrected version will have been changed in a small way so it appears more different than it should be. By looking at the values themselves, all of the years are in a very close spread of values; different only to 4 significant figures.

3.4 Final Corrected Count Rates

The following section showcases the final corrected results of the correction and begins to outline the uses for them. Overall, again some of the channels are better corrected than others, the successes and shortcomings of each channel are with each set of results.

3.4.1 TH1: Iron and 'Heavy' Particles

This is the most problematic of the channels, any of the techniques used on the other channels could not be used on this channel. The very large range of the channel in energy and the vast range of masses expected to be caught in this channel mean there are many unstructured readings in here.

The singular nature of this channel meant that plots such as counts against energy couldn't be generated, the efficiency analysis was therefore also limited, and of course checking the overall mission consistency of the channel is considerably harder. The dead layer is impossible to check in this channel, the energy movement cannot be quantified using a single energy to a single channel count.

All things considered this channel is the worst-off. There is very little to be done further than the original correction, and thus it has been left to only the alterations made by the original correction as shown in Figure 3.2-4.

3.4.2 TS1, TS2, TS3: Sulphur

The three sulphur channels are the best of the correction. The positioning of the channel and the close confines of the counts within them make it ideal for the correction to function the best it can. The sulphur channels suffer only loss of counts to the channels below and to the efficiency drops, this reduces the confusion of trying to balance out the gains and losses that other channels must contend with. The three in line channels allow the creation of the simple power spectrum, allowing the overall changes in the channel to be well tracked over the mission, whilst also allowing for dead layer calculations.

TS1 (Figure 3.4-1) contains the highest of the sulphur counts. In comparison to both the original and the first correction the sulphur channel now contains far higher counts in

the later years of the mission. Especially in 2003 the data seems to be overly high, but using the increase in count with the reduction in distance from Jupiter, these high values are not out of place. In the very close orbits of 2003 the data does drop in counts. This section of the data is the final decent into Jupiter and it is expected to both cut out reasonably far away and to be very anomalous data; this drop is most likely an artefact of the descent.

Also in comparison to the original data the increase in counts towards Jupiter matches well with the expected trend. In the original plot the early year data can be seen to have a very similar trend upwards which is cut off by the conservative orbits of the early mission. As the original data progresses forward in time this trend drops away leaving only very low counts. The correction matching these trends in the later years gives a good indication of how well the correction is functioning, even if for a simple case.

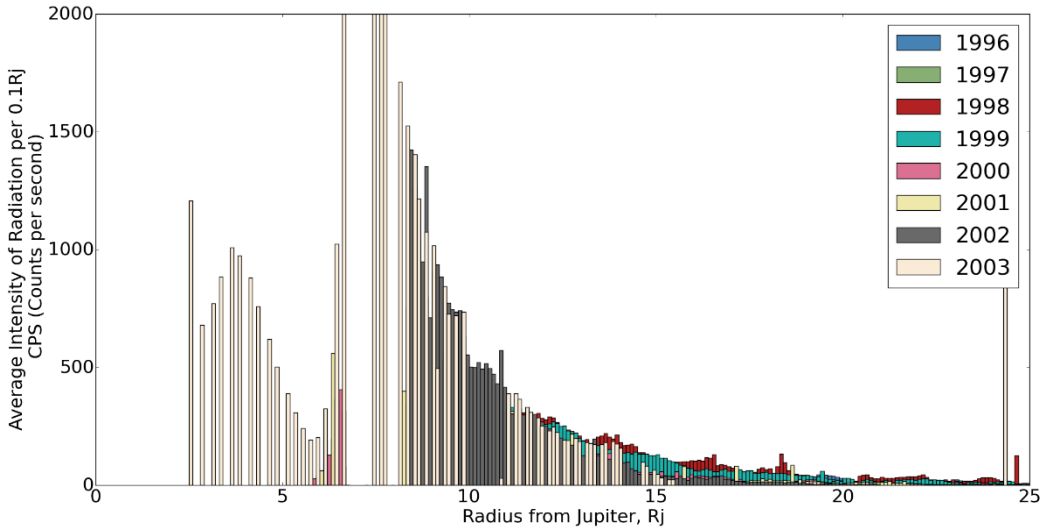

Figure 3.4-1: Final correction of TS1 channel.

TS2 (Figure 3.4-2) is the next in the line of the sulphur channels. The correction of this channel falls a little short in the final years of the mission, from 1999 and onward there is still some of the earlier years visibly higher in count rate behind the more recent data. This can be attributed to the way the CV (correction values from section 2.5.1) are grouped over the full element. The grouping crosses the boundary of the priority system built into the detector, whilst this is most significant in the time of flight PHA graphs it is still possible that the counts have been in some way affected by the choice of channels in each priority. A way to combat this in future would be to use each of the channels completely individually to compute the CV, thus eliminating the slightly lower value for correction.

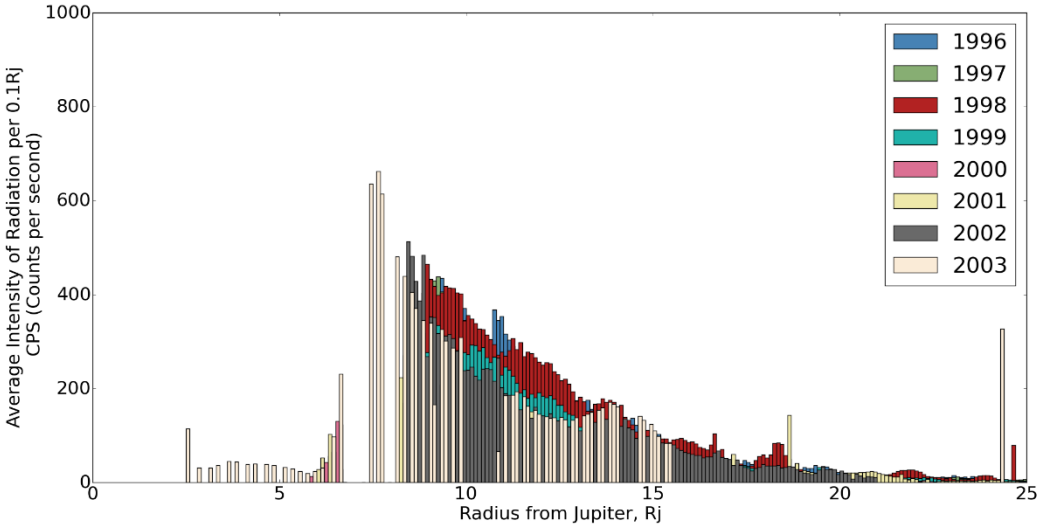

Figure 3.4-2: Final correction of TS2 channel.

Aside from this, the correction is still a vast improvement over the original data. Many of the comments made for TS1 can be made as well for this channel. Overall the count rates are highly improved for this channel.

TS3 (Figure 3.4-3) also contains very high count-rates compared to TS2. This is most likely again due to the priority system and the grouping of the correction value used. When looking at the original data the counts for sulphur do increase with energy and thus TS3 is expected to be quite high in counts. The consistency in the count rates over the mission years is very high in this channel the corrected data for later years matching against the early.

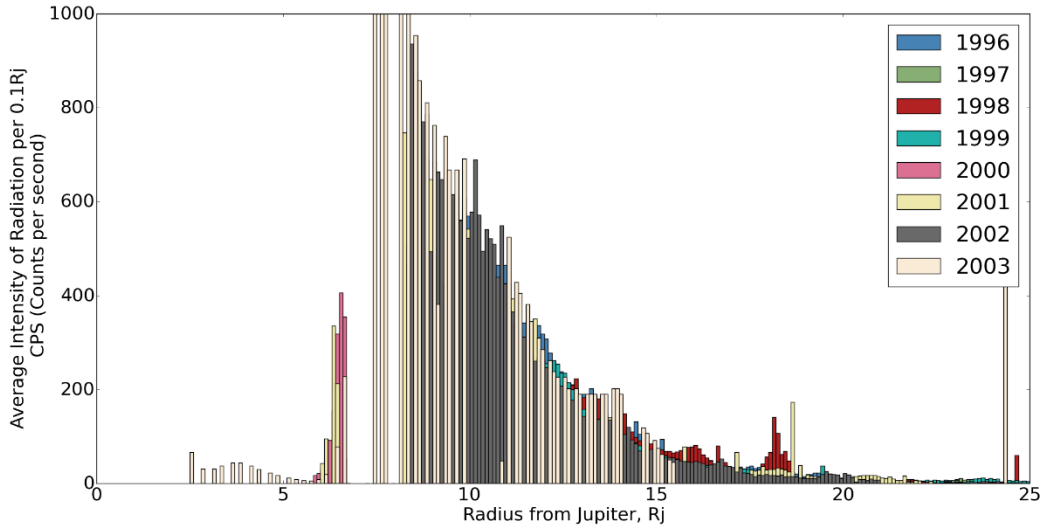

Figure 3.4-3: Final correction of TS3 channel

Overall the only issues with the Sulphur channels are the priority system and how TS1 being in a higher priority rightly contains more counts than looks feasible. In the original data, this would have been a problem regardless, and is something that can be solved by fitting over the data and distributing counts per the priority system. This is likely to be a recurring theme in the data sets.

3.4.3 TO1, TO2, TO3, TO4: Oxygen

The oxygen channels proved by far to be the most complex, to apply the correction method to. Not only did the channel lose particles to the channels beneath, it also gained significantly more from the sulphur channels above.

The Oxygen channels are split between TO1 and the rest, this stems from the formation of the channel boundaries. TO1 spans the full Time of flight range as both the rest of the oxygen and sulphur channels (Figure 3.2-3 shows the formation of the channels). The counts from this channel covered both oxygen and sulphur, meaning over all it could be treated in much the same way as the sulphur channels but with far less loss from the lower boundary of the channel.

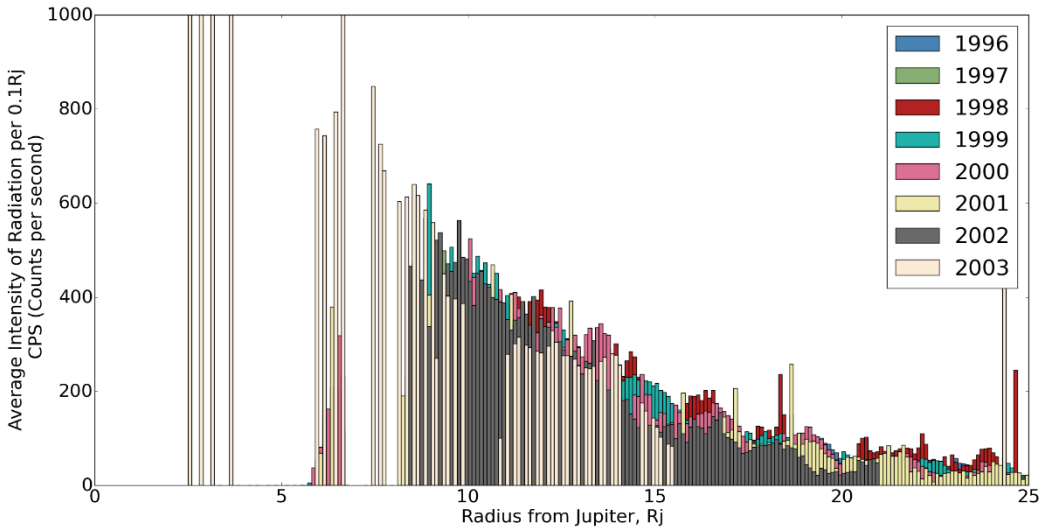

Figure 3.4-4: Final correction of TO1 channel

Considering the final corrected data set, the values haven't altered much at all. This is somewhat expected as there was very little bulk movement in the channel to correct for. The main issue corrected is overpopulation in the final years of the mission. The majority of this is due more to the "sideways" movement of particles from TS1 and TO2.

TO2 (Figure 3.4-5) is the first of the pure oxygen channels. The initial counts in the final years of the mission again over-counted the oxygen. The presence of the TS1 channel above is the primary source of these counts. In the first iteration of the correction to the overall count rate was too drastically lowered. The cause of this was the additional efficiency from the sulphur channels. Whilst the values in the sulphur channel accounted for the loss of efficiency, the particles being mis-registered in the oxygen channel would also have to account for the particles lost to the efficiency drop.

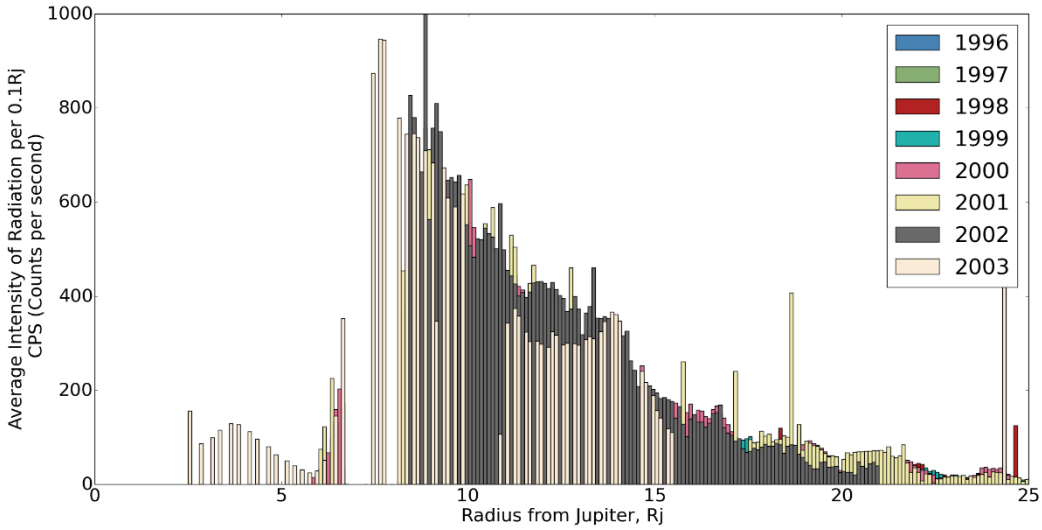

Figure 3.4-5: Final correction of TO2 channel

The correction method including the additional efficiency wasn't as effective for rest of the oxygen channels; where the first iteration took too many particles, this iteration added particles. This is a fault of the correction where there are particles moving between the channels; the correction cannot account for what it cannot see. In this case the efficiency drops in the counts coming from the sulphur channel. The solution to this is to consider the difference in sulphur channel before and after the correction considered the efficiency drop. The difference in counts is the amount of counts purely from the efficiency drop. A large portion of these are what is being lost to the oxygen channel, and thus can be removed from the oxygen channel.

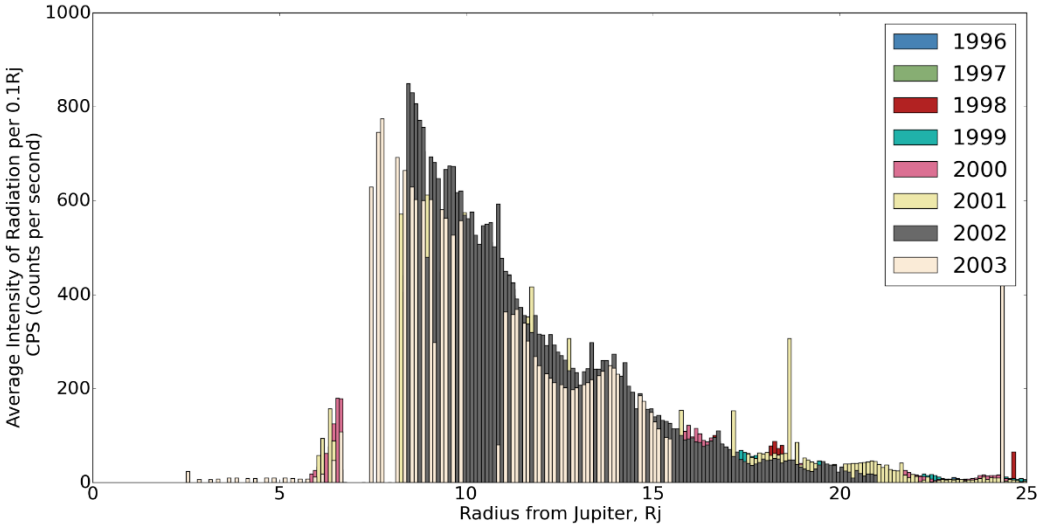

Figure 3.4-7: Final correction of TO3 channel

Channel TO3 (Figure 3.4-7), was treated in the same way as TO2. The final correction was again too high and needed the removal of the additional sulphur particles. The final values are an improvement over the initial correction, which had similarly removed far too many of the values. This trend of removing too many values spans the three main oxygen channels and is caused by initially not accounting for the efficiency. In doing so, the correction process sees there is an increase in the oxygen counts, thus lowering the counts during correction. This doesn't account for the overall drop in counts as they fall into the TA channels or the drop in efficiency. Thus, the correction affects the data too much.

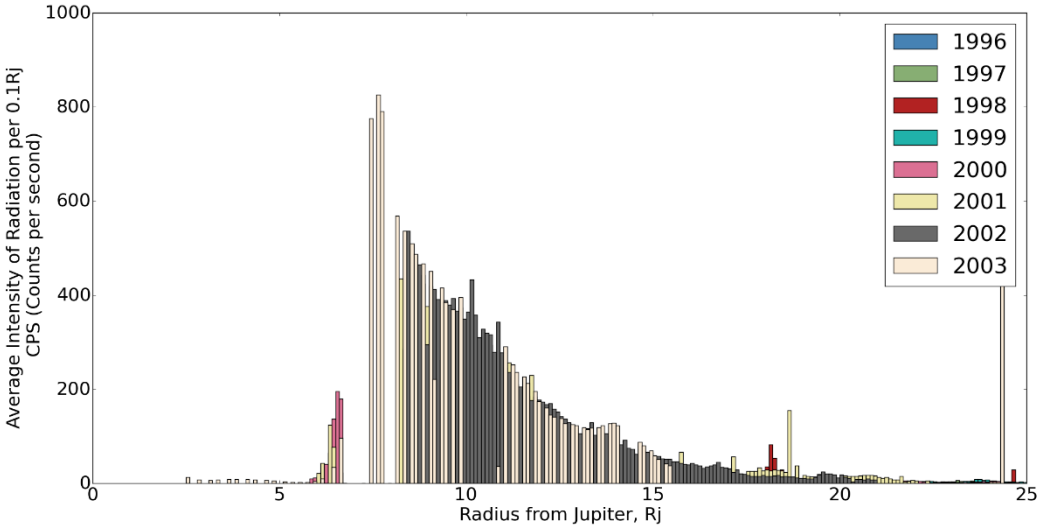

Figure 3.4-6: Final correction of TO4 channel

The same is seen in TO4 when comparing the first and final versions of the correction (Figure 3.4-6 and Figure 3.2-10).

3.4.4 TA1, TA2: Helium

The helium channels were the lowest counts recorded during the mission, and they also offered the most challenge in correcting. Much like the TH1 channel the lack of data points make making power law comparisons far harder, and far more prone to errant values. With the rest of the channels, with three or more channels per element, with one errant value there are still two others to base the power law off, making these anomalies easier to spot. This is not the case with the helium channels.

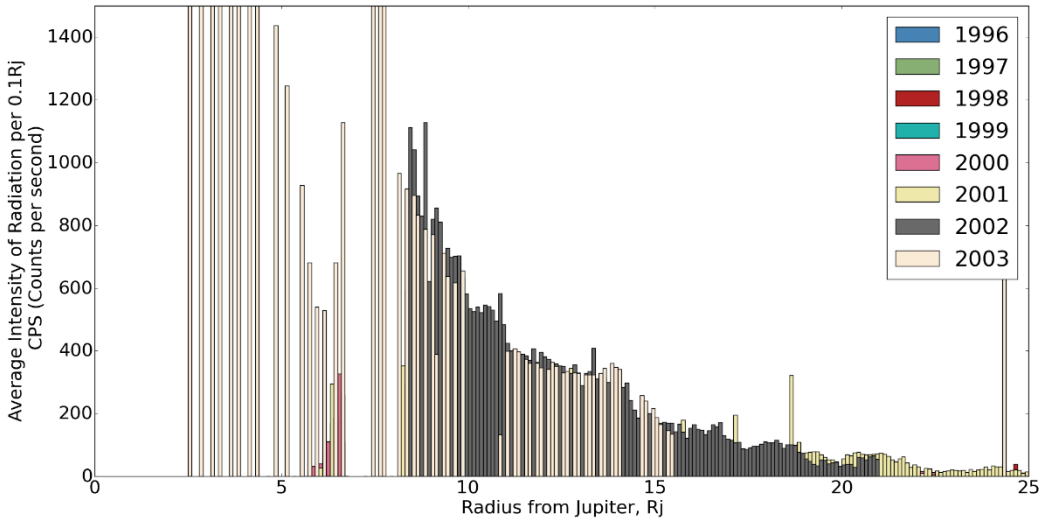

Figure 3.4-8: Final correction of TA1 channel

The process is still the same as with the other channels, in this case the number of particles slipping from the oxygen channel were not significant enough to warrant the addition of these values to the final result as was done for the Oxygen channels. Figure 3.4-8 shows the final correction of the first helium channel. The early years of the mission are not easily visible behind the later years, this is due in part to the difficulties in assessing the power laws of the helium and correctly accounting for all the factors affecting these channels. TA2 also suffers from this, as seen in Figure 3.4-9. In general, the counts for helium were very low to begin with, this is something that can be seen in section 3.2.5 and the high rate PHA plots (section 2.3). In all cases the loci defining the helium is low, thus it is

likely to be a low constituent of the environment, or found predominantly in areas that Galileo did not visit.

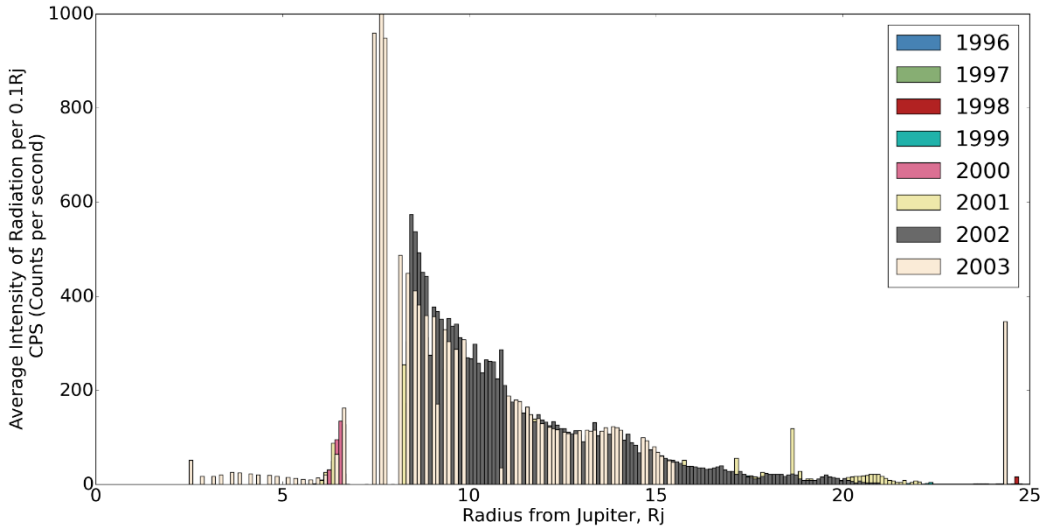

Figure 3.4-9: Final correction of TA2 channel

3.4.5 TP1, TP2, TP3: Hydrogen

The final channels corrected count the single protons in the Jovian System. Overall there was very little needing to be corrected about the TP channels. The very light mass means the particles deposit far less energy into the dead layer as they pass through. This is seen in the initial data, the CV and the efficiency correction. Each channel sits at the lower boundary of the instrument, the channels are not losing counts to a lower channel; this leaves the main cause of loss to be the drop in overall efficiency.

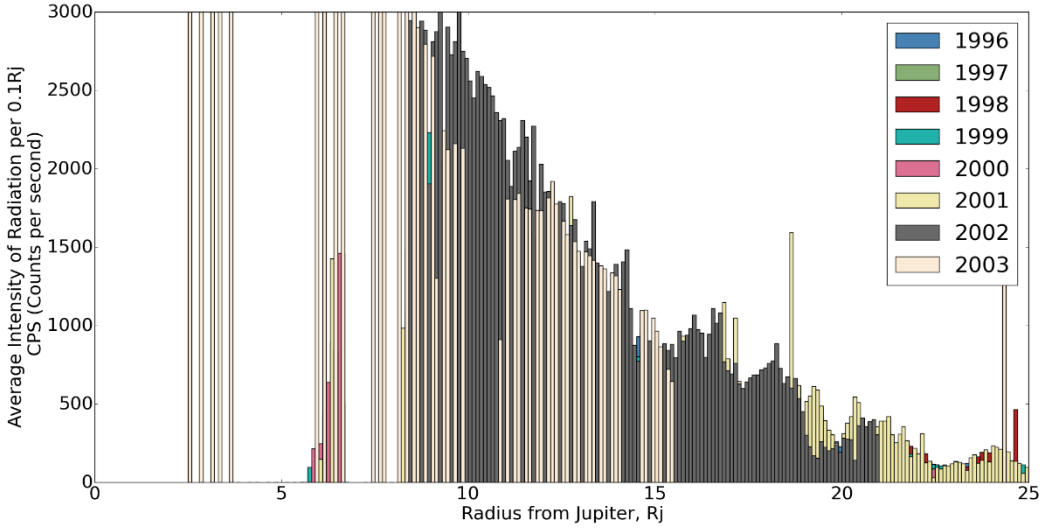

Figure 3.4-10: Final correction of TP1 channel

The count rates for these channels are now very high in comparison to the original, this is a good match for the expected ratios of particles; as will be investigated later in this chapter.

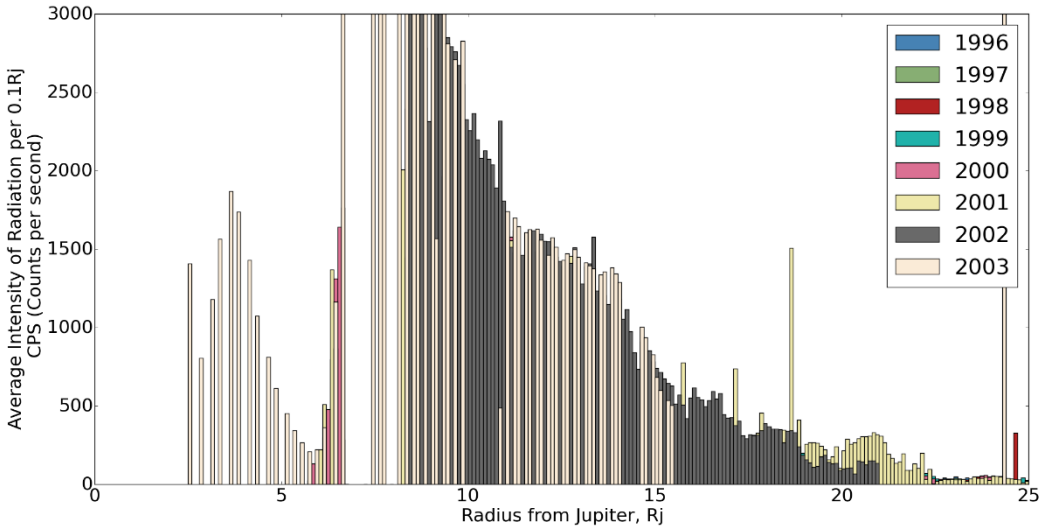

Figure 3.4-11: Final correction of TP2 channel

Figure 3.4-10 and Figure 3.4-11 show the first two proton channels, TP1 and TP2. These values are almost double the original counts of the channel, as is the same with all the TP channels. The increase from year to year of the counts is still consistent. Counts from 1996 and 2000 can be seen behind the later years, despite the initial evaluation that the TP channels would not need much correcting. The initial evaluation determines there would be

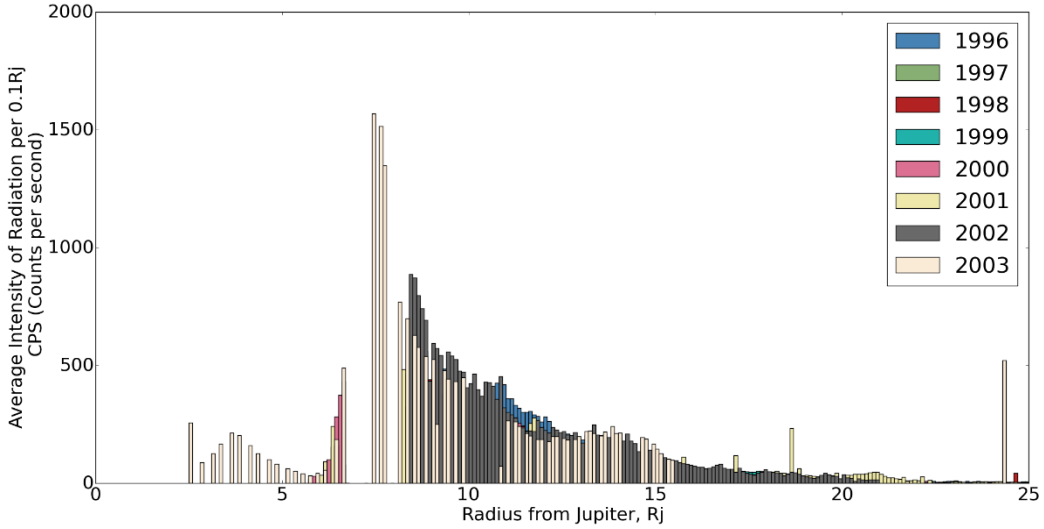

Figure 3.4-12: Final correction of TP3 channel

very little of the counts lost to the increasing dead layer and this is still true, however, now the count loss is correctly attributed to the efficiency.

The final channel is shown in Figure 3.4-12 of TP3. Contrary to the previous channels TP1 and TP2, this contains far fewer counts. This is due to the nature of the detector. Particles at the upper end of the energies expected in this channel, are not fully measured. The protons have such a high energy and low mass they have enough velocity to fully penetrate the depth of the detector. When this occurs the particle still deposits some energy in the detector so a count is registered, however the energy deposited will be less than if the particle had stopped inside of the detector. This effect is the main source of error in the correction of the PHA plots as described in section 2.6. The results of this effect can also be seen in the PHA plots; Figure 2.6-2, along the proton element track, at a point very close to the boundary between TP2 and TP3, the track appears to turn around and lie at a tangent to the expected path. This turning can also be seen in the instrument calibration diagrams, Figure 2.2-2, the expected track of protons and helium turn in the higher energies. This effect is described in section 2.4.5.1, in relation to the thickness of the dead layer and changes of this turning point.

3.5 Comparison to Voyager Data

The correction of the Galileo data is entirely based on the data itself. This internal self-consistency for the correction meant there were no external sources of error in the correction. However, the correction can only be as good as the input data.

This can be limiting in making sure the correction is accurate and hasn't wildly changed the data far from the original limits and expectancies. The only way to test this is to compare the corrected data, to both the original Galileo data and to an external source of similar data. Jupiter has had a few visits so far, more than any of the other giants. The highly analysed data set of the two flybys of Voyager One and Two make its data sets the perfect candidates for a comparison to the EPDs correction.

3.5.1 Major comparisons in the literature:

With the advances made by the Galileo satellite, and the new influx of data, since insertion into the Jovian system many comparisons have been made with Voyager data sets. Until the arrival of Galileo at Jupiter, the two Voyager satellites were the most recent and well-equipped craft to have taken measurements within the radiation zone. Whilst they rapidly enhanced the understanding of the Jovian system at the time, the data they provided was only a snapshot in comparison to the extended data that Galileo sent back.

The data from voyager has been highly analysed, during the mission and for many years following (Ness, 1992). Both Voyager missions carried a Plasma Science Instrument (PSI), each in turn taking data during its respective flyby of many aspects of the Jovian plasma (Bagenal et al., 2017, Bridge et al., 1977). The whole of the data sets from the Voyagers during their flybys, have been recently extensively re-analysed (Bagenal et al., 2017, Bodisch et al., 2017, Dougherty et al., 2017). Unfortunately, this analysis is so recent that it was not available during the final stages of the EPD correction and thus can only be referred to in passing.

Instead, Radioti et al. (2005) describe a complete comparison of the Voyager and Galileo EPD data; focusing on the specific ratios of Oxygen, Sulphur, Helium and Hydrogen. During the introduction they also include comparison data of all measurements taking in the Jovian system for completeness. The study is split into two halves: the first a comparison of

the PHA data, high resolution data against the Voyager observed ion energy spectra. The second half used the real-time count rates and compares the abundance ratios of the first 15 Galileo orbits to the ratios recorded by Voyager. This second half can be directly applied to the corrected count rates correction; providing both a comparison to the original EPD data and the Voyager data in one go.

3.5.2 Preparing the data

In the paper Radioti et al., (2005), they use 4 specific ratios for the overall data comparison. These are selected to cover the masses and energies measured by both instruments as best as possible. The ratios used are shown in Table 3.5-1 along with the specific energy used for each ratio. The energy bands are in KeV/nuc; this is energy of the element by the number of nucleons it is made up of. This unit is widely used as it makes clear comparisons of the amount of energy a particle had by mass rather than individually.

Ratio	Specific Energy per nucleon (KeV/nuc)
S/O	39
S/He	68
O/He	89
p/He	185
All	800

Table 3.5-1: Relative abundance ratios at specific energy per nucleon used for comparison.

Converting the count rates of each channel into these specific values is relatively straightforward and can be achieved by using the power law for each element. From the power law the specific values can then be found using logarithm laws, picking out the required energy per nucleon for each element. Table 3.5-2 gives the energy for each required specific energy. This is very simply the Specific Energy per Nuc, multiplied by the number of nucleons in the element.

The power spectra used for calculating the counts at each energy are those used in section 3.3.1. The count rates are evaluated at the energy at the centre of each channel box, with the power law being generated from there. A power law evaluating the counts at different energies is simply then calculated using the equation of the line in log space.

The values of the count rates aren't perfect; this is a draw-back of the channel count rates that there are only two to four data points available for each element. In the published comparison they make no mention of how they have dealt with this. A way to get around

Element	Specific Energy (KeV/Nuc)	Measured Energy (KeV)
S	39	1248
	68	2848
	800	25600
O	39	624
	89	1424
	800	12800
He	68	272
	89	356
	185	740
	800	3200
p	185	370
	800	1600

Table 3.5-2: Specific Energy per Nucleon converted to Kev for each element.

this problem is to use averages of the PHA data for each element over the energy range and map the distributions found onto the count rates. However, these values from the High rate PHA plots are only taken during the flyby events, which may affect the distributions of the elements. Mapping the count rates to the distributions is also complicated enough without having to adjust for flyby activity.

With both axes of the power law in log-space the formula for working out the count rate at a given energy is calculated as follows, where R is the count rate and E is the Energy (Note: this is not the Specific energy per nucleon, but the measured energy calculated in Table 3.5-2).

$$\ln R = M \times \ln E + C \tag{26}$$

Where M is the gradient of a straight line. If the values of count rate and energy are already logged values, the basic equations of a straight line can be applied. The same is true of, C, the constant or the crossing point of the y axis. The equations for each are described as follows:

$$M = \frac{\overline{xy} - \bar{x}\bar{y}}{\overline{x^2} - \bar{x}^2} \tag{27}$$

$$C = \bar{y} - M\bar{x} \tag{28}$$

The equation to calculate the count rate at any energy can be simplified to the equation below:

$$e^{\ln R} = e^{(\ln E^M + C)} \tag{29}$$

$$R = E^M \times e^C \tag{30}$$

This equation allows the count rate at any energy to be calculated from the power law. However, when using the count rate power law, the values extracted are the exact value at that point. This isn't very useful as at the very high energies as the power law determines the value will be very close to the smallest limit. Instead when using power law values the convention is to use an integral power law, or the summation of each rate previous. This can be calculated by integrating equation (30).

$$\int_{Intercept}^{Count\ Rate} y\, dE = \int_{0}^{R} e^C E^M\, dE \tag{31}$$

$$\int_{0}^{R} y\, dE = e^C \int_{0}^{R} E^M\, dE \tag{32}$$

$$\int_{0}^{R} y\, dE = \left[\frac{e^C E^{M+1}}{M+1}\right]_{count\ Rate} - \left[\frac{e^C E^{M+1}}{M+1}\right]_{Intercept} \tag{33}$$

The integration limits span from the intercept to the count rate at the energy required. At the intercept the value of the counts is zero, this is the equivalent of the start of the mission and so this part of the equation can be removed.

$$\int_{0}^{R} y\, dE = \left[\frac{e^C E^{M+1}}{M+1}\right]_{count\ Rate} \tag{34}$$

The final step in preparing the data itself, is within the channel boxes themselves. The count rates for each channel count the total number of particles that are measured over the whole of the channel boundary. When working out the distribution using the power law method, by just using the measured count rate the calculated rate would be far too high. When using the value of the count rate, the particles measured are distributed along the energy range and the TOF range of the channel. To account for this, the measured count rate is divided by the area of the channel.

For the channels with very narrow boundaries the loci of the elements fill the majority of the channel boundary, this is a very simple process. In the case of the proton

channels however, the loci lie near the upper boundary. In these cases, the boundaries have been moved to account for how much of the channel area the element takes up.

With the data now in the correct units and distribution, the section of data required to match the Voyager data needs to be extracted from the set. In the initial comparison by (Radioti et al., 2005) only the data from Voyager 2 was used in the comparison. They also only used the first 15 orbits of the Galileo data; this is likely to be to try and minimise the

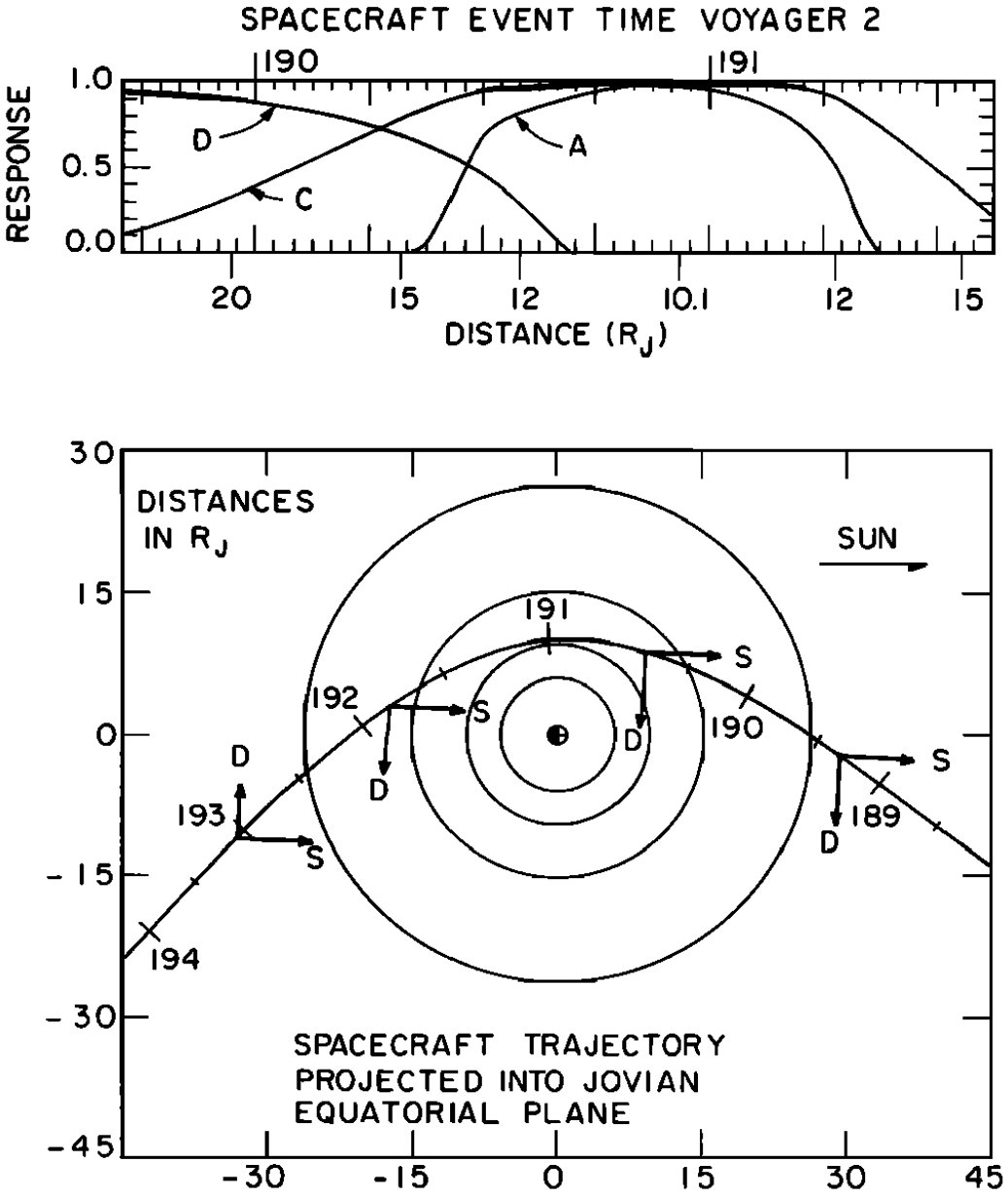

Fig. 2. The Voyager 2 trajectory and instrument response, in the same format as that used for Figure 1. Closest approach is at 10.1 R_J (2230 UT on DOY 190, 1979).

Figure 3.5-1: Documented Trajectory of Voyager 2 during its flyby of Jupiter in 1979. Figure 2 of the publication (McNutt et al., 1981) with caption.

known degradation in the data. This is not something that needs to be considered now, and thus the whole of the overlapping data set is used.

During the influx of data from the Voyager missions, there were many publications that described both the interior of the Jovian system and the path Voyager took through it. A complete overview of the Voyager missions can be found in the following papers including the orbital paths shown in Figure 3.5-1 (McNutt et al., 1981, Bagenal et al., 2017, Banaszkiewicz and Ip, 1993).

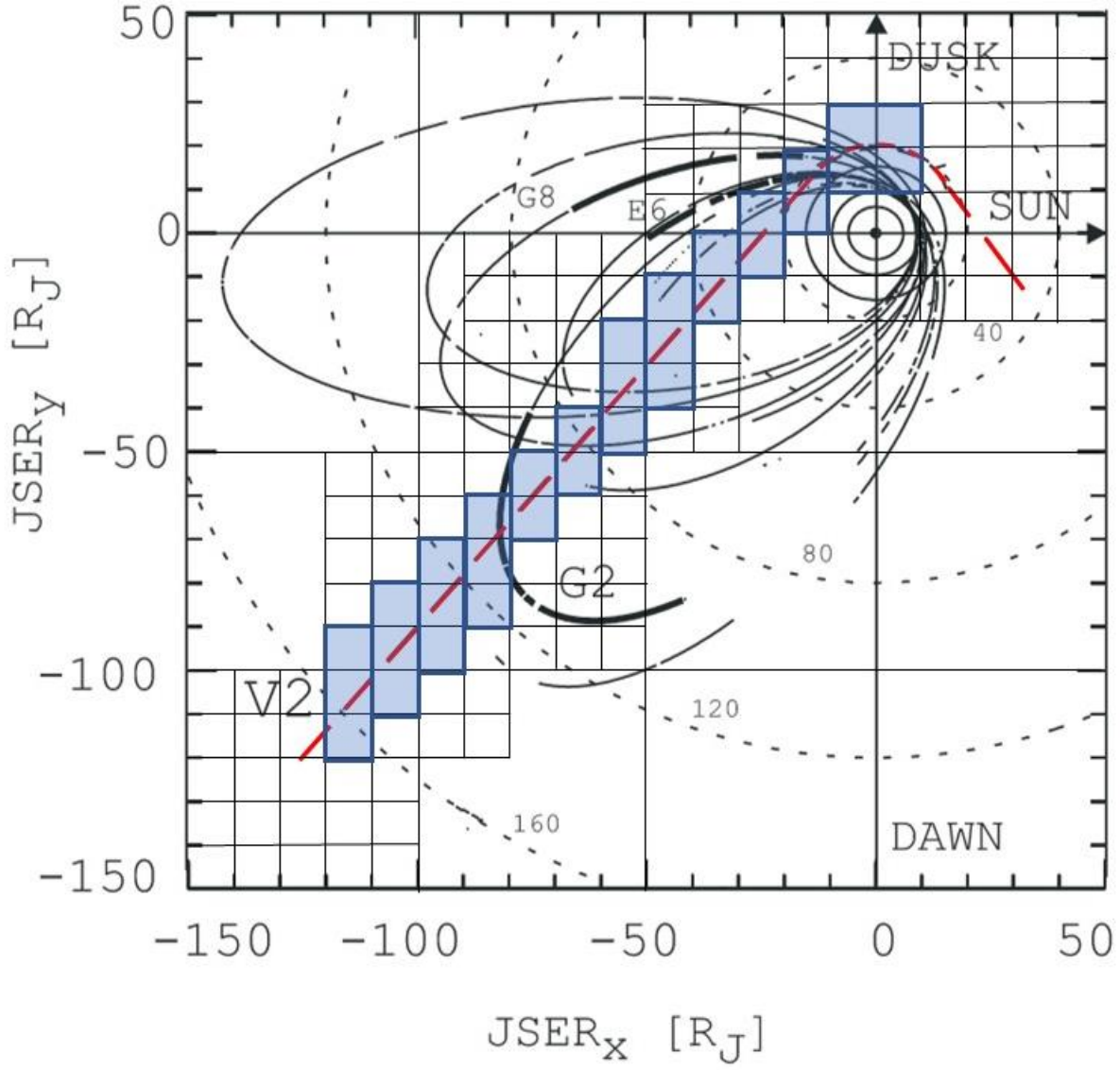

Figure 3.5-2: Voyager trajectory (red dash line) overview used in *Radioti et al.* overlaid with a grid at every 10R$_J$, blue boxed areas show the corrected Galileo data to be used in the correction.

Figure 3.5-1 is unfortunately a very zoomed in view of the Jovian system reaching only 45RJ whereas the reach of Jupiter's magnetosphere can range from 100RJ to as far as

400RJ in the Magnetotail (Bagenal et al., 2004). Instead of using this view of the Voyager (Figure 3.5-1) trajectory; Radioti et al. used a view shown in Figure 3.5-2. The base image of the trajectory and the first 15 Galileo orbits, comes from the publication itself. The additional grid lines and blue boxes denote the areas of data where the corrected Galileo data is taken from.

Many of the boxed areas don't contain data, much as the visible orbits suggest. However, the use of the full mission data means there is far more data populating the close to Jupiter areas within 10 and 20RJ.

The data within the shaded areas of Figure 3.5-2 is then averaged by radius to match with the results range previously compared. This step collates the orbits into a single and concise data set over the radii available.

3.5.3 Initial Comparisons

The initial comparisons were computed using a very fine bin width, to match the accuracy of the data. Whilst the values were accurate to the expected values the huge number of data points presented far too much on the plot to make an accurate comparison

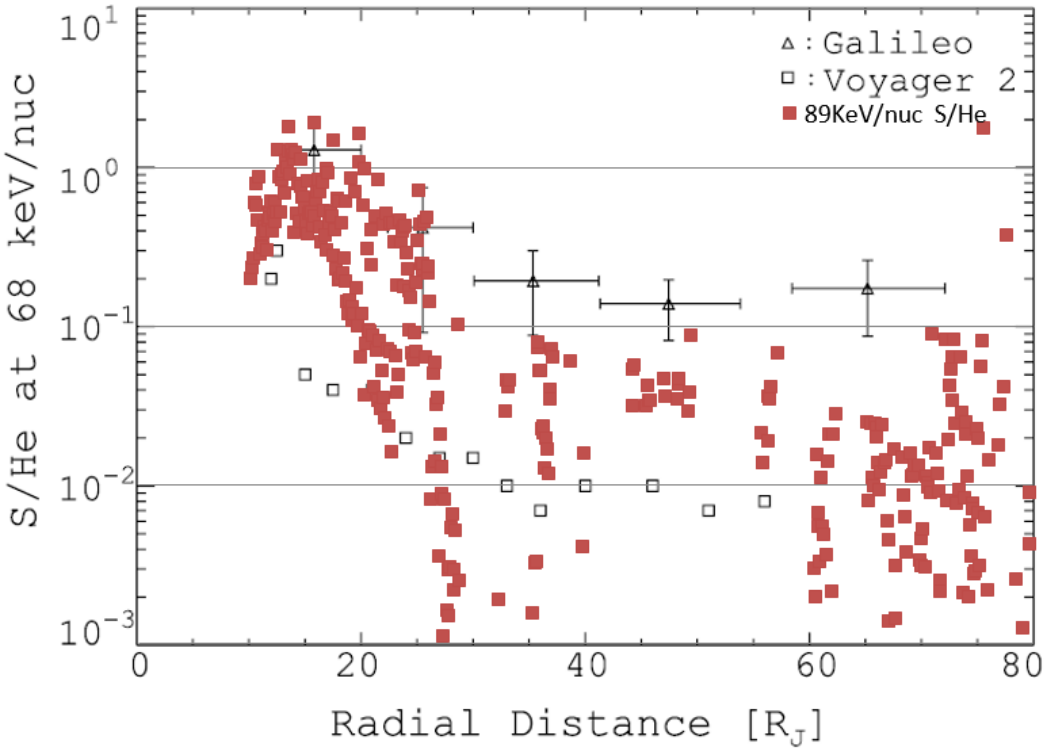

Figure 3.5-3: First look at original against corrected data, comparison. The corrected data in red is overlaid on the same plot produced in (Radioti et al., 2005).

of the original data. This can be clearly seen in Figure 3.5-3, where the red points of the new data swamp the ratio values calculated previously.

To better view the new ratios the binning range of the radii, is increased to match that in the publication. This also has the added improvement of reducing the computation power needed for the integrated count rates.

3.5.3.1 S/O ratios

Figure 3.5-4 gives a first look at how much effect the correction has had on the Galileo data. With the marked differences in the increases in sulphur channels and decreases in oxygen channels the ratios are expectedly different. The main effect is seen closest to Jupiter, where the ratio reaches 0.7. The marked drop that follows up to the 30Rj mark fits within the values recorded originally and with those from the Voyager mission. From this point the corrected data fits more with the Voyager data, keeping within the 0.3 to 0.05 range.

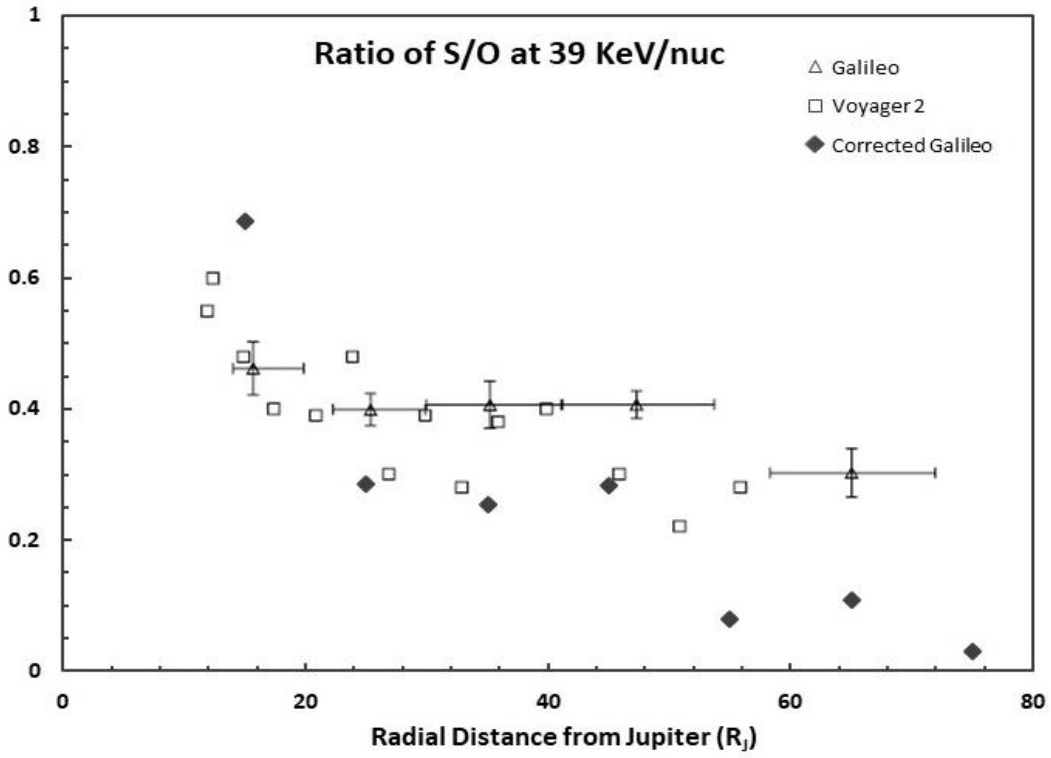

Figure 3.5-4: Ratio of the integrated power laws of Sulphur against Oxygen at 39KeV/nuc, for the corrected data set, original data set, and Voyager 2 measurements from (Radioti et al., 2005).

By correcting the values, the aim was to develop a more accurate view of the particles in the Jovian system. The Voyager mission, whilst only carrying an early iteration of the particle detector on-board Galileo, would still have likely recorded a more realistic, if

limited, view of the system. This is because of the conditions the detectors were working under. For Voyager 2 passing through the Jovian system in a matter of days, the detector would have only been briefly exposed to the damaging ions in the environment. Galileo, on the other hand, took measurements for 8 years, even using only the first 15 orbits of the mission the degradation of the silicon would have already have been taking effect.

3.5.3.2 S/He, O/He and p/He ratios

The ratios of key elements against helium as the distance from Jupiter is increased are of interest. The helium in the Jovian system is mainly from the Solar wind entering through reconnection of the magnetosphere, this element is found mainly throughout the magnetosphere as opposed to the oxygen and sulphur that drop off far more rapidly. The decreasing ratios with radial distance are an indicator of this, and are seen throughout the element by helium ratios discussed.

The helium count rate channels were the hardest to correct for out of all the elements, due to only two channel points. The same effect continues here in how the power spectrum suffers from the lack of data points. The integrated energy spectrum with radius

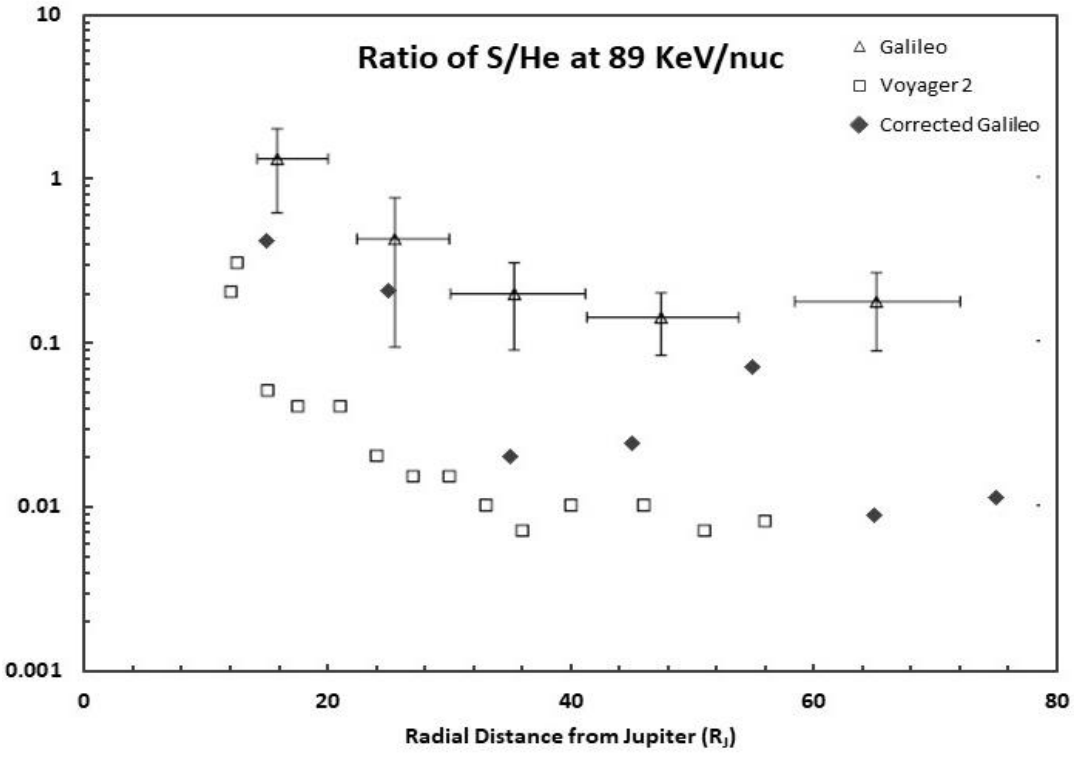

Figure 3.5-5: Ratio of the integrated power laws of Sulphur against Helium at 89KeV/nuc, for the corrected data set, original data set, and Voyager 2 measurements from (Radioti et al., 2005).

suffers from the same inaccuracies from the data itself. Despite these drawbacks the results are promising, at both 89KeV/nuc and 800KeV/nuc against the sulphur values.

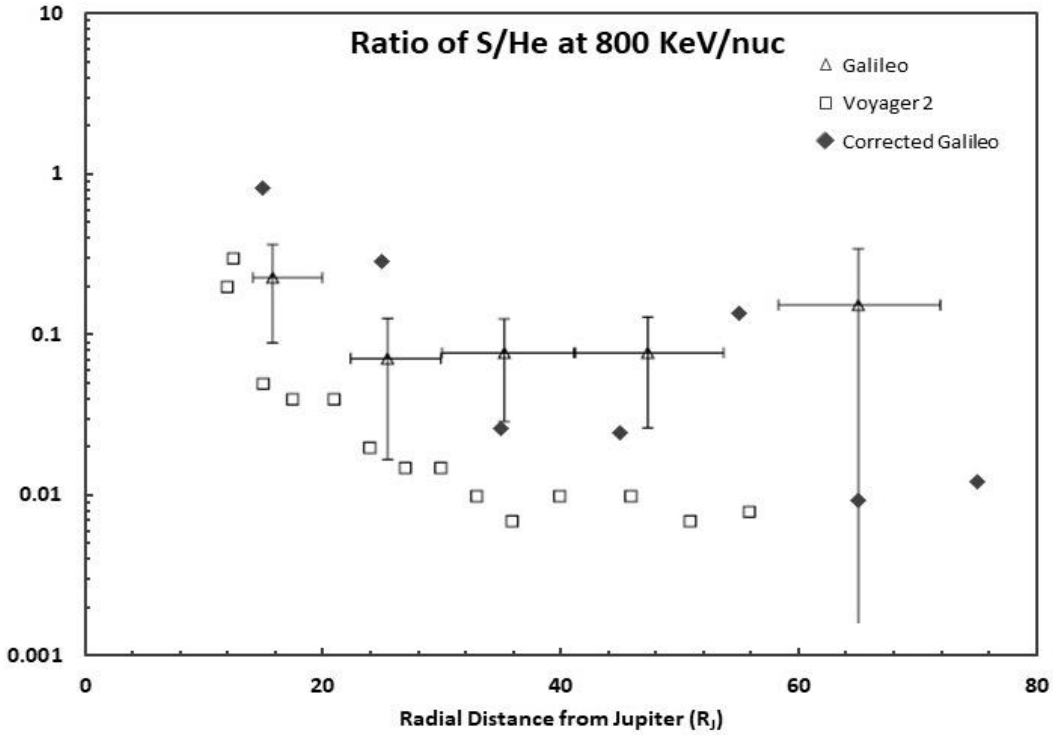

Figure 3.5-6: Ratio of the integrated power laws of Sulphur against Helium at 800KeV/nuc, for the corrected data set, original data set, and Voyager 2 measurements from (Radioti et al., 2005).

The values sit as expected between the Voyager 2 and Original Galileo results, whist keeping the expected trend of tapering off with radial distance. the aim of the comparison with original and Voyager data set was to check the validity of the count rate correction, to make sure it still fits within expected results. This first look has proved the correction is doing as required and has produced the desired results.

The oxygen against helium ratios are much the same. The marked increase in the ratio around 50RJ persists with both oxygen and sulphur, suggesting the helium drops around the point. A possible cause of this is the inequality of the day and night side on the magnetosphere. The dayside of the magnetosphere can fluctuate around the distance of 50RJ.

The only anomalous result comes from the S/He at 800KeV/nuc. At around 50RJ the ratio rapidly increases then decreased again with the following data point. the starting values are also higher than the Galileo value ratios available. A test of this issue would be to compare the same ratio of the full data set rather than limiting it to the areas shown in Figure 3.5-2.

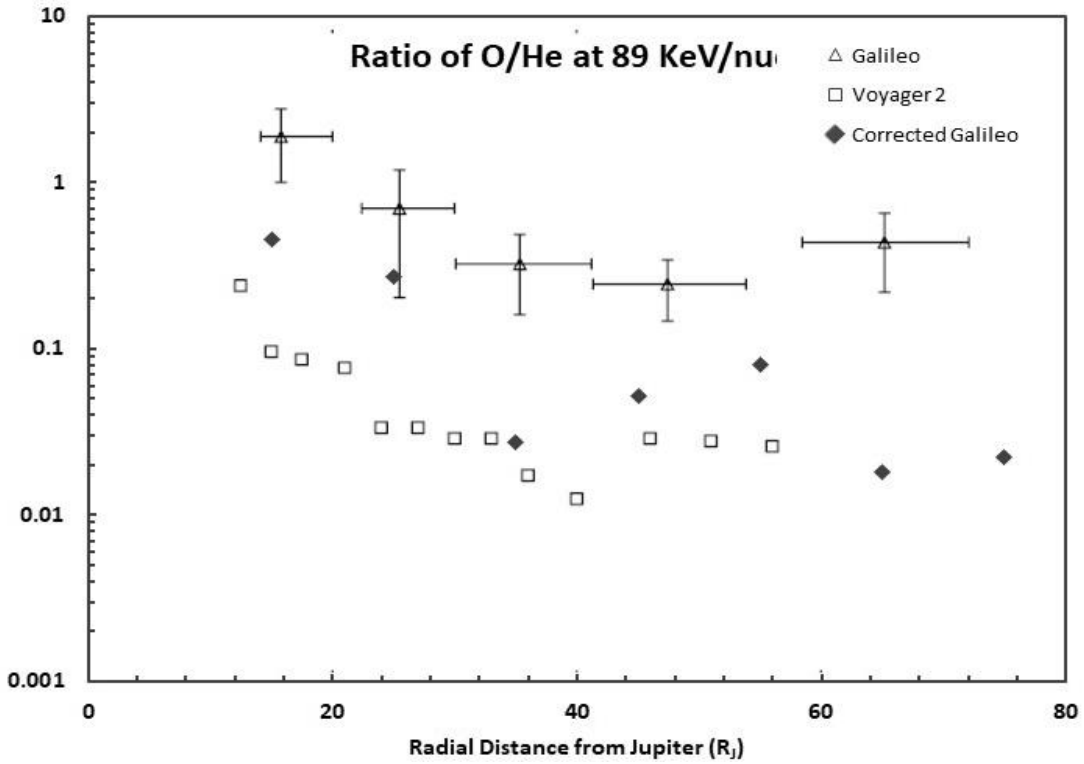

Figure 3.5-7: Ratio of the integrated power laws of Oxygen against Helium at 89KeV/nuc, for the corrected data set, original data set, and Voyager 2 measurements from (Radioti et al., 2005).

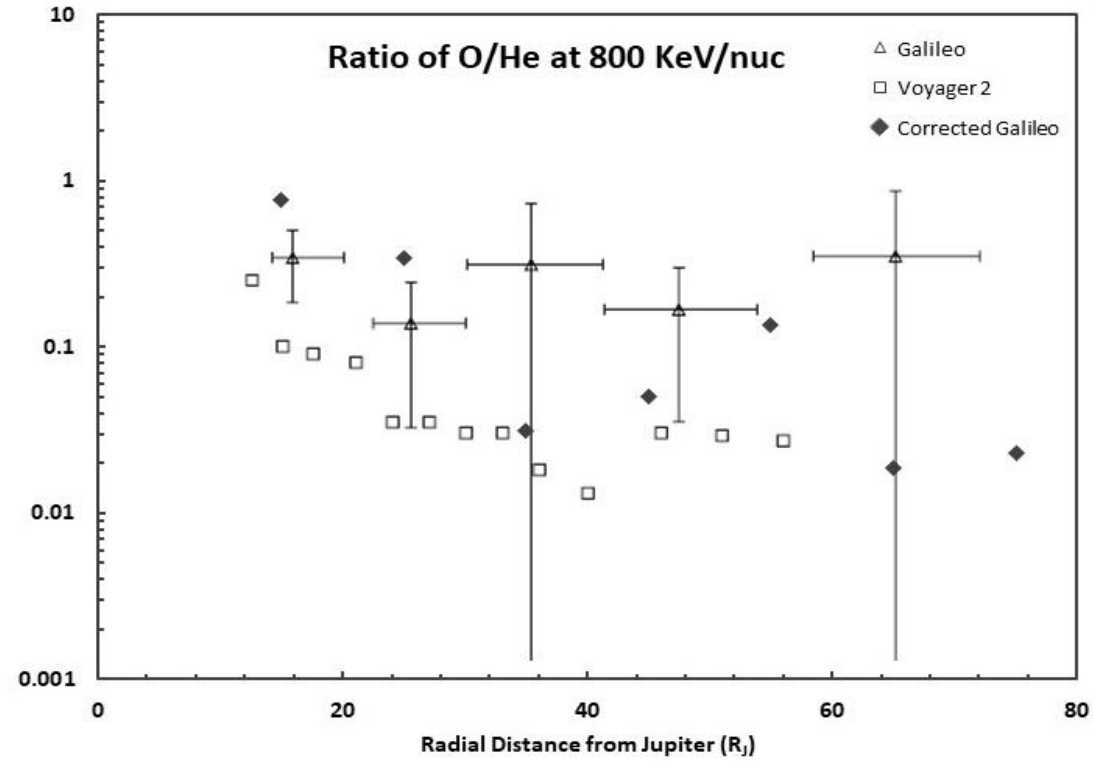

Figure 3.5-8:Ratio of the integrated power laws of Oxygen against Helium at 800KeV/nuc, for the corrected data set, original data set, and Voyager 2 measurements from Radioti et al., 2005.

From here is where problems arise in the ratios generated. When comparing the ratios of the protons against helium, the ratios are two orders of magnitude lower than expected. Having seen from Figure 3.5-5, Figure 3.5-6, Figure 3.5-7 and Figure 3.5-8, the values of helium are correct, this means the correction of the Proton channels are where the fault lies. In this case the values are far too small for the values of helium. This mis-alignment is present at both 185KeV/nuc and 800Kev/nuc as can be seen in Figure 3.5-9a and b.

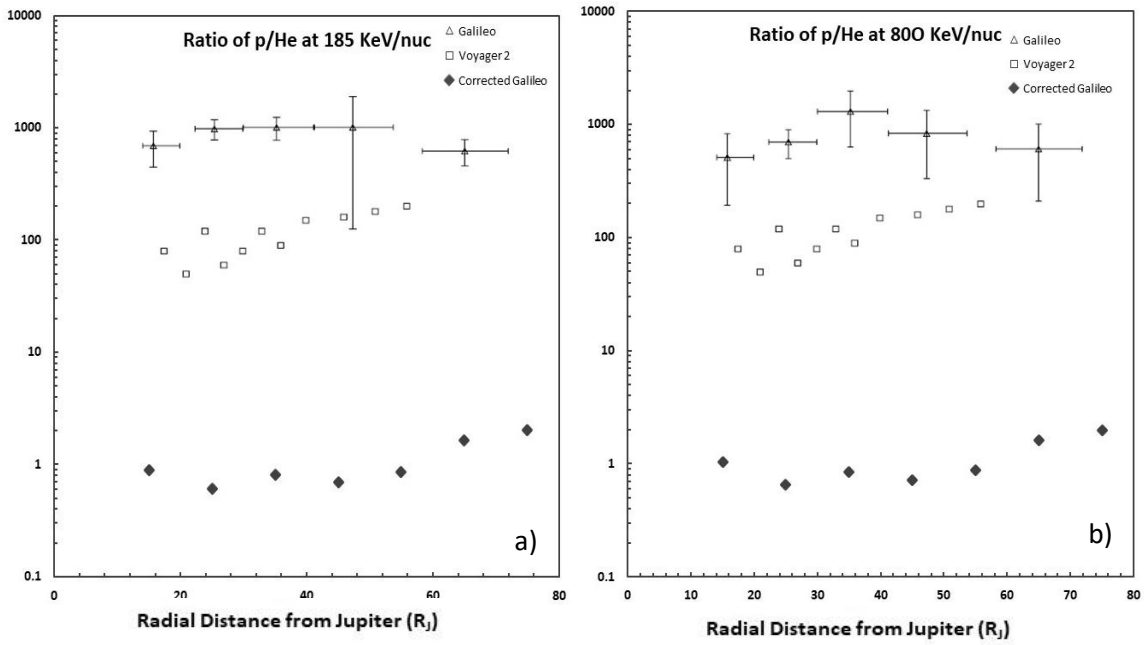

Figure 3.5-9: Ratio of the integrated power laws of Protons against Helium at: a) 185KeV/nuc and b) 800KeV/nuc, for the corrected data set, original data set, and Voyager 2 measurements from Radioti et al., 2005.

To determine if the far lower proton values were caused by the correction, the original data was tested in the same method and produced the same results.

3.5.4 Problems with the ratio calculations

3.5.4.1 Helium depletion at 50Rj

First the significant drop in the helium values around 50RJ need to be investigated, the simplest step is to do this is to remove any of the orbits where the spacecraft may have passed out of the magnetosphere on the dayside. This is quite simple as can be seen in the orbit map shown in Figure 3.5-2. Only the late mission orbits take Galileo out towards the day side of the magnetosphere.

By taking out the orbits after E18 (22 November 1998), there is no chance that there might be a crossing of the magnetosphere either on the front or dawn/dusk side. The ratios are then re-calculated using the same method.

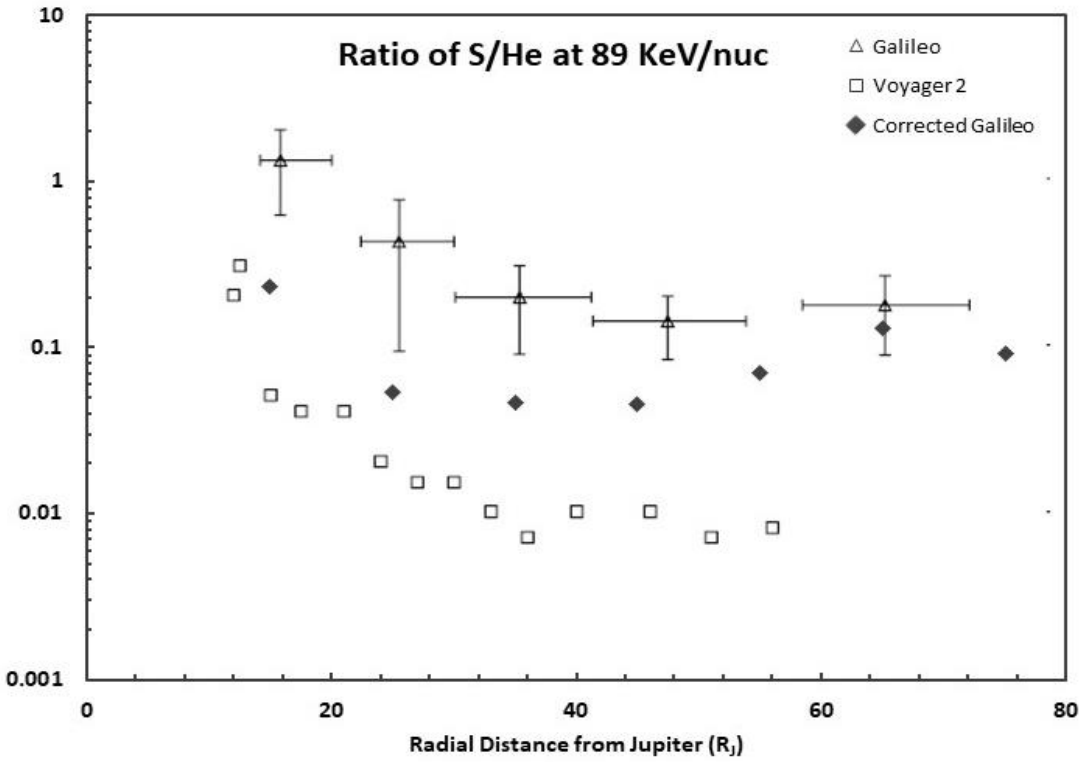

Figure 3.5-10: Ratio of the integrated power laws of Sulphur against Helium at 89KeV/nuc, for the pre-1999 corrected data set, original data set, and Voyager 2 measurements from (Radioti et al., 2005).

Figure 3.5-10 and Figure 3.5-12 show the new ratios of sulphur and helium, at 89KeV/nuc and 800Kev/nuc. The ratio peak at 50RJ has now disappeared, with the ratios still fitting into the expected range between the Galileo and Voyager 2 data sets. In Figure 3.5-12, the values are far closer to the Galileo data than before. This indicates either a lower overall value of helium in the pre-1999 orbits, or more likely, a higher overall value of sulphur. The effect of the correction is an increased amount of sulphur counts, by extrapolating the helium and sulphur values out to 800KeV/nuc the increase in these channels could have been amplified. The same could be true for the helium values as the channels have also overall increased; though not as extremely as for sulphur.

Despite this the values are still well within the expected rates and match well with the existing data. To further investigate the matter, the exact values would need to be compared rather than just the ratio.

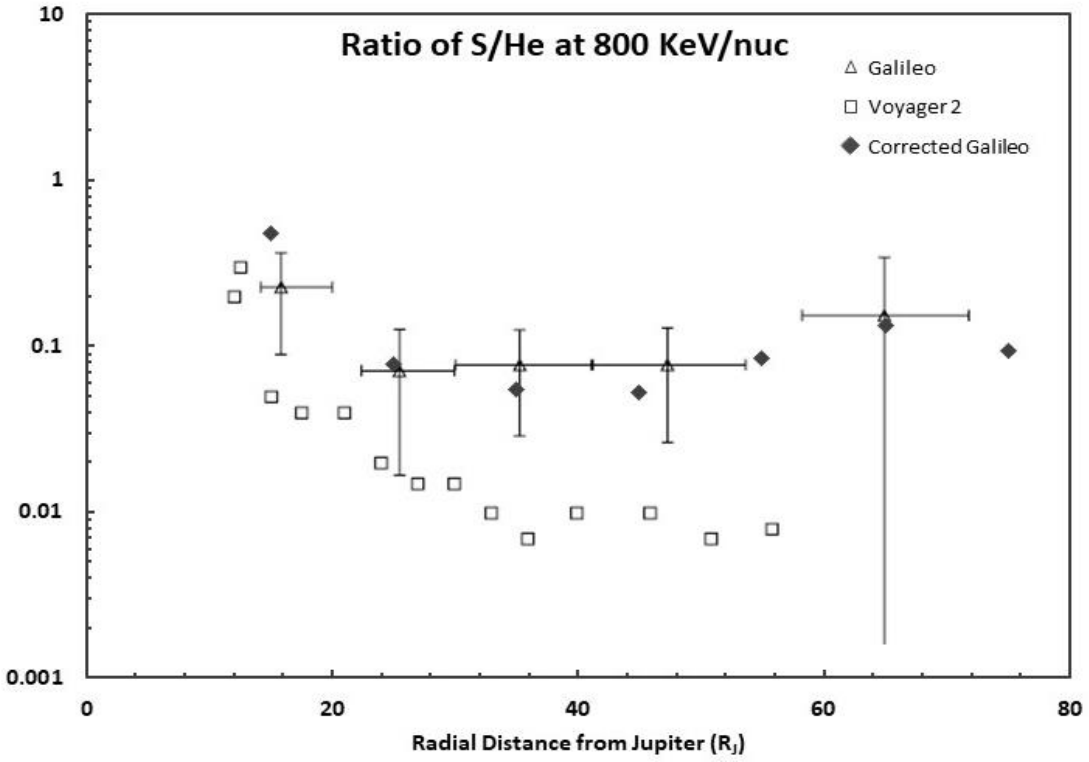

Figure 3.5-12: Ratio of the integrated power laws of Sulphur against Helium at 800KeV/nuc, for the pre-1999 corrected data set, original data set, and Voyager 2 measurements from (Radioti et al., 2005).

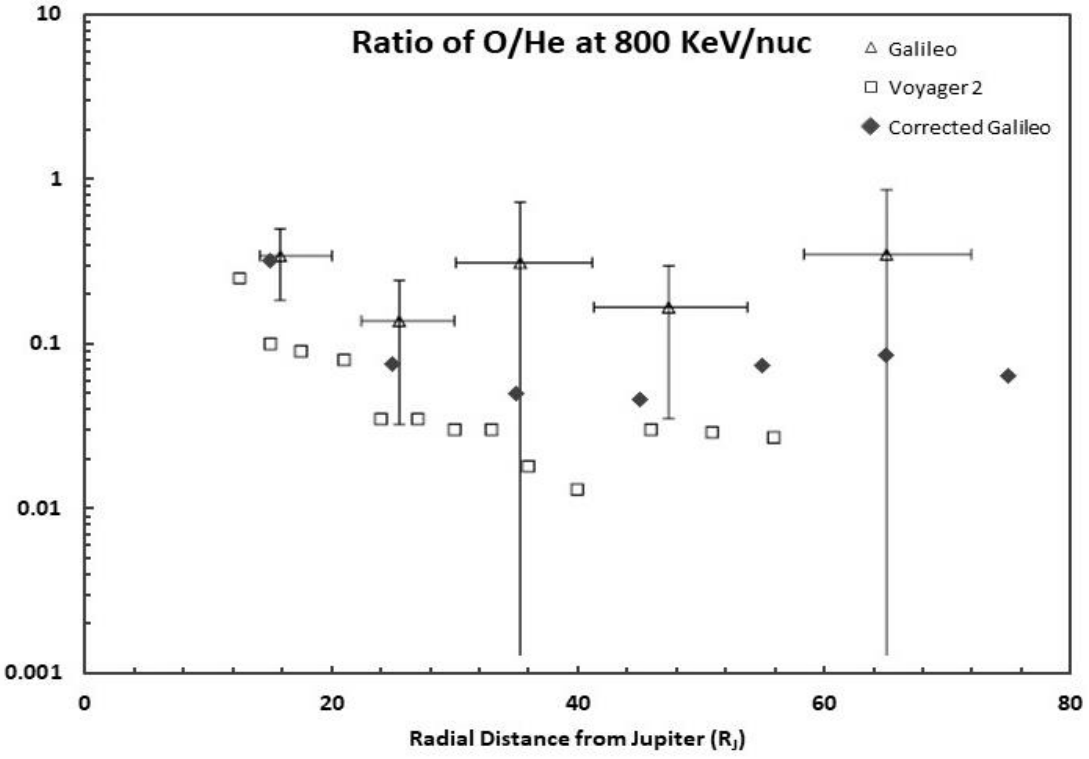

Figure 3.5-11: Ratio of the integrated power laws of Oxygen against Helium at 800KeV/nuc, for the pre-1999 corrected data set, original data set, and Voyager 2 measurements from (Radioti et al., 2005).

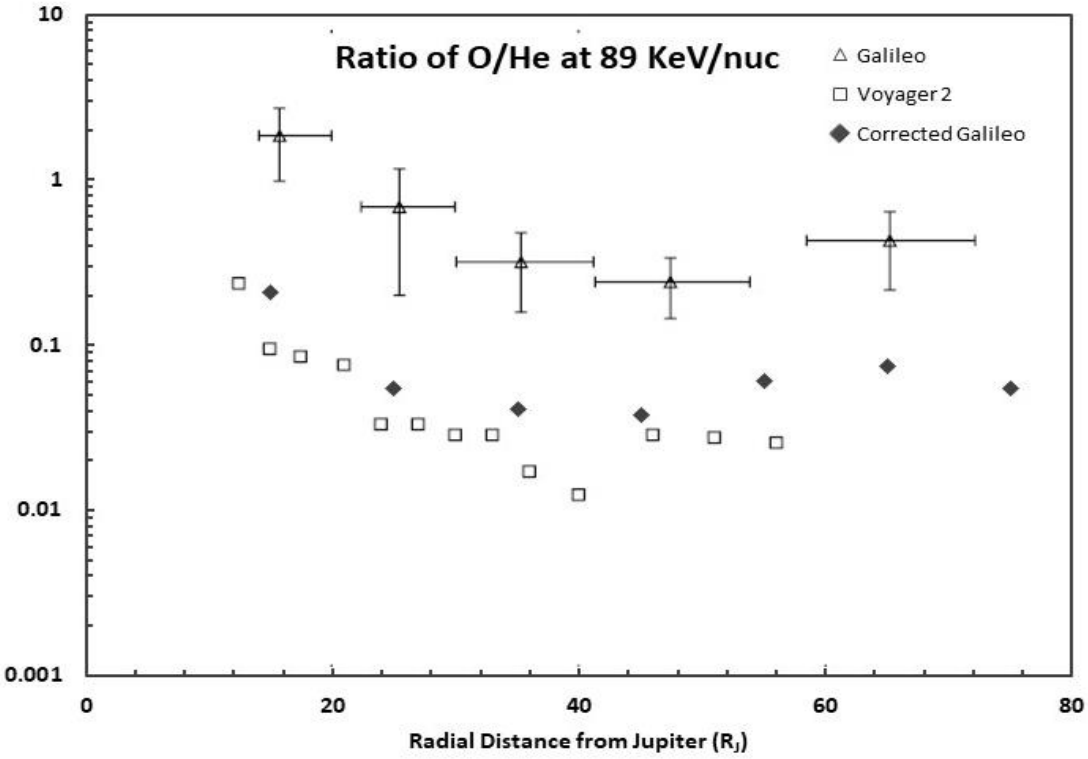

Figure 3.5-13: Ratio of the integrated power laws of Oxygen against Helium at 89KeV/nuc, for the pre-1999 corrected data set, original data set, and Voyager 2 measurements from (Radioti et al., 2005).

The new ratios for oxygen against helium are shown in Figure 3.5-13 and Figure 3.5-11, the increase in the ratio around 50RJ is again now gone. With this result, the likelihood of the 50RJ anomaly being caused by crossing of the magnetopause is far higher. Whereas in the sulphur/helium ratio the values fit close with the Galileo values, for oxygen/helium the values are lower. Rather than an increase in helium, disagreeing with the results of S/He, a decrease in oxygen fits with the expected trends of the correction. looking in the prediction of the correction (Figure 3.2-3), the calculated ratios of oxygen, sulphur and helium, fall in to the expected trend patterns.

3.5.4.2 Low Proton Count

The final issue to solve with the comparison ratios, is with the proton counts. Having assured that the issues with the S/He and O/He are caused by the magnetopause crossings, the issues now with the p/He can be pinned to the proton counts. The main problem is that the proton counts are far too low reducing the ratio number (Figure 3.5-9). The figure suggest that the values of protons should be 2 to 3 orders of magnitude larger than the helium. From the raw values this is not the case.

As the original data channels of hydrogen were also tested to eliminate the correction method as the fault, the alternative fault must be an additional factor causing the channel to not pick up counts. As mentioned previously the priority system built into the recording system (introduced in section: 2) and explained in detail in sections: 2.2.1 and 2.5.3), was designed to reduce the amounts of hydrogen counts measure as to not swamp the detections. This is likely to be the issue being faced here.

This leaves a gap in the comparison if the hydrogen channels cannot be used. However, there is another metric that was recorded by the EPD that can be used in place of these channels. Before the priority system selects the interesting readings, every particle entering the detector passes through a foil releasing an electron for the start signal MCP to register. The count rate of this MCP does contain counts of all the elements, but as such effort was taken to reduce the hydrogen counts it stands that the majority of the counts registered will be hydrogen.

The ratios using these secondary counts are shown in Figure 3.5-14 and Figure 3.5-15. Both ratios have considerably more error now as these counts from the start signal are not exclusively hydrogen. However, overall, they match far better to the expected ratios.

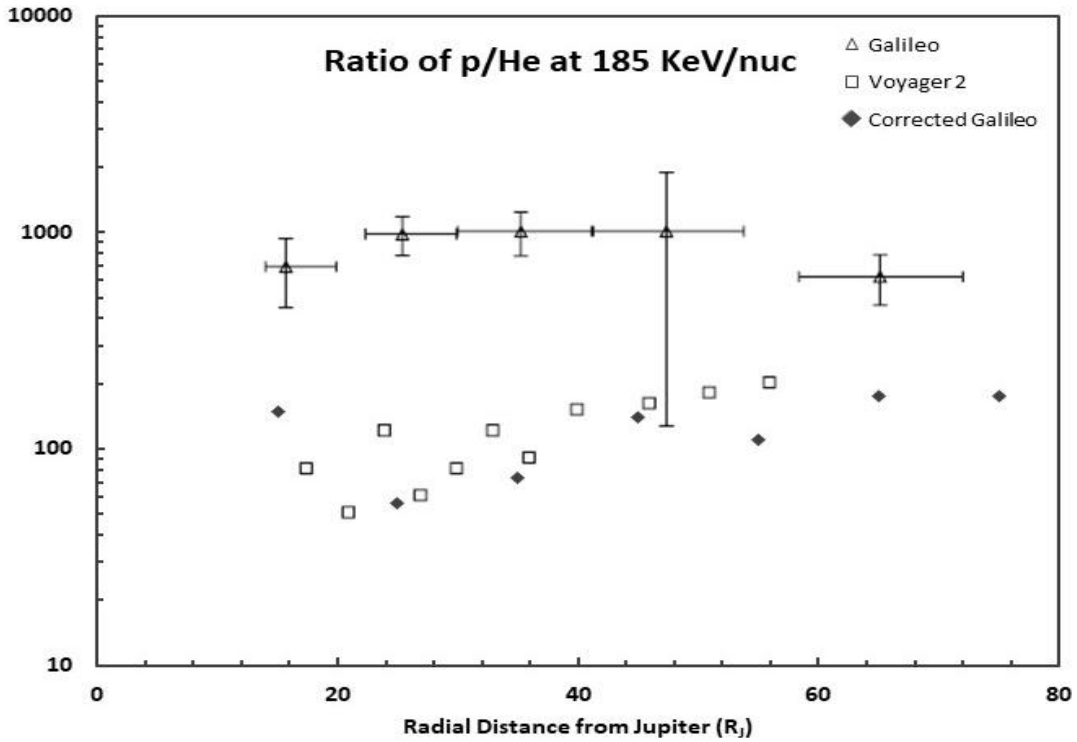

Figure 3.5-14: Ratio of the start TOF MCP counts against the integrated power law of Helium at 185KeV/nuc, for the pre-1999 corrected data set, original data set, and Voyager 2 measurements from (Radioti et al., 2005).

With only a single channel count the integrated spectrum cannot be used for the start signals, as is done with the other channels. The counts are simply all the measured particle and are thus the equivalent of the integrated spectrum over all energies measured. In terms of the comparison this means that the best representation of the ratio is against the 800KeV/nuc helium, as these counts cover the largest range of the energies (Figure 3.5-15).

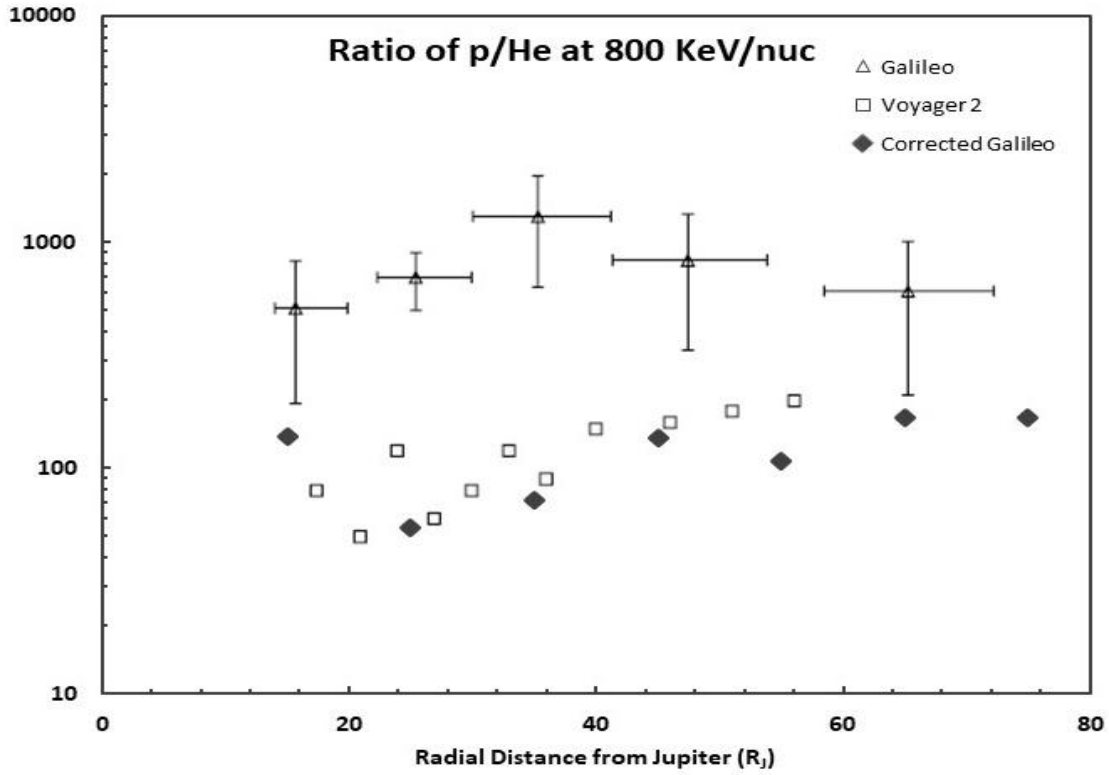

Figure 3.5-15: Ratio of the start TOF MCP counts against the integrated power law of Helium at 800KeV/nuc, for the pre-1999 corrected data set, original data set, and Voyager 2 measurements from (Radioti et al., 2005).

3.6 Conclusions

Having the corrected PHA plots, gave a good starting point to the correction of the count rates. The understanding gained in how the counts are moving from channel to channel, allows for a better estimate of what the correction constants should be.

The correction of the count rates, required two iterations and updates to the method. Developing something so unique from scratch was complicated and though the process I found a far better understanding of the effect the decay had on the instrument. The channels were not all as straightforward to correct as others, with the sulphur and oxygen channels being the main priority to improve as much as possible. The aim was to use the data in the next chapter for calculating sputtering values.

The final result of the corrected channels was rather abstract. Only when the values were analysed in relation to the Voyager data sets and original data, were the alterations really seen. The errors incurred during the correction process are complex to quantify. They encompass the CV value generated from the original data, the estimations of the counts during instrument down time, efficiency drop calculations estimating totally uncounted particles, and the overall error in the correction itself. The aim in the devised method is to improve only within the limits of the original. By comparing with early, less affected averages, and overall with both original and external data, the error is expected to be always within what has been recorded.

The effectiveness of this, truly shines in the comparison to Voyager 2's data. By matching with these results, the correction can be deemed valid and valuable. However, as with any data collection the best results always come from the most recent measurement meaning the true effectiveness of the correction will not be fully realised until more data has been taken either by the current JUNO mission or the upcoming JUICE mission.

4 Sputtering on Europa: An Initial Estimation of Surface Age.

Having corrected and improved upon the original data, the final step is to evaluate the impact this has on the surface of the moons. Much research has already been done on the effect sputtering has on the surface of the moons (Ip et al., 2000, Cassidy et al., 2013, Galli et al., 2018); however, the change in composition ratios will influence the volume of material removed from the surface. The first section of this chapter will focus on re-calculating this effect, primarily for Europa; though the calculations could be applied to the other moons.

With a more accurate view of the movement of material on the surface of Europa, the final investigations focus on the surface itself and the overlapping of features. Preliminary investigations show that the age of one section of the surface in relation to another could be dated using the sputtering values.

4.1 Analysis of New EPD data during the Europa flybys.

During the flybys the EPD recorded both in high rate and real-time (count rate) mode so as to truly capture the environment experienced by each moon. This allows investigations on the flybys to be done using not only the raw count numbers of particles but also the distribution of the counts for each element over energy.

The flybys of most interest are from later in the mission. These contain the data that is far more affected by the decay and thus will now have been more significantly improved. Along with this, there are key flybys that can be analysed which have the possibility of containing significant events such as plumes. Flyby E12 is the prime candidate for suspected plume activity (Huybrighs et al., 2017, Roth et al., 2017)

4.1.1 Flyby Data

The data available over the flybys are very limited for the high rate PHA plots. The downlink shortcomings meant the availability of data became sparse even for areas of

interest, like flybys. The count rate data however, does have a large amount of data available. The actual flybys were very quick, with the count rate data reduced to approximately 11 min averages over most of the mission this means there aren't very many data points covering the closest approach.

For each flyby analysed the count rate data is taken from one day either side of the flyby closest approach day, covering three days in total over each flyby event. This allows for more of the approach and departure of the flyby to be analysed as the instrument passes the moon and leaves again.

In picking out the data ranges, each flyby is well documented, allowing the closest data packet to be identified during the closest approach. There is some calculation involved in this to convert the given dates and times of the flybys to the decimal date given for the count rate data (note: when converting the values of day count begin at one rather than at zero). Whilst this 24-hour difference may not make much difference in the correction process; for identifying the closest approach data this is very important.

The standard date format is: YYYY.DOY:hh:mm:ss; where YYYY is the year, DOY is the day of year from 1 to 365, hh is the hour of the day in 24-hour format, mm denoted minuets and ss is the second count. This system is used for denoting for the PHA data and in the descriptions of the flybys. To convert this to match the decimal year used for the count rate data the following calculation is used (35):

$$YYYY.\left(\frac{DOY-1}{365}+\frac{hh}{365\times 24}+\frac{mm}{365\times 24\times 60}+\frac{ss}{365\times 24\times 60\times 60}\right) \quad (35)$$

The dates of all the flybys are listed in Table 1.6-1, where the date is given both as a conventional date and in Day Of Year (taking account for leap years). By converting these dates into decimal year, along with the decimal date for the surrounding days, the flyby data set can be pulled from the main bulk of data.

There are 4 main flybys of note to look at. These are E4, E12, E 15 and E26. E12 is the most interesting with the possibility of plume activity suspected (Huybrighs et al., 2017). E26 is the last of the Europa flybys and demonstrates the vast differences in the data from the before and after correction and the opposite is true of E4 being the first of the Europa flybys, with E15 being an example of a typical flyby.

The most important factor in the effects of sputtering on the surfaces of the moons is the ratio of Sulphur to Oxygen. These being the largest of the expected species will contribute to the most erosion on the moons. The following images show the changes Sulphur and Oxygen over the three flybys of interest. Figure 4.1-1 and Figure 4.1-2 shows the changes in the E12 flyby. The flyby itself is marked as the blue line. This is the distance in thousand km from the point of closest approach.

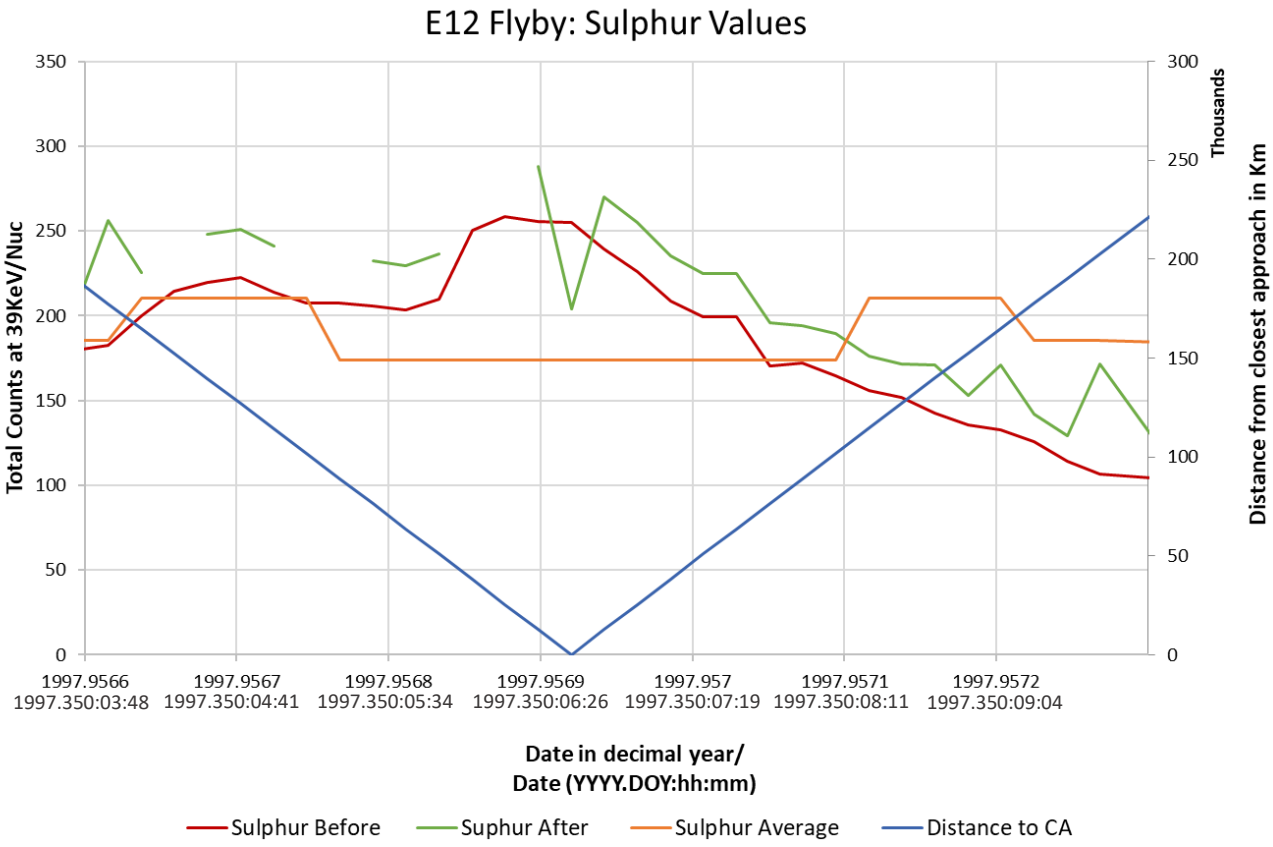

Figure 4.1-1: Sulphur values of the E12 flyby. Showing the before correction value, the post correction value and the post correction all data average for the distance from Jupiter over the whole mission.

Knowing the values of the average readings from around the Europa orbit gives a huge amount of information on how the proximity of the moon affects the ratios of the elements. By removing all the flyby data from the mission, the values of the averages can be considered a baseline of the environment. Comparing this to the flyby readings the effect of the moons can be found. The same can be done by averaging only the flyby data by radius. This is very similar but by focusing on the flybys, events at are unique to one flyby will be more obvious. This is a method that can be used for finding or identifying plume events.

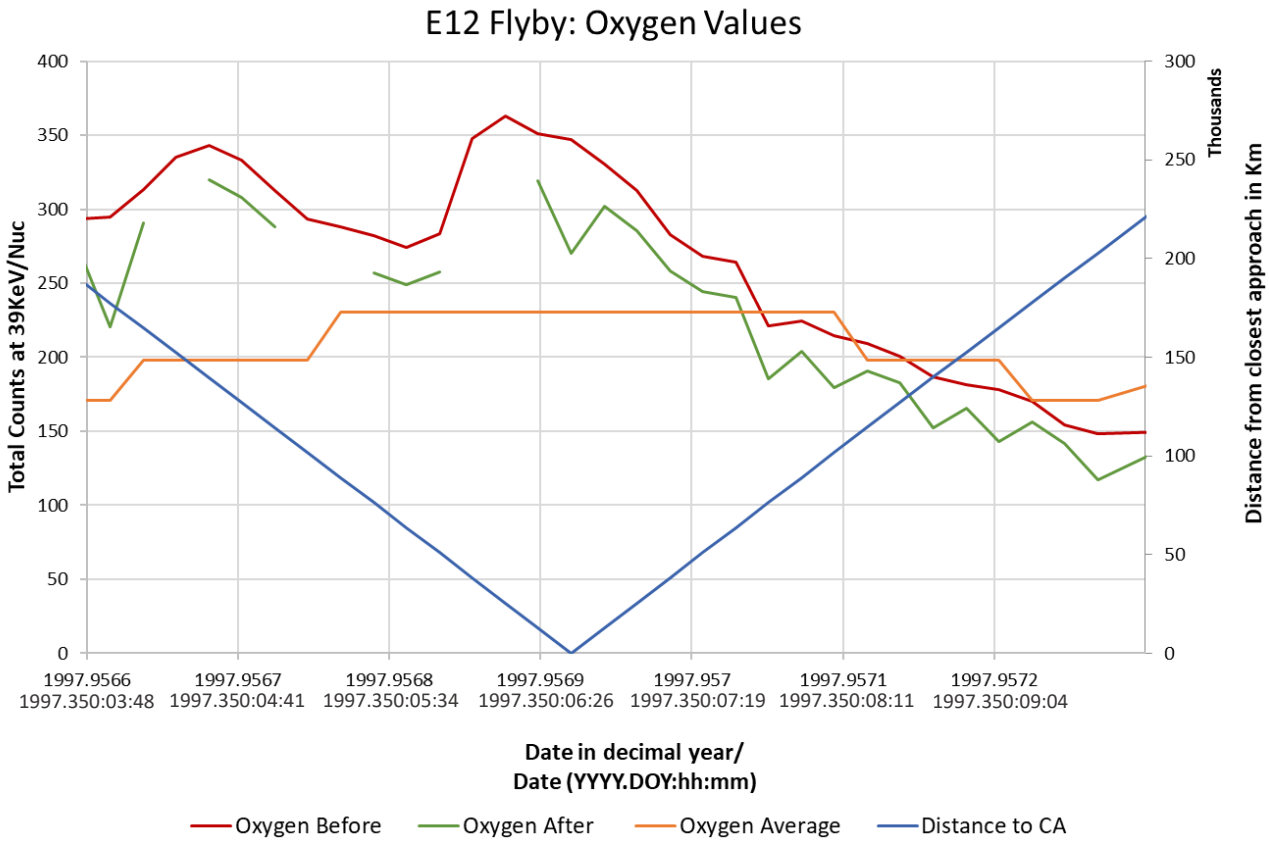

Figure 4.1-2: Oxygen values of the E12 flyby. Showing the before correction value, the post correction value and the post correction all data average for the distance from Jupiter over the whole mission.

In this analysis the averages are of the whole mission; to give a general overview of the data up close.

In this case looking at the data in terms of the closest approach isn't very useful. The 11 min averages of the count rate data are so sparse that, combined with the speed of the spacecraft during the flyby, means there are very few data points within a reasonable range of the moon. A better approach is to take the closest approach readings and analyse the intensity and flux, calculating a general sputtering yield for the surface of Europa.

4.1.2 Flux Rate vs. Count Rate

The EPD measured in count rate. This is the number of particles hitting the detector per second; and in the case of the EPD, this value is then averaged over approximately 11 minutes to minimise the downlink size of the data. To use these count rates for sputtering calculations on the surface of the moons they first need to be converted to a flux, or intensity. The problem in doing this is that it is dependent on the detector.

Instead of counts, sputtering calculations done using either intensity or flux; where intensity of counts is the flux multiplied by the viewing solid angle of the detector in steradians. A conversion is also needed to go between count rate and flux. This is based on the detector itself and how efficiently it can count over the energy ranges, along with the overall area for counts to impact upon. The common notation for intensity is:

$$\text{Differential intensity} = j(\alpha, E) \tag{36}$$

Where α, is the direction of the instrument pointing at the time, and E is the energy range of the instrument. This then becomes:

$$j(\alpha, E) = \frac{r(\alpha, E)}{G\ \Delta E} \tag{37}$$

r is the count rate measured, ΔE is a measure of the energy bands the detector can measure between, and G is the geometric factor of the detector. The geometric factor is a measure of the physical size of the detector, and its viewing angle in steradians. In a simple analysis, this can be considered as the surface size of the detector multiplied by the 4π viewing angle. In a more complex analysis, the geometric factor also considers the response of the detector.

A detector's area is not uniformly efficient; particles at the extreme range of energy are less likely to be counted by the detector as a real reading than those well within the energy bounds. To account for this, the geometric factor can be considered as a function of energy. When this value is multiplied by the efficiency, it is known as the response function of the detector.

Appendix A of Mauk et al., (2004) gives a detailed description of the response function for each element channel, and the associated parameters. For the purposes of this research, the simpler approach is being used. The value for the geometric factor for each channel is a commonly used value calculated by the instrument team. The available values are pre-combined with the efficiency of the channel; the values used are listed in Table 1.4-1.

The conversion from counts to differential intensity is described by equation (38). Using the parameters in Table 1.4-1 the count rates can be simply added to the equation and converted.

$$Differential\ intensity = \frac{counts}{(bandwidth: high - bandwidth: low) \times G} \quad (38)$$

This conversion was applied to the whole data set as well as the specific flyby values, to give an overview of the full data intensities.

Channel	Geometric Factor Channel	Bandwidth (kev)	
		Low	High
TP1	0.001	80	220
TP2	0.0011	220	540
TP3	0.0006	540	1040
TA1	0.0025	27	155
TA2	0.003	155	1000
TO1	0.001	12	26
TO2	0.0025	26	51
TO3	0.0035	51	112
TO4	0.0035	112	562
TS1	0.002	16	30
TS2	0.003	30	62
TS3	0.0035	62	310
TH1	0.003	20	200

Table 4.1-1: Parameters for converting count rate to intensity.

4.1.3 Count Distribution

The channels available for each element are very limited, meaning there is missing information on how the counts are distributed along the energy dependence. To fill these gaps, the energy distribution can be determined by looking at the PHA data from the flyby events.

Whilst the correction of the PHA data doesn't involve the channel boundaries, as an additional function, dependent on final position of the particle it is assigned to the appropriate channel box. This was intended as a check on the correction process to make sure enough of the particles were within the boundaries of the instrument. Instead, having each particle assigned to a channel, and thus an element, means the individual elements can be extracted and analysed separately.

Over the flybys the PHA data is very precise, with multiple readings being taken every second. Despite this the plots can still appear very sparse as each point makes up an individual reading.

Identifying the flybys in the full data set was done using the same method as in section 4.1.1, converting the flyby closest approach date and time into decimal date using equation (35.

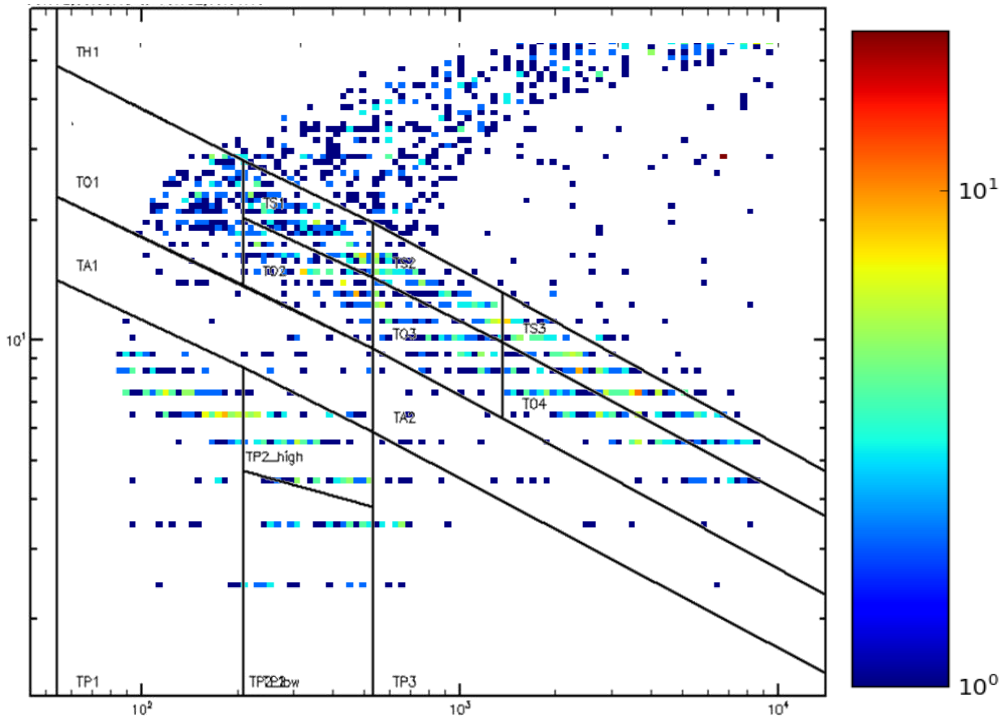

Figure 4.1-3: PHA plot over the E4 flyby overlaid with channel boundaries. Closest approach in 1996 day 354, at 06:52:58

The sparseness of the PHA data can be seen in the flyby plots in Figure 4.1-3, Figure 4.1-5, and Figure 4.1-4. The flyby itself is such a quick event that even at the high record rate there are very few data points to accumulate as a PHA plot. This effect caused issue in section 2.4, due to the lack of visible loci of the elements. The plots generated for section 2.4 had to have sufficient data over a single recording to be suitable to compare the calibration dead layer to.

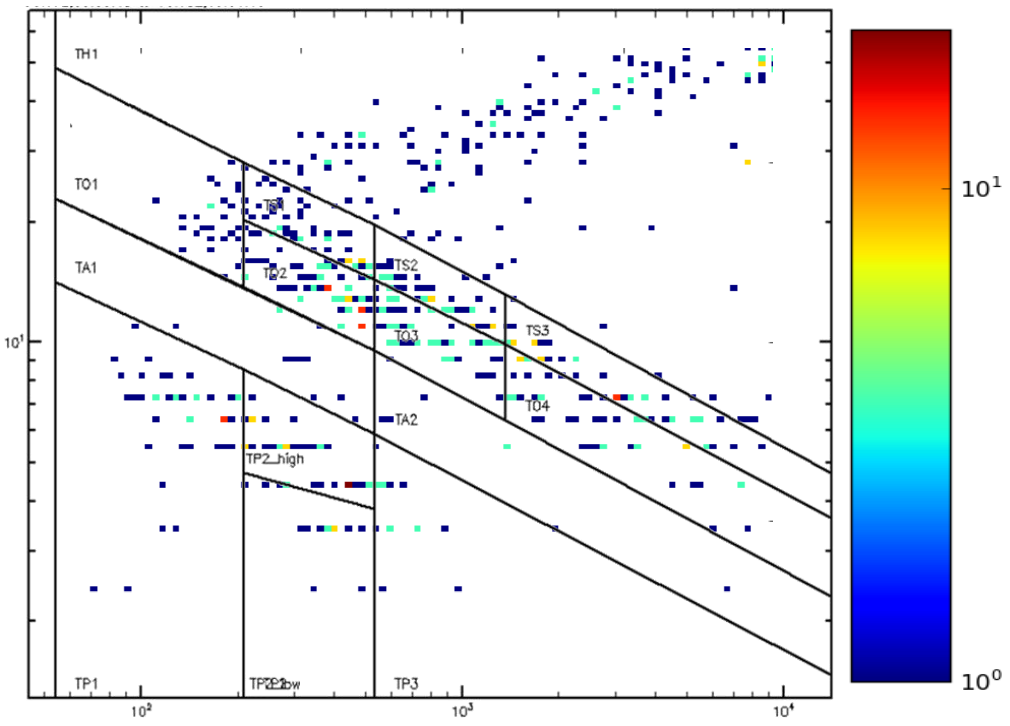

Figure 4.1-5: PHA plot over the E12 flyby overlaid with channel boundaries. Closest approach in 1997 day 350, at 12:03:02

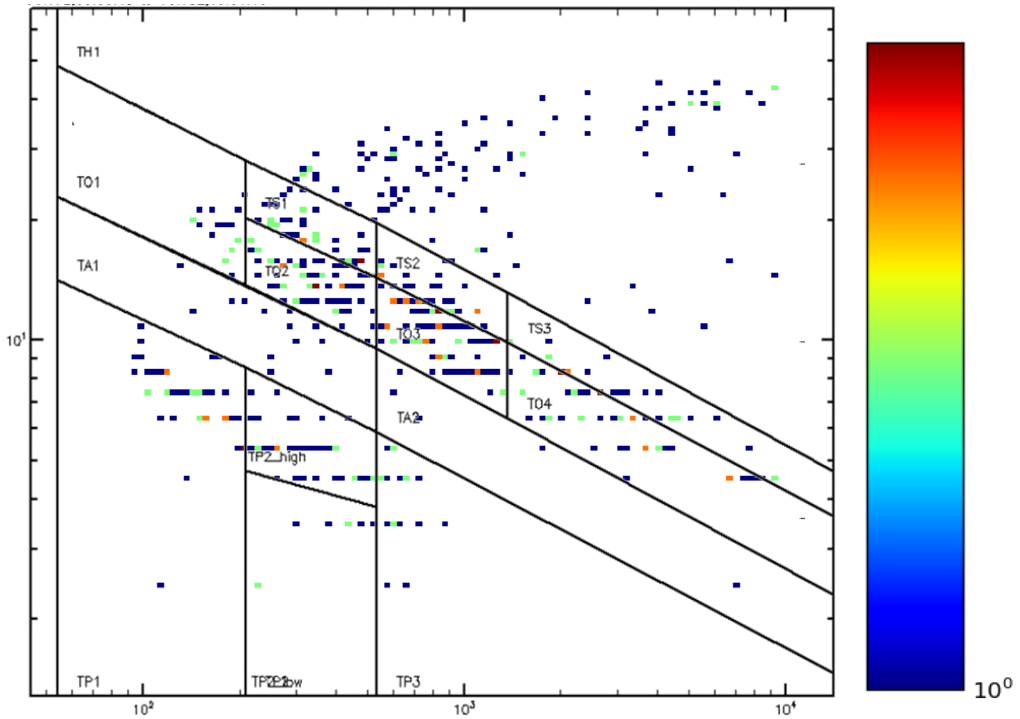

Figure 4.1-4: PHA plot over the E26 flyby overlaid with channel boundaries. Closest approach in 2000 day 3, at 17:59:56

The next step is to isolate the element data to determine the distribution. By using the channel binning in the correction method, the channels for a single element can be put together. The data can then be binned by energy, resulting in a histogram of the distribution by energy for each individual element.

Knowing the distribution of each element is very illuminating. The nature of the high rate data causes it to be limited by the priority system, only the recordings of interest to the current priority are recoded therefore many of the particles will only be recorded as counts. The percentage recorded however should be consistent over the three sulphur channels when matched with the integration of the PHA distribution between the associated energy bounds.

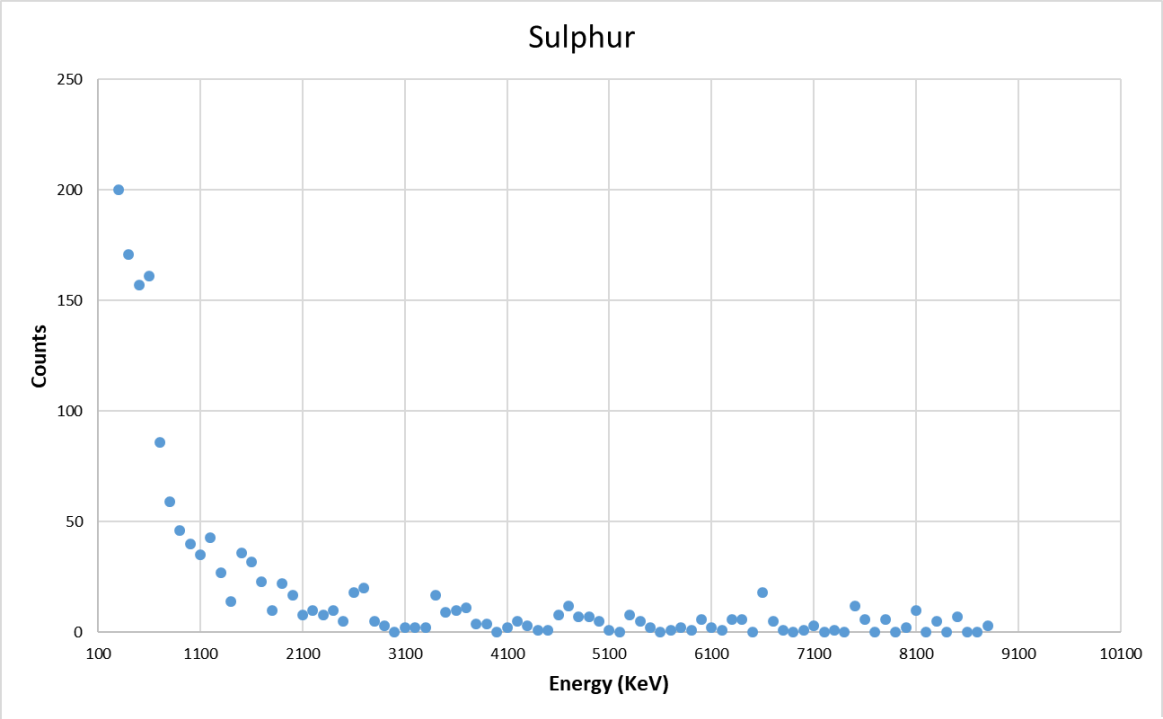

Figure 4.1-6: Histogram of sulphur energy distribution during E12.

Fitting the distribution is done using a simple exponential, using the inbuilt fitting function of python. The elements all fall within the exponential and are well fit using the simple form. The fitting function generates the parameters a, b, and c, that best match the shape of the particle numbers.

$$y = ae^{\frac{b}{cx}} \quad 39$$

The fitting parameters used are given in Table 4.1-2. Figure 4.1-7 shows the fit of the sulphur distribution. The values fluctuate too much for fit to match every point, with the small dip at the low energy around 150 counts cause the fit to be a little sharp during the initial decrease and then causes it to not tend very closely at higher energies.

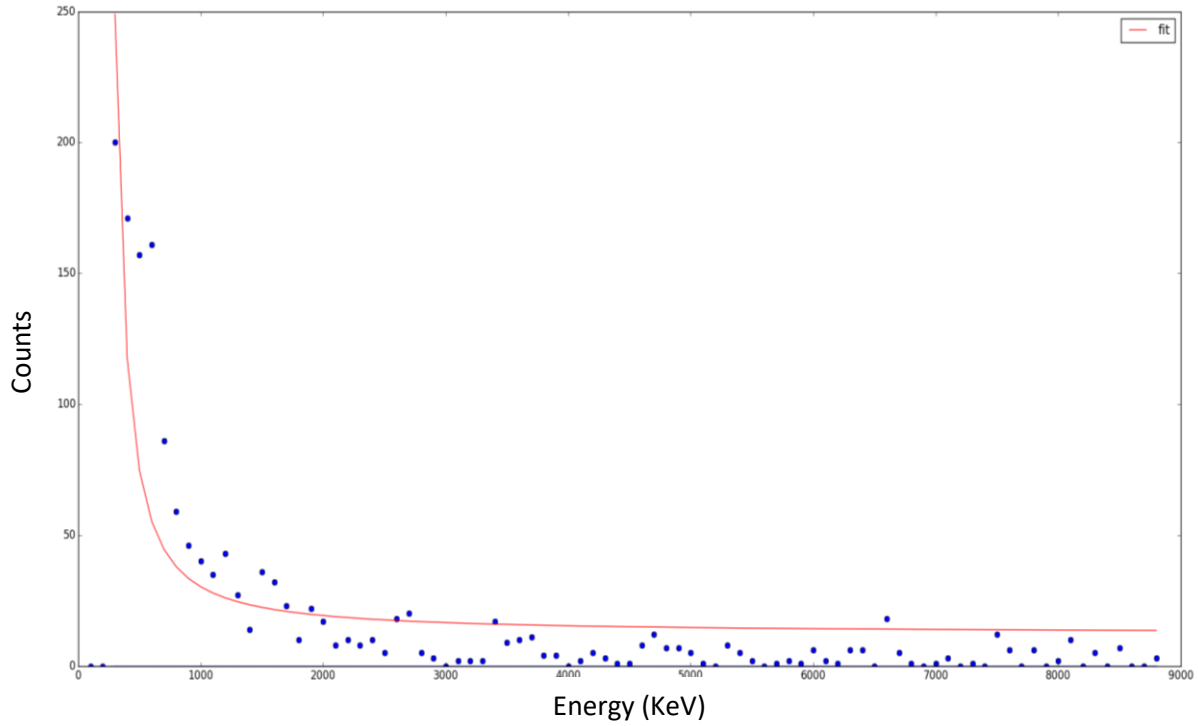

Figure 4.1-7: Fitting of Sulphur distribution

When converting the intensities into the sputtering rate, the distribution of the counts along a single channel wasn't required. By using the energy bounds of the channels and matching these with the integration of the sputtering yield by energy, the individual channel values could be used directly.

Element	a	b	c
Sulphur	12.2421915	$-3.24944216 \times 10^{5}$	$-3.59555975 \times 10^{2}$
Oxygen	43.4801972	$-1.19880231 \times 10^{6}$	$-1.98678420 \times 10^{3}$
Helium	3.82765038	$-7.43239388 \times 10^{3}$	-35.35317313
Hydrogen	21.4401157	$-7.03979210 \times 10^{4}$	$-2.93177209 \times 10^{2}$

Table 4.1-2: fit parameters a, b, and c, for each element distribution.

4.2 Sputtering

The following section overviews the process of sputtering on a porous icy surface as opposed to a more solid non porous structure. The cold environment of Europa and the nature of its icy surface influences the usual sputtering processes.

4.2.1 Sputtering on Icy Surfaces

There are two major processes the determine the sputtering yield; the number of particles ejected for every impacting particle (Fama et al., 2008). These are known as elastic and electronic processes. Elastic sputtering is well understood and can be described with billiard ball like cascade scenarios, electronic sputtering is less understood. The basis of electronic sputtering was discovered during laboratory testing when the cascade prediction of sputtering yield was far exceeded (Brown et al., 1978). The discrepancy was attributed to the electronic energy deposited near the surface.

4.2.1.1 Elastic Sputtering:

When an energetic ion impacts a surface the kinetic energy that it has will dissipate until the particle stops. In a perfect system this energy will pass on to each particle it hits in a billiard ball fashion. However, this can also be more complicated than merely a particle hitting the surface and another particle moving. Overall, there are four kinetic mechanisms that can happen during the impact of a high-energy particle into a surface (Figure 4.2-1) (Ziegler et al., 2010, Johnson, 1998):

a) The incoming atom hits the surface atom and when neither atom has over the displacement energy then they both stay put: Interstitial
b) The incoming atom hits the surface atom; the surface atom retains a higher energy than the displacement energy from the incoming atom. The incoming atom replaces the surface atom as the surface atom sputters from the surface.
c) The incoming atom hits the surface atom; energy passes to the surface atom causing movement deeper into the surface. This surface atom in turn impacts with another surface atom passing the energy again. This continues until the energy has been suitably distributed (B) or a sequential atom leaves the surface (A).

d) The incoming atom hits the surface atom; the energy of the incoming atom distributes evenly leaving both the surface and the incoming atom with a higher energy than the displacement energy. They both move on ejecting two atoms for one incoming.

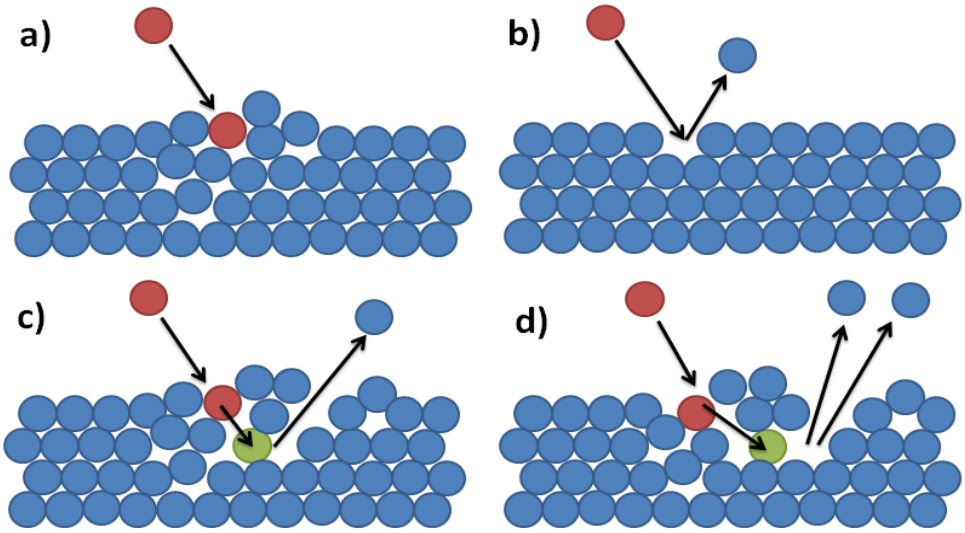

Figure 4.2-1: Billiard Ball dynamical motion showing the four main cases of sputtering. Each initiated by a single particle impacting a surface.

At any point the mechanisms in c and d can repeat ejecting multiple particles at any stage of the cascade. If the kinetic energy remains in the system, there will be movement amongst the particles and some can be driven from the surface.

In a perfectly elastic system there would be no energy loss between impacts and the passing on of momentum between one particle and another. However, in a realistic inelastic system some of the kinetic energy from the impacting particle is imparted into the surface. this is the source of the electrical sputtering

4.2.1.2 Electrical Sputtering

Electrical sputtering is a combination of effects cause by the charged nature of the impacting particles and the structure of the impacted surface. There is also a dependency on the energy of the impactors and the temperature of the surface.

The publications Fama et al., (2007) and Fama et al., (2008), give full detail to this effect. They describe an increase of electric sputtering (S_E) at very low energies, the expected yield from S_E, given as Y_E, passes through a maximum then decreases again with an increase in energy deposited in the ice layer. This can give two values of Y_E for a given

energy. They also determine that the yield is not purely proportional to the energy deposited, but also to the type of impactor.

In Fama et al., (2007) they proposed instead that Y_E at low velocities dominated by a Coulomb repulsion whilst being enhanced by the ionization on the surface of the moons by electron capture caused by the impacting particle.

4.2.1.3 Sputtering Yield

All sputtering is a combination of both elastic and electric sputtering. Electric is independent of temperature (Fama et al., 2008), however it dominates the yield at the very low energies. As the energy increases to those more regularly expected around the surface of Europa, the elastic sputtering becomes the more prominent contributor to the overall sputtering yield. The change in the mechanisms sits around 100KeV (Cassidy et al., 2013). Above this energy the yield becomes dependent on the temperature; due to the interactions on the surface affecting the structure (Carlson et al., 2009).

Strictly speaking the process of radiolysis is not ejecta as is usually defined as sputtering. The effect of radiolysis on Europa's surface is the decomposition of ice producing H_2 and O_2. These escaping H and O molecules contribute to the atmosphere of Europa. Despite this the radiolysis is still counted in the temperature dependent yield calculations. This means that this portion of erosion on the surface cannot be calculated using the incoming flux on the surface as it is independent of the impacting particles. However, the temperature dependence only takes effect above 100KeV; when evaluating the sputtering yield from the EPD data the individual particles are mostly under this threshold (Table 4.2-1)

The yield is also highly dependent on the surface the particles are interacting with (Cassidy et al., 2013). Sputtering is not uniform over the surface, the differing grain sizes of the porous regolith like ice structures means as sputtering continues the surface will become more uneven (Domingue and Verbiscer, 1997). This unevenness of the surface lowers the sputtering yield; the sputtered particles from deeper in the surface become far more likely to re-impact the surface on their way out rather than being cleanly ejected. These particles simply re-embed or freeze to the surface and so then cannot be counted towards the yield.

However, the regolith of the surface does assist the sputtering process too; the crystalline structure that allows this non-uniformity to appear on the surface also aids in the sputtering yield. An incoming particle can impact on any of the randomly oriented grain structure and sputter a particle off it. Under testing these two effects cancel each other out and are mostly ignored when calculating sputtering yields (Cassidy and Johnson, 2005).

4.2.2 Sputtering Rate

The calculations of sputtering on the surface of the moons has been heavily investigated; both in physical test and in theory through modelling. This has culminated in known sputtering yield by energy curves for the elements in the Jovian system (Cassidy et al., 2013, Fama et al., 2008, Fama et al., 2007, Johnson et al., 2008).

Cassidy et al., (2013), offer a review of the theoretical and experimental sputtering yields, piecing together from low to higher energies the changes in the yields with energy and element. They conclude that there is a split in sputtering mechanisms at 100KeV where the electric and elastic dominance changes.

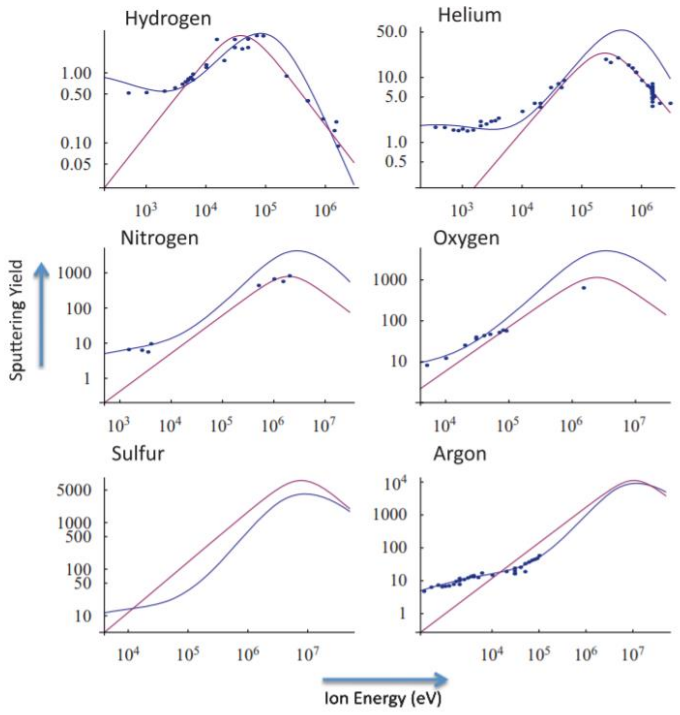

Fig. 3. Compilation of sputtering yield data and theory. Experimental data points best match the Fama et al. curve (blue) below ~100 keV and match the Johnson curve (red) above 100 keV. There are no available experimental results for sulfur ion sputtering, but the calculated sputtering yield is shown here because sulfur is the most important sputtering agent at Europa. The data were compiled from various experimental sputtering papers by R. E. Johnson and M. Liu at http://people.virginia.edu/~rej/h2o.html. Note that the cold ions hit Europa at ~ 500 eV (oxygen) or ~ 1000 eV (sulfur) while the hot ions have a wide range of energies (100s of keV to MeV). (For interpretation of the references to color in this figure legend, the reader is referred to the web version of this article.)

Figure 4.2-2: sputtering yields from Cassidy et al., (2013), showing two modelling results, red and blue curves, overlaid with experimental results from Fama et al.,(2008).

This split can be seen in Figure 4.2-2 the red lines (modelled using the electric sputtering theory) and blue lines (modelled using elastic sputtering theory) mark the separate theories that were used to try and match the data. The red line fits best above 100KeV; with investigations in this area most done by Johnson. R. The blue line is developed by Fáma, from experimental data in the low energy range. These sputtering rates can be applied to the intensity rates calculated above in section 4.1.2 to generate a rudimentary estimation of the global sputtering rate.

A note on units for the intensity with the sputtering rate; the sputtering rate is given in units of eV rather than KeV. Therefore, from this point on the energy units will be in eV to keep consistency and reduce any conversion errors later in the calculation.

The intensity can be easily converted into eV units be including the energy boundaries in eV rather than KeV. This puts the final units of intensity as: $cm^{-2}s^{-1}eV^{-1}$. The sputtering yield, given as a function of energy in Figure 4.2-2, needs to be integrated over the limits of each channel. By limiting the integration between each channel boundary, the distribution of the counts over the channel are no longer needed. The limits for the sputtering yields need to be integrated over are given in Table 4.2-1.

Channel	Lower limit (eV/amu)	Upper limit (eV/amu)
TS1	6562 (6.5KeV)	16562 (16KeV)
TS2	16562 (16KeV)	42968 (42KeV)
TS3	42968 (42KeV)	312500 (312KeV)
TO1	3437 (3.4KeV)	13125 (13KeV)
TO2	13125 (13KeV)	33125 (33KeV)
TO3	33125 (33KeV)	85937 (85KeV)
TO4	85937 (85KeV)	625000 (625KeV)
TA1	18333 (18KeV)	176666 (176KeV)
TA2	176666 (176KeV)	3333333 (333KeV)
TP1	27500 (27KeV)	105000 (105KeV)
TP2	105000 (105KeV)	265000 (265KeV)
TP3	265000 (265KeV)	5000000 (5000KeV)

Table 4.2-1: Channel boundary limits for sputtering yield integration.

Before this integration can be done the decision must be made to which of the sputtering yield curves to best match against from the two available models in Figure 4.2-2. Despite the experimental data on the lower energy sputtering, for simplicity and ease of fitting the yields have been taken using the data, compiled from various experimental sputtering papers by R. E. Johnson and M. Liu available at http://people.virginia.edu/~ rej/ h2o.html.

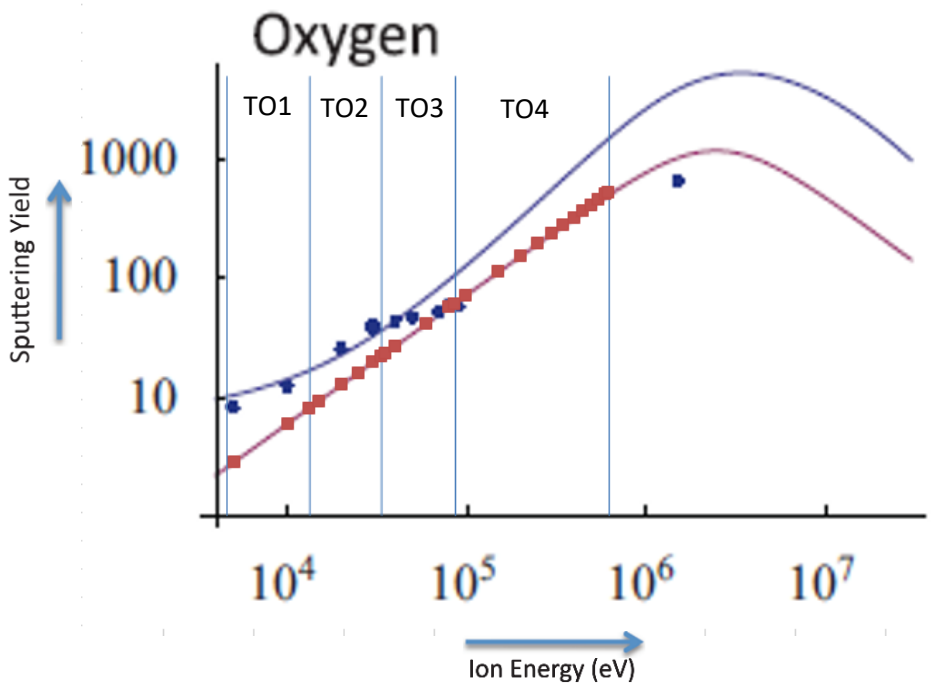

Figure 4.2-3: Red points: Fit of the Oxygen sputtering yield to be integrated over, channel boundaries are marked in the blue vertical lines. (Blue points show experimental results)

Once the yield has been fitted the integration can be done between the channel boundaries. For oxygen this is shown in Figure 4.2-3 with the vertical lines denoting the channel boundaries. The integrated values for the yields of each channel can then be simply multiplied by the intensity of the channel itself at closest approach.

For helium, the decision to fit to the higher energy experimental yield from RE Johnson is clearer. There is a high volume of experimental data spanning the range of the instrument, the same is true of the Hydrogen fitting, and to some extent the oxygen.

The impactor contributing the most to the sputtering on the surface of the moons is sulphur, however, there has been no experimental research done into the physical processes on water ice, until very recently. This means that the yields for sulphur, at the time of this study, are purely based on applying the theory of the other elements to sulphur

without experimental results to back them up. This can be seen in Figure 4.2-6 with the lack of dark blue markers of real data.

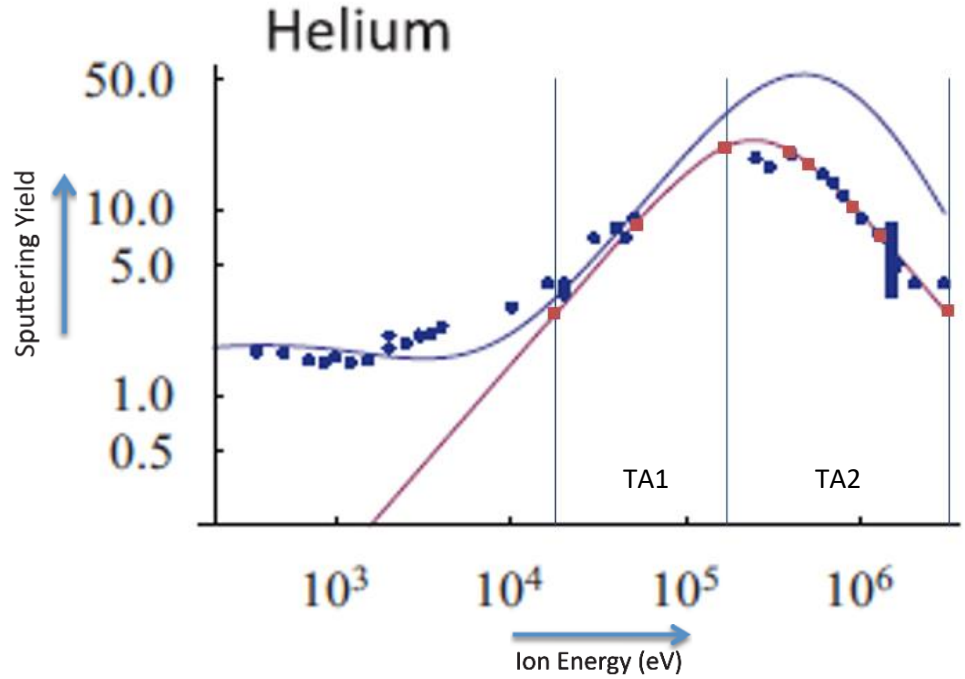

Figure 4.2-4: Red points: Fit of the Helium sputtering yield to be integrated over, channel boundaries are marked in the blue vertical lines. (Blue points show experimental results)

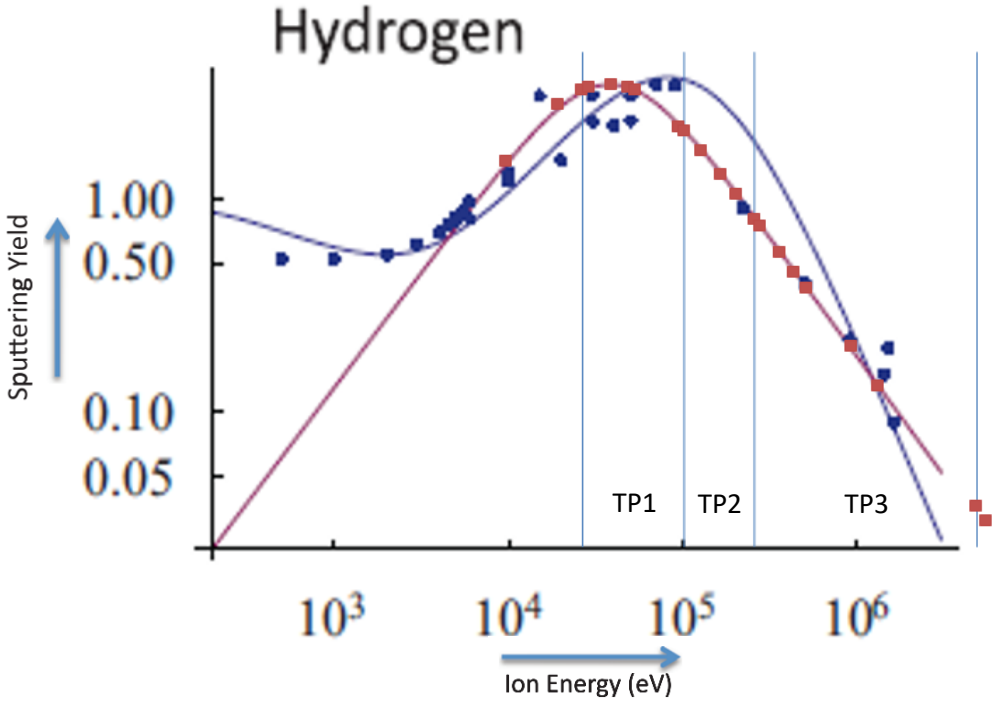

Figure 4.2-5: Red points: Fit of the Hydrogen sputtering yield to be integrated over, channel boundaries are marked in the blue vertical lines. (Blue points show experimental results)

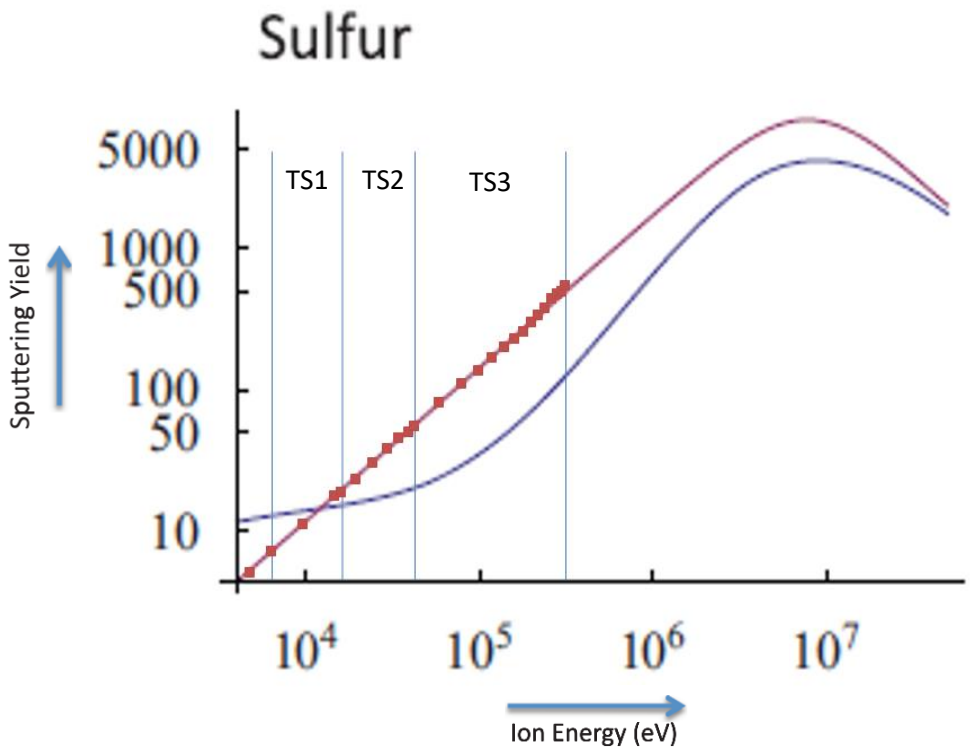

Figure 4.2-6: Fit of the Sulphur sputtering yield to be integrated over, channel boundaries are marked in the blue vertical lines. (Blue points show experimental results)

The decision to use the sputtering yields predicted using electric sputtering theory proved valid with the completion of the fist sulphur sputtering on ice measurements, completed by (Galli et al., 2018). They found that the experimental results matched better with this prediction than that produced using the elastic sputtering theory. This can be seen in the matching figure (Figure 2 of Galli et al., 2018) in the publication.

This method of calculating the sputtering yields, bypasses some of the more complex subtleties of the methods described in (Cassidy et al., 2013, Carlson et al., 2009, Paranicas et al., 2002). For a truer calculation the directionality of the flyby needs to be considered, the portion of the moon covered by the closest approach will be affected differently as due to the dichotomy of the surface and the co-rotation speed of the surrounding plasma.

The simplicity of the calculation however is not a major issue as the aim in this case is to investigate the changes the correction has had on the sputtering yield. Even though the new values cannot be accurately compared to current literature, the comparison of a before and after correction sputtering rate is valuable nonetheless.

4.2.3 Results and Comparisons

The sputtering yield is then multiplied by the channel intensity and summed, this gives the overall sputtering rate per cm^2 per second. This is a global rate, an average over the surface that does not take into account any dichotomy of the surface or the directional flow of the co-rotation. As mentioned above the values calculated are a very rough estimate, used to assess the usefulness of the corrected data with regards to the changes in ratios.

Table 4.2-2 gives the rough values of the global sputtering rate of particles being lifted from the surface of Europa per second. These values are generated from the corrected data sets. Overall, they match well with the previously calculated values for whole surface rates.

Element	Total Sputtering Rate from Europa per second (s^{-1})			
	E4	E12	E15	E26
Sulphur	~4.03×10^{26}	~3.12×10^{27}	~4.00×10^{27}	~4.43×10^{27}
Oxygen	~2.00×10^{26}	~1.03×10^{27}	~1.17×10^{27}	~1.43×10^{27}
Helium	~1.26×10^{26}	~3.04×10^{26}	~3.30×10^{26}	~4.04×10^{26}
Hydrogen	~2.53×10^{25}	~7.53×10^{25}	~8.28×10^{25}	~7.32×10^{25}
Total:	~7.54×10^{26}	~4.53×10^{27}	~5.58×10^{27}	~6.34×10^{27}

Table 4.2-2: Estimations of the number of particles lifted from the surface per second over the surface of Europa, due to sputtering, using corrected data.

The interesting factor of the data however is not in matching the values to those previously calculated, but in the effect the correction has had on the values. To investigate this, the before and after data for the flybys of interest are split into constituent parts. The values for the first of the Europa flybys is shown in Table 4.2-3. The values are grouped by channel, and given as an average sputtering rate over a cm squared area.

As expected the bulk of the sputtering rate comes from the oxygen and sulphur particles, this is the same both before and after the correction. The overall increase is not that large, however most notable is where the increases come from. Despite decreases in TO2 and TO3, the increases in all sulphur channels make up for this loss. Interestingly there is an additional increase in the higher energy oxygen channel TO4. This is most likely as

there is a considerable influx of particles from the sulphur channels into it that the correction may not fully account for whilst, in addition, accounting for the decrease in efficiency. The oxygen channels being the most complicated to correct for, may have suffered an imbalance in removing the incoming particles whilst adding those lost to efficiency issues.

Channel	E4 flyby Sputtering rate Pre-Correction ($cm^{-2}s^{-1}$)	E4 flyby Sputtering rate Post-Correction ($cm^{-2}s^{-1}$)
TS1	~9.81×10^{6}	~9.96×10^{6}
TS2	~1.66×10^{6}	~1.69×10^{6}
TS3	~1.38×10^{6}	~1.40×10^{6}
TO1	~3.34×10^{5}	~3.34×10^{5}
TO2	~2.95×10^{5}	~2.91×10^{5}
TO3	~3.61×10^{6}	~2.95×10^{6}
TO4	~5.35×10^{5}	~2.88×10^{6}
TA1	~1.69×10^{5}	~1.68×10^{5}
TA2	~1.17×10^{5}	~3.90×10^{6}
TP1	~6.29×10^{5}	~6.03×10^{5}
TP2	~1.28×10^{5}	~1.23×10^{5}
TP3	~9.20×10^{4}	~9.10×10^{4}
Total	~1.88×10^{7}	~2.44×10^{7}

Table 4.2-3: Sputtering rate breakdown during the E4 flyby calculated from original data and corrected data.

There is also a high increase in TA2; the higher helium channel. This is very significant increase in terms of the sputtering rates; increasing by around a factor of 20. As another of the complicated elements to correct, the issue is again likely to be similar to the issue with TO4.

Another possibility to account for these large increases is in the accuracy of closest approach. For each flyby the singular value of the closest approach is taken; in each channel this is a single value out of 84117 values. It is possible that during the correction the process of filling the missing data with estimates and then removing these estimates post correction, could have shifted the indices of the true closest approach. With the count rates reduced to eleven-minute averages with data compression the peak of the values at the closest approach can be very different the values on either side. The best way to counter this is to assess the surrounding values or to average the changes.

Channel	Average over E4 flyby Sputtering rate Pre-Correction ($cm^{-2}s^{-1}$)	Average over E4 flyby Sputtering rate Post-Correction ($cm^{-2}s^{-1}$)	Difference (Corrected – Original)
TS1	~1.01×10^{7}	~1.02×10^{7}	1.45×10^{5}
TS2	~1.73×10^{6}	~1.76×10^{6}	2.74×10^{4}
TS3	~1.38×10^{6}	~1.40×10^{6}	2.60×10^{4}
TO1	~3.31×10^{5}	~3.3×10^{5}	-4.37×10^{1}
TO2	~3.09×10^{5}	~3.06×10^{5}	-3.90×10^{3}
TO3	~3.14×10^{5}	~3.06×10^{5}	-8.54×10^{3}
TO4	~5.18×10^{5}	~2.89×10^{6}	2.37×10^{6}
TA1	~1.65×10^{5}	~1.64×10^{5}	-1.35×10^{3}
TA2	~1.25×10^{5}	~4.21×10^{6}	4.09×10^{6}
TP1	~1.35×10^{5}	~6.51×10^{5}	-2.82×10^{4}
TP2	~1.35×10^{5}	~1.30×10^{5}	-4.61×10^{3}
TP3	~9.99×10^{4}	~9.89×10^{4}	-1.07×10^{3}

Table 4.2-4: Sputtering rate average from during the E4 flyby calculated from original data and corrected data

.

Table 4.2-4 contains the averages of the three nearest data points for each channel and the difference between the before and after correction values. A positive difference denotes an increase in counts from the correction process and a negative difference is a decrease in counts. Overall the changes in counts are small in comparison to the average values. This is expected with the nearness to the beginning of mission and low thickness of dead layer.

Looking at other flybys shows the same pattern of increases in the sulphur channels, decreases in the oxygen channels and low change in the other channels. In all cases the highest energy channel of each element loci are gaining more particles than the rest; or losing the least if the difference over the whole set is still decreasing. This is due to the amount of energy shift at high energy. Visually this can be seen in Figure 2.5-1, the high energy particles do not lose as much energy when passing through the dead layer. This has the effect of fewer particles slipping from a high mass channel into a low mass channel; i.e. from TS3 to TO4 or TO4 to TA2. Therefore, the effect of the particle movement correction is not as well balanced in these channels.

This is still seen even when averaging over all the flybys (Table 4.2-5). As the decay becomes more severe, the correction will be more balanced in the high energy channels.

The energy lost to the dead layer becomes higher in all channels with a thicker dead layer, however in the higher channels the amount lost becomes significant enough that the correction can account correctly for it.

Channel	Average over All flyby Sputtering rate Pre-Correction ($cm^{-2}s^{-1}$)	Average over All flyby Sputtering rate Post-Correction ($cm^{-2}s^{-1}$)	Difference (Corrected – Original)
TS1	3.43×10^{7}	4.79×10^{7}	1.69×10^{7}
TS2	7.25×10^{6}	8.49×10^{6}	1.86×10^{6}
TS3	2.17×10^{7}	2.74×10^{7}	6.93×10^{6}
TO1	1.12×10^{6}	1.03×10^{6}	2.32×10^{4}
TO2	1.35×10^{6}	9.65×10^{5}	-3.08×10^{5}
TO3	2.63×10^{6}	2.00×10^{6}	-5.98×10^{5}
TO4	2.00×10^{7}	1.89×10^{7}	3.50×10^{6}
TA1	9.25×10^{5}	7.51×10^{5}	-4.22×10^{4}
TA2	9.58×10^{5}	6.20×10^{6}	7.00×10^{6}
TP1	1.02×10^{6}	9.12×10^{5}	1.11×10^{4}
TP2	3.90×10^{5}	3.51×10^{5}	1.00×10^{4}
TP3	4.00×10^{5}	3.54×10^{5}	-5.75×10^{2}
Total	9.20×10^{7}	1.15×10^{8}	3.53×10^{7}

Table 4.2-5: Sputtering rate average over all flybys calculated from original data and corrected data.

The total average change is relatively small; the decreases of some of the channels counteracting the increases. The amount of sputtering that each element contributed also plays an important role in this, that is difficult to see when working in the units of sputtering. In terms of average count rates; the sulphur channels gain fewer particles than the oxygen channels lose. However, as the sulphur particles are a far higher contributor to the sputtering rate, there is still an increase in the number of particles sputtered from the surface, even though there is a net decrease in the number of particles hitting the surface on average.

4.2.4 Comparison with Current Estimations

Much of the research into the sputtering on Europa is calculated in terms of depth of surface eroded over the lifetime of Europa. The common units for this is metres per gigayears (Gyr); Gyr in this case is used in place of billion years to avoid confusion. Table

4.2-6 contains some of the earlier and more recent estimates of the surface erosion rate on Europa; not all of these are calculated from sputtering.

Depth in Gyrs	Sputtering rate	Author/Paper	Comments
6m – 100m	-	Johnson et al, 1981 Eviatar et al, 1981	Pre-Galileo data
200m	-	Ip et al., 1998	Net erosion rate, Early Galileo EPD data
14m	-	Tiscareno et al., 2002	Estimated 42% - 86% redeposit on the surface.
16m	-	Cooper et al., 2001	Globally Averaged
70m	$\sim 7 \times 10^{9}\ cm^{-2}\ s^{-1}$ or $\sim 2 \times 10^{27}\ s^{-1}$	Cassidy et al., 2012	Globally Averaged
-	$\sim 2 \times 10^{27}\ s^{-1}$	Paranicas et al., 2002	Globally Averaged

Table 4.2-6: Collection of current literature estimates of sputtering/erosion rates on Europa

Both Cassidy et al., (2013) and Paranicas et al., (2002) use the same sputtering yield values; the ones that I have also used in generating sputtering rates. These publications are two of very few that have included a specific value of the sputtering rate calculated from EPD data. The other estimations in Table 4.2-6 either use other methods for the erosion rate or have only passed over the sputtering in passing; some even using pre-EPD and very early EPD data.

In comparing the before and after values with those available in the literature, the accuracy is very hard to pin-point. With each conversion of units from the raw counts rates introduces variability into the final values. Despite this when comparing directly, using the E12 orbit values, as has been used in Paranicas et al., (2002) both the before and after values match well at:

Pre-correction data global sputtering rate:	$3.90 \times 10^{27}\ s^{-1}$
Post-correction data global sputtering rate:	$4.53 \times 10^{27}\ s^{-1}$

The values of the original data are higher than the previously calculated rate; however as mentioned when reducing this to raw values only a few counts can make a difference when converting between units. The corrected version is, as expected higher than the original. Even accounting for a very small average increase in actual count rates. the increase is where it has the most impact on the sputtering rate; in the sulphur particles.

4.3 Conclusions

This chapter focuses on combining the results of the previous two chapters (2 and 3). Using the corrected PHA plots for an idea of the distribution of the particles, and the overall count rates combined with this to fully grasp how many and at what energy the particles are impacting the surface of Europa.

Converting from an overall count of the number of particles to the sputtering yield is a long series of calculations, that whilst long is relatively straightforward. Interestingly the effect of small changes is the most important finding in this chapter. The additional sulphur and reduced oxygen were relatively balanced; breaking down the overall sputtering and investigating the individual constituents allowed even more insight into the operation of the instrument.

The final results of averaging over all the flybys together, separated by channel, helps to show how the sputtering rate can be easily affected and shows just how important the accuracy of the numbers needs to be. Even with this need for accuracy, it is likely that many of the current estimations are lower than they should be. By only looking into the closest approach count rates; and not accounting of any non-uniformity over the surface, the sputtering fluctuations are not investigated. A full comprehensive study of the surface can be completed in future to update the expected results.

Whilst the correction will offer a better picture of the situation close to the surface of Europa the true reality will not be apparent until the arrival of NASA's Europa Clipper for the Europa surface, or ESA's JUICE for Ganymede's surface.

5 Surface Age

The final chapter focusses on the applications of the sputtering values for dating the surface of Europa. It presents a proof of concept method for combining the sputtering rates and the in-depth geological knowledge of the surface to begin assessing the date/age of the surface and its features. With the arrival of Europa Clipper and JUICE to the Jovian system the high mapping capabilities of these two spacecraft, will only improve on the possibilities presented here.

5.1 Surface Feature Formation and Cross Cutting

This method is based on the geological technique identifying cross cutting in the features of the surface. This is a commonly used method for dating surface features and identifying which areas are older than others. However, this method can only give information on the general timeline of the features; 'this one is older than that one' for example. To get a better understanding of the surface age the time gaps between the features need to be investigated.

In section 1.4.3 the connection between the visual appearance of linea and their age was described in detail. This is the basis for dating the surface. By focusing mainly on the linea that cover the surface abundantly the overlaps can be used to gather information on how the areas in-between are related to each other in a time scale.

The ages of the linea, as described above, are described by their visual appearance form above. By looking at these features again and instead considering that there is a significant amount of height erosion also contributing to the appearance of the feature, a more useable classification is developed. The mechanism for generating the ridges is suggested to be a crack in the ice shell which allows the 'slush' from beneath to be pushed up. During Europa's orbit the gravitational stresses from Jupiter and the other moons cause the cracks to open and close, as the slush from beneath forms into the symmetrical multi-ridged formation.

Research from Hoyer et al., (2014) and Fagents et al., (2000) explains formation and mechanisms of these features, whilst offering in depth analysis of specific linea. A more

general approach focusing on the formations is Greenberg et al., (1998) and Geissler et al., (1998) who offer an overview of general formation processes. The best visuals of the formation mechanics described above are from figures 2 and 6 of Greenberg et al., (1998), shown in Figure 5.1-1.

Interpreting this and combining it with the classification in section 1.4.3, the formation can be thought of as a cross section. With each ridge formed in the intermediary time there will be an amount of erosion to the material. With each ridge addition not only will the previous ridge be older it will contain less material. Consider then the stages of formation:

- Fractures (Youngest of the lineaments): These are very narrow and tend to only show-up as a one-pixel wide line on images even at very high resolution. This is the base point of the aging, the initial formation cannot be dated, except by the surrounding formations which it is cutting across (more on this later)
- Ridges (next youngest): These have a raised relief (100 – 200m altitude) they can have double or multiple ridges symmetrically on both sides. The difference in the heights from the initial ridge, now the outer ridge, and the new inner formation will give some estimation of the time cycle. Assuming the same amount of material is produced each for each ridge, the amount lost determines the time passed.
- Triple bands: (Older): These have multiple ridge sets flanked by smooth dark margins. The same is true of any additional ridges, dependent on the amount of material produced each time and the erosion rate, the period of time between each ridge formation can be calculated based on the height differences.
- Ancient bands (Oldest): These are very similar to the triple bands but they are no longer active. As they age, they relax; this is characterised by a change in the albedo. The ancient bands stand out as their albedo is brighter than the surrounding albedo. The relaxation of the non-active bands can be solely attributed to erosion. By comparison to other bands in the area and the suspected initial height of the ridges, the overall age of the bands can be determined from the overall material lost.

This can in theory be used to give some indication of the age of a feature from initial eruption to non-active scar on the surface. To date features in relation to others around it,

the process of cross cutting can be used. Section 1.5.2.3, covers the basics of how features can be overlaid and the simplistic approach to determining age from these clues. This allows for a timeline to be built up from one feature to the next rather than focusing on a singular feature and simply knowing its age, the age of a largely active area can be found.

By assessing the age of the each linea, as each feature crosses another the difference in the undercut feature will be the time of formation of the overlying line. Of course, in this context the ages are in relation to the oldest visible feature, with any older surfaces lost underneath the newer features. However, any other method of dating the surface i.e. crater counting, are also limited by this overlaying of features. Commonly this visibility of an oldest feature determines the resurfacing age.

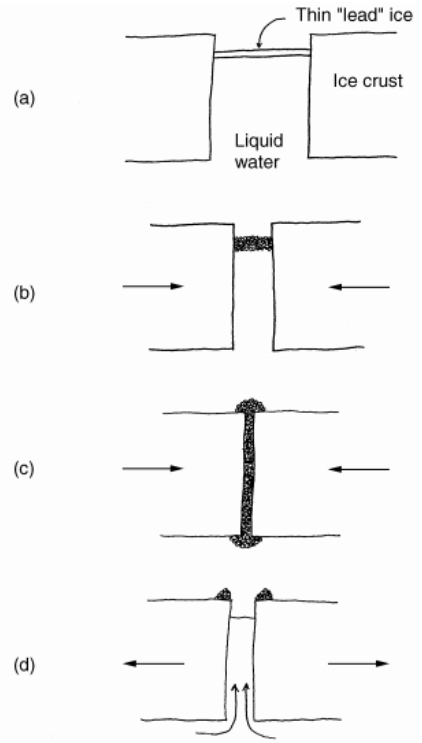

FIG. 2. A model for ridge formation by diurnal working of a preexisting crack. (a) After the crack opens and fills with liquid water, ice quickly forms at the fresh surface. (b) The crack then closes, forming a narrowing, but vertically thickening, raft of crushed ice. (c) Some of the slurry is squeezed onto the surface as the crack closes. (d) The crack reopens, leaving a double ridge of surface deposit, and liquid water enters renewing the cycle.

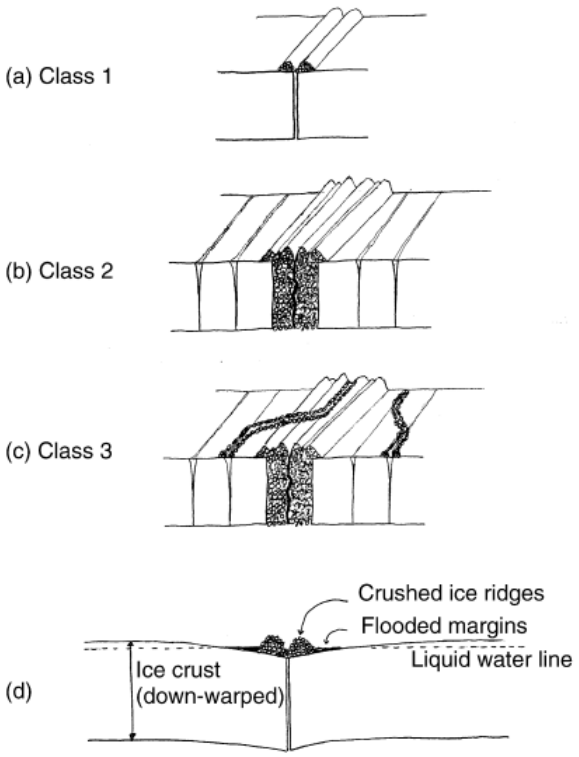

FIG. 6. Schematic cross-sections of the classes of ridges defined here, showing structure expected on the basis of our model of their formation. (a) Class 1 forms by repetitive diurnal working as shown in Fig. 2. (b) Incomplete extrusion of ice debris allows a crack to ratchet open during the diurnal working, creating a Class 2 ridge structure. If there is crustal downwarping due to the load, parallel side cracks may form. (c) Diurnal working may activate some of the side cracks along all or part of their lengths, building small lateral ridges analogous to formation of Class 1 or 2, but becoming part of an interbraided complex characteristic of Class 3. (d) If the weight of ridge complex warps the crust enough that part of the surface is below the water line, liquid may seep through the porous ridges and flood the margins, modifying and coloring the surface, as observed on Europa.

Figure 5.1-1: Ridge formation diagrams from (Greenberg et al., 1998).

As mentioned in section 1.5.2.3, there are many flaws with cross cutting as a method of dating a surface. One of the key drawbacks on the surface of Europa is the high number of linea and the sometime vastly confusing winding nature of them. To cover the whole surface using this method would require a thorough study and possibly the awaited imaging promised by the upcoming NASA mission Europa Clipper. Instead the method can be investigated and tested on a small section of the surface with sufficient imaging and reasonably simple linea formations.

The area of surface to be tested was selected based on the available features clearly visible, and the high-resolution images from multiple angles. This allows the formation of height maps of the surface and interesting features to investigate.

5.1.1 Imaging the Surface

The whole surface of Europa was mapped by SSI the Solid-State Imaging device, on board Galileo. The coverage was extensive and incredibly detailed for the limitations of the spacecraft downlink; however, the high-resolution coverage is patchy. Only a very small portion of the surface was covered with the highest resolution available. Figure 5.1-2 maps the outlines of all the available images, colour coded to their orbit. The variation in the areas covered is due to the differences in orbit, approach and lighting conditions of the moon at the time of closest approach.

To analyse the surface in enough detail to assess the ages and erosion rates of the ridges, the images need to be of high enough resolution. In addition to this to ascertain the height profiles of the ridges, there needs to be an overlap of the images such that an elevation model can be generated. The highest resolution images captured by SSI are shown in Figure 5.1-3, together with zooms of the selected regions.

Whist these areas offer the highest resolution there is very little overlap of the images in which to construct a height map of the area. A commonly used set of overlapping images is a small section near the Tyre crater, to the southeast of the main impact structure. First investigated and published during conference proceedings Chuang et al., (1998) and further investigated by Kadel et al., (2000), the images offer a perfect opportunity for forming 3-dimensional images; more on the process of this later.

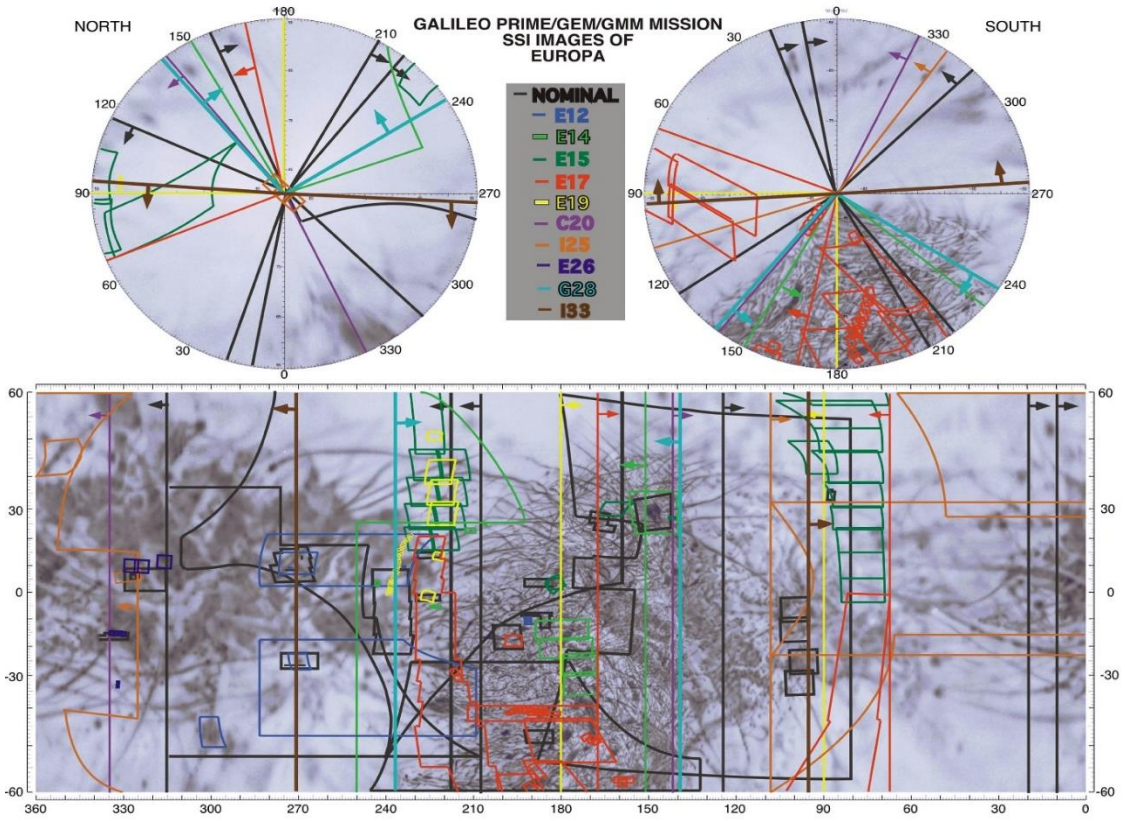

Figure 5.1-2: Overlapping coverage of the Galileo flybys of Europa and the camera views available from chapter 15 of (Bagenal et al., 2004)

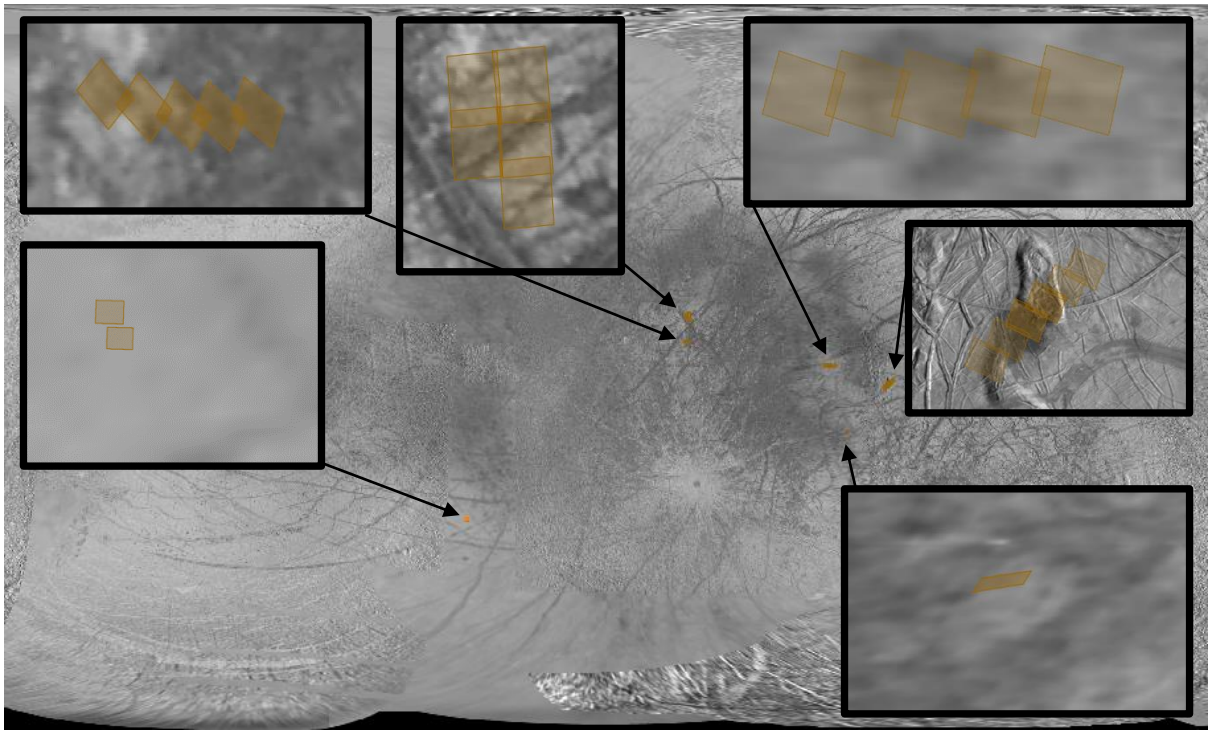

Figure 5.1-3: Outline map of High resolution areas of coverage from SSI, generated using USGS's (US Geology Survey) PILOT mapping software (https://pilot.wr.usgs.gov/)

The images individually don't appear to overlap from the square images available in the Planetary data system, but under closer inspection the common features can be picked out and matched. During the E15 flyby the images were taken in swift succession, during the overpass. First set taken is shown highlighted in red in Figure 5.1-4, taken from left to right as seen in the orientation of the image. The remaining three images were taken approximately 7 minutes later, from a more overhead position of the spacecraft.

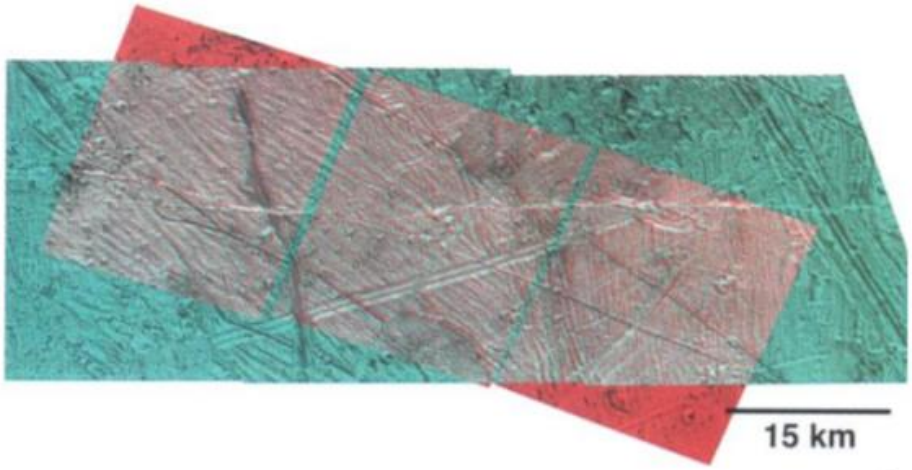

Plate 1. Three-dimensional anaglyph of a portion of the high-resolution E-15 image data.

Figure 5.1-4:Overlapping of singular images from SSI mapped to form a stereo set with which a 3D image and height map can be produced. Image from (Chuang et al., 1998) conference proceedings later published, with caption, in (Kadel et al., 2000).

The very short time gap between the two image sets is vital in this case for adapting the images into a stereo set. For almost all the other image overlaps, the images were taken during separate orbits. This changes the illumination of the features and can generate false heights with elongated or contracted shadows. In these images the light is from the lower left of the image, with north towards the top of the image.

Figure 5.1-5 shows the first image set taken during the approach. Taken looking towards the pole the images appear somewhat shortened due to the curvature of the latitude of the surface; compared to the viewing angle of the camera on a flat surface. The north pole of Europa is to the top right of the image, with the spacecraft at a far lower latitude and with a close longitude of: 14.667˚ and 148.243˚. The image location is at: 31.267˚ and 142.865˚ Latitude and Longitude; the coordinates marking the top left-hand corner of the left most image.

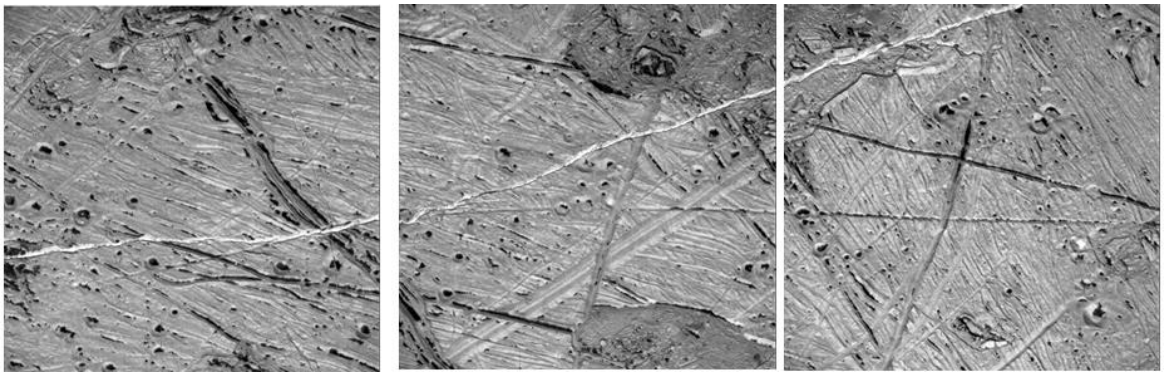

Figure 5.1-5: Composite image of the first set of Images shown in red in Figure 5.1-4. Images taken at: 1998-05-31 21:10:34

The images are taken in a scanning motion from left to right in Figure 5.1-5, starting with the furthest point from the camera working closer. The slight offset in the images seen in Figure 5.1-4 shows the movement of the spacecraft during the duration of the image capture.

Comparing this to the other set of images (Figure 5.1-6); although they are taken very shortly after, the spacecraft is now at a position of 13.477˚ Lat. and 109.583˚ Long. Whist this is further away from the image site; the angle of viewing is favourable. The same scanning method is used in this case, however there is less curvature to deal with.

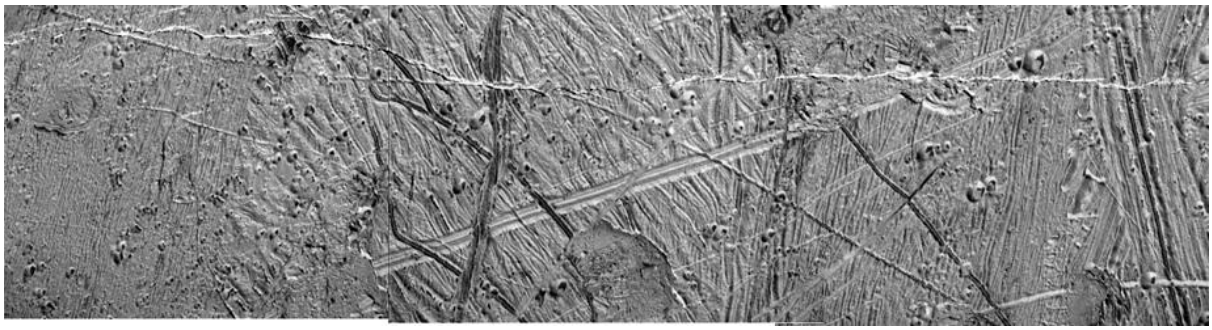

Figure 5.1-6: Composite image of the second image set. Taken at: 1998-05-31 21:17:38. Shown in blue in Figure 5.1-4.

When viewing the image sets individually it can be hard to see how they overlap, given the positioning of the spacecraft. Both image sets need to be adjusted to fit the features together, and to account for the viewing angle. These difficulties have always been associated with imaging a curved surface as a flat image. However, most mapping software systems such as Arc GIS, contain inbuilt routines for calculating these alterations.

Using mapping routines, the images are simple to overlay and within reasonable accuracy. In addition to this, the outline can be overlaid onto any globe of choice: Figure 5.1-7. The figure also shows a rough estimation of the overhead flight path of the spacecraft

between the two image sets. This also illustrates the viewing angles of the camera for each image, better explaining how the image set were taken and the unusual overlap they have.

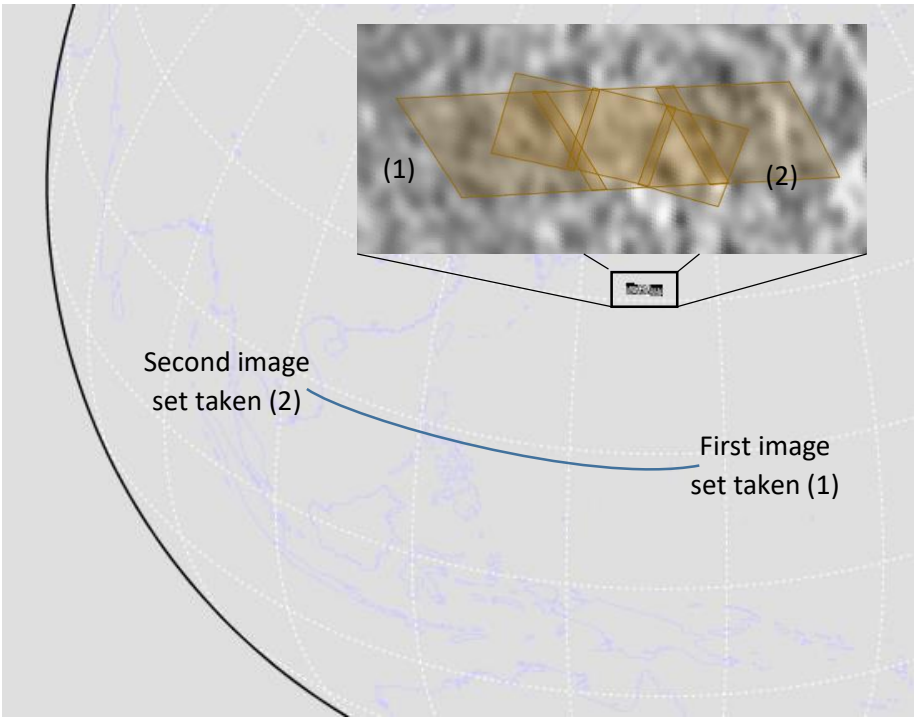

Figure 5.1-7: Position of selected images of Europa's surface at equivalent longitude and Latitude on Earth.

5.2 Heights of the Features on the Surface

Converting stereo images into a height profile, or Digital Elevation Model (DEM), is a complicated process. The somewhat limited availability of these overlapping images for the surface of Europa however, means this process has already been done for all the available data including the set, in question.

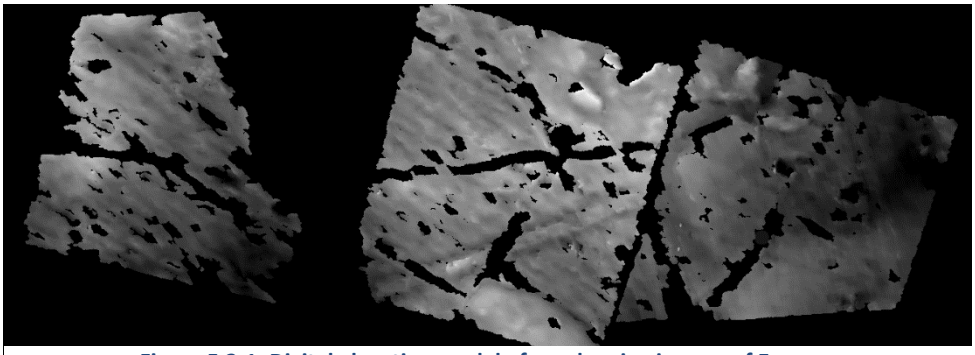

Figure 5.2-1: Digital elevation model of overlapping images of Europa.

Figure 5.2-1 shows the DEM of the overlapping image set. The black areas indicate areas where no data is available; the remaining data is a scale between black and white where the darkest areas are the lowest and the bight highlights are the peaks and high areas. The DEM was produced by Dr Tony Cook, from Aberystwyth University, during his time at the Centre for Earth and Planetary Studies at the Smithsonian's National Air and Space Museum in 2002.

The process of computing the stereo pair into the DEM is described in Cook and Robinson., (2000), as part of the same mapping technique used for the surface of Mercury. The described preferable parameters for stereo pairs are valid for the Europa images; determined by how the DEM is calculated. To acquire high accuracy of height elevation the stereo angle between the images needs to also be high.

There are a few other conditions for the stereo pair that those shown in Figure 5.2-2, these are described in the proceedings Day et al., (1992). These are mostly limiting to the condition of the stereo pair, as stated above in section 5.1.1, such as ensuring the illumination is similar.

The basis for the DEM method begins with the MATCHER software. This allows the images to be overlapped to a high degree of accuracy by determining seed locations. When

overlapped, due to the distortions of the globe shape the features do not always line up. MATCHER determines key locations where they should overlap using pattern matching of the pixels in distinct features; selecting seed points over the images. The algorithm then used the seed position on the reference image, using spacecraft location for accurate longitude and latitude of the image location, to apply distortions to the overlapping image using an adaptive least-squares algorithm (ALS).

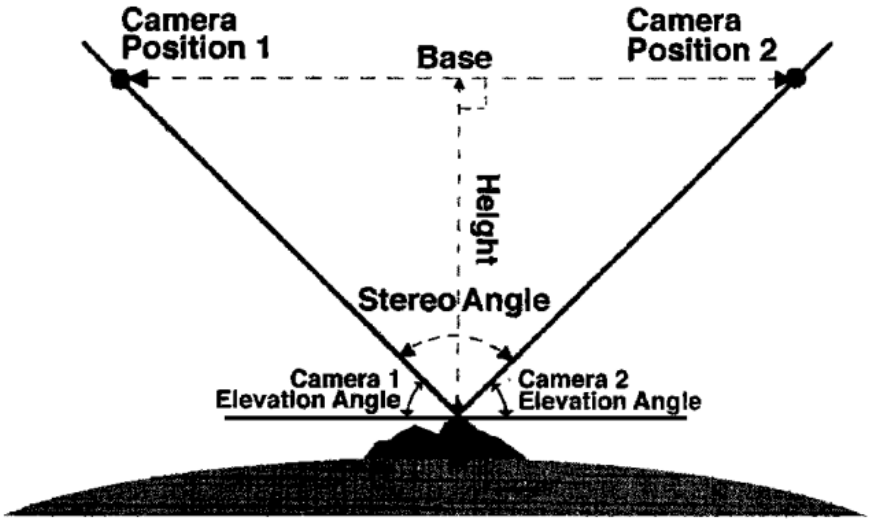

Figure 1. Simplified definition of stereo angle, base, and height. The stereo height accuracy A is defined as $A = R_p K/(B/H)$, where R_p is the poorest image resolution, $K = 0.2$ (precision of measurement in pixels) for CCD cameras or $K = 1.0$ for vidicon cameras such as the Mariner 10 cameras, B is the base, and H is the height.

Figure 5.2-2: from Cook and Robinson, 2000; diagram of the stereo image set us required for optimal digital elevation models.

This ALS algorithm matches the sets of points within the two images. From there a region growing algorithm allocates and predicts points on both images aligning them together over the image set. With the two images correctly aligned the DEM is produced using GOTCHA software written by Tim Day at University College London (Day et al., 1992).

The GOTCHA software is a 'shape-from-shading' algorithm that computes integratable gradients at each iteration. Each iteration is smaller than the previous for a user defined number of iterations and starting sizes. Shape-from-Shading algorithms use the relation between image intensity and surface slopes; using the surface illumination angle and direction to constrain the slope. This is why the surface illuminations need to be very

similar in the stereo pair. Frankot and Chellappa, (1988) describes the process of shape-from-shading in full, with the mathematical description.

GOTCHA builds on the basic algorithm in its iteration through sizes of interest, for use with larger areas. As the area is decreased over each iteration, the scale and accuracy of the depth is increased. The smallest details won't be available over the whole of the image however, a larger size iteration will already be covering the area (Day et al., 1992). The smaller the area the more detail will be available in the deeper areas. From the geometry of the images there are many areas where the surface is not clear, higher areas hiding low area behind them.

This is a reason for some of the missing data in the DEM (Figure 5.2-1). The missing areas line up with the largest and most height variant of the linea visible in the selected

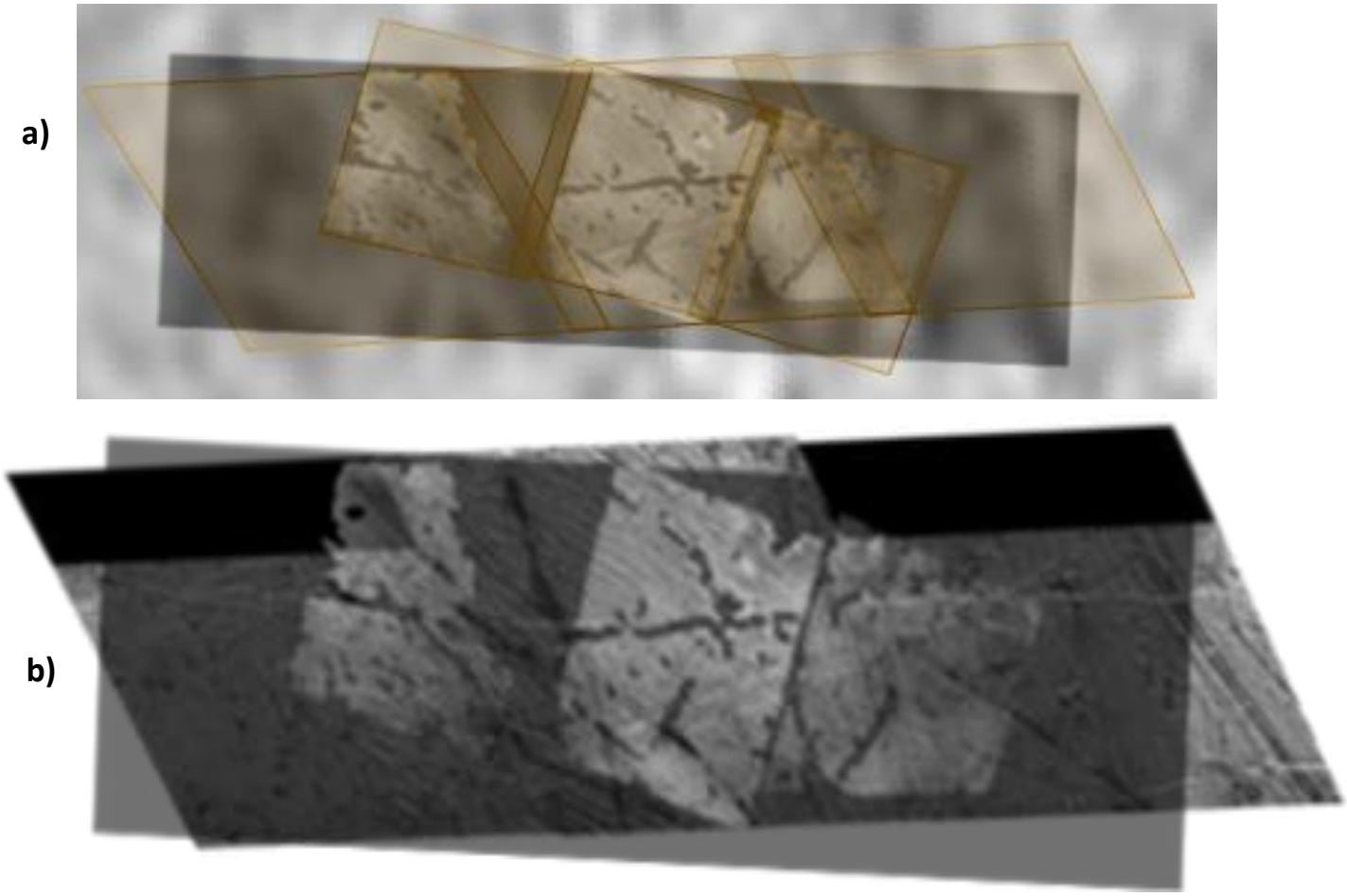

Figure 5.2-3: a) DEM overlaid with the outline of the image sets, for clarity in image orientation. b) DEM overlaid with both image sets to show the features between the missing areas.

area. By overlaying the original image with the DEM it is clearer which areas are missing, and what features have caused the errors in the calculation function.

Identifying features of the DEM in relation to the original image is difficult. Using transparency of the DEM and overlaying the images, illustrates which features which are obscured behind the DEM faults. The main cause of faults comes from the division between the original images; where the three images in each set align the MATCHER, software may have struggled to fit across any gaps in the image. It may also be that the images were dealt with individually, in this case not guaranteeing there is continuity across features as they pass through each image.

The secondary cause of faults in the DEM image comes from the very sharp changes in the surface. Figure 5.2-4 highlights some of the missing areas in question. By looking at the original image the issues of calculating the DEM come from very dark or very bright features; these are where the height changes would be the most extreme and there the stereo mapping would need to be the most accurate. The DEM resolution sits at 50m by 50m for each pixel. The feature highlighted in orange (in Figure 5.2-4), is both very bright and very thin. This combination pushes the limits of the accuracy that can be obtained by this method.

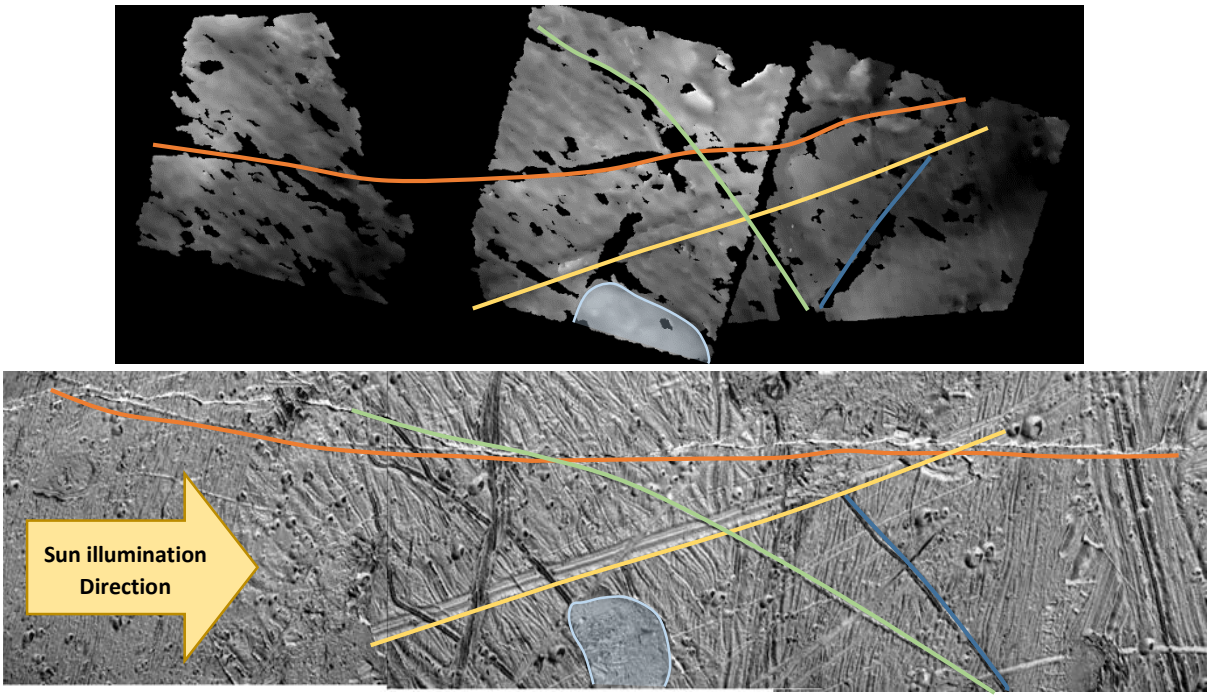

Figure 5.2-4: Notable features highlighted in both original image and DEM for clarity and to illustrate areas of missing heights in the DEM.

The areas that are accurately picked out are those with gradual height changes, along with the wider and larger features. One of the features of interest that has been accurately identified is highlighted in yellow in Figure 5.2-4. The wide multi-band linea spans two thirds of the image and appears as similar distinct ridges in the DEM. This linea will be the focus for the analysis of the erosion on the surface.

The data present in the DEM is not perfect; since the production of this DEM in 2002 the process and methodologies have improved for generating heights on planetary surfaces. Despite this, the availability of software and expertise to produce a DEM from the available data is limited. Nevertheless, the DEM is sufficient to investigate the proof of concept of surface age from erosion calculations. For further work a far more detailed DEM over far more of the surface would be required to sufficiently allow the dating of the surface.

The first step in this analysis is to extract the height values from the DEM over the areas of interest. This is done using the limits of the colour scale and the heights allocated to each colour. The colour scale runs from darkest at 0 in decimal RGB number format, to brightest at 255. The heights for these are given as: DN255 = -0.288Km and DN0 = -0.8Km, giving 0.7712 Km between the two extremes.

This gives a set height for each colour on the scale between 225 and 0. Using Python the values can be extracted for specific cross sections of the image. Using a drag and drop line selection, the pixel colour values are extracted for all the pixels dissected by the line regardless of how much of the pixel is selected. This can cause some noise in the height profile as both full and partial pixels are added to the line array.

Once the array has been extracted, the values are fitted over the length of the line; rather than using the number of pixels the line dissects. The fitting always over a larger degree than the number of pixels crossed and the extracted colour values. This stops the colour transition from being blocky over sharp colour gradients.

The axis of the height profiles is set between the limits of the DEM colour scale in Km, rather than the individual profile. This is to allow for comparison between multiple profiles. The colour scale of the DEM has also been changed for the clarity of the user selecting the line of the profile. This is seen in Figure 5.2-5. Whilst making no changes to the

overall colour scale, the use of Python's 'afmhot' colour scale makes selecting locations for investigation by eye simpler, for the height profiles to be extracted.

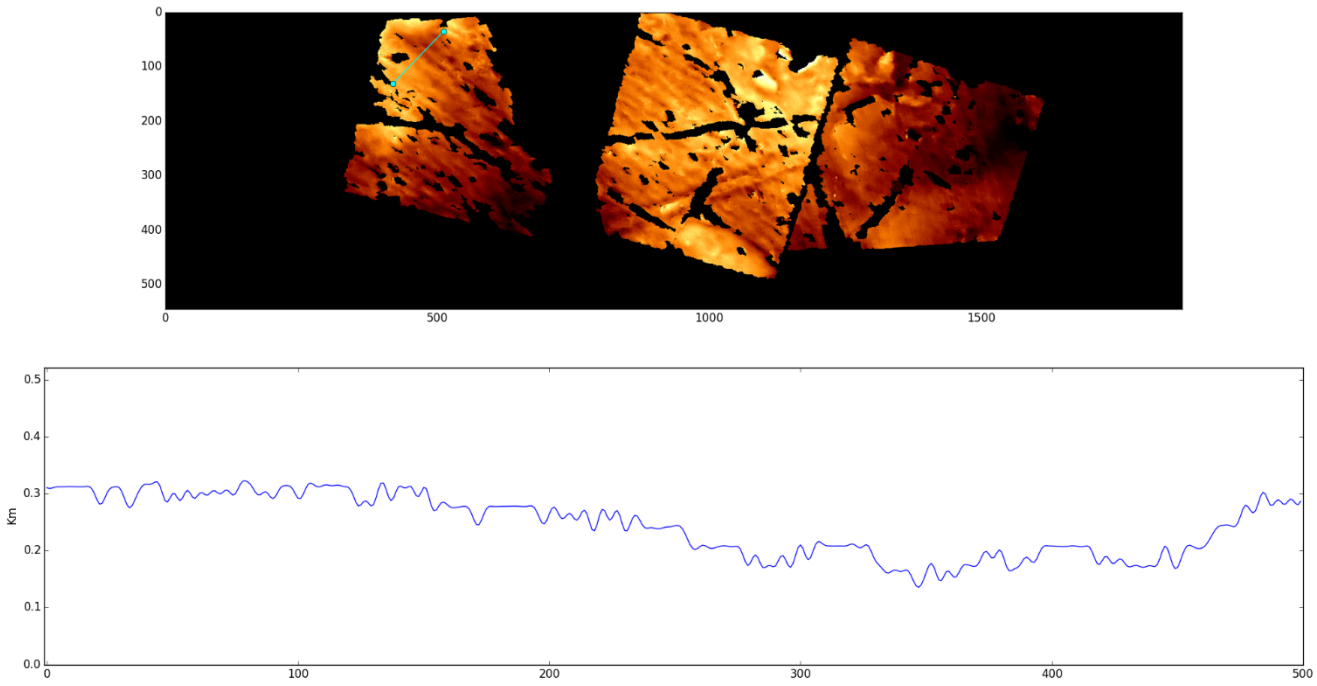

Figure 5.2-5: Example of the height profile extraction routine output.

It is worth noting at this point that the heights derived from the DEM are relative rather than absolute. This means that the determined highest and lowest points are only in relation to the available height range visible in the image, and not a defined distance from the spacecraft or centre of Europa. To investigate this further these height scales would need to be more ridged, and better defined; however, in this case the relative heights are useable.

5.2.1 Extracting Height Profiles

A variety of locations over the surface were investigated. Focusing on a different features and surface textures to best grasp the heights and changes available over the surface. Figure 5.2-6 shows all the areas and height profiles investigated over the coverage of the DEM. Only a few of these were deemed to be useful for attempting to determine age, however they were each chosen for the interesting features in the area; described following.

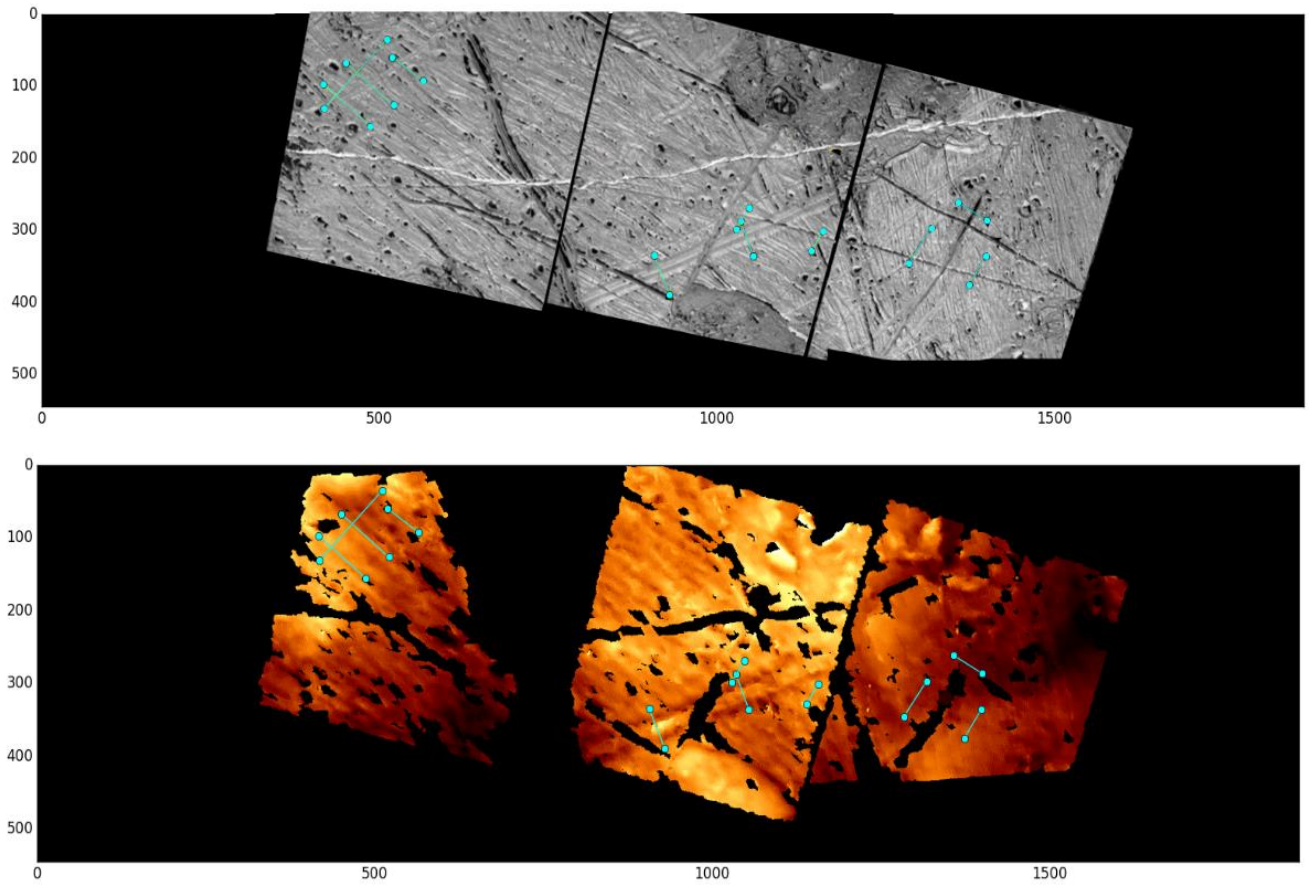

Figure 5.2-6: Overlay of all height selections investigated. Each profile line cut is marked on the DEM (Bottom) and original image (Top) in cyan.

The four left-hand profiles, of Figure 5.2-6, cover a relatively flat, but multi banded terrain. The images of the surface show a continuous expanse of lateral linea in the direction of bottom-left to top-right. the profiles were selected to cut these linea in an attempt to see the highs and lows of the side-by-side linea formation. Unfortunately, there is a large amount of noise making the individual highs and low difficult to pick out. The single profile aligned with the rows of linea, is positioned to see a single feature cutting

across the expanse. Again, the noise and occasional crossing of the linea underneath do not allow this feature to be picked out.

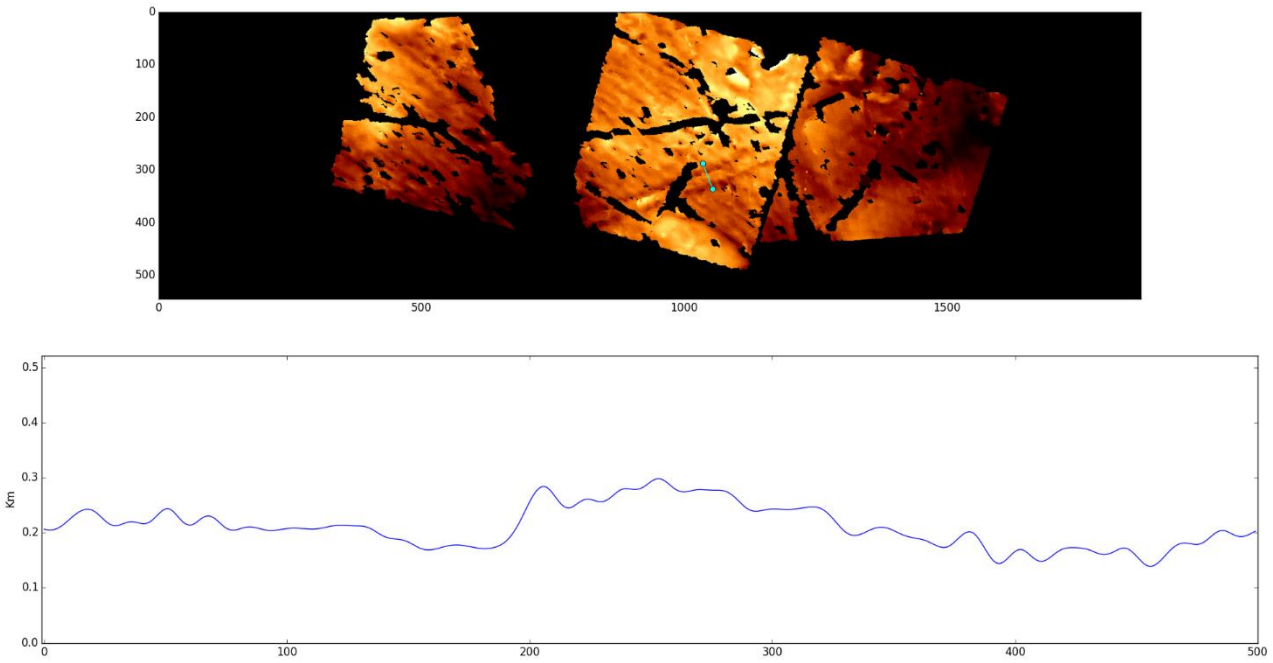

Figure 5.2-8: Upper height profile over the large wide-band linea.

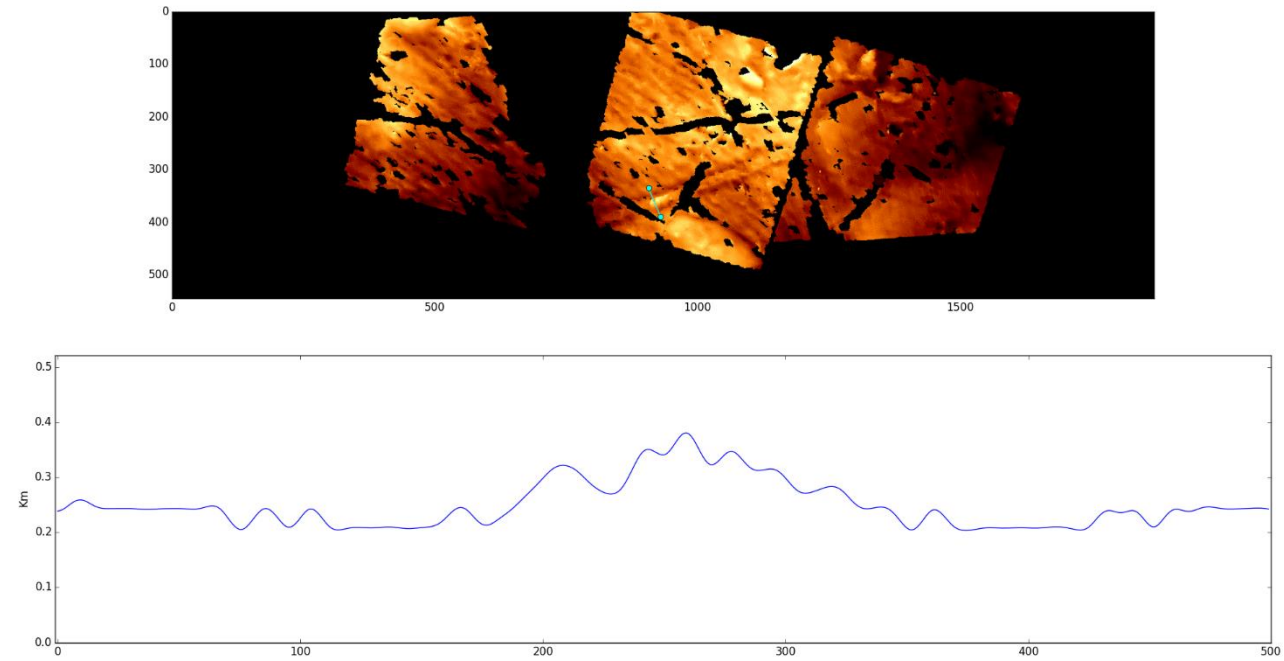

Figure 5.2-7: Lower height profile over the large wide-band linea.

The three profiles selected on the right-hand side of the DEM were chosen to view the dark features of the two horizontal and single vertical lines. Again, the features were unable to be distinguished from the surrounding relatively flat landscape. Most likely in this case it the features in question are too small to be picked up by the DEM resolution. From

the original image, it is clear they are very thin distinct changes in height; however, with a similar height profile on either side the DEM will only pick up a small change from the think area of darkness.

The final set of profiles chosen, sit in the centre panel of the DEM. They are positioned to sit, two across the main wide-band linea, and two across the underlying features the main band has cut across. This feature is a large feature with a gradual change that is still clearly seen even in the DEM. In this case the profiles of the features are clearly visible. Figure 5.2-8 and Figure 5.2-7 show the height profiles over the wide-band linea.

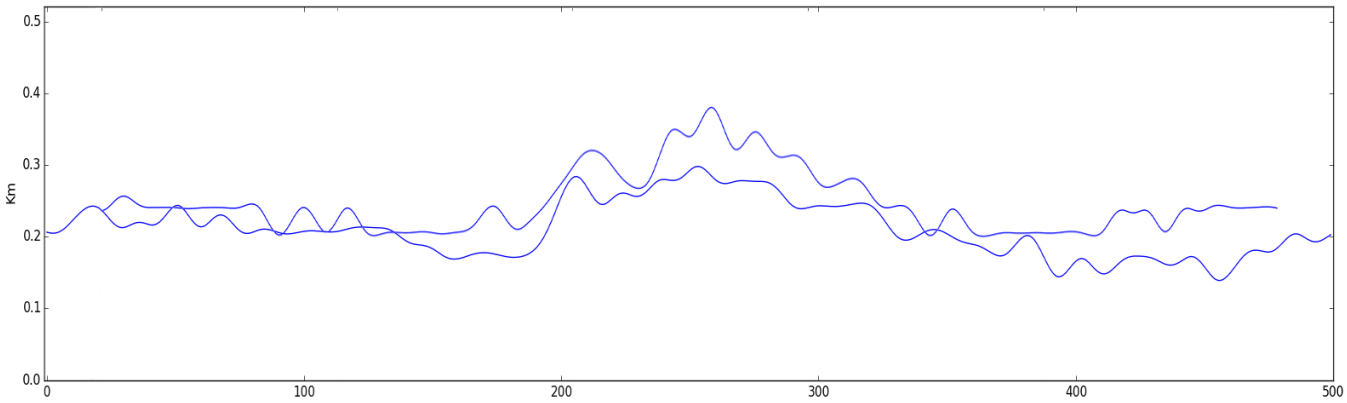

Figure 5.2-9: Overlaid comparison of the two wide-band profiles, aligned using the highest peak in each profile as a marker.

Both profiles show the distinct and expected series of peaks thought to some from the continual opening and up-filling of ice that cause these types of features. For an in-depth study the feature would need to be sampled along its whole length to assess any changes; however, for the scope of these preliminary investigations, two points will suffice. Figure 5.2-9 shows the overlay of the two profiles. When choosing the path of the profile to take ensuring the feature was in the middle of the profile was impossible. To account for this the profiles have been aligned using the sharp increase on the left-hand side, and the centre peak of the feature. The heights are all relative so no adjustments were needed in this axis.

The other two profiles from the central region of the DEM sit on either side of the main band. These profiles were initially chosen to also cut across a smaller feature that continues into the right-hand side of the DEM to gather more information on that feature. Unfortunately, as already seen the DEM cannot pick up features that small. To better

characterise the changes in the wide-band linea, another two profiles were taken; these are close to the crosscut region and cover a longer span of the feature than those shown above.

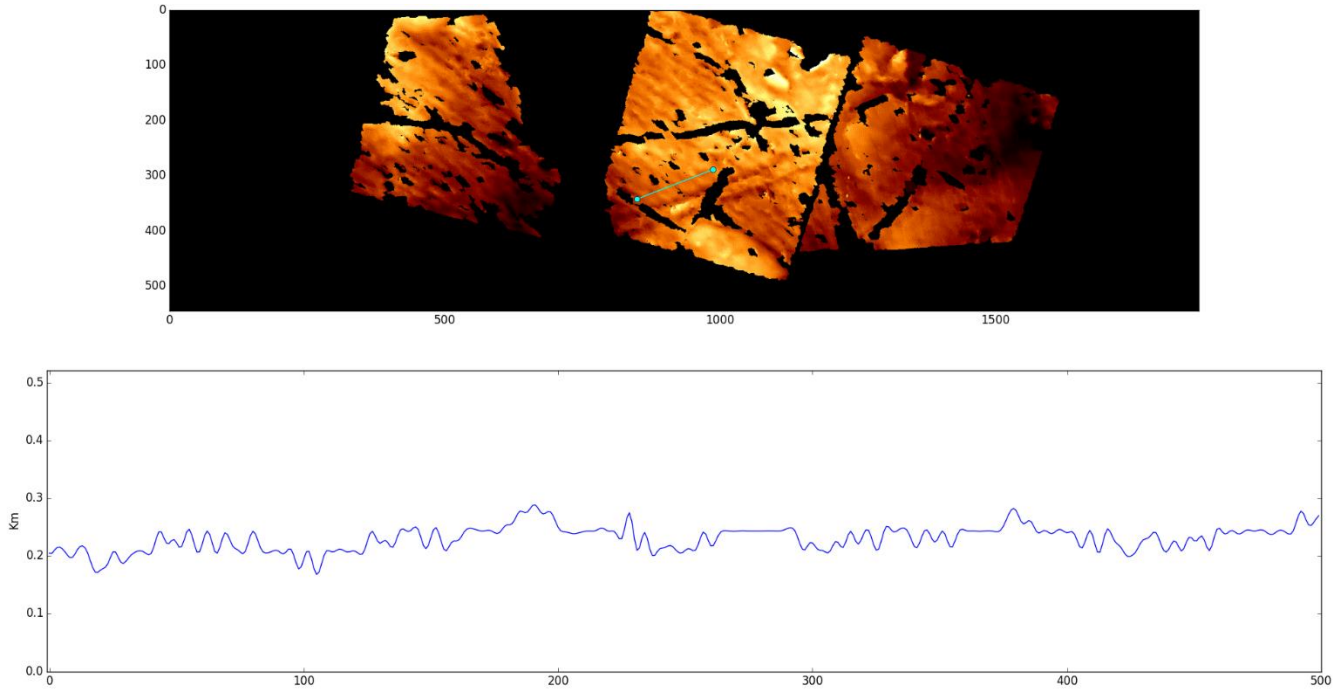

Figure 5.2-10: Upper height profile alongside the large wide-band linea.

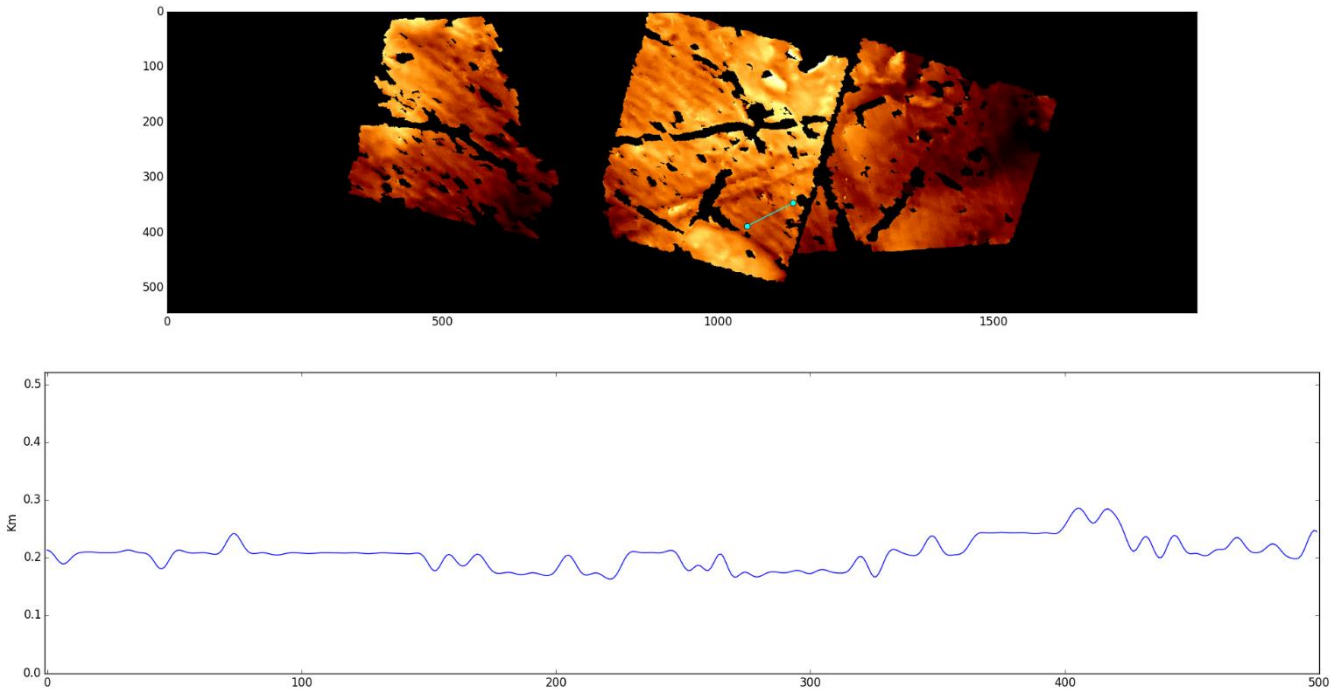

Figure 5.2-11: Lower height profile alongside the large wide-band linea.

Figure 5.2-10 and Figure 5.2-11 show the profiles and positions of the new selections. These profiles are far longer than those previously taken and this shows in the apparent detail that can be seen. This is simply an artefact in how the program fits the heights along a set number of points. Figure 5.2-12 some the lengths of each profile in comparison to each other, accounting for the differences in length of selection.

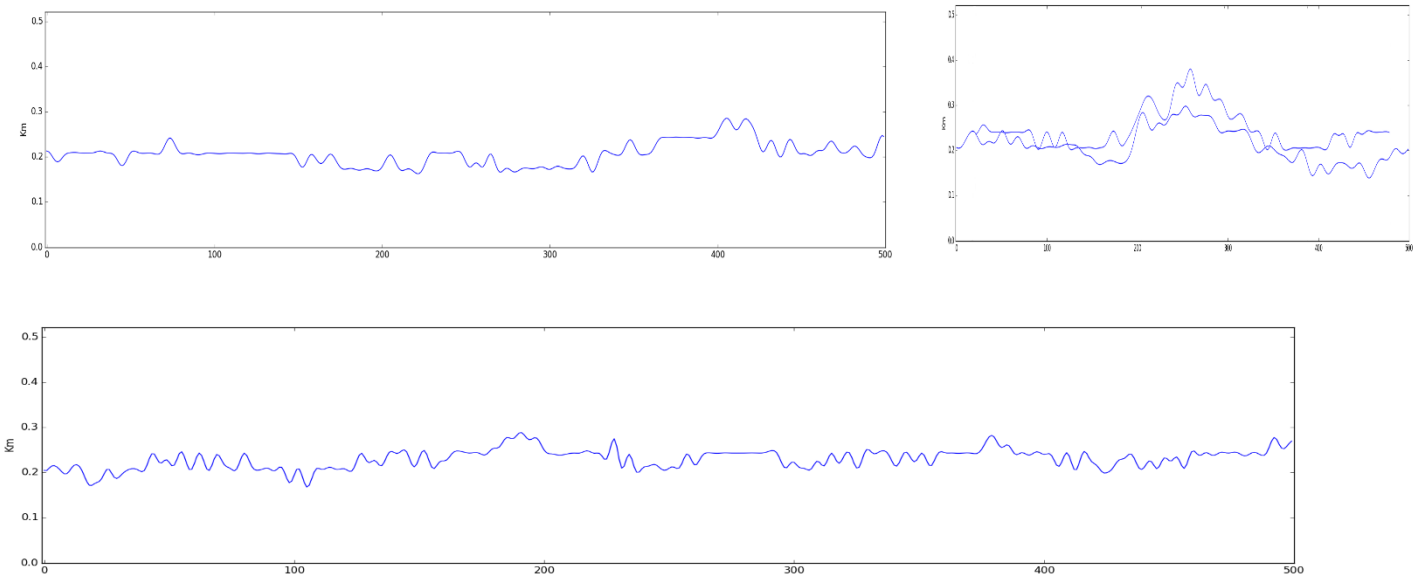

Figure 5.2-12: Direct comparison of the lengths of the profiles of interest. Top left: Lower height profile from alongside the large wide-band linea, Top right: both profiles from the wide-band linea, Bottom: Upper heigh profile from alongside the wide-band linea.

The side profiles cannot be lined up in the same manner as the profiles over the wide-band; not only are the features too indistinct to match up by eye, the possibility of the two sides of the band slipping during the formation is very high. If the profiles were very close to the cross cut point and the resolution of the DEM was higher, then this could be used as a method to more accurately determine 'plate' movement around formations such as this.

5.2.2 Evaluating Height Change into Surface Age

Having selected the location to investigate and having extracted the height profiles along the selections, the next step is in assessing how much the profiles are changing with age and if an age range can be determined. To do this there are a few assumptions that need to be made.

Section 5.1 describes the theory behind determining the age between each stage of the evolution of a wide-band linea. Whilst this method is sound, the resolution of the DEM is not accurate enough to truly pick out each ridge of the band. Instead another estimation can be made using the profiles of the main feature and its surrounding surface.

By using the assumption that the features beneath the wide-band were formed in the same manner as the wide-band itself, and are simply far further along in their life cycle; the age difference between the band itself and the surface beneath it can be estimated. Yet more assumptions are needed to make this estimation; the largest of these is an Earth based geological assumption. On Earth you can assume that higher more exposed features will be eroded faster than flat ground. It also assumes that any eroded material that does not escape will be deposited in the lowest areas, effectively filling pits and troughs. The nature of ice and frosting effects on Europa however, will alter how material is deposited, and where. These effects have not been investigated on a small scale. Tiscareno and Geissler., (2003) have however, investigated re-distribution from sputtering on a global scale; considering magnetic field along with the orbit and rotation of Europa. These findings are too large scale to be used in conjunction with this study.

A promising further study, would be to investigate this re-distribution on a local scale and compare it to the geological processes on Earth. Yet, I suspect it would have to be delayed until high quality stereo imaging and height profiles can be built up of the surface.

With the assumptions in place, the process of estimating the surface age is then based on the change in material volume from one profile to the other. Using the side profile as a baseline, the volume difference compared to the profile across the band will be the amount of material to be eroded by the sputtering processes. Cassidy et al., (2013) estimated that one third of the water ice sputtered from the surface would have enough energy to escape. Using the change in volume and applying this loss rate the number of particles sputtered can be determined. Cassidy et al., (2013) also estimated the number of particles sputtered value, using the loss rate, that corresponds to their global sputtering rate.

Calculating the area change in the height profiles is done using the output values along each selection. Each height point corresponds to the pixel location from the DEM this means the lengths of the selections are accurate to the surface coverage.

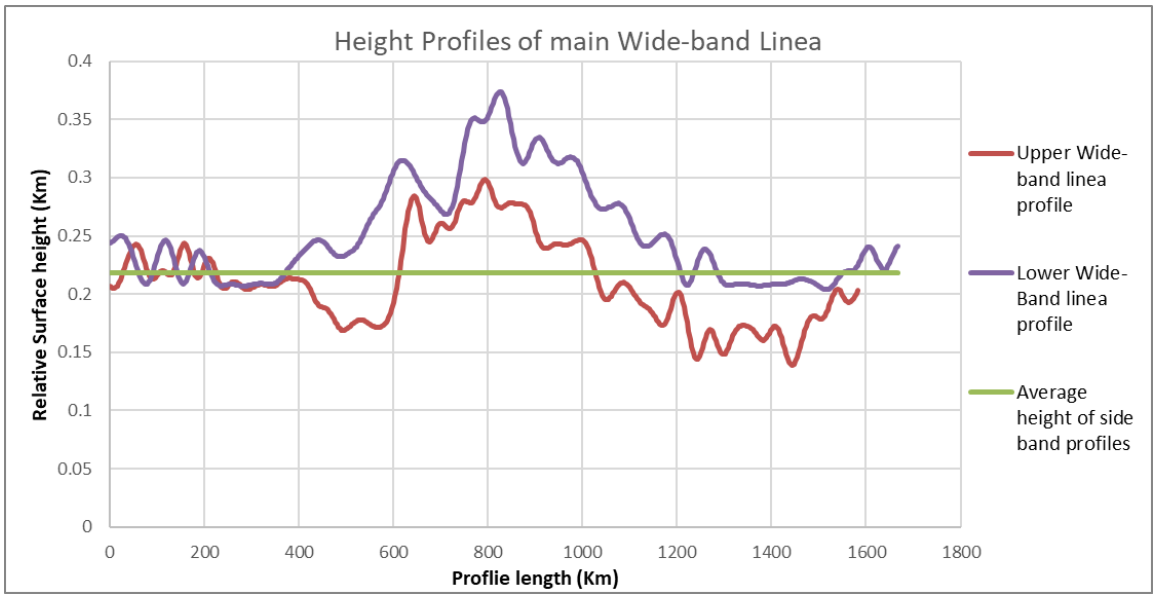

Figure 5.2-13: Profiles across the Wide-band Linea against the average height from the surface alongside the band.

The area changes need to be calculated from a base line, in this case the height of the surrounding surface. This height varies over the selected sections and contains a lot of small ripples from old features underneath the main band. To account for this the values are averaged over the length.

Figure 5.2-13 shows the average of the side profiles plotted with the wide-band profiles to show the height the central band reaches in its youngest area. The wide-band profiles are plotted to their true length calculated using pixel number at 50Km a pixel. Note again how the overall shape of the band does not align when plotted like this. The volume of material to be eroded will be an average of the height profiles; of the amount of material above the average side surface height. To calculate this average, first the profiles need to be aligned.

Laterally the central peak and the sharp slopes on either side of the band are used for the alignment. Once in position it is clearer how there is an overall decrease in height of the band. The shape however, remains the same. This points to the wide-band having been formed on a sloping surface originally; or the formation was uneven is some way. Even

though the heights from the DEM are relative with each other and should be consistent, the heights don't account for any large-scale slopes and gradients.

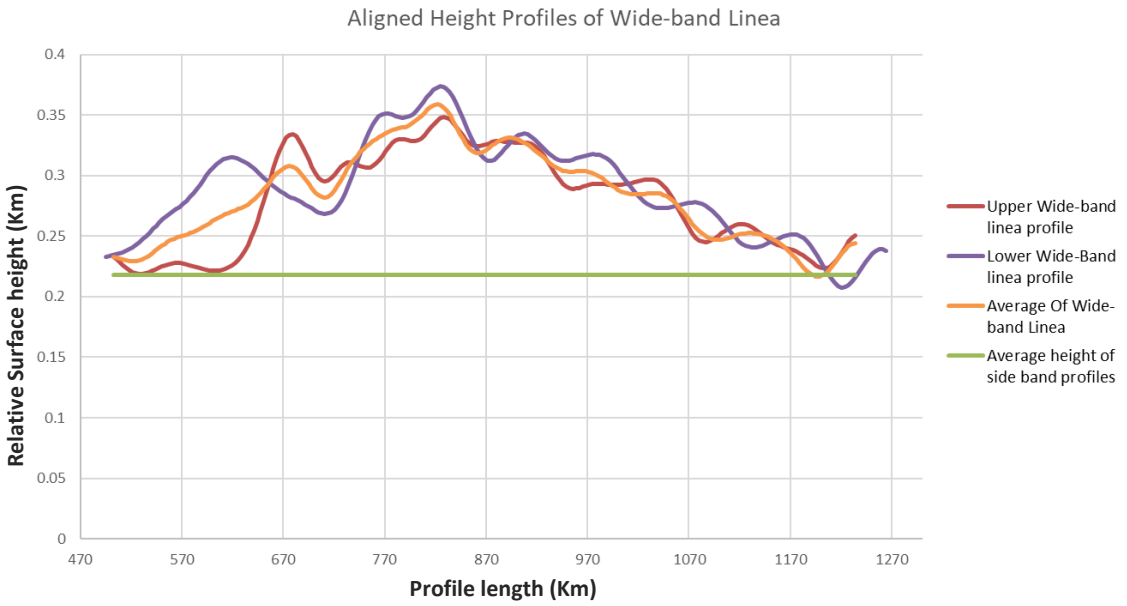

Figure 5.2-14: Height and Position aligned profiles of the Wide-band Linea, with the average of the profiles included. The length of the profiles cropped to the width of the wide-band.

Figure 5.2-14 shows the profiles correctly aligned. The profiles have been cropped to only show the wide-band feature, so as to not include the surrounding peaks and troughs of the side surface being compared against. The area shown in the average profile can be calculated to:

$$48.001 \times 10^{10}\ cm^2 \tag{40}$$

With the total sputtering rate per second per cm^2 area, is given by:

$$1.15 \times 10^{8}\ cm^{-2}s^{-1} \tag{41}$$

Using the volume of the profile in this way to calculate the age of the sputtering is not an accurate representation of how the surface would be eroded. if calculated using the whole area, it would be as if the whole volume were stacked upon each other, and sputtered layer by layer. In reality, all of the surface area will be sputtered evenly for the duration of the features lifetime. The height changes over the width of the wide-band, are

very small compared to its total width, when calculating the surface length there is very little difference in the straight-line width and surface width.

Using the surface length and dividing the area by this value, evens out the sputtering erosion over the surface. Over the whole of the surface, the total depth of material to be sputtered is equivalent to the total area divided by the width of the wide-band linea: $65m$

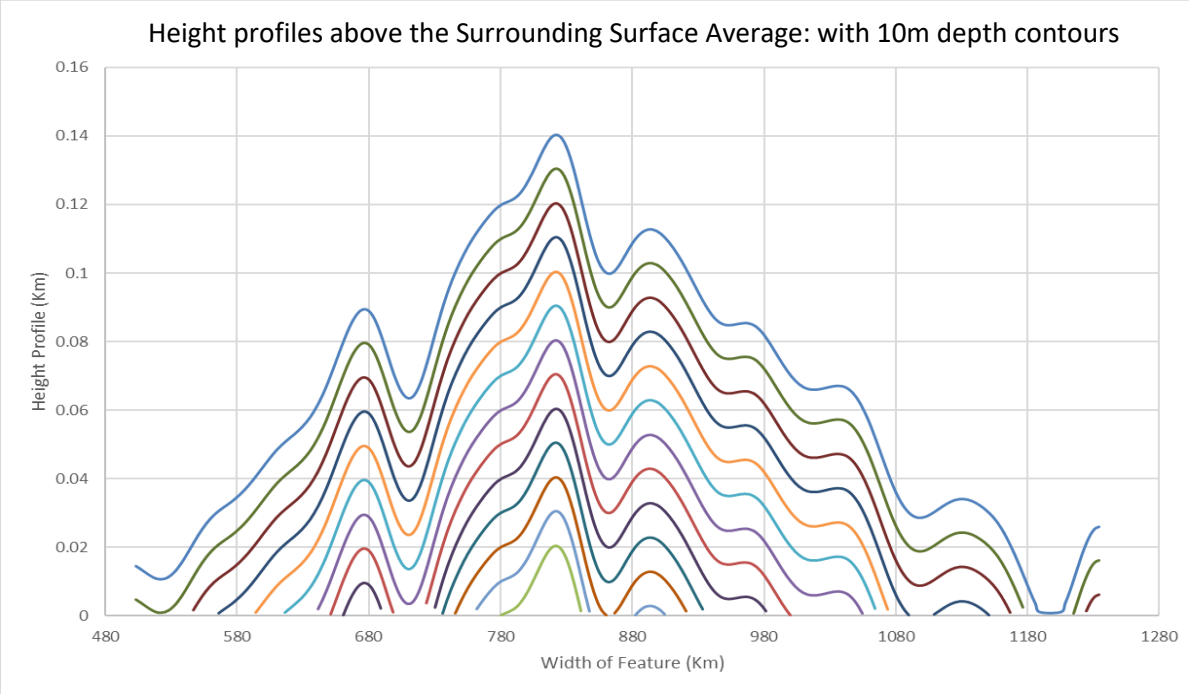

Figure 5.2-15: Height profile above the surrounding surface average with contour profiles at every 10m depth from the surface.

The time taken to erode 65m of surface is calculated from the total sputtering yield above (41). The density of the regolith ice determines the volume of particles removed from the surface per second allowing the depth over time to be evaluated. Taken from estimations in Cassidy et al., (2013) the density, in number of particles per unit area, of the ice regolith is likely to be on average $\sim 3 \times 10^{22}\ cm^{-3}$. This would equate to approximately 50Gys, when using the corrected sputtering rate. This rate is lower than the sputtering rate used in Cassidy et al., (2013) which when used to calculate time of erosion would give approximately 1Gys.

This disparity between the two estimations is huge in terms of time taken to erode a surface, however the overall difference in sputtering yield was not very large at all. This really highlights this importance of the accuracy of the sputtering yields and the compositional differences used to calculate them.

As a comparison the erosion times can be calculated for both the before and after correction sputtering yield values. With the post correction erosions time sitting at ~50Gys the pre-correction erosion time sits closer to ~65Gys. This is having calculated the sputtering yields in the same manner, using an average of the peak intensities measured during the Europa flybys.

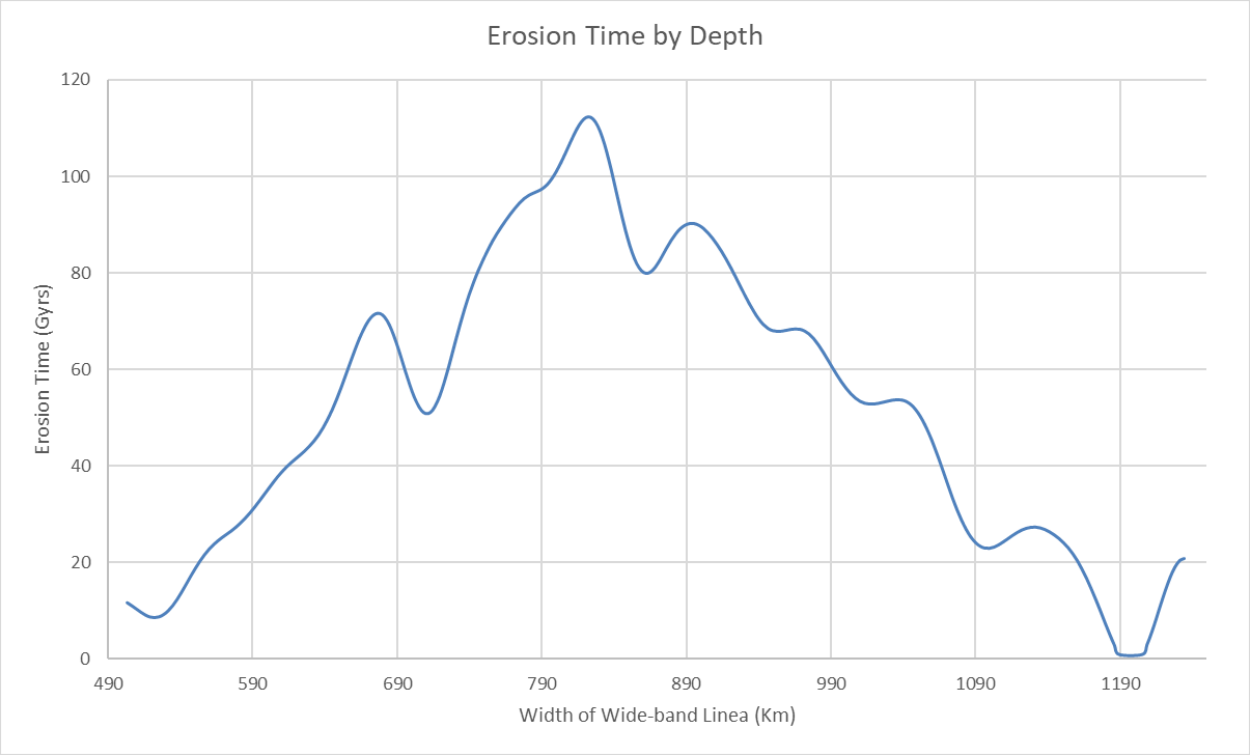

Figure 5.2-16: Ice erosion time by depth over the width of the Wide-band linea.

These erosion rates are for the volume of material being eroded in an even distribution over the width of the linea. However, the central portion will take far longer to erode and the outer, lower, edges will be eroded very fast. A better assumption is that the erosion will happen in a series of layers. Figure 5.2-15 shows these layers as 10m depth contours beneath the original height profile. Using the calculated sputtering yield (41), the erosion time for 10m is approximately 8Gyr. This would mean the very shallow peaks eroded within 20Gys and the central peak still being visible after over 100Gys.

This principle can be applied to the heights of the profile individually to produce Figure 5.2-16. This is the height profile with a rescaled axis now showing the time in Gys for the profile to be eroded. Of course, all of the surface is being eroded at a similar rate to the peaks of wide-band linea, however for all of the material that is lifted off the surface two

thirds of it re-settles. This movement of particles evens out the peaks, leaving the surface looking similar to the surrounding profiles.

In addition to this the overall times taken are not very realistic. This is in part due to the calculation of the Sputtering yield and the non-uniformity of the sputtering over the surface. It is also worth considering how dominant a process the erosion is, and how other mechanisms will also erode the surface.

The main point to consider with the erosion times given in Figure 5.2-16, is that with only a slightly higher sputtering yield, the time taken is greatly reduced. This again highlights the necessity of a well constrained sputtering yield, when considering the erosion due to sputtering.

5.3 Conclusions

The quality and resolution of the DEM is the main limiting factor in this investigation. With the arrival of JUICE and Europa Clipper the availability of accurate and widespread DEMs will allow this technique to be developed. Despite this, as a proof of concept for a method of estimating ages of features and surfaces, the process is straightforward and can produce an estimation of erosion times.

The estimations calculated are un-realistic in relation to the age of the moon itself. However; when comparing to the values in literature for estimations of surface age it is easily apparent why there is such a high spread. The sputtering yield on the surface directly correlates to the erosion rate on the surface, the methods of calculating this shown in Chapter 4 illustrate how only a few counts in the EPD detector can have a huge impact on the yield and thus the erosion rate.

Assuming a realistic time estimate, they still offer an interesting window into the history of the Jovian system. By using the sputtering rate to work backwards and evaluate how the features have changes over time, there is a key assumption being made that the sputtering rate has been consistent over the lifetime of the feature. This is most likely not the case. The sputtering erosion is based on the density and composition of the plasma in the plasma disk, this is driven directly from the output of Io. Any changes in the development of Io over the course of the ~65Gys of erosion estimated here, would have impact on the composition and density.

By using additional methods of dating the surface, such as crater counting, any discrepancies can be linked to changes in the system. Whist any discrepancies found this way would have very little useable information, the knowledge of a change in the system will help in any formation and evolution models available for Io or the system as a whole.

There is still a huge amount of analysis that can be done on the surface and the age estimates. These include completing a larger survey of the surface and combining cross cutting features to expand into a timeline of features. There is also work that can be done in investigating in more detail, how much the features can be dated in stages of formation. This applies mainly to the larger wide-band linea, for example.

6 Conclusions

6.1 General Conclusions

The process of the research presented here in-fact began with the final research chapter. The aim was to study the surface and develop a model for estimating the ages of specific areas and to complete a large-scale study of the feature cross cutting. In the early investigations the quality of the available data was clearly in question. When looking specifically at the late mission flybys the decay present in all required data sets was too significant to ignore.

From this discovery of the data decay during the mission from the radiation environment, the priorities of research changed, to improving the data to a useable state. Chapter 2 opens with the investigations on how bad the issues are, and rapidly settles on a fit of how the dead layer build up in the sensitive volume progressed over the mission. Using this progression, the energy lost can be calculated and the correction can be made to the energy readings. This correction is very robust, its only drawback is in the use of static values of the energy loss. In practice these will change dependent on the initial energy of the incoming particle. However, in using the static values consistently throughout the correction the error incurred by this is minimised. The drop-off in accuracy is well accounted for in the final results.

The effect of the correction puts the plasma composition within the expected ranges for all the element loci. However, this is only half of the story. The PHA plots are the high-resolution data of the most interesting particles that impact the detector. This data is only available for very short period of the mission and is prioritised for the heavier element readings. Available over the majority of the mission, however is the low-resolution count rate data that forms the basis of chapter 3.

Correcting the count rate channel data, was by far the most complicated of all the research done for this project. The correction is built on an understanding of how the channels were changing, gained during the correction of the PHA plots; the correction itself is purely numerical. Using the averages of the channels and a starting estimation of how each channel will have changed, the iterative formulation of the correction was calculated.

This process was a trial and error system, using the expected results and the visible results to adjust the formula each time until the method produced the expected returns.

The final result of the corrected channels was rather abstract. Only when compared against the Voyager data sets and original data, were the alterations really seen. The errors incurred encompass the CV value generated from the original data, the estimations of the counts during instrument down time, efficiency drop calculations estimating totally uncounted particles, and the overall error in the correction itself. The aim in the devised method is to improve only within the limits of the original. By comparing with early, less effected averages, and overall with both original and external data, the error is expected to be always within what has been recorded.

The comparison to the Voyager data set shows just how well the correction has worked, lifting the original count rates whilst still keeping the data within reasonable ranges. This correction will be made available to the scientific community, along with the data set of the PHA plots so that these advancements can be used in investigations going towards the upcoming JUICE mission, or the NASA Clipper mission. It is only at this point that the true accuracy, or at least improvements in the accuracy will be seen.

With a corrected data set in hand, chapter 4 begins to approach the original question in the calculation of the erosion rate. The sputtering yield determines how many particles will be removed from the surface of the moons in relation to the number hitting the surface. Using known yields, the surface sputtering was calculated and then compared to those previously calculated. Whilst the resulting values for sputtering don't fully match with those calculated by others, the comparison between the pre- and post-correction, illustrates just how important the accuracy of the count rate is.

Chapter 5, continues as chapter 4 leaves off, applying the sputtering yield in terms of erosion time. Looking in detail at the surface, the final section of research pulls height profiles from digital elevation models of Europa's surface, analysing them to determine the age of individual visible features.

This chapter was strongly limited by the DEM resolution available. With the arrival of JUICE and Europa Clipper the availability of accurate and widespread DEMs will allow the techniques tested here to be developed. Despite this, as a proof of concept for a method of

estimating ages of features and surfaces, the process is straightforward and produces reasonable estimations in erosion times. The application of the sputtering rates to erosion in years of the surface, very simply illustrates how small changes and inaccuracies can have a huge effect on the conclusions drawn. The differences in using the pre- and post-correction values as a basis for the erosion time illustrate why the corrections of chapters 2 and 3 are so valuable.

6.2 Further Work

The main area of research that I would continue with given more time, is the work on the surface of the moons. I would like to complete a far larger survey of the surface and even investigate the surfaces of the other moons; notable Ganymede with its challenging magnetosphere and Io in the heart of the most energetic plasma.

There is much more work to be done in finalising the correction. Making the corrected data publically available with the original data is something that I will continue to do along with the publication of the correction methods. There are also other uses for the corrected data that could be researched further, such as the investigations in to the mass loading and any further modelling work that can be updated. The insertion orbit of Juno could also be included and combined with the corrected data set filling in some of the gaps between the orbits of Galileo and the planet itself.

I would also like to investigate more into the sputtering on the surface. The assumptions made when calculating the sputtering yield, assumed that the whole surface was uniform and evenly sputtered. This is not the case and I would like to apply the corrected values to current sputtering models to truly compare the differences. An addition to this is the very recent work on laboratory measurements to measure the sulphur sputtering in water ice, has been completed with could be added to the verify the values used. I would also be interested in continuing and assisting with measuring this, on the basis of the sulphur sputtering is the most important in the Jovian system

“not everything that can be counted counts, and not everything that counts can be counted”

– William Bruce Cameron

From: Informal Sociology: A Casual Introduction to Sociological Thinking, 196

7 References

AYDIN, A. 2006. Failure modes of the lineaments on Jupiter's moon, Europa: Implications for the evolution of its icy crust. *Journal of Structural Geology,* 28**,** 2222-2236.

BAGENAL, F. 2007. The magnetosphere of Jupiter: Coupling the equator to the poles. *J. Atmos. Sol.-Terr. Phys.,* 69**,** 387-402.

BAGENAL, F., DOUGHERTY, L. P., BODISCH, K. M., RICHARDSON, J. D. & BELCHER, J. M. 2017. Survey of Voyager plasma science ions at Jupiter: 1. Analysis method. *Journal of Geophysical Research-Space Physics,* 122**,** 8241-8256.

BAGENAL, F., E. DOWLING, T. & B. MCKINNON, W. 2004. *Jupiter: The Planet, Satellites and Magnetosphere (Cambridge Planetary Science),* The Pitt BuildingTrumpington street Cambridge UK, Cambridge University Press.

BAGENAL, F., SIDROW, E., WILSON, R. J., CASSIDY, T. A., DOLS, V., CRARY, F. J., STEFFL, A. J., DELAMERE, P. A., KURTH, W. S. & PATERSON, W. R. 2015. Plasma conditions at Europa's orbit. *Icarus,* 261**,** 1-13.

BAKLOUTI, D., SCHMITT, B. & BRISSAUD, O. 2008. S2O, polysulfuroxide and sulfur polymer on Io's surface? *Icarus,* 194**,** 647-659.

BANASZKIEWICZ, M. & IP, W. H. 1993. THE VELOCITY DISTRIBUTION-FUNCTIONS OF OXYGEN AND SULFUR IONS IN THE IO PLASMA TORUS. *Advances in Space Research-Series,* 13**,** 331-335.

BELTON, M. J. S. 2000. Results of the Galileo solid state imaging (SSI) experiment. *PLANETARY IONOSPHERES AND MAGNETOSPHERES,* 26**,** 1641-1647.

BELTON, M. J. S., KLAASEN, K. P., CLARY, M. C., ANDERSON, J. L., ANGER, C. D., CARR, M. H., CHAPMAN, C. R., DAVIES, M. E., GREELEY, R., ANDERSON, D., BOLEF, L. K., TOWNSEND, T. E., GREENBERG, R., HEAD, J. W., NEUKUM, G., PILCHER, C. B., VEVERKA, J., GIERASCH, P. J., FANALE, F. P., INGERSOLL, A. P., MASURSKY, H., MORRISON, D. & POLLACK, J. B. 1992. THE GALILEO SOLID-STATE IMAGING EXPERIMENT. *Space Science Reviews,* 60**,** 413-455.

BHATTACHARYA, B., THORNE, R. M., WILLIAMS, D. J., KHURANA, K. K. & GURNETT, D. A. 2005. Diffuse auroral precipitation in the jovian upper atmosphere and magnetospheric electron flux variability. *Icarus,* 178**,** 406-416.

BIERHAUS, E. B., CHAPMAN, C. R. & MERLINE, W. J. 2005. Secondary craters on Europa and implications for cratered surfaces. *Nature,* 437**,** 1125-1127.

BILLINGS, S. E. & KATTENHORN, S. A. 2005. The great thickness debate: Ice shell thickness models for Europa and comparisons with estimates based on flexure at ridges. *Icarus,* 177**,** 397-412.

BODISCH, K. M., DOUGHERTY, L. P. & BAGENAL, F. 2017. Survey of Voyager plasma science ions at Jupiter: 3. Protons and minor ions. *Journal of Geophysical Research-Space Physics,* 122**,** 8277-8294.

BRIDGE, H. S., BELCHER, J. W., BUTLER, R. J., LAZARUS, A. J., MAVRETIC, A. M. & SULLIVAN, J. D. 1977. PLASMA EXPERIMENT ON 1977 VOYAGER MISSION. *Space Science Reviews,* 21**,** 259-287.

BROWN, W. L., LANZEROTTI, L. J., POATE, J. M. & AUGUSTYNIAK, W. M. 1978. SPUTTERING OF ICE BY MEV LIGHT-IONS. *Physical Review Letters,* 40**,** 1027-1030.

BURGER, M. H. & JOHNSON, R. E. 2004. Europa's neutral cloud: morphology and comparisons to Io. *Icarus,* 171**,** 557-560.

CARLSON, R. W., CALVIN, W. M., DALTON, J. B., HANSEN, G. B., HUDSON, R. L., JOHNSON, R. E., MCCORD, T. B. & MOORE, M. H. 2009. *Europa,* United States of America, The University of Arizona Press in collaboration with the Lunar and Planetary Institute.

CASSIDY, T. A. & JOHNSON, R. E. 2005. Monte Carlo model of sputtering and other ejection processes within a regolith. *Icarus,* 176**,** 499-507.

CASSIDY, T. A., PARANICAS, C. P., SHIRLEY, J. H., DALTON, J. B., TEOLIS, B. D., JOHNSON, R. E., KAMP, L. & HENDRIX, A. R. 2013. Magnetospheric ion sputtering and water ice grain size at Europa. *Planetary and Space Science,* 77**,** 64-73.

CHANÉ, E., SAUR, J. & POEDTS, S. 2013. Modeling Jupiter's magnetosphere: Influence of the internal sources. *Journal of Geophysical Research: Space Physics,* 118**,** 2157-2172.
CHUANG, F. C., KADEL, S. D., KLEMASZEWSKI, J. E. & GREELEY, R. Geomorphologic Mapping and Stereo Analysis of Chaos Regions Southeast of the Tyre Multi-Ringed Impact Structure. Fall AGU 1998, 1998 San Francisco, California, USA.
CLARK, G., MAUK, B. H., PARANICAS, C., KOLLMANN, P. & SMITH, H. T. 2016. Charge states of energetic oxygen and sulfur ions in Jupiter's magnetosphere. *Journal of Geophysical Research-Space Physics,* 121**,** 2264-2273.
COLLINS, G. C., HEAD, J. W., PAPPALARDO, R. T. & SPAUN, N. A. 2000. Evaluation of models for the formation of chaotic terrain on Europa. *Journal of Geophysical Research-Planets,* 105**,** 1709-1716.
COOK, A. C. & ROBINSON, M. S. 2000. Mariner 10 stereo image coverage of Mercury. *Journal of Geophysical Research-Planets,* 105**,** 9429-9443.
COWLEY, S. W. H. & BUNCE, E. J. 2003. Corotation-driven magnetosphere-ionosphere coupling currents in Saturn's magnetosphere and their relation to the auroras. *Annales Geophysicae,* 21**,** 1691-1707.
COX, R. & BAUER, A. W. 2015. Impact breaching of Europa's ice: Constraints from numerical modeling. *Journal of Geophysical Research-Planets,* 120**,** 1708-1719.
DALTON, J. B., CRUIKSHANK, D. P., STEPHAN, K., MCCORD, T. B., COUSTENIS, A., CARLSON, R. W. & CORADINI, A. 2010. Chemical Composition of Icy Satellite Surfaces. *Space Science Reviews,* 153**,** 113-154.
DAY, T., COOK, A. C. & MULLER, J.-P. Automated Digital Topographic Mapping Techniques for Mars. American Society of Photogrammetry & Remote Sensing, 1992 Washington D.C.: International Archives of Photogrammetry and Remote Sensing, 801-808.
DOMINGUE, D. & VERBISCER, A. 1997. Re-analysis of the solar phase curves of the icy Galilean satellites. *Icarus,* 128**,** 49-74.
DOUGHERTY, L. P., BODISCH, K. M. & BAGENAL, F. 2017. Survey of Voyager plasma science ions at Jupiter: 2. Heavy ions. *Journal of Geophysical Research-Space Physics,* 122**,** 8257-8276.
FAGENTS, S. A., GREELEY, R., SULLIVAN, R. J., PAPPALARDO, R. T., PROCKTER, L. M. & GALILEO, S. S. I. T. 2000. Cryomagmatic mechanisms for the formation of Rhadamanthys linea, triple band margins, and other low-albedo features on Europa. *Icarus,* 144**,** 54-88.
FAMA, M., SHI, J. & BARAGIOLA, R. A. 2008. Sputtering of ice by low-energy ions. *Surface Science,* 602**,** 156-161.
FAMA, M., TEOLIS, B. D., BAHR, D. A. & BARAGIOLA, R. A. 2007. Role of electron capture in ion-induced electronic sputtering of insulators. *Physical Review B,* 75**,** 4.
FIGUEREDO, P. H. & GREELEY, R. 2004. Resurfacing history of Europa from pole-to-pole geological mapping. *Icarus,* 167**,** 287-+.
FOSSEN, H. 2010. *Structural Geology,* The United States of America, New York, Cambridge University Press, New York.
FRANKOT, R. T. & CHELLAPPA, R. 1988. A METHOD FOR ENFORCING INTEGRABILITY IN SHAPE FROM SHADING ALGORITHMS. *Ieee Transactions on Pattern Analysis and Machine Intelligence,* 10**,** 439-451.
GALLI, A., VORBURGER, A., WURZ, P., CERUBINI, R. & TULEJ, M. 2018. First experimental data of sulphur ions sputtering water ice. *Icarus,* 312**,** 1-6.
GEISSLER, P. E., GREENBERG, R., HOPPA, G., MCEWEN, A., TUFTS, R., PHILLIPS, C., CLARK, B., OCKERT-BELL, M., HELFENSTEIN, P., BURNS, J., VEVERKA, J., SULLIVAN, R., GREELEY, R., PAPPALARDO, R. T., HEAD, J. W., BELTON, M. J. S. & DENK, T. 1998. Evolution of lineaments on Europa: Clues from Galileo multispectral imaging observations. *Icarus,* 135**,** 107-126.
GREENBERG, R., GEISSLER, P., HOPPA, G., TUFTS, B. R., DURDA, D. D., PAPPALARDO, R., HEAD, J. W., GREELEY, R., SULLIVAN, R. & CARR, M. H. 1998. Tectonic processes on Europa: Tidal stresses, mechanical response, and visible features. *Icarus,* 135**,** 64-78.

HENDRIX, A. R., BARTH, C. A., HORD, C. W. & LANE, A. L. 1998. Europa: Disk-resolved ultraviolet measurements using the Galileo ultraviolet spectrometer. *Icarus,* 135**,** 79-94.
HENDRIX, A. R. & JOHNSON, R. E. 2008. CALLISTO: NEW INSIGHTS FROM GALILEO DISK-RESOLVED UV MEASUREMENTS. *Astrophysical Journal,* 687**,** 706-713.
HOWARD, A. D. & MOORE, J. M. 2008. Sublimation-driven erosion on Callisto: A landform simulation model test. *Geophysical Research Letters,* 35**,** 4.
HOYER, L., KATTENHORN, S. A. & WATKEYS, M. K. 2014. Multistage evolution and variable motion history of Agenor Linea, Europa. *Icarus,* 232**,** 60-80.
HUDDLESTON, D. E., STRANGEWAY, R. J., BLANCO-CANO, X., RUSSELL, C. T., KIVELSON, M. G. & KHURANA, K. K. 2000. IO-Jupiter interaction: Waves generated by pickup ions. *Planetary Ionospheres and Magnetospheres,* 26**,** 1513-1518.
HURFORD, T. A., SARID, A. R. & GREENBERG, R. 2007. Cycloidal cracks on Europa: Improved modeling and non-synchronous rotation implications. *Icarus,* 186**,** 218-233.
HUYBRIGHS, H. L. F., FUTAANA, Y., BARABASH, S., WIESER, M., WURZ, P., KRUPP, N., GLASSMEIER, K. H. & VERMEERSEN, B. 2017. On the in-situ detectability of Europa ' s water vapour plumes from a flyby mission. *Icarus,* 289**,** 270-280.
IP, W. H., KOPP, A., WILLIAMS, D. J., MCENTIRE, R. W. & MAUK, B. H. 2000. Magnetospheric ion sputtering: The case of Europa and its surface age. *Planetary Ionospheres and Magnetospheres,* 26**,** 1649-1652.
JOHNSON, R. E. 1998. Sputtering and desorption from icy surfaces. *Solar System Ices,* 227**,** 303-334.
JOHNSON, R. E., FAMA, M., LIU, M., BARAGIOLA, R. A., SITTLER, E. C., JR. & SMITH, H. T. 2008. Sputtering of ice grains and icy satellites in Saturn's inner magnetosphere. *Planetary and Space Science,* 56**,** 1238-1243.
JOHNSON, T. V. 2000. The Galileo mission to Jupiter and its moons. *Scientific American,* 282**,** 40-49.
JUN, I., GARRETT, H. B., SWIMM, R., EVANS, R. W. & CLOUGH, G. 2005. Statistics of the variations of the high- energy electron population between 7 and 28 jovian radii as measured by the Galileo spacecraft. *Icarus,* 178**,** 386-394.
KADEL, S. D., CHUANG, F. C., GREELEY, R., MOORE, J. M. & GALILEO, S. S. I. T. 2000. Geological history of the Tyre region of Europa: A regional perspective on Europan surface features and ice thickness. *Journal of Geophysical Research-Planets,* 105**,** 22657-22669.
KATTENHORN, S. A. 2002. Nonsynchronous rotation evidence and fracture history in the Bright Plains region, Europa. *Icarus,* 157**,** 490-506.
KATTENHORN, S. A. & PROCKTER, L. M. 2014. Evidence for subduction in the ice shell of Europa. *Nature Geoscience,* 7**,** 762-767.
KHURANA, K. K. 2001. Influence of solar wind on Jupiter's magnetosphere deduced from currents in the equatorial plane. *Journal of Geophysical Research-Space Physics,* 106**,** 25999-26016.
KHURANA, K. K., KIVELSON, M. G., STEVENSON, D. J., SCHUBERT, G., RUSSELL, C. T., WALKER, R. J. & POLANSKEY, C. 1998. Induced magnetic fields as evidence for subsurface oceans in Europa and Callisto. *Nature,* 395**,** 777-780.
KIVELSON, M. G., KHURANA, K. K., JOY, S., RUSSELL, C. T., SOUTHWOOD, D. J., WALKER, R. J. & POLANSKEY, C. 1997. Europa's magnetic signature: Report from Galileo's pass on 19 December 1996. *Science,* 276**,** 1239-1241.
KIVELSON, M. G., KHURANA, K. K., RUSSELL, C. T., VOLWERK, M., WALKER, R. J. & ZIMMER, C. 2000. Galileo magnetometer measurements: A stronger case for a subsurface ocean at Europa. *Science,* 289**,** 1340-1343.
KIVELSON, M. G. & RUSSELL, C. T. 1995. *Introduction to Space Physics,* United States of America by Cambridge University Press New York, Cambridge University Press.
KUSKOV, O. L. & KRONROD, V. A. 2005. Internal structure of Europa and Callisto. *Icarus,* 177**,** 550-569.
LELLOUCH, E. 2005. Io's atmosphere and surface-atmosphere interactions. *Space Science Reviews,* 116**,** 211-224.

MARTIN, A. & MCMINN, A. 2018. Sea ice, extremophiles and life on extra-terrestrial ocean worlds. *International Journal of Astrobiology,* 17**,** 1-16.

MAUK, B. H., MITCHELL, D. G., MCENTIRE, R. W., PARANICAS, C. P., ROELOF, E. C., WILLIAMS, D. J., KRIMIGIS, S. M. & LAGG, A. 2004. Energetic ion characteristics and neutral gas interactions in Jupiter's magnetosphere. *Journal of Geophysical Research-Space Physics,* 109.

MCNUTT, R. L., BELCHER, J. W. & BRIDGE, H. S. 1981. POSITIVE-ION OBSERVATIONS IN THE MIDDLE MAGNETOSPHERE OF JUPITER. *Journal of Geophysical Research-Space Physics,* 86**,** 8319-8342.

MOORE, J. M., ASPHAUG, E., SULLIVAN, R. J., KLEMASZEWSKI, J. E., BENDER, K. C., GREELEY, R., GEISSLER, P. E., MCEWEN, A. S., TURTLE, E. P., PHILLIPS, C. B., TUFTS, B. R., HEAD, J. W., PAPPALARDO, R. T., JONES, K. B., CHAPMAN, C. R., BELTON, M. J. S., KIRK, R. L. & MORRISON, D. 1998. Large impact features on Europa: Results of the Galileo nominal mission. *Icarus,* 135**,** 127-145.

MOORE, J. M., CHAPMAN, C. R., BIERHAUS, E. B., GREELEY, R., CHUANG, F. C., KLEMASZEWSKI, J., CLARK, R. N., DALTON, J. B., HIBBITTS, C. A., SCHENK, P. M., SPENCER, J. R. & WAGNER, R. 2004. *Callisto,* United Kingdom: University Press, Cambridge, University Press Cambridge.

MORRISON, D. & BURNS, J. A. 1976. *Jupiter Studies of the interior, atmosphere, magnetosphere and satellites.*

Jovian Satellites, USA, Tuscon, Arizona, The University of Arizona Press.

NESS, N. F. 1992. PROJECT VOYAGER - A GRAND TOUR TO THE GIANT PLANETS JUPITER, SATURN, URANUS AND NEPTUNE. *Plasma Physics and Controlled Fusion,* 34**,** 1759-1766.

NIMMO, F., PROCKTER, L. & SCHENK, P. 2005. Europa's icy shell: Past and present state, and future exploration. *Icarus,* 177**,** 293-296.

NORTHON, K. Sept. 26, 2016. *NASA's Hubble Spots Possible Water Plumes Erupting on Jupiter's Moon Europa* [Online]. [Accessed].

PARANICAS, C., MAUK, B. H., KHURANA, K., JUN, I., GARRETT, H., KRUPP, N. & ROUSSOS, E. 2007. Europa's near-surface radiation environment. *Geophysical Research Letters,* 34.

PARANICAS, C., MAUK, B. H., RATLIFF, J. M., COHEN, C. & JOHNSON, R. E. 2002. The ion environment near Europa and its role in surface energetics. *Geophysical Research Letters,* 29**,** 4.

PRIETO-BALLESTEROS, O., KARGEL, J. S., FERNANDEZ-SAMPEDRO, M., SELSIS, F., MARTINEZ, E. S. & HOGENBOOM, D. L. 2005. Evaluation of the possible presence of clathrate hydrates in Europa's icy shell or seafloor. *Icarus,* 177**,** 491-505.

RADIOTI, A., KRUPP, N., WOCH, J., LAGG, A., GLASSMEIER, K. H. & WALDROP, L. S. 2005. Ion abundance ratios in the Jovian magnetosphere. *Journal of Geophysical Research-Space Physics,* 110**,** 11.

REEVES, G. D., CAYTON, T. E., GARY, S. P. & BELIAN, R. D. 1992. THE GREAT SOLAR ENERGETIC PARTICLE EVENTS OF 1989 OBSERVED FROM GEOSYNCHRONOUS ORBIT. *Journal of Geophysical Research-Space Physics,* 97**,** 6219-6226.

ROTH, L., RETHERFORD, K. D., IVCHENKO, N., SCHLATTER, N., STROBEL, D. F., BECKER, T. M. & GRAVA, C. 2017. DETECTION OF A HYDROGEN CORONA IN HST Ly alpha IMAGES OF EUROPA IN TRANSIT OF JUPITER. *Astronomical Journal,* 153**,** 10.

SCHMIDT, B. E., BLANKENSHIP, D. D., PATTERSON, G. W. & SCHENK, P. M. 2011. Active formation of 'chaos terrain' over shallow subsurface water on Europa. *Nature,* 479**,** 502-505.

SKINNER, T. E. & DURRANCE, S. T. 1986. NEUTRAL OXYGEN AND SULFUR DENSITIES IN THE IO TORUS. *Astrophysical Journal,* 310**,** 966-971.

SMITH, C. G. A. & AYLWARD, A. D. 2009. Coupled rotational dynamics of Jupiter's thermosphere and magnetosphere. *Annales Geophysicae,* 27**,** 199-230.

SORENSEN, T. C., ARMSTRONG, T. R., PAVANASAM, A. G. & TAHERION, S. 2005. Galileo energetic particle detector observations of the spatial distributions and energy spectra of > 1 and > 11 MeV electrons in the 10-40 R-J region of the jovian magnetosphere. *Icarus,* 178**,** 395-405.

TISCARENO, M. S. & GEISSLER, P. E. 2003. Can redistribution of material by sputtering explain the hemispheric dichotomy of Europa? *Icarus,* 161**,** 90-101.
WALKER, R. J. & OGINO, T. 2003. A simulation study of currents in the Jovian magnetosphere. *Planetary and Space Science,* 51**,** 295-307.
WILLIAMS, D. J. 1996. Jupiter - At last! *Johns Hopkins Apl Technical Digest,* 17**,** 338-356.
WILLIAMS, D. J., MCENTIRE, R. W., JASKULEK, S. & WILKEN, B. 1992. THE GALILEO ENERGETIC PARTICLES DETECTOR. *Space Science Reviews,* 60**,** 385-412.
ZAHNLE, K., ALVARELLOS, J. L., DOBROVOLSKIS, A. & HAMILL, P. 2008. Secondary and sesquinary craters on Europa. *Icarus,* 194**,** 660-674.
ZAHNLE, K., DONES, L. & LEVISON, H. F. 1998. Cratering rates on the Galilean satellites. *Icarus,* 136**,** 202-222.
ZIEGLER, J. F., ZIEGLER, M. D. & BIERSACK, J. P. 2010. SRIM - The stopping and range of ions in matter (2010). *Nuclear Instruments & Methods in Physics Research Section B-Beam Interactions with Materials and Atoms,* 268**,** 1818-1823.